

AD-A244 461



2

PL-TR-91-2276(III)

DTIC  
S  
C  
D

**DEVELOPMENT OF A MAGNETOSPHERIC  
SPECIFICATION MODEL**

**Volume III: Appendices F and G**

J. W. Freeman	B. A. Bales
R. A. Wolf	R. V. Hilmer
R. W. Spiro	A. Nagai
G-H. Voigt	R. Lambour
B. A. Hausman	

Rice University  
Department of Space Physics & Astronomy  
Houston, TX 77251

30 June 1991

Final Report Volume III  
15 November 1987-31 March 1990

**APPROVED FOR PUBLIC RELEASE; DISTRIBUTION UNLIMITED**



PHILLIPS LABORATORY  
AIR FORCE SYSTEMS COMMAND  
HANSCOM AIR FORCE BASE, MASSACHUSETTS 01731-5000

01 1210 020

91-17496



This technical report has been reviewed and is approved for publication.

*Michael A. Heinemann*

MICHAEL A. HEINEMANN  
Contract Manager  
Space Plasmas and Fields Br.  
Space Physics Division

*Nelson C. Maynard*

NELSON C. MAYNARD, Chief  
Space Plasmas and Fields Br.  
Space Physics Division

FOR THE COMMANDER

*Rita C. Sagalyn*

RITA C. SAGALYN  
Director  
Space Physics Division

This report has been reviewed by the ESD Public Affairs Office (PA) and is releasable to the National Technical Information Service (NTIS).

Qualified requestors may obtain additional copies from the Defense Technical Information Center. All others should apply to the National Technical Information Service.

If your address has changed, or if you wish to be removed from the mailing list, or if the addressee is no longer employed by your organization, please notify PL/TSI, Hanscom AFB, MA 01731. This will assist us in maintaining a current mailing list.

Do not return copies of this report unless contractual obligations or notices on a specific document require that it be returned.

REPORT DOCUMENTATION PAGE

Form approved  
GPO Cat. # 90-0123

Public reporting burden for this report is estimated to average 1 hour per response, including the time for reviewing instructions, searching existing data sources, gathering and maintaining the data needed, and completing and reviewing this collection of information. Send comments regarding this burden estimate or any aspect of this collection of information, including suggestions for reducing this burden, to Washington Headquarters Service, Paperwork Project (0122-0046), Washington, DC 20503.

1. AGENCY USE ONLY (Leave blank) 2. REPORT DATE: 30 June 1991 3. REPORT TYPE AND DATES COVERED: Final (15 Nov 1987-31 Mar 1990) Vol III

4. TITLE AND SUBTITLE  
Development of a Magnetospheric Specification Model  
Volume III: Appendices F and G

5. FUNDING NUMBERS  
PE 62101F  
PR 2688  
TA 04  
WU GB

6. AUTHOR(S)  
J. W. Freeman, R.A. Wolf, R. W. Spiro, G-H. Voigt, B. A. Hausman, B. A. Bales, R. V. Hilmer, A. Nagai, R. Lambour

Contract:  
F19628-87-K-0001

7. PERFORMING ORGANIZATION NAME(S) AND ADDRESS(ES)  
Rice University  
Department of Space Physics & Astronomy  
Houston, TX 77251

8. PERFORMING ORGANIZATION REPORT NUMBER

9. SPONSORING/MONITORING AGENCY NAME(S) AND ADDRESS(ES)  
Phillips Laboratory  
Hanscom AFB, MA 01731-5000  
Contract Manager: Michael Heinemann/PHG

10. SPONSORING/MONITORING REPORT NUMBER  
PL-TR-91-2276(III)

11. SUPPLEMENTARY NOTES

12a. DISTRIBUTION STATEMENT (If applicable)  
**APPROVED FOR PUBLIC RELEASE; DISTRIBUTION UNLIMITED**

12b. DISTRIBUTION CODE

Rice University has developed a practical computer model that is capable of specifying electron and ion fluxes in the middle magnetosphere during geomagnetic storms. The model, called the Magnetospheric Specification Model (MSM), uses ground-based and satellite data from the Space Forecast Center-Environment Data Base to establish initial and boundary conditions and to determine input parameters for the magnetic and electric field models. These input values are updated every 15 minutes, and new output fluxes are computed for the same times. The primary function of the MSM is the specification of fluxes of 1-100 KeV electrons in the geostationary orbit region. However, it is also designed to specify a broad range of additional parameters for the global ionospheric-magnetospheric system, including fluxes of 1-50 KeV ions, auroral electron precipitation and ionospheric electric fields.

14. SUBJECT TERMS  
Electron fluxes    Spacecraft charging    Magnetic storms  
Ion fluxes        Radiation belts        Proton fluxes  
Magnetosphere    Space radiation       Geomagnetic storms  
Trapped radiation    Energetic particles

15. NUMBER OF PAGES  
239

16. PRICE CODE

17. SECURITY CLASSIFICATION OF REPORT  
Unclassified

18. SECURITY CLASSIFICATION OF THIS PAGE  
Unclassified

19. SECURITY CLASSIFICATION OF ABSTRACT  
Unclassified

20. LIMITATION OF ABSTRACT  
SAR

**CONT OF BLOCK 13:**

The model is accompanied by an application program that allows specification of fluxes at an arbitrary point in the magnetosphere within the modeling region. Consistent with its primary function, the MSM has been tested against spacecraft data for 2 substantial storms and has been shown to produce a good characterization of the enhancements of 40 KeV electron fluxes in the equatorial plane. The model never failed to predict high fluxes when they were observed, although it did predict high fluxes in some cases when they were not observed and it did fail to predict flux dropouts observed by the spacecraft. The MSM is ready for adaptation for use in an operational setting where the goal is real-time and retrospective specification of hazardous charged particle fluxes associated with geomagnetic storms.

Appendix F

**A MAGNETOSPHERIC MAGNETIC FIELD MODEL  
WITH FLEXIBLE INTERNAL CURRENT SYSTEMS**

by

Robert V. Hilmer

Accession For	
DTIC US&A	<input checked="" type="checkbox"/>
DTIC TAB	<input type="checkbox"/>
Unannounced	<input type="checkbox"/>
Justification	
By	
Distribution/	
Availability Codes	
Avail and/or	
Dist	Special
A-1	

Rice University  
Department of Space Physics and Astronomy  
Houston, Texas  
May 1989



RICE UNIVERSITY

A MAGNETOSPHERIC MAGNETIC FIELD MODEL  
WITH FLEXIBLE INTERNAL CURRENT SYSTEMS

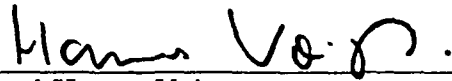
by

ROBERT VINCENT HILMER

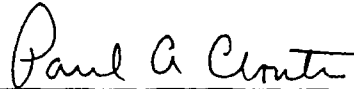
A THESIS SUBMITTED  
IN PARTIAL FULFILLMENT OF THE  
REQUIREMENTS FOR THE DEGREE

DOCTOR OF PHILOSOPHY

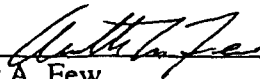
APPROVED, THESIS COMMITTEE:



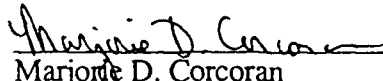
Gerd-Hannes Voigt  
Senior Research Scientist  
Center for Space Physics, Chairman



Paul A. Cloutier  
Professor of Space Physics and Astronomy



Arthur A. Few  
Professor of Space Physics and Astronomy



Marjorie D. Corcoran  
Associate Professor of Physics

Houston, Texas

May, 1989

A MAGNETOSPHERIC MAGNETIC FIELD MODEL  
WITH FLEXIBLE INTERNAL CURRENT SYSTEMS

by Robert Vincent Hilmer

Abstract

A three dimensional  $\mathbf{B}$ -field model of the Earth's magnetosphere satisfying the condition  $\nabla \cdot \mathbf{B} = 0$  is described. Highly flexible ring and cross-tail current systems are combined with the vacuum  $\mathbf{B}$ -field model of Voigt [1981], a fully shielded dipole within a fixed magnetopause geometry. The ring current consists of nested eastward and westward flowing current distributions which tilt with and remain axially symmetric about the magnetic dipole axis. To include realistic flexing of the current sheet with dipole tilt, the intensity and position of the westward flowing cross-tail current in the midnight meridian can be represented by arbitrary functions of the distance along the magnetotail.

Model configurations are completely specified by four initial physical input parameters: the dipole tilt angle, the magnetopause stand-off distance, the geomagnetic index  $D^{st}$ , and the midnight equatorward boundary of the diffuse aurora. These parameters determine the relative position and strength of both the ring and cross-tail currents and provide for a diverse array of configurations including many degrees of magnetotail field stretching. The resulting equatorial flux levels,  $\Delta B$  profiles, and the dipole tilt-dependent shape and position of the neutral sheet compare well with observations. With additional input parameters, the reconfiguration of the geomagnetic tail during magnetospheric substorms is modeled and incorporated into a magnetic field simulation of an observed substorm event. The ring and cross-tail currents, as prescribed by the set of initial input parameters, follow a physically reasonable sequence of development and magnetic flux densities are in general agreement with geosynchronous observations of the event.



## Acknowledgments

I would like to thank Hannes Voigt for his thoughtful guidance and enthusiastic support throughout my graduate career. I am also grateful for having had the privilege of working with Dick Wolf, John Freeman, and Bob Spiro and thank them for their support and invaluable contributions to my research. Thanks also to Arthur Few, Paul Cloutier, and Marjorie Corcoran for serving on my committee.

Special recognition and many warm thanks go to Frank, Hector, Patrick, and Ian and Rene for showing me that there is life beyond these borders and that much of it can be experienced without ever leaving the dinner table. To Naomi, Duane, and Juan for spiritual guidance. To Carole and David for adopting the Yankee foreign student from Jersey. To Umbe and Maria for the intangibles that only "sisters" can provide. To Elle and the rest of the nightshift for hangin' in there. And to all of the students and staff members in the department for creating an extraordinarily pleasant and friendly working environment.

Finally, I am deeply indebted to the Boston firm of Burns, Caruso, Ruderman, Thomas, and Vitale, and would like to thank them for their long distance friendship and cheerful hospitality during my many rejuvenative sabbaticals to their fair city.

Funding for this research was provided by NSF grant ATM-87-01208 and AFGL contracts F19628-87-K-0001 and F19628-86-C-0029.

*To my father,  
for a lifetime of love and opportunity.*

## Table of Contents

Abstract	ii
Acknowledgments	iii
1. Modeling the Earth's Magnetosphere	1
1.1. Introduction	
1.2. Modeling Approach	
1.3. Model Components	
1.4. Physical Approximations	
1.5. Overview	
2. The Vacuum Dipole Configuration	8
2.1. Introduction	
2.2. The Voigt Vacuum Configuration	
3. The Ring Current	20
3.1. Introduction	
3.2. Modeling Approach	
3.3. Ring Current Magnetic Field and Current	
3.4. Comments	
4. The Magnetotail Current	34
4.1. Introduction	
4.2. Modeling Approach	
4.3. Cross-Tail Current Magnetic Field	
4.3.1. A Single Current Segment	
4.3.2. Current Sheet Placement	
4.3.3. Cross-Tail Filament Intensity Profile	
4.3.4. Segment Length and Positioning	
4.3.5. The Y Dependence	
4.4. Cross-Tail Current	
4.5. Comments	
5. Input Parameter Selection	64
5.1. Introduction	
5.2. Vacuum Dipole Parameters	
5.3. Ring Current Parameters	
5.4. Cross-Tail Current Parameters	
5.5. Comments	

6. Integration of Model Components: The Nominal Magnetosphere	80
6.1. Introduction	
6.2. Total Magnetic Field and Current	
6.3. Input Parameter Sensitivity	
7. Reconfiguration of the Geomagnetic Tail During Magnetospheric Substorms	101
7.1. Introduction	
7.2. Disruption Current and Geomagnetic Tail Field Collapse	
7.3. Comments	
8. Physical Comparisons	115
8.1. Introduction	
8.2. CDAW-6 Magnetic Field Simulation	
8.2.1. Simulation Overview	
8.2.2. Comparison with Magnetic Field Data	
8.3. Shape and Position of the Neutral Sheet	
8.4. $\Delta B$ Profiles	
9. Summary and Conclusions	143
References	147

## 1. Modeling the Earth's Magnetosphere

### 1.1. Introduction

The complexity of the Earth's magnetosphere is exemplified by the variety of currents required to support its magnetic field structure in the presence of flowing solar wind plasma and the interplanetary magnetic field (IMF). In addition to the magnetic field generated in the Earth's interior, the major contributors to this structure are the "Chapman-Ferraro" current at the magnetopause, the ring current, the cross-tail current, and the "Birkeland" or field aligned currents (see Figure 1.1). The intensities of these currents fluctuate constantly as they feed into each other and are redistributed within the magnetospheric current network.

Models of these magnetic fields and currents are constructed for a variety of purposes. On the most basic level, their output can be compared with observations to enhance our understanding of the interrelationship between magnetic field structures and the behavior of the various current systems. There are also very specific applications. For example, field models can be used to organize satellite data. They can provide the spatial mapping link required to translate the effects of ionospheric electric fields to magnetospheric locations in calculations of large-scale plasma motions [e.g., Harel et al., 1981; Spiro and Wolf, 1984]. They can also be incorporated into specification models which describe the motion and distribution of energetic particles in satellite orbital environments and their precipitation into the ionosphere [Tascione et al., 1988].

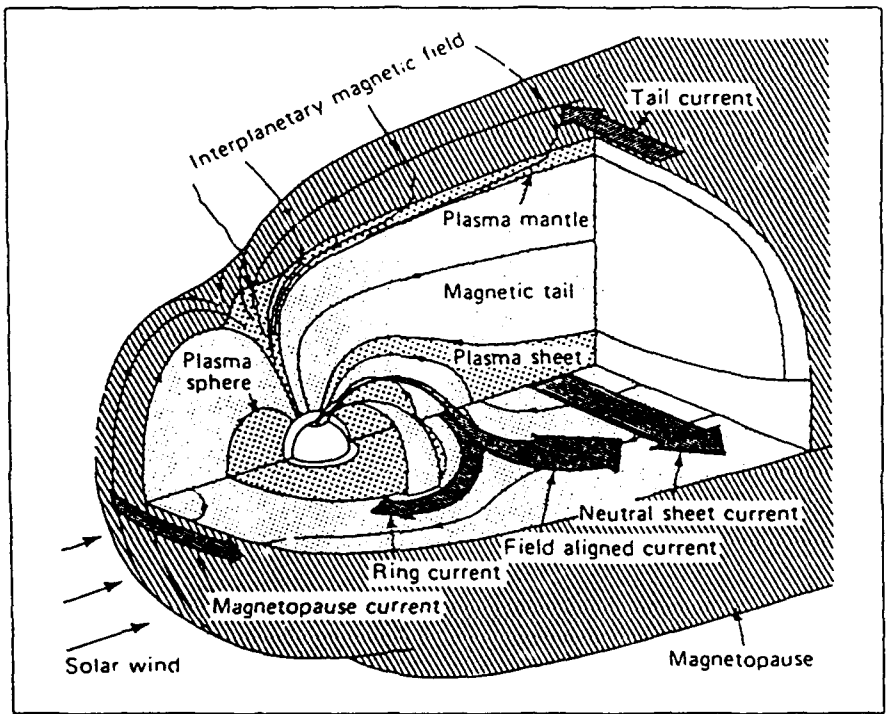


Fig. 1.1. Schematic of the large-scale currents flowing in the Earth's magnetosphere (from Magnetospheric Currents, Geophys. Monogr. Ser., 28, edited by T. A. Potemra, p. viii, AGU, Washington, D. C., 1984).

A model of magnetic fields and currents must be able to realistically represent many diverse magnetospheric configurations as well as the most typical or "average" configuration. The specification of these configurations must rely on physical input parameters which can be related to measurable quantities such as the solar wind pressure, geomagnetic disturbance indices, and ionospheric boundary locations of auroral precipitation. The possible permutations of these quantities then define a framework or parameter space within which to describe and relate the different configurations.

The model currents should be physically reasonable and flexible enough to describe the dramatic changes observed in magnetic field patterns. These changes include the distortion of magnetic field magnitudes and mapping characteristics caused by the displacement, growth, and decay of the ring and cross-tail currents, the warping of the plasma sheet associated with the tilting of the Earth's main field, and the modification of the Chapman-Ferraro currents in response to magnetopause size variations. An extreme example of dynamic magnetic field variation is the observed reconfiguration of the geomagnetic tail during magnetospheric substorms.

The purpose of this work is to develop a mathematical model of the Earth's magnetospheric magnetic field which meets all the above criteria. While there are models which adequately represent some of the characteristics just listed, there are no models that contain the flexibility to represent a majority of them, and none that can easily simulate the stages of development of a magnetospheric substorm.

## 1.2. Modeling Approach

Ideal magnetohydrodynamic (MHD) models represent the highest level of quantitative mathematical representation of the Earth's magnetosphere. They can be used

to treat all aspects of the solar wind-magnetosphere system as they provide a unified view of the time development of magnetic and electric fields and plasma convection. The next level of representation is supplied by magnetohydrostatic (MHS) models which assume that the magnetosphere reaches a quiet state of equilibrium and include only very small particle-flow velocities. These models describe time-dependent processes in terms of a slowly varying series of equilibrium states. A review of the different levels of magnetospheric equilibrium representation is provided by Voigt [1986].

While both MHD and MHS models address physical plasma phenomena from a unified point of view, they are characterized by complex and lengthy numerical procedures and are not easily adaptable to the variety of situations we would like to represent. These factors inhibit their use as convenient computational tools, so we turn instead to a more descriptive approach.

From a plasma-physical point of view, the next two levels of magnetic field description are represented by semi-empirical and empirical models. These models do not provide a self-consistent treatment of fields and plasma but rather stress the quantitative reproduction of the observed magnetic field vectors (see the reviews by Walker [1976, 1979] and Stern [1987b] for discussions of these two types of magnetospheric models). The purely empirical models rely on large data sets sorted according to geomagnetic disturbance levels. They lead to fixed average pictures of the magnetosphere using representations based on polynomial expansions with large numbers of coefficients. These models offer little flexibility and contain unphysical distributions of current. In contrast, semi-empirical models include more physically reasonable current distributions to reproduce observed magnetic field configurations. By incorporating modular structures to represent the various current systems, this type of model can provide a high degree of flexibility as the different current components can be



adjusted independently.

We will use a modular semi-empirical approach that relies exclusively on physical input parameters to specify model configurations. This will facilitate application of the model to many different situations and aid in the physical interpretation of model output.

### 1.3. Model Components

The Earth's total magnetospheric magnetic field,  $\mathbf{B}_T$ , can be represented as the sum of contributions from individual internal sources paired with their respective Chapman-Ferraro current fields, namely

$$\mathbf{B}_T = \mathbf{B}_d + \mathbf{B}_{rc} + \mathbf{B}_{tail} + \mathbf{B}_{cfd} + [ \mathbf{B}_{cfrc} + \mathbf{B}_{cftail} ] \quad (1.1)$$

The internal magnetospheric sources include the Earth's main field  $\mathbf{B}_d$  and the distributed ring and cross-tail currents,  $\mathbf{B}_{rc}$  and  $\mathbf{B}_{tail}$ , respectively. The remaining terms,  $\mathbf{B}_{cfd}$ ,  $\mathbf{B}_{cfrc}$ , and  $\mathbf{B}_{cftail}$ , originate from the Chapman-Ferraro currents flowing on the magnetopause surface which confine the magnetic flux of the Earth's main field, ring current field, and cross-tail current field within the magnetopause boundary.

Representations will be provided or developed for the first four terms in equation (1.1). The development of the different components will be carried out separately as each has a preferred coordinate reference frame. We direct our efforts toward representation of the internal field sources. Interactions with the IMF are not addressed, and its magnetic field is assumed to be completely shielded from the interior of the magnetosphere. Also note that magnetic field aligned currents, which contribute greatly to the distortion of the near-earth magnetic field environment, will not be specifically included in this presentation.

#### 1.4. Physical Approximations

The lack of proper representation for the bracketed quantities in equation (1.1) represents a violation of magnetopause boundary conditions as both magnetic flux and current penetrate this surface. This compromise, in combination with the use of a fixed magnetopause shape that is not self-consistently determined using pressure balance calculations, diminishes the physical relevance of our magnetopause boundary. For this reason, no emphasis will be placed on detailing the regions immediately adjacent to this boundary.

All model components will adhere strictly to the requirement that magnetic flux be conserved, namely

$$\nabla \cdot \mathbf{B} = 0 \quad (1.2)$$

Only static representations will be considered ( $\partial/\partial t = 0$ ); consequently, all currents are also divergence-free and follow from the magnetic field as

$$\mathbf{J} = \frac{1}{\mu_0} (\nabla \times \mathbf{B}) \quad (1.3)$$

Although magnetohydrostatic equilibrium (i.e.,  $\mathbf{J} \times \mathbf{B} = \nabla P$ ) is not addressed in this presentation, the flexibility of the current structures should facilitate consideration of this problem on limited spatial scales in the future.

#### 1.5. Overview

We begin with a brief review of the representation to be used for the Earth's main

magnetic field and its associated magnetopause shielding field. The ring and cross-tail current systems are developed in Sections 3 and 4, respectively, and a procedure for selecting model input parameters is presented in Section 5. The model components are integrated to depict the nominal magnetosphere, and the relative impact of the various input parameters on the model are discussed in Section 6. A special state of the magnetosphere, involving the reconfiguration of the geomagnetic tail during magnetospheric substorms, is modeled using a procedure developed in Section 7. Section 8 presents three different physical comparisons of model results with observations. First, there is a brief review of a magnetospheric substorm event simulation performed to explore the physical consequences of the assumptions leading to our input parameter selection procedure. Second, the behavior of the model's magnetic neutral sheet as it tilts with the Earth's main field is examined. Finally, model  $\Delta B$  profiles, which provide a measure of the influence of current sources external to the Earth, and their evolution with changing geomagnetic activity levels are examined and compared with observationally determined profiles.

## 2. The Vacuum Dipole Configuration

### 2.1. Introduction

The Earth's main magnetic field is the dominant magnetic field in the magnetosphere up to a distance of about ten Earth radii. The complete shielding of this field within a fixed magnetopause surface provides a well defined volume within which to locate our ring and cross-tail current systems. If the shielding method can accommodate both the tilting of the main field within the given magnetopause shape and changes in magnetopause size, e.g., compression due to increased solar wind pressure, then many of the observed physical effects attributed to these variations should become partially, if not fully, evident. These effects include the redistribution of magnetic flux and the warping of the magnetic neutral sheet. Note that while a vacuum magnetic field configuration does not have a true neutral sheet, which is usually associated with the presence of current, we adopt the following definition to facilitate comparison with non-vacuum configurations. The neutral sheet is defined as the surface separating field lines of opposite polarity, i.e., where the magnetic component parallel to the line connecting the Earth and the Sun,  $B_{T,x}$ , changes sign.

If tilt effects can be represented in a physically reliable and predictable manner with a vacuum configuration, then the contributions from additional current systems required to maximize the realism of the completed magnetospheric configurations can be determined through comparison with observations. One magnetospheric model that incorporates

vacuum configurations fulfilling the above criteria is described by Voigt [1981].

The magnetic field model of Voigt [1981] consists of the Earth's dipole field, an equatorial ring current, a tail current system, and magnetopause surface currents which control the amount of magnetic flux passing through that boundary. It accounts for dipole-tilt effects and is capable of representing both fully shielded and open magnetospheric states such that interaction with the IMF can be simulated. The analytic solution is derived by treating the magnetopause as an infinitesimally thin discontinuity and enforcing boundary conditions requiring that the magnetic field component normal to the magnetopause surface is equal to zero.

As our starting point, we choose vacuum dipole configurations given by the Voigt model to represent the Earth's main field and its magnetopause shielding field. These sources correspond to the terms  $\mathbf{B}_d$  and  $\mathbf{B}_{cf}$  in equation (1.1). A dipole field is a good approximation for the Earth's main magnetic field, so higher-order magnetic moments are not included at this time. We must first review the model and demonstrate some of its critical physical characteristics, e.g., the mapping properties of magnetic field lines, the equatorial flux distribution, and the motion of the magnetic neutral sheet in relation to that of the Earth's dipole. Awareness of these basic properties is crucial to the development of the other internal current systems.

## 2.2. The Voigt Vacuum Configuration

The Earth's main magnetic field is represented by a centered dipole with moment  $M_d = 6.37104 \times 10^{24}$  (nT-m<sup>3</sup>) which provides a northward pointing magnetic field of 30,746 nT at the equator on the Earth's surface. The magnetopause surface consists of a semi-infinite cylinder of radius R extending anti-sunward together with a hemispherical

cap of the same radius to represent the dayside and a portion of the nightside magnetopause. The radial distance  $R$ , as with all distances referred to in this presentation, is expressed in units of Earth radii ( $1 R_E = 6,371 \times 10^3$  m).

The central axis of the magnetopause structure coincides with the  $x$  axis of the geocentric solar magnetospheric (GSM) coordinate system, where the positive GSM  $x$  axis connects the Earth and the Sun. The GSM  $y$  axis is defined to be perpendicular to the Earth's magnetic dipole such that the  $x$ - $z$  plane contains the dipole axis. The positive  $z$  axis is in the same sense as the northern magnetic pole. The dipole tilt angle  $\psi$  is measured relative to the  $z$  axis in degrees with positive values corresponding to the northern magnetic pole tilting sunward. The GSM system will be used exclusively throughout this discussion to represent Cartesian coordinates so specific reference to it will not always be made.

The distance from the center of the Earth to the dayside magnetopause along the  $x$  axis is the stand-off distance  $r_0$ . This distance is typically less than the radius of the magnetotail, so the Earth (at the origin of our coordinate system) lies sunward of the cap-cylinder interface by a distance equal to  $(R - r_0)$ . Even though the magnetopause shape is not determined self-consistently via pressure balance calculations, the shape of the dayside magnetopause is reasonable owing to the Earth's off-set from this interface (see Figure 9 of Walker [1976]).

The mapping of magnetic field lines emanating from the Earth in the noon-midnight plane is illustrated in Figure 2.1. The dipole field is compressed to fit within the defined magnetopause shape producing a noon-midnight asymmetry in the field structure. All field lines become tangent to the magnetopause at that boundary. Magnetic cusps separate the last field line that maps through the dayside equatorial plane and the first field line to go tailward, i.e., between  $82^\circ$  and  $84^\circ$  latitude on the dayside of the upper panel,

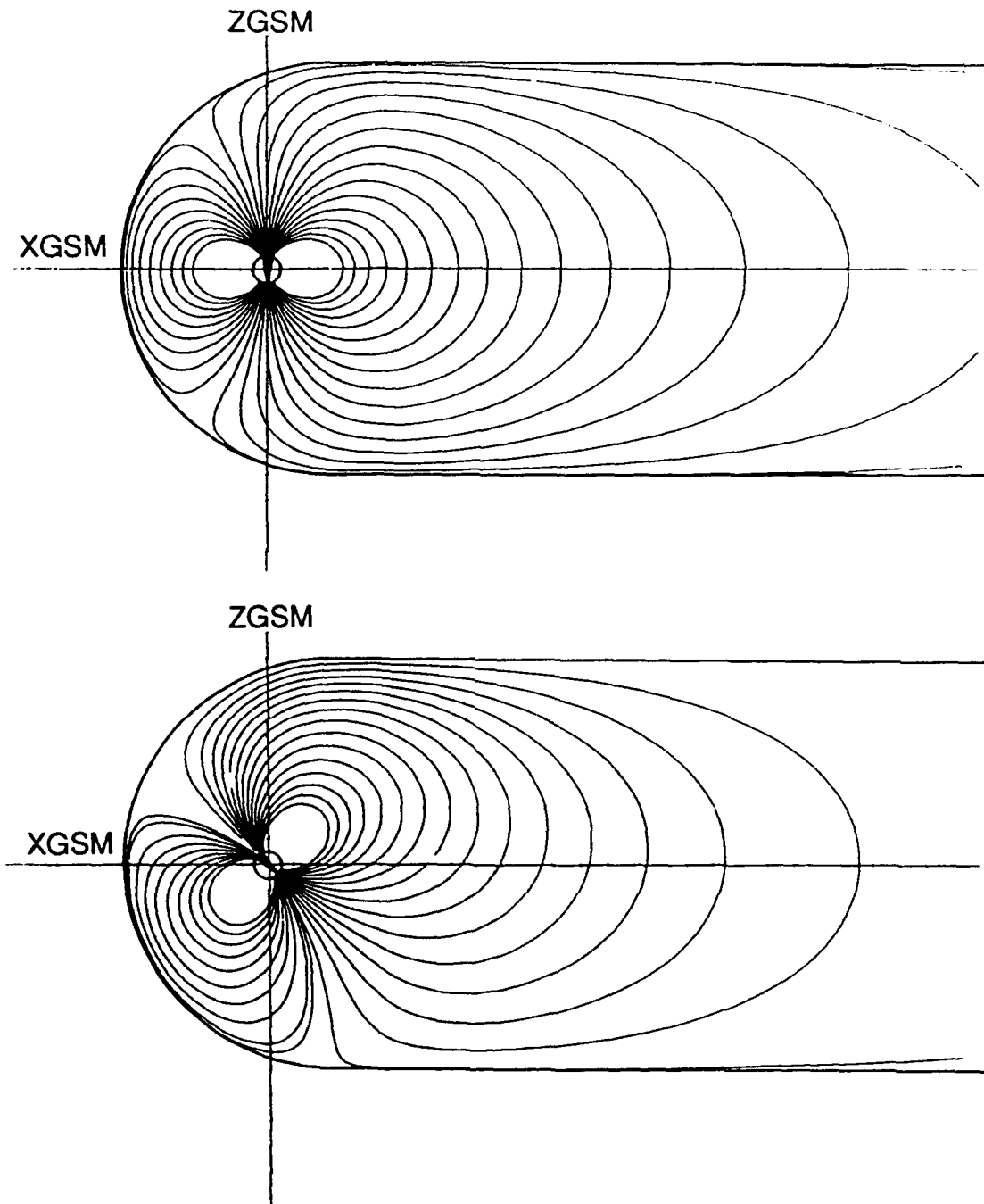


Fig. 2.1. Magnetic field lines in the noon-midnight meridian of a vacuum configuration having  $r_0 = 11 R_E$  and  $R = 16 R_E$  with  $\psi = 0^\circ$  and  $45^\circ$  in the upper and lower panels, respectively. Field lines start from the nightside latitude of  $66^\circ$  and are separated by intervals of  $2^\circ$  in latitude.

and a magnetotail with very rounded field lines forms. When the dipole tilts the cusp position moves to higher latitudes as more flux manages to map through the dayside. Note that for this presentation all latitudes are measured relative to the magnetic dipole in units of degrees.

For the zero-tilt configuration in Figure 2.1, mapping field lines from sets of points at constant latitude to the equatorial plane results in the ring structures shown in Figure 2.2. The lowest latitude of  $56^\circ$  maps to the inner ring and higher latitudes map to progressively larger distances from Earth and form more distorted rings. With all of the magnetic flux being confined within the magnetopause, no incomplete rings will form in the equatorial plane for the vacuum case. Even with the shielding the mapping patterns are fairly rounded and reveal the dipolar nature of the field.

Varying magnetopause size affects the field mapping properties in the magnetotail's midnight meridian ( $y = 0$ ) as illustrated in Figure 2.3. The same latitude maps farther down the magnetotail as the magnetopause gets larger. The limit of this process is represented by the original dipole field and corresponds to an infinite stand-off distance and magnetotail radius. This mapping dependence can be explained from the point of view of magnetic flux conservation.

Figure 2.4 shows the contribution of the magnetopause shielding currents to the equatorial flux levels along the  $x$  axis. The total field magnitudes are obtained by adding the dipole field strength to the value of these individual functions. As the magnetopause gets larger, the magnetic field strength decreases in the equatorial plane and a fixed amount of magnetic flux must pass through a greater area of the equatorial plane. The spreading of this flux translates into field lines reaching more distant magnetotail regions.

Contours of constant equatorial magnetic field strength are shown in Figure 2.5 for the zero-tilt configuration. The dipole field declines very quickly with distance down the



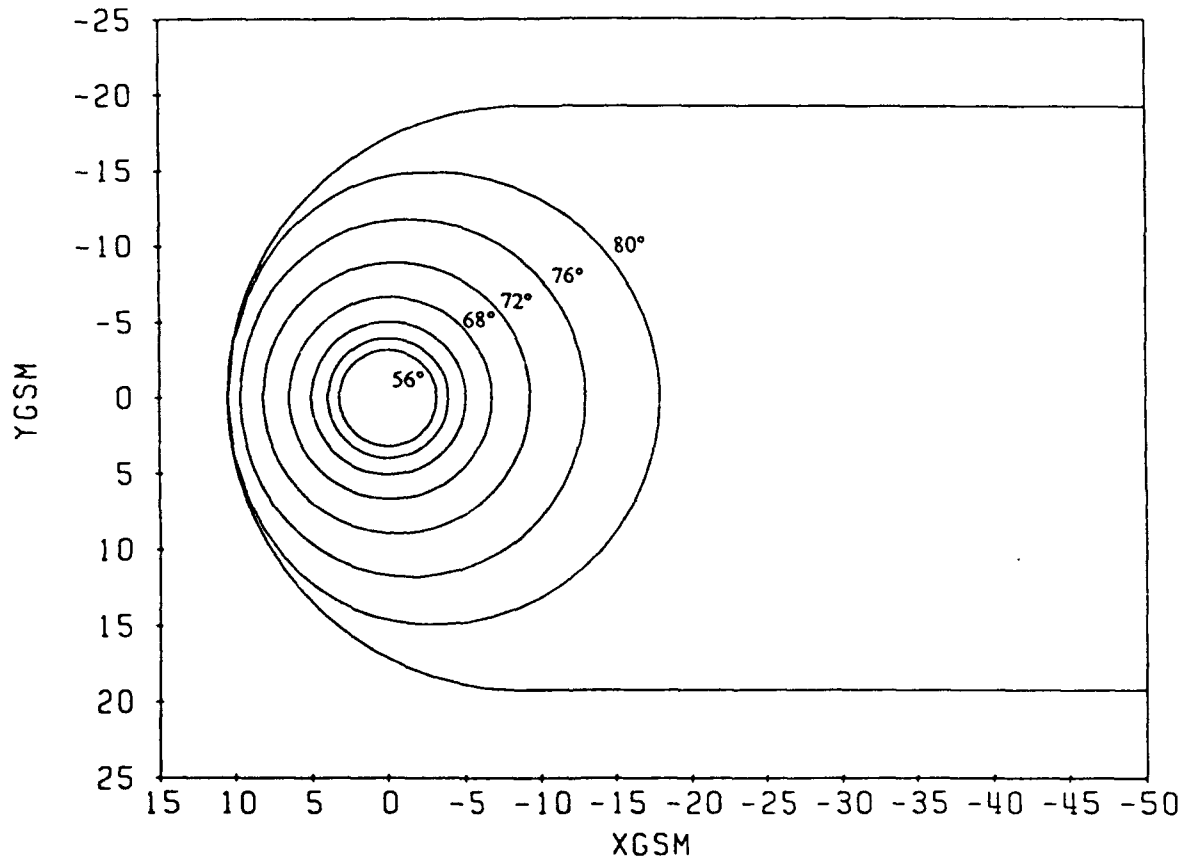


Fig. 2.2. Mapping of magnetic field lines from rings of constant latitude to the equatorial plane for a vacuum configuration with  $\psi = 0^\circ$ ,  $r_o = 10.5 R_E$ , and  $R = 19.2 R_E$ . The inner most ring maps from the Earth's surface at  $56^\circ$  latitude with successive rings separated by  $+4^\circ$  of latitude.

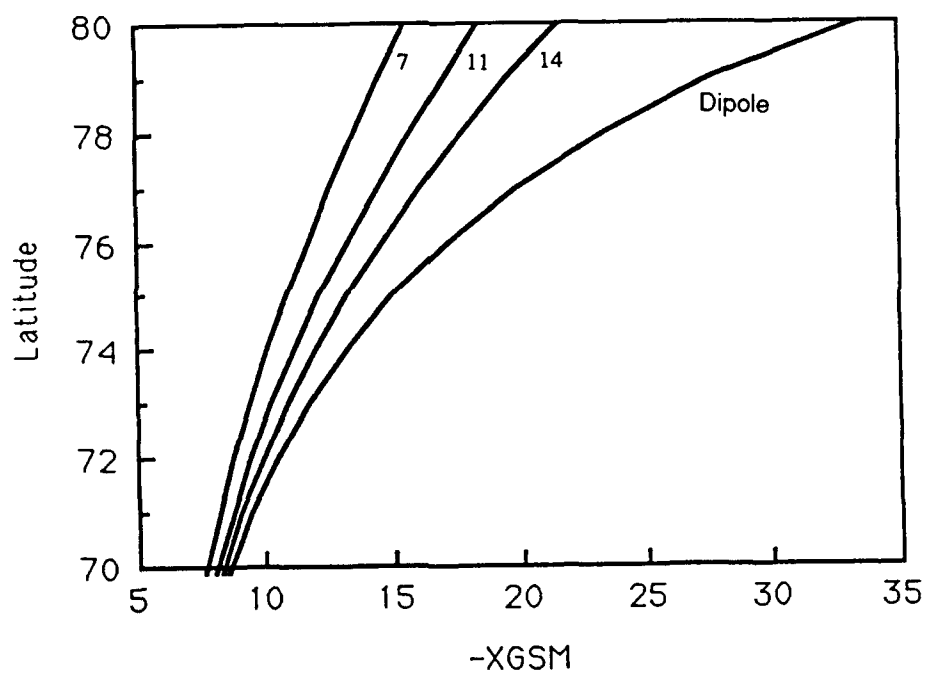


Fig. 2.3. Midnight latitude as a function of the corresponding midnight meridian equatorial mapping distance with  $\psi = 0^\circ$  for vacuum configurations with  $r_0 = 7, 11, 14 R_E$  and  $R = 17, 20, 27 R_E$ , respectively, and for the magnetic dipole representing the Earth's main field.

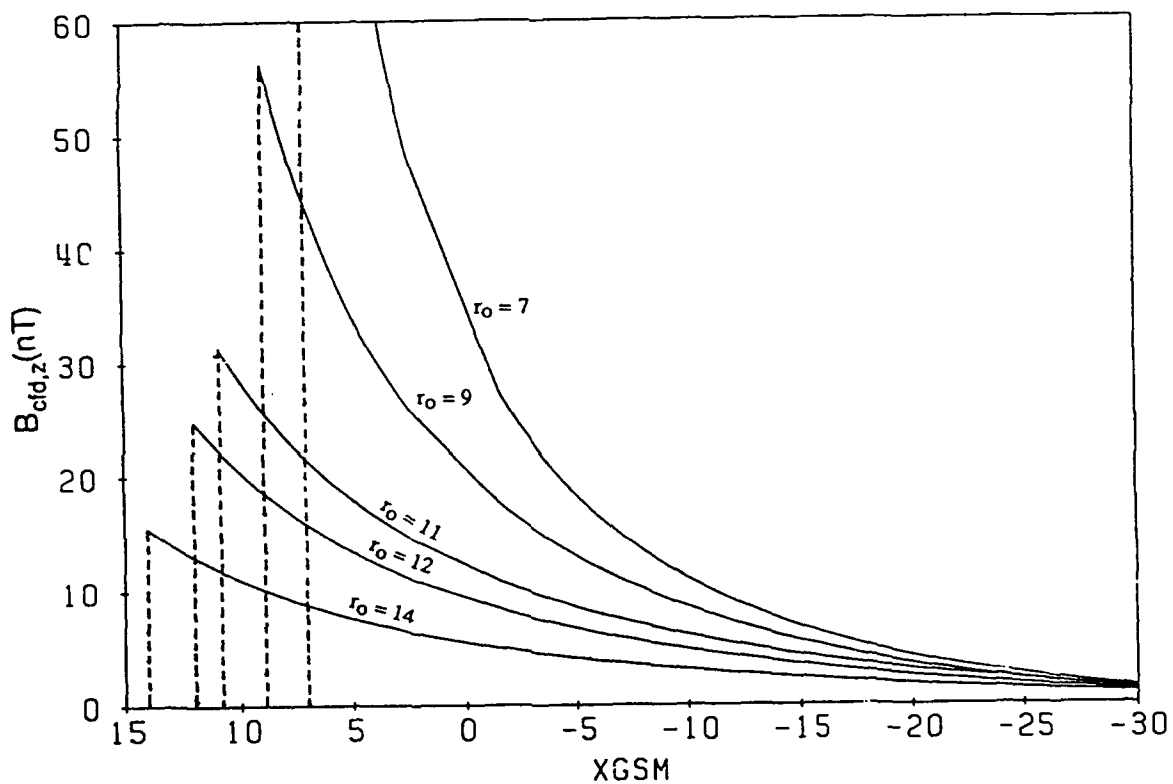


Fig. 2.4. The function  $B_{cfd,z}$  along the  $x$  axis for vacuum configurations with  $r_0 = 7.0, 9.0, 11.0, 12.0,$  and  $14.0 R_E$  and  $R = 17.0, 17.6, 20.0, 21.9,$  and  $27.0 R_E$ , respectively. Owing to complete shielding each function is equal to zero for  $x > r_0$ .

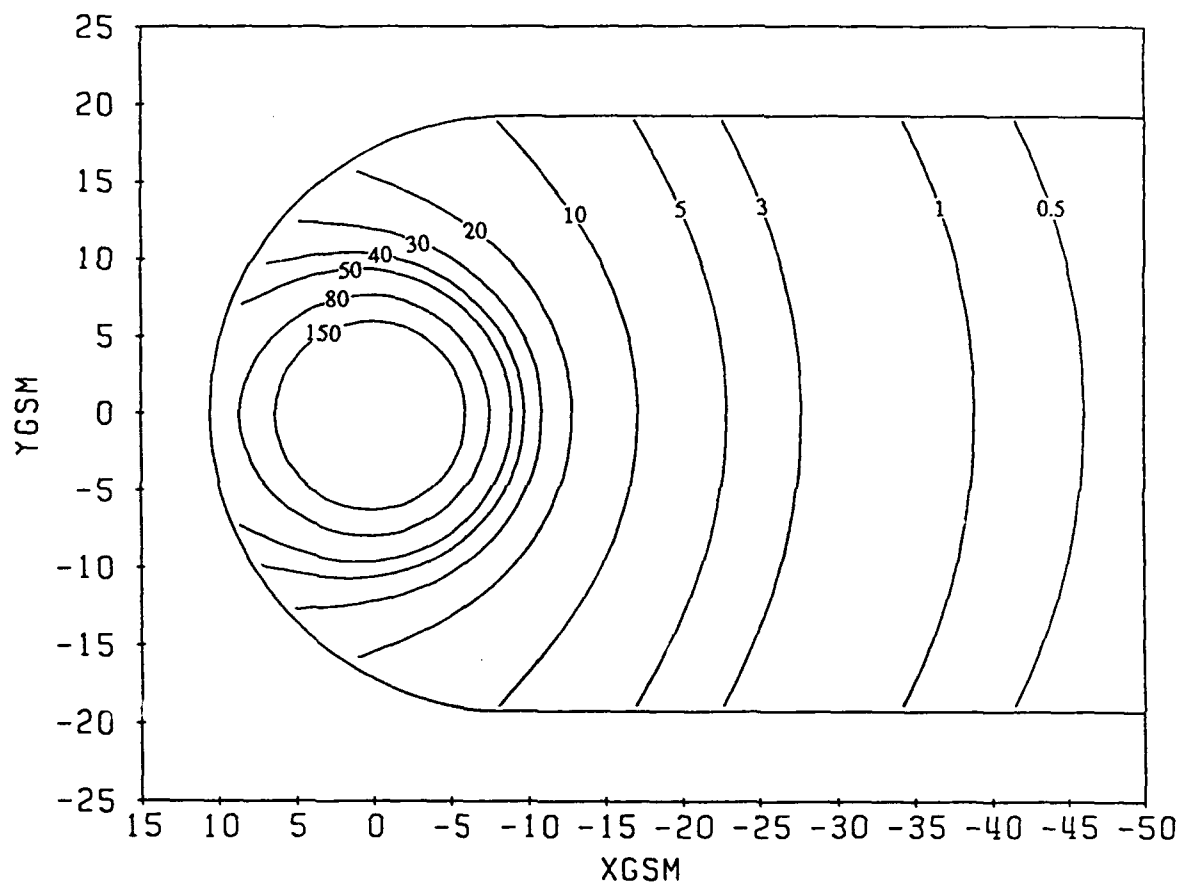


Fig. 2.5. Contours of constant magnetic field magnitude (nT) in the equatorial plane for a vacuum configuration with  $\psi = 0^\circ$ ,  $r_0 = 10.5 R_E$ , and  $R = 19.2 R_E$ . Outside of the defined magnetopause boundary  $|B| = 0$ .

tail and the shielding fields from the previous figure, even though very small in the far tail, dominate that region. The equatorial magnetic field reaches its maximum strength at the center of the tail and decreases toward the flanks.

The dipole shielding currents flow on the magnetopause surface. Near the equatorial plane the dipole shielding current flows sunward along the dawn side (+y) of the magnetopause, passes eastwardly across the front side and returns tailward along the dusk side (-y) magnetopause. In addition, the current flows from dusk to dawn both over and under the magnetotail lobes. The general flow pattern as viewed from above the north pole is counter clockwise for both the upper and lower halves of the magnetopause, thus the dipole shielding current contribution to the equatorial plane flux is in the positive z direction.

Although we have thus far stressed the field magnitudes of the equatorial plane for zero dipole tilt cases, these values represent a relative field strength minimum as the field gains strength as we move into the lobes. In the magnetotail the equatorial plane also corresponds to the magnetic neutral sheet, which is commonly defined as the surface where the x component of the magnetic field changes sign. For cases with  $\psi \neq 0$  the shape of the neutral sheet is dramatically different.

Figure 2.6 illustrates the position of the neutral sheet in the midnight meridian and y-z plane for several dipole tilt angles. As  $|\psi|$  increases the neutral sheet is drawn farther away from the equatorial plane in the near-tail midnight meridian (upper panel), bends away from the dipole magnetic equator to reach a point of maximum deflection, and then gradually approaches the x-y plane with distance down the tail. In the y-z plane (lower panel) the neutral sheet experiences maximum deflection at the tail center and the sheet is actually deflected in the opposite direction for the outer portions of the flanks. This pattern of deflection dampens out and the neutral sheet approaches the equatorial plane

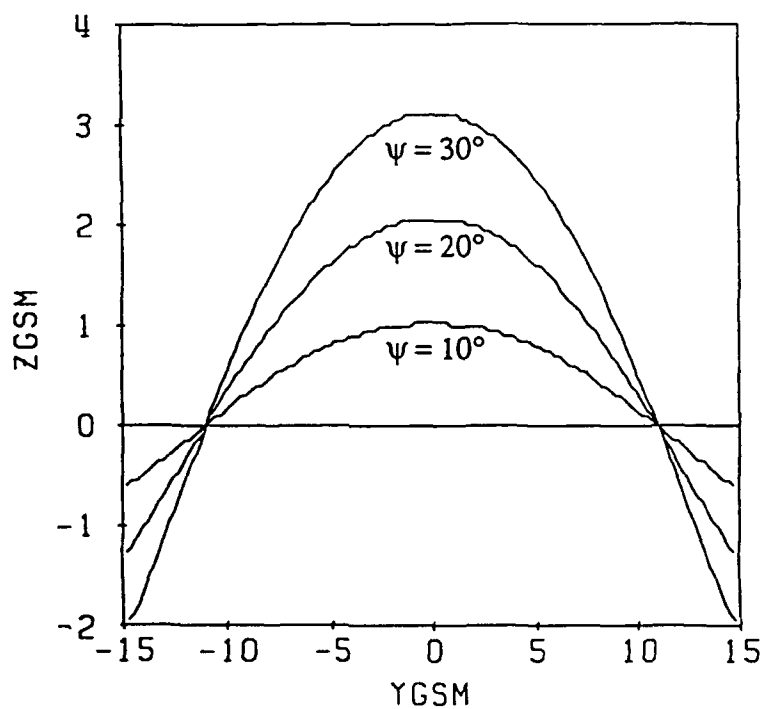
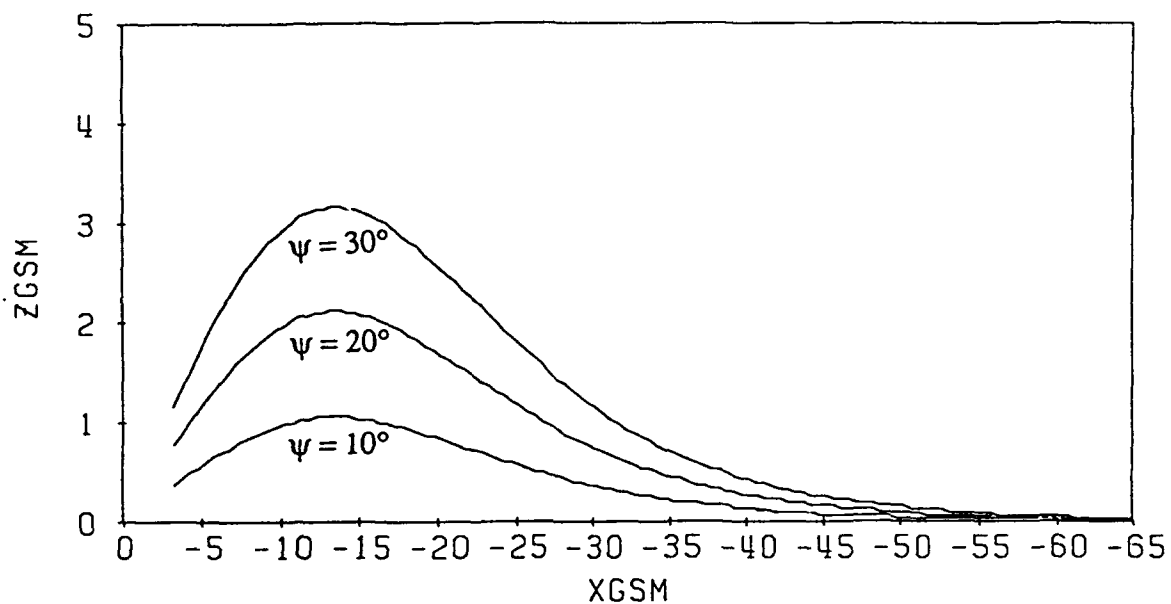


Fig. 2.6. The position of the magnetic neutral sheet for a vacuum configuration having  $r_0 = 10.5 R_E$ ,  $R = 19.2 R_E$ , and  $\psi = 10^\circ$ ,  $20^\circ$ , and  $30^\circ$ . The upper panel illustrates the neutral sheet location in the midnight meridian plane while the lower panel provides a view in the  $y$ - $z$  plane at  $x = -15 R_E$ . Note that the scale of the  $z$  axis has been expanded relative to the  $x$  and  $y$  dimensions.

along the entire width of the tail, following the behavior of center of the neutral sheet, as indicated in the upper panel. With perfect magnetopause shielding this behavior reflects the fact that the total flux passing through the southern lobe must also pass through the northern lobe on its return to the Earth.

These basic characteristics of the vacuum configurations of the Voigt [1981] model will be carefully considered when developing the ring and cross-tail current systems as well as the input parameter selection procedure. In this way, each component can be designed to best complement the vacuum configuration characteristics to achieve the most realistic description of the magnetosphere. We begin with the specification of the ring current model.

### 3. The Ring Current

#### 3.1. Introduction

The ring current is composed of geomagnetically trapped particles, predominantly protons, which originate in both the ionosphere and the solar wind. The particles form a structure that is approximately axially symmetric about the magnetic dipole axis and is also centered about the dipole equatorial plane.

Ring current intensity can change via several generation and decay mechanisms related to the general activity level in the magnetosphere. The ring current tends to strengthen and move earthward during magnetically active times, e.g., during times of increased auroral activity, and tends to weaken and expand during quieter time periods. Ring current growth can, for example, result from enhanced earthward convection of plasma sheet particles and energetic ions streaming out of the ionosphere on auroral field lines. The two main decay mechanisms seem to be charge exchange and pitch angle diffusion. See Balsiger [1983], Lyons and Williams [1984] and Williams [1981, 1986, 1987] for overviews of ring current composition and generation and decay processes.

The current is produced by a combination of processes, including particle pressure gradient drift, magnetic field line curvature driven drift, and particle gyration effects [Parker, 1957]. With particle pressure gradients dominating current generation, the basic character of the current can be revealed from particle pressure information alone. The total particle energy density [Smith and Hoffman, 1973] and particle pressure [Lui et al.,



1987] both peak at radial distances around 3 to 4  $R_E$  near the equatorial plane indicating a reversal of the particle pressure gradient. With the magnetic field pointing northward throughout the equatorial region of the inner magnetosphere, the ring current changes sign near the pressure maximum as indicated by the magnetohydrostatic force balance condition

$$\mathbf{J} \times \mathbf{B} = \nabla P \quad (3.1)$$

Due to the decrease of the magnetic field with radial distance, the broader higher-altitude westward current dominates the lower-altitude eastward current to generally produce a southward deflection of the magnetic field at Earth. This is true even though the inner positive pressure gradient and the peak magnitude of eastward current density can be larger than the corresponding outer ring current quantities [e.g., Lui et al., 1987]. The eastward portion of the ring current is, however, responsible for important variations in the magnetic field distribution.

A convenient way to quantitatively illustrate the magnetic field distortions due to external current sources is by means of the quantity  $\Delta B$ , defined by Sugiura et al. [1971] as the observed magnetic field magnitude minus the magnitude of a geomagnetic reference field. The eastward current lessens the effects of the westward current near the Earth such that the greatest magnetic field depression, i.e., the most negative  $\Delta B$  values, occur at radial equatorial distances of approximately 3  $R_E$  [Sugiura et al., 1971; Sugiura, 1972; Su and Konradi, 1975] even during magnetically active times [Cahill, 1966; Hoffman, 1973]. Although ring current development is not an axially symmetric process [e.g., Sugiura, 1972; Fukushima and Kamide, 1973; Siscoe and Crooker, 1974 and ref. within], with growth predominate in the afternoon and evening magnetic local times, the final character of particle pressure and magnetic field distributions are fairly symmetric

about the Earth [Hoffman, 1973; Smith and Hoffman, 1973; Sugiura, 1973] and are usually intensified relative to the initial quiet state.

### 3.2. Modeling Approach

Ring current models come in many different forms and have been developed for a variety of different purposes, including application to single event data analysis investigations of very localized and dynamic processes and incorporation into globally time averaged models of the magnetospheric magnetic fields. For a review of ring current theory and the earlier models see Carovillano and Siscoe [1973].

There are many models that use measured or assumed particle pressure distributions to calculate self-consistently the currents and associated magnetic fields [e.g., Akasofu et al., 1962; Hoffman and Bracken, 1965, 1967; Sozou and Windle, 1969; Sckopke, 1972]. They include either isotropic or anisotropic treatments of the plasma particle pressure and use force balance constraints similar to equation (3.1). Time dependent models of ring current evolution exist which utilize both linear [e.g., Davies, 1977] and nonlinear time dependent methods [e.g., Feldstein et al., 1984], while the model of Siscoe [1979] demonstrates a method intermediate to the static self-consistent and time dependent models and describes the quasi-self-consistent generation of the ring current from pre-storm conditions.

Another class of models is empirically based, with emphasis placed on reproducing observed magnetic field patterns, and are designed with fewer physical constraints. Included in this group are representations with single wire loops or a system of strategically placed wire loops, as with the magnetospheric model of Olson and Pfitzer [1974], and ones with a flat current disk as used by Sugiura and Poros [1973]. In

addition, there is the magnetic dipole related formulation used by Tsyganenko and Usmanov [1982] and Tsyganenko [1987] and more recently, the very promising method of Kosik [1989] which is based on the use of toroidal and poloidal vector fields.

A problem with the typical self-consistent toroidal models, as pointed out by Sugiura et al. [1971] and Sugiura [1972], is that they tend to have maximum field depressions near the center of the their ring current belts that recover too quickly before leveling off toward Earth. The time dependent models, while interesting in their own right, tend to have limited spatial applicability. Finally, the empirically based models, except the one mentioned by Kosik which is not flexible enough for our purposes, have obvious fundamental problems concerning the resulting magnetic field patterns and/or the unphysical nature of the current structure (i.e., they contain current discontinuities or do not include eastward traveling currents).

We are therefore left with the task of developing a highly flexible ring current model which includes both physically reasonable current and magnetic field distributions. This will be accomplished by constructing a current system, derived from magnetic vector potentials, that includes both eastward and westward traveling current.

### 3.3. Ring Current Magnetic Field and Current

An Earth-centered cylindrical coordinate system  $(\rho, \phi, z)$ , with the  $z$  axis aligned with the ring-current central axis and anti-parallel to the geodipole, is adopted to take advantage of the ring current's axially symmetric structure. The ring current lies centered in the dipole equatorial plane and tilts with the dipole in the GSM  $x$ - $z$  plane.

The ring current formulation begins with a function  $A_\phi(\rho, z)$  which we identify as the  $\phi$  component of the magnetic vector potential satisfying the Coulomb gauge  $\nabla \cdot \mathbf{A} = 0$ .

The function  $A_\phi$  contains two parts, each differing from a pure dipole potential by the last term in the denominator.

$$A_\phi = \frac{4B_+\rho_+^3\rho}{[\rho^2 + z^2 + 4\rho_+^2]^{3/2}} + \frac{4B_-\rho_-^3\rho}{[\rho^2 + z^2 + 4\rho_-^2]^{3/2}} \quad (3.2)$$

The quantities  $B_+$ ,  $B_-$ ,  $\rho_+$ , and  $\rho_-$  are the ring current input parameters. The first term leads us to an eastward traveling current system with characteristic radius  $\rho_+$  and produces a maximum northward magnetic deflection of size  $B_+$  at the center of the Earth. Similarly, the second term results in a westward traveling current distribution with characteristic radius  $\rho_-$  and a maximum southward magnetic deflection  $B_-$ . Note that Tsyganenko and Usmanov [1982] and Tsyganenko [1987] begin with a vector potential similar to the second term of equation (3.2), but exclude eastward traveling currents from their description. The factors of 4 in the denominators help establish a physically reasonable relationship between the total current and magnetic field distributions, as will be shown below, while the factors of 4 in the numerators are just a mathematical convenience.

In cylindrical coordinates, this single component vector potential (equation (3.2)) produces two axially symmetric magnetic field components,  $B_\rho$  and  $B_z$ , as determined by

$$\mathbf{B} = \nabla \times \mathbf{A} \quad (3.3)$$

The ring current magnetic field components are

$$B_{rc,\rho} = \frac{12B_+\rho_+^3\rho z}{[\rho^2 + z^2 + 4\rho_+^2]^{5/2}} + \frac{12B_-\rho_-^3\rho z}{[\rho^2 + z^2 + 4\rho_-^2]^{5/2}} \quad (3.4)$$

$$B_{rc,\phi} = 0 \quad (3.5)$$

$$B_{rc,z} = 4B_+\rho_+^3 \frac{2z^2 - \rho^2 + 8\rho_+^2}{[\rho^2 + z^2 + 4\rho_+^2]^{5/2}} + 4B_-\rho_-^3 \frac{2z^2 - \rho^2 + 8\rho_-^2}{[\rho^2 + z^2 + 4\rho_-^2]^{5/2}} \quad (3.6)$$

where  $B_+$  and  $B_-$  are expressed in nanoTesla (nT) and  $\rho$ ,  $z$ ,  $\rho_+$ , and  $\rho_-$  are in units of Earth radii. With equations (3.4) to (3.6) derived from a vector potential the ring current magnetic field automatically satisfies the conservation of flux condition  $\nabla \cdot \mathbf{B} = 0$ .

In the typical situation, with  $|B_-| > |B_+|$  and  $\rho_- > \rho_+$ , the magnetic field in the dipole equatorial plane,  $B_{rc,z}$ , varies as shown in Figure 3.1. The quantity  $B_{rc,z}$  is negative near the Earth, reaches a minimum around  $\rho = 3 R_E$  and recovers to small positive values before diminishing again with greater radial distance. Figure 3.2 shows contours of ring current magnetic field strength, symmetric about both the  $z = 0$  plane and the  $z$  axis, in a plane containing both  $\rho$  and  $z$ . The maximum field strength is found in the  $z = 0$  plane, at the location of the minimum in Figure 3.1, and declines steadily in all directions beyond a spherical radial distance of about  $4 R_E$ .

A single current component  $J_{rc,\phi}$ , divergence free per construction, is responsible for the ring current magnetic field, namely

$$J_{rc,\phi}(\rho, z) = \frac{240\rho}{\mu_0} \left[ \frac{B_+\rho_+^5}{[\rho^2 + z^2 + 4\rho_+^2]^{7/2}} + \frac{B_-\rho_-^5}{[\rho^2 + z^2 + 4\rho_-^2]^{7/2}} \right] \quad (3.7)$$

The ring current density distribution has its maximum intensities in the dipole equatorial

The function  $A_\phi$  contains two parts, each differing from a pure dipole potential by the last term in the denominator.

$$A_\phi = \frac{4B_+\rho_+^3\rho}{[\rho^2 + z^2 + 4\rho_+^2]^{3/2}} + \frac{4B_-\rho_-^3\rho}{[\rho^2 + z^2 + 4\rho_-^2]^{3/2}} \quad (3.2)$$

The quantities  $B_+$ ,  $B_-$ ,  $\rho_+$ , and  $\rho_-$  are the ring current input parameters. The first term leads us to an eastward traveling current system with characteristic radius  $\rho_+$  and produces a maximum northward magnetic deflection of size  $B_+$  at the center of the Earth. Similarly, the second term results in a westward traveling current distribution with characteristic radius  $\rho_-$  and a maximum southward magnetic deflection  $B_-$ . Note that Tsyganenko and Usmanov [1982] and Tsyganenko [1987] begin with a vector potential similar to the second term of equation (3.2), but exclude eastward traveling currents from their description. The factors of 4 in the denominators help establish a physically reasonable relationship between the total current and magnetic field distributions, as will be shown below, while the factors of 4 in the numerators are just a mathematical convenience.

In cylindrical coordinates, this single component vector potential (equation (3.2)) produces two axially symmetric magnetic field components,  $B_\rho$  and  $B_z$ , as determined by

$$\mathbf{B} = \nabla \times \mathbf{A} \quad (3.3)$$

The ring current magnetic field components are

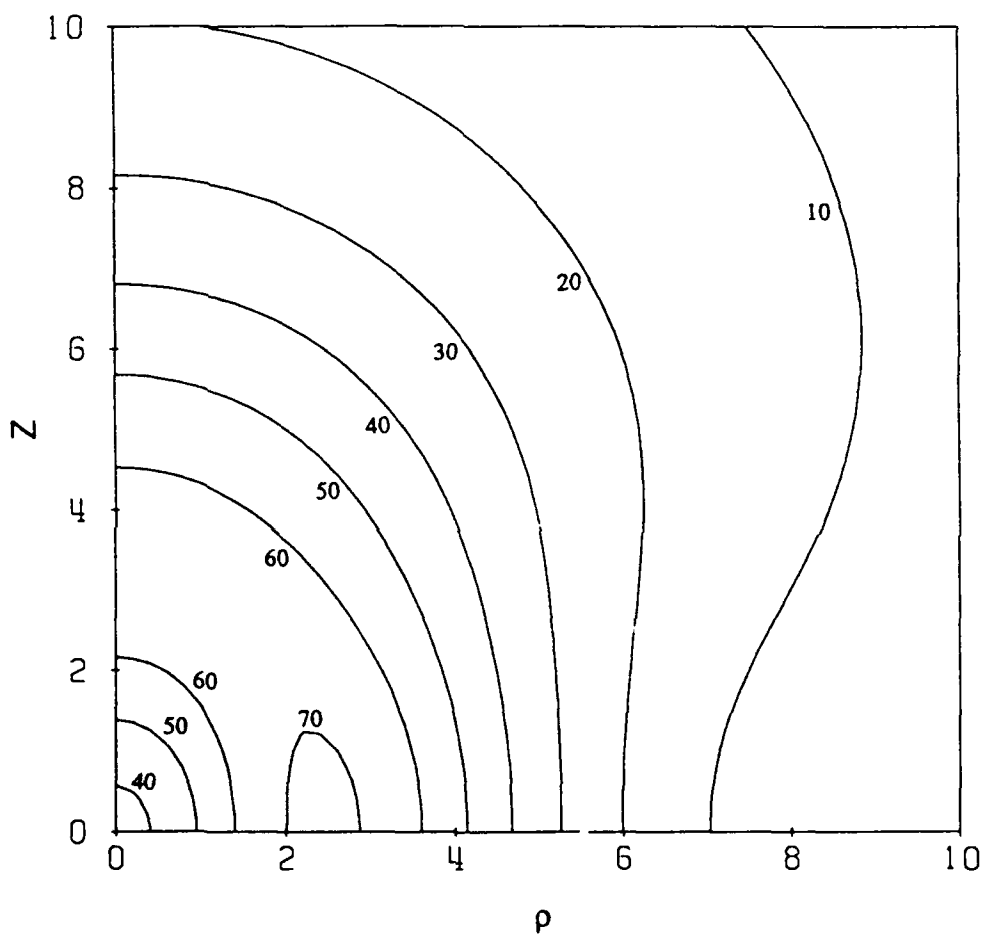


Fig. 3.2. Contours of constant ring current magnetic field magnitude (nT) as they vary with  $\rho$  and  $z$ . The maximum field strength occurs in the dipole equatorial plane near  $\rho = 3 R_E$  and declines steadily beyond a spherical radial distance of about  $4 R_E$ .

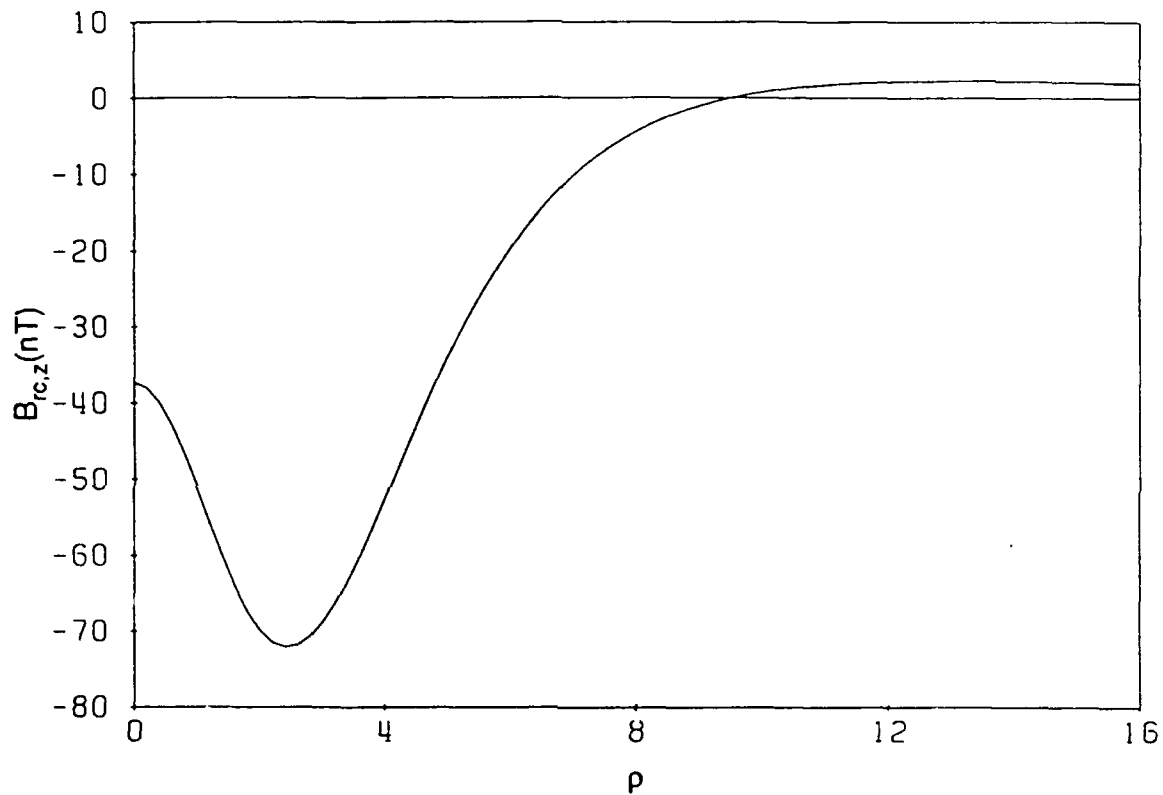


Fig. 3.1. Magnetic field strength of the ring current as a function of radial distance in the dipole equatorial plane,  $B_{rc,z}(\rho, z = 0)$ . The combination of eastward and westward traveling currents results in a maximum negative contribution near  $\rho = 3 R_E$ . The model ring current represented in Figures 3.1 to 3.4 has input parameters  $B_- = -310.0$  nT,  $B_+ = 272.2$  nT,  $\rho_- = 2.8 R_E$ , and  $\rho_+ = 2.1 R_E$ .



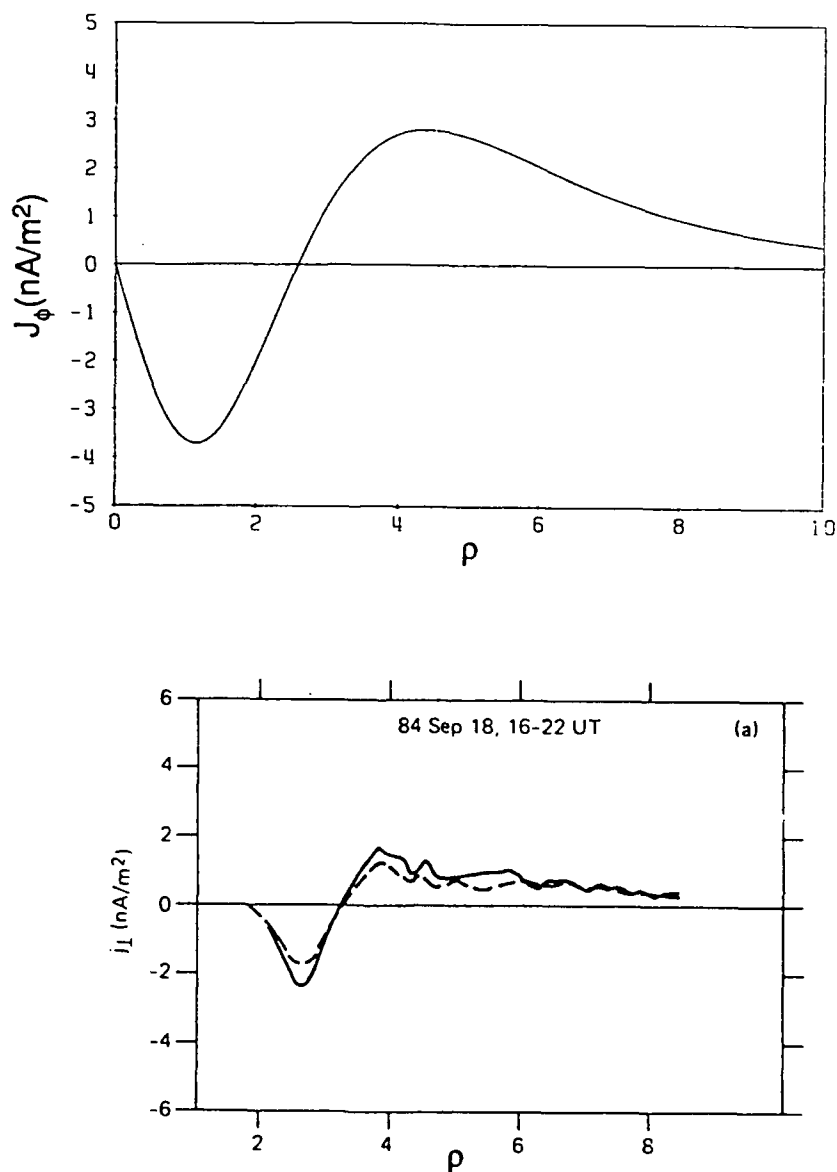


Fig. 3.3. Ring current density  $J_{rc,\phi}$  as a function of radial distance in the dipole equatorial plane. Positive and negative current densities indicate westward and eastward flow, respectively. The upper panel illustrates a model ring current distribution and the lower panel shows the current deduced by Lui et al. [1987] from particle measurements using the AMPTE spacecraft. The dashed curve is from a satellite reference pass before enhanced activity began.

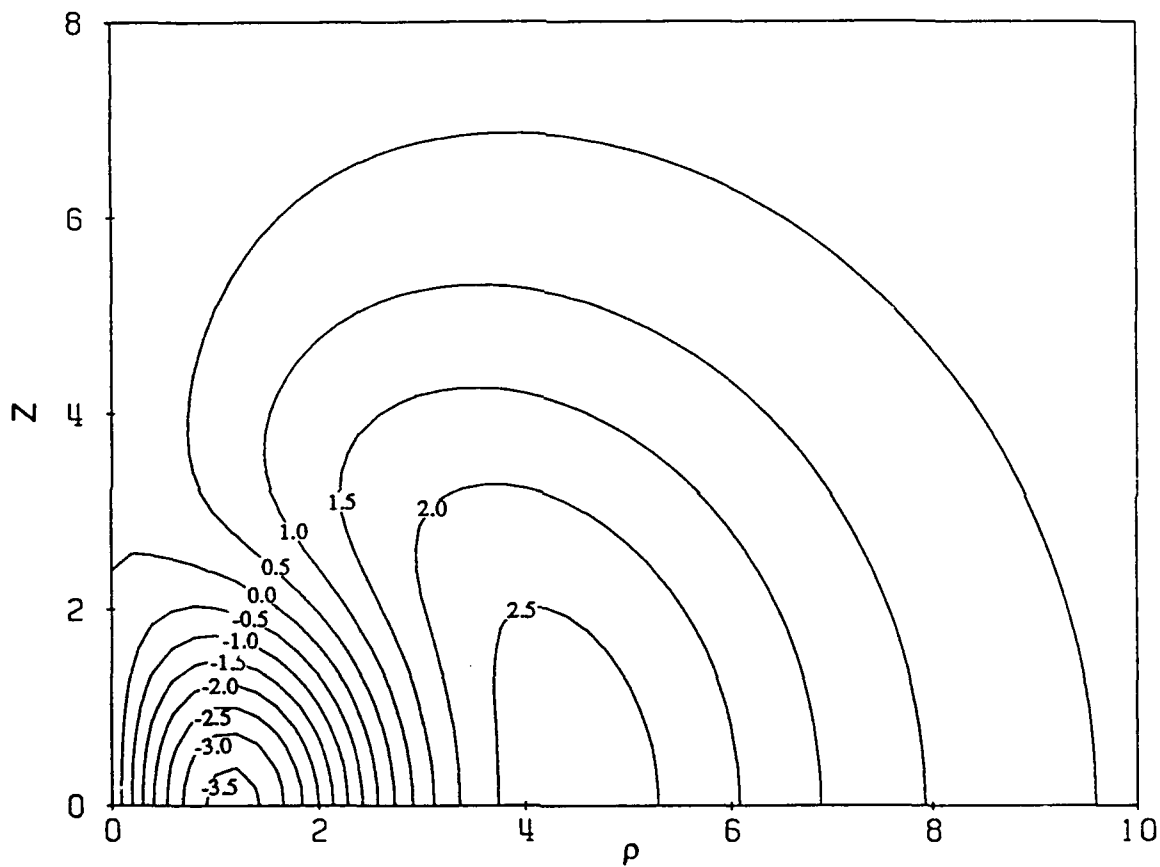


Fig. 3.4. Contours of constant azimuthal ring current density ( $\text{nA}/\text{m}^2$ ) as a function of  $\rho$  and  $z$ . Positive and negative values denote westward and eastward traveling current, respectively.

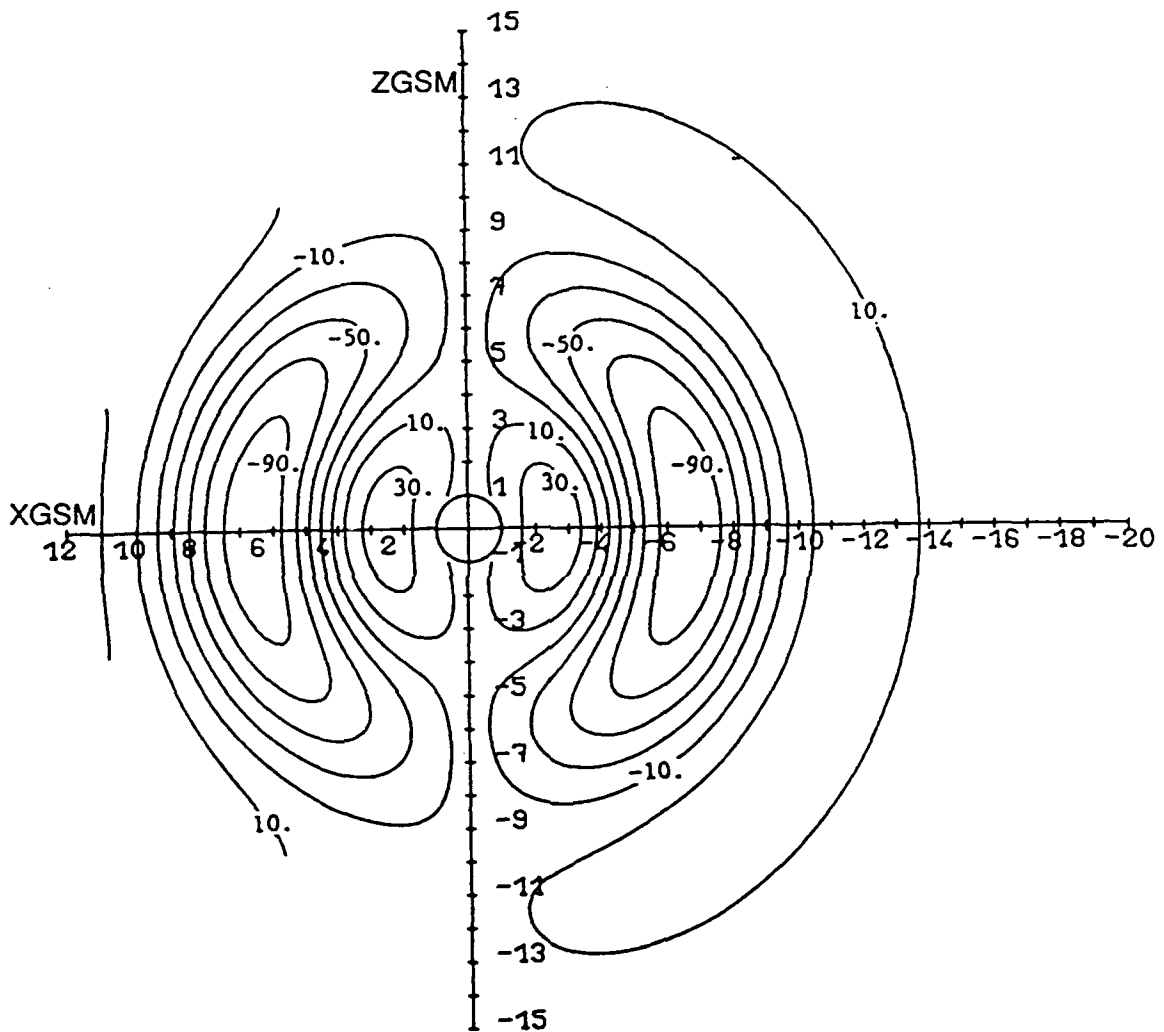


Fig. 3.5. Contours of constant azimuthal current density in the noon-midnight meridian derived by Kosik [1989] using an observed average  $\Delta B$  profile. For comparison with Figure 3.4 the sign convention must be switched and the numerical values multiplied by 0.124 to get ( $\text{nA}/\text{m}^2$ ).

$$\rho_o = 2\rho_+ \left[ \frac{1 - Q(\rho_-/\rho_+)^2}{Q - 1} \right]^{1/2} \quad \text{with} \quad Q = \left[ \frac{B_+\rho_+^5}{B_-\rho_-^5} \right]^{2/7} \quad (3.8)$$

This can be used to locate the peak of the ring current plasma particle distribution and follow the relative motion of the ring current from model to model in a quasi-static convection time sequence, for example.

Although we restrict our ring current treatment to symmetric cases in this presentation, the need for including local time variations [e.g., Stenig and Winch, 1987] could easily be satisfied. Equations (3.4) through (3.6) could be multiplied by any function of  $\phi$ , e.g.,  $F(\phi) = 1 + \sin^2[(\phi/2) + C]$ , to create an asymmetric ring current without violating flux or current conservation conditions. This transformation would introduce  $\rho$  and  $z$  current components which would concentrate or spread the current depending on the value of the angle  $\phi$ . The constant could then be adjusted, for example, to concentrate the current and field strength in the dawn nightside region (2000-2400 MLT) in order to simulate the asymmetric growth of the ring current. Note that magnetic local time (MLT) is fixed with respect to the solar direction with 1200 MLT and 2400 MLT corresponding to the noon (+x) and midnight (-x) directions, respectively, while 1800 MLT and 0600 MLT correspond to the dawn (-y) and dusk (+y) directions, respectively.

### 3.4. Comments

This tilt dependent ring current model contributes some very important key features to the magnetospheric magnetic field model. First, it is capable of reproducing critical  $\Delta B$  features such as the minimum encircling the Earth in the dipole equatorial plane while

simultaneously providing physically reasonable current distributions. Although the dipole shielding currents contribute significantly to the  $\Delta B$  profile, as shown in Figure 2.4, they cannot provide field variations on such small spatial scales. We shall see that this is true of the cross-tail current as well. Second, with only four input parameters,  $B_+$ ,  $B_-$ ,  $\rho_+$ , and  $\rho_-$ , the model is extremely flexible and can easily provide a wide range of ring current configurations. In addition, we briefly note here several other important benefits that will make themselves more evident in later sections.

The ring current can help substantially to extend the equatorial mapping distances of ionospheric field lines while also keeping field strengths in the inner magnetosphere reasonable and holding magnetopause boundary violations to a relative minimum. The presence of the eastward current lessens both the magnetic field depression at the Earth's surface and the ring-current magnetopause normal component that a purely westward current distribution would provide. It does not, however, reduce significantly the magnetic field stretching capabilities attributed to the outer ring current.

The procedure for determining the ring current input parameters for specific conditions in the magnetosphere will be tied to the expected  $\Delta B$  profiles and the other contributing sources which determine the profile. This procedure will be presented in Section 5. We turn next to the development of a magnetotail current system.

## 4. The Magnetotail Current

### 4.1. Introduction

The Earth's magnetotail is divided into two lobes of oppositely directed magnetic flux by a diamagnetic plasma sheet. The strength of the magnetic field lines mapping from the southern to the northern polar cap reaches a minimum as field lines thread through the plasma sheet to form a neutral sheet near the equatorial plane. It is the cross-tail current concentrated within the plasma sheet which supports the magnetic field of the lobes. The basic magnetotail structures, including the plasma sheet, the lobes, and the plasma sheet boundary layer which separates them, exist in coherent form beyond distances of  $200 R_E$  [Bame et al., 1983; Slavin et al., 1983, 1985; Eastman et al., 1984; Hones et al., 1984; Tsurutani et al., 1984].

The plasma sheet thickens toward the flanks [Bame et al., 1967; Meng and Mihalov, 1972; Fairfield, 1979] while equatorial flux levels also increase, at distances from  $x \approx 10$  to  $40 R_E$ , to roughly double the magnitude found near the tail's central axis [Fairfield, 1979, 1986]. It is contiguous with the outer ring current [Coleman and Cummings, 1971; Frank, 1971; Sugiura, 1972] and bends around the Earth in the equatorial plane extending into the dayside magnetosphere [Sugiura, 1972]. In addition, the neutral sheet, which coincides with the x-y plane for zero dipole tilt, flexes in both the x-z [Fairfield et al., 1987] and y-z planes [e.g., Fairfield, 1980] for non-zero tilt angles. See Fairfield [1987] for a more detailed review of magnetotail structure and Balsiger [1983]

for details on plasma sheet particle composition.

#### 4.2. Modeling Approach

The relationship between the equatorial magnetic flux distribution and the cross-tail current imbedded within the plasma sheet is of fundamental importance to our understanding of the nightside magnetosphere. The vacuum dipole field configuration, even with the addition of the ring current described previously, needs to have the magnetic field lines of the nightside stretched tailward much more to agree with observations. While a cross-tail current is the obvious candidate for a solution, the exact current distribution required has been very difficult to determine.

The rapid equatorial field strength decrease down the tail as the dipole field weakens must be modified by weakening further the magnetic field of the inner most magnetospheric regions while boosting slightly the equatorial field magnitudes at more distant locations (see Figure 2.5). This type of redistribution of flux can produce the desired equatorial flux patterns and magnetic field mapping properties and also helps to reproduce the observed noon-midnight asymmetry in the equatorial  $\Delta B$  distribution [Sugiura et al., 1971] to which our present symmetric ring current cannot contribute. Note that this must be done in a precisely controlled manner such that unwanted negative, i.e., southward, equatorial magnetic fields can be avoided.

There have been several different methods developed to describe the currents and magnetic field of the magnetotail. Some of the more elaborate three dimensional efforts have concentrated on specific aspects of magnetotail physics including time-dependent reconnection using magnetohydrodynamics [e.g., Birn and Hones, 1981], time-dependent self-consistent plasma convection [e.g., Birn and Schindler, 1983],

asymptotic approaches for describing equilibria in the far tail [Birn et al., 1977; Birn, 1979], and the shape and position of the plasma sheet as it is influenced by the tilt of the Earth's dipole [Voigt, 1984]. See Voigt [1986] for a review of magnetotail equilibrium configurations and slow adiabatic convection. While these methods illuminate well certain characteristics of the magnetotail, they are not practical for our purposes because they are either too location specific, i.e., applicable to only far tail regions, do not include dipole-tilt related effects, or do not possess adequate flexibility to model extreme magnetospheric configurations.

Some of the semi-empirical methods for describing the cross-tail current sheet incorporate flat infinitesimally thin current sheets [Williams and Mead, 1965; Voigt, 1972], a set of contiguous uniform current sheets of finite width and thickness with each sheet having a different current density [Willis and Pratt, 1972], a set of current "wires" [Olson, 1974], a flat current sheet of uniform thickness [Sugiura and Poros, 1973], or a flat current sheet constructed of filaments of distributed current [Tsyganenko and Usmanov, 1982; Tsyganenko, 1987]. Similarly, each of these methods is deficient for our purposes for one or more of the following reasons: they contain discontinuities in magnetic fields or current, use flat constructions which prevent proper flexing of the current sheet in both the x-z and y-z planes, require an inordinate number of unphysical coefficients for specification, or lack flexibility (i.e., rely on fixed patterns of current intensity along the length of the current sheet). We must therefore develop a new cross-tail current representation.

To avoid spatial discontinuities in both the magnetic field and current formulations, we employ a technique introduced by Tsyganenko and Usmanov [1982] and construct each cross-tail segment out of an infinite number of adjacent diffuse magnetic filaments. In order to properly represent the dipole-tilt dependent curvature of the current sheet in



the x-z plane, the cross-tail current sheet will be formed by linking together short straight segments of cross-tail current which are arranged to approximate this curvature. This technique also increases the models flexibility by permitting the representation of current intensity profiles which are arbitrary functions of distance along the length of the plasma sheet. The arrangement requires the input of only a few physical parameters yet allows us to control precisely the resulting magnetic flux distribution.

#### 4.3. Cross-Tail Current Magnetic Field

Our first step is to determine the general expressions for the magnetic field components of a single cross-tail current segment.

##### 4.3.1. *A Single Current Segment*

The basic constituent of a cross-tail current segment is a magnetic filament which corresponds to an infinitely long diffuse line of current perpendicular to the GSM x-z plane and centered at some position  $(x_0, z_0)$ . The magnetic field strength of each axially symmetric filament varies with radial distance from the filament center,  $\rho_f$ , as

$$F(\rho_f) = \frac{\rho_f}{\rho_f^2 + \delta^2} \quad \text{with} \quad \rho_f = [(x - x_0)^2 + (z - z_0)^2]^{1/2} \quad (4.1)$$

The distance  $\delta$  is the characteristic half-thickness of the filament. This parameter will be held constant for the entire length of the magnetotail even though the current sheet thickness increases tailward according to force balance calculations [Voigt, 1984]. The segment procedure can easily be used to include this feature if future observations concur with the theory.

If  $s_0$  is a position on a curve in the  $x$ - $z$  plane, corresponding to the point  $(x_0, z_0)$ , and  $B(s_0)$  specifies the filament strength at that position, then the components of the magnetic field due to a small length of current can be written in differential form, namely

$$dB_x = \frac{(z - z_0)}{\rho_f} B(s_0) F(\rho_f) ds_0 \quad (4.2)$$

$$dB_z = -\frac{(x - x_0)}{\rho_f} B(s_0) F(\rho_f) ds_0 \quad (4.3)$$

The function  $B(s_0)$  is, of course, proportional to the current density at the center of a filament and  $ds_0$  is an incremental distance along the curve. The total magnetic field due to the filaments used to construct any curve can then be determined by integrating (4.2) and (4.3) along the curve's path between the end points. If the curve is a straight segment with end points  $(x_n, z_n)$  and  $(x_f, z_f)$ , then the filament position coordinates  $x_0$  and  $z_0$  are no longer independent and we can write

$$z_0 = M(x_0 - x_n) + z_n \quad \text{with} \quad M = \frac{z_f - z_n}{x_f - x_n} \quad (4.4)$$

where  $M$  is the slope of the segment in the  $x$ - $z$  plane. In addition, if the filament field strength  $B(s_0)$  varies linearly with distance along the segment, then it also has a linear dependence on  $x_0$  and can be expressed in terms of  $x_0$  such that

$$B(s_0) = B(x_0) = B_n + S(x_0 - x_n) \quad \text{with} \quad S = \frac{B_f - B_n}{x_f - x_n} \quad (4.5)$$

The quantities  $B_n$  and  $B_f$  refer, respectively, to the filament strength at the near and far

edges of the segment relative to the Earth while  $x_n$  and  $x_f$  are the x coordinates of the near and far edges, respectively. With each segment having a constant slope, the differential  $ds_o$  is directly proportional to  $dx_o$ .

$$ds_o = \sqrt{M^2 + 1} dx_o \quad (4.6)$$

where  $M = (dz_o/dx_o)$  is the slope introduced in equation (4.4). Substituting equations (4.4) - (4.6) into (4.2) and (4.3) we can express the components of the magnetic field due to a single current segment of arbitrary slope as the single variable integrals

$$B_x^{(i)}(x, z) = \int_{x_f}^{x_n} \frac{[z - M(x_o - x_n) - z_n][B_n + S(x_o - x_n)]}{(x - x_o)^2 + [z - M(x_o - x_n) - z_n]^2 + \delta^2} \sqrt{M^2 + 1} dx_o \quad (4.7)$$

$$B_z^{(i)}(x, z) = \int_{x_f}^{x_n} \frac{-(x - x_o)[B_n + S(x_o - x_n)]}{(x - x_o)^2 + [z - M(x_o - x_n) - z_n]^2 + \delta^2} \sqrt{M^2 + 1} dx_o \quad (4.8)$$

The integration is done from the far edge  $x_f$  to the near edge  $x_n$  of each segment as we move toward more positive x values in the magnetotail. Analytic solutions can be found by writing the numerators and denominators in terms of quadratics in  $x_o$ . The quadratic coefficients for the numerator of equation (4.7) are

$$\begin{aligned} m_x &= -MS \\ n_x &= -M(B_n - Sx_n) + S(Mx_n + z - z_n) \\ p_x &= (Mx_n + z - z_n)(B_n - Sx_n) \end{aligned} \quad (4.9)$$

while those of (4.8) are

$$\begin{aligned}
m_z &= S \\
n_z &= B_n - S(x_n + x) \\
p_z &= -x(B_n - Sx_n)
\end{aligned}
\tag{4.10}$$

The denominators of (4.7) and (4.8) are the same and have the quadratic coefficients

$$\begin{aligned}
a &= M^2 + 1 \\
b &= -2[x + M(z - z_n + Mx_n)] \\
c &= x^2 + (z - z_n + Mx_n)^2 + \delta^2
\end{aligned}
\tag{4.11}$$

The magnetic field components of a segment of cross-tail current having the end points  $(x_n, z_n)$  and  $(x_f, z_f)$  with current intensity varying linearly along its length are

$$B_x^{(i)}(x, z) = \frac{m_x}{a^{1/2}}(x_n - x_f) + \frac{an_x - bm_x}{2a^{3/2}}L(x, z) + \frac{2a(ap_x - cm_x) - b(an_x - bm_x)}{a^{3/2}(4ac - b^2)^{1/2}}T(x, z)
\tag{4.12}$$

$$B_z^{(i)}(x, z) = \frac{m_z}{a^{1/2}}(x_n - x_f) + \frac{an_z - bm_z}{2a^{3/2}}L(x, z) + \frac{2a(ap_z - cm_z) - b(an_z - bm_z)}{a^{3/2}(4ac - b^2)^{1/2}}T(x, z)
\tag{4.13}$$

where the functions  $L(x, z)$  and  $T(x, z)$  are given by

$$L(x, z) = \ln \left[ \frac{ax_n^2 + bx_n + c}{ax_f^2 + bx_f + c} \right]
\tag{4.14}$$

$$T(x, z) = \tan^{-1} \left[ \frac{2ax_n + b}{(4ac - b^2)^{1/2}} \right] - \tan^{-1} \left[ \frac{2ax_f + b}{(4ac - b^2)^{1/2}} \right] \quad (4.15)$$

When a segment is parallel to the GSM equatorial plane then  $M = 0$  and expressions (4.14) and (4.15) can be simplified. Each segment, having neither a  $B_y$  component nor any  $y$  dependence, provides a divergence-free magnetic field so the entire cross-tail current magnetic field also satisfies the condition  $\nabla \cdot \mathbf{B} = 0$ . Although the magnetic  $y$  component can play an important role in the physics of the magnetotail (e.g., see Hilmer and Voigt [1987]), including the dawn-dusk displacement of the auroral zone, we continue on with our present approach. We now need to develop a method for positioning these segments to best represent the dipole-tilt dependent behavior of the cross-tail current sheet in the midnight meridian.

#### 4.3.2. *Current Sheet Placement*

A major point to be considered when trying to determine the proper placement of the cross-tail current sheet at the midnight meridian is its impact on the final location of the magnetic neutral sheet. The neutral sheet is defined as the surface separating field lines of opposite polarity, i.e., where  $B_{T,x} = 0$ , and with  $B_{T,y}$  and  $B_{T,z}$  usually being small compared to the  $x$  component, it also represents the surface of minimum magnetic field strength in the magnetotail. For dipole tilt angle  $\psi = 0$  the neutral sheet is coincident with the equatorial plane, thus the cross-tail current sheet can simply be placed in that same plane. The situation changes dramatically, however, when the Earth's dipole field is tilted. To continue, we must first consider the relative locations of the neutral sheet and the cross-tail current sheet.

A state of balance between plasma particle pressure and magnetic pressure exists roughly throughout the magnetotail. This was first demonstrated by Fairfield et al.

[1981a] with simultaneous measurements in the plasma sheet and the magnetotail lobes and supports the idea that the plasma sheet is in the vicinity of the neutral sheet [Bame et al., 1967]. While equation (3.1) might be used to show that the location of maximum plasma particle pressure coincides with the neutral sheet, the exact location of the cross-tail current within the plasma sheet need not be the same. Speiser and Forbes [1981] report, however, that the current tends to be concentrated near the central region of the plasma sheet. We will locate our cross-tail current along a path which, in combination the other magnetic field sources, produces neutral sheet configurations consistent with observations.

The position of the neutral sheet relative to the equatorial plane varies with both annual and diurnal changes of the dipole tilt angle  $\psi$  [e.g., Murayama, 1966; Speiser and Ness, 1967; Russell and Brody, 1967; Fairfield and Ness, 1970; and Bowling, 1974]. For positive values of  $\psi$  (e.g., during summer in the northern hemisphere) the neutral sheet in the midnight meridian is elevated above the x-y plane by varying amounts depending on the distance from Earth. Accordingly, for negative dipole tilt angles the neutral sheet drops below the x-y plane.

With much of the midnight meridian neutral sheet (i.e., beyond  $x \approx -15 R_E$ ) being shifted by a relatively constant amount above or below the x-y plane, many authors express this displacement in the form  $\Delta z = H_d \sin \psi$ , where  $H_d$  is the "hinging distance". This is the radial distance where the neutral sheet would intersect the dipole equatorial plane at midnight if the neutral sheet remained at a constant distance  $\Delta z$  from the x-y plane.

One of the more comprehensive studies was performed by Fairfield [1980], using IMP 6, 7, and 8 data from distances between  $x = -16$  and  $-40 R_E$ , who characterized the neutral sheet with the constant  $H_d = 10.5 R_E$ . By reviewing previous attempts to

characterize the neutral sheet and comparing with earlier data taken closer in, he also concluded that there is no tendency for the neutral sheet to return to the x-y plane at large distances. Gosling et al. [1986], using ISEE 2 data from  $x = -15$  to  $-19 R_E$ , came up with the revised constant  $H_d = 9.0 R_E$ . Estimates for  $H_d$  range from  $5.25$  to  $11 R_E$ .

While this type of characterization seems to work for distances beyond  $15 R_E$ , the notion of there actually being a hinge or extremely sharp deflection of the neutral sheet nearer the Earth seems very unphysical and it is more likely that the hinging occurs over an extended region rather than at a point (e.g., see Figure 5 of Voigt [1981]). Observations confirming this idea were presented by Fairfield et al. [1987] using AMPTE/CCE data obtained inside geocentric distances of  $8.8 R_E$ . They found that the neutral sheet gradually bends away from the dipole equatorial plane starting at a distance of roughly  $4 R_E$ . Their preliminary results indicate that the neutral sheet displacement from the dipole equatorial plane is  $\Delta z_{SM} = 7 \sin^2[5(-x_{SM} - 4)] \sin \psi$  for  $x_{SM} \leq -4 R_E$  (the term in brackets is in units of degrees), with the solar magnetic coordinate  $x_{SM}$  being in the dipole equatorial plane,  $z_{SM}$  being anti-parallel to the dipole, and  $y_{SM}$  being the same as  $y$  in the GSM system.

With the dipole field dominating the near-earth region, the Voigt [1981] vacuum configuration midnight meridian neutral sheet, see Figure 2.6, remains in the dipole equatorial plane for several Earth radii for non-zero tilt situations. To insure that the neutral sheet is not displaced in this region we will align the near-earth cross-tail current sheet along the curved path detailed above. Farther down the tail, the neutral sheet of our vacuum configuration quickly returns to the x-y plane. In order to get the observed far tail neutral sheet displacement, the cross-tail current sheet will be placed at the expected neutral sheet position as it is the dominant factor in determining neutral sheet position in that magnetotail region. Since the cross-tail current sheet is a continuous distribution of

plasma, we need to construct a single function describing current sheet placement which satisfies the requirements for both the near and far tail.

Two key points along the current sheet are used to determine the placement of the entire length of the current sheet in the midnight meridian for tilted configurations. The first point  $(x_1, z_1)$  is where the current sheet begins to bend away from the dipole equatorial plane in the tailward direction, at a distance of  $x_{SM} = -4 R_E$  [Fairfield et al., 1987]. The second point  $(x_2, z_2)$  is farther down the tail where the current sheet first becomes parallel to the tail axis. Initially, we will determine the second point by assuming that both points are equidistant from the hinging point  $(-H_d \cos \psi, H_d \sin \psi)$ . In the GSM coordinate system, these two points can be written in terms of the hinging distance and the dipole tilt angle as

$$(x_1, z_1) = (-4 \cos \psi, 4 \sin \psi) \quad (4.16)$$

$$(x_2, z_2) = (4 - H_d [1 + \cos \psi], H_d \sin \psi)$$

Earthward of the first point the current sheet lies in the dipole equatorial plane and tailward of the second point it is positioned parallel to the GSM x-y plane. We require that the function describing the current sheet placement between these two points must join them such that the complete curve is continuous in both position and slope. The function  $z_h(x, H_d, \psi)$ , describing the displacement of the cross-tail current sheet above or below the magnetospheric equatorial plane for all distance along the tail axis, is

$$\begin{aligned} z_h &= -x \tan \psi & \text{for } x > x_1 \\ z_h &= a_0 + a_1 x + a_2 x^2 + a_3 x^3 & \text{for } x_1 \geq x \geq x_2 \\ z_h &= H_d \sin \psi & \text{for } x < x_2 \end{aligned} \quad (4.17)$$



where  $x_1$  and  $x_2$  are defined in equation (4.16) and the coefficients for the middle portion of the curve are

$$a_3 = \frac{2[z_2 - z_1] - [x_1 - x_2]\tan\psi}{3[x_1 - x_2][x_1^2 - x_2^2] + 2[3x_1x_2^2 - x_1^3 - 2x_2^3]} \quad (4.18)$$

$$a_2 = -\frac{\tan\psi + 3a_3[x_1^2 - x_2^2]}{2[x_1 - x_2]} \quad (4.19)$$

$$a_1 = -x_2[2a_2 + 3a_3x_2] \quad (4.20)$$

$$a_0 = z_1 - a_2x_1[x_1 - 2x_2] - a_3x_1[x_1^2 - 3x_2^2] \quad (4.21)$$

The current sheet position function  $z_h(x, H_d, \psi)$  is plotted in Figure 4.1 for several different dipole-tilt angles using a hinging distance  $H_d = 9.0 R_E$  as determined by Gosling et al. [1986]. For all tilt angles the function is aligned with the dipole equatorial plane near Earth, bends out of that plane to smoothly join with the straight far tail position in a continuous manner. The end points of our current segments will be located on this curve.

This function agrees very well with the near-earth midnight ( $< 8.8 R_E$ ) observations parameterized by Fairfield et al. [1987] and gives a current sheet position that is, for example, within  $0.01 R_E$  of their position for a tilt angle of  $\psi = \pm 20^\circ$ . The same function also matches the observed position in the  $15\text{-}20 R_E$  region [Gosling et al., 1986] and tailward, thus the intermediate region from  $8.8 - 15.0 R_E$  should also be well represented. Our initial assumption concerning the location of the second critical point proves to be very reasonable as any change in the value of  $x_2$ , equation (4.16), displaces the curve from the average observed position. Note that the distance  $H_d$  will remain fixed for all

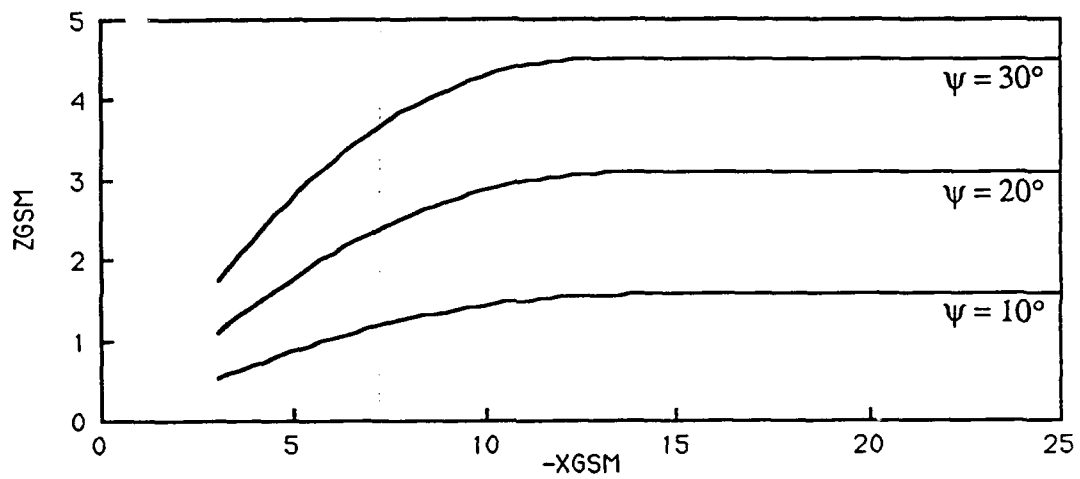


Fig. 4.1. The cross-tail current sheet position at midnight for dipole tilt angles  $\psi = 10^\circ$ ,  $20^\circ$ , and  $30^\circ$  as described by equation (4.17). The cross-tail current sheet bends away from the dipole equatorial plane and smoothly levels off to become parallel to the GSM equatorial plane beyond middle tail distances.

magnetic activity levels throughout this presentation even though the hinging distance decreases systematically for more active times [Fairfield, 1980].

We have incorporated observational information from several distance regimes in the tail into a single representation of the current sheet position which allows us to better represent the location of the magnetic neutral sheet in the midnight meridian. We will discuss the impact of this choice on the behavior of the complete neutral sheet later in Section 8. We turn next to the development of a cross-tail filament intensity profile.

#### 4.3.3. *Cross-Tail Filament Intensity Profile*

The average behavior of cross-tail current intensity as a function of the distance from Earth can be characterized in the following manner. The tail lobe magnetic field strength decreases with distance from Earth [e.g., Behannon, 1968; Mihalov and Sonett, 1968; Bird and Beard, 1972], so it is reasonable to assume that the cross-tail current, which is primarily responsible for the lobe field strength, declines accordingly, e.g., exponentially.

The dynamic behavior can also be approximated. Very simple magnetic field models [e.g., Lui, 1978; Kaufman, 1987] have been used to estimate that large increases in current strength near the front edge of the plasma sheet, and not in the distant tail, are required to get the observed field stretching in the tail during the substorm growth phase. It has also been deduced from observations that the largest current and magnetic field energy changes take place inside  $10 R_E$  [e.g., McPherron, 1972] and that the current in the near tail grows to several times its quiet-time amplitude [e.g., Aubry et al., 1972]. The change in particle profiles marking the inner edge of the plasma sheet indicate that the boundary can be quite distinct [Balsiger, 1983], while the extreme variability of the field configuration in that region was noted by Hedgecock and Thomas [1975]. To be enable

us to accommodate both the gradual current strength decrease expected in the far tail and the more dynamic changes which can typify the inner edge, we assume a filament strength profile which decreases exponentially with distance from the plasma sheet inner edge.

The filament strength profile  $B_w(s)$ , or equivalently the current intensity profile, is basically a function of the distance along the curve described by equation (4.17) and is used to supply the segment endpoint values  $B_n$  and  $B_f$  of equation (4.5). In this way, the strength of the filament at the far edge of any current segment matches that of the filament at the near edge of the adjacent tailward segment. The distance  $s$ , associated with a segment endpoint on the curve, is defined as the sum of the distance to the current sheet inner edge,  $s_I$ , and the cumulative length of all segments earthward of that end point.

$$\begin{aligned}
 B_w(s) &= 0 && \text{for } s < s_I \\
 B_w(s) &= B_I \left[ \frac{B_c}{B_I} \right]^{(s-s_I)/(s_c-s_I)} && \text{for } s_I \leq s \leq s_c \\
 B_w(s) &= B_c && \text{for } s > s_c
 \end{aligned} \tag{4.22}$$

The function  $B_w(s)$  is zero earthward of  $s_I$  and decreases exponentially with distance from the inner edge value of  $B_I$  to a constant value  $B_c$  at the distance  $s_c$ . The function remains fixed equal to  $B_c$  beyond  $s_c$ , which is set at a distance of  $100 R_E$  for this presentation (similar to the distance used by Willis and Pratt [1972]). The ratio  $[B_c/B_I]$ , with values ranging between zero and unity, determines how quickly the current intensity decreases along the current sheet. Smaller values ( $\approx 0$ ) indicate that there is a relatively large enhancement of the current at the inner edge, while larger values ( $\approx 1$ ) indicate a current

intensity profile that is fairly constant along the entire length of the magnetotail.

#### 4.3.4. *Segment Length and Positioning*

The length of the segments used are determined by making a compromise between minimizing the number of steps to reduce computing time and making the segment steps small enough to adequately approximate the desired input current intensity profile and current sheet position. For a good approximation, small segments are required earthward of the point  $(x_2, z_2)$  where the sheet is curved. The filament or current strength decreases exponentially, so segments of gradually increasing length are employed as we move tailward. The far end of the tail, where both of the functions  $B_w(s)$  and  $z_h(x)$  are flat, can be represented by a single large segment. With this in mind we have, starting from the inner edge, 8 segments of length  $2 R_E$ , 3 segments of length  $5 R_E$ , 3 of  $10 R_E$ , 1 of  $39 R_E$ , and a final segment of length  $250 R_E$ . The current sheet contains  $n_s = 16$  segments with a combined total length of  $350 R_E$ .

The distance to the inner edge,  $s_I$ , remains a constant for all dipole tilt angles, as there is no evidence to show that the inner edge moves radially when the dipole tilts, and the segment lengths and current content remain fixed. The segments are arranged such that the far edge of one coincides with the near edge of the segment immediately tailward. All of the segment edges remain on the dipole-tilt dependent curve specified by equation (4.17).

#### 4.3.5. *The Y Dependence*

The shielded dipole vacuum configuration of Voigt [1981], described in Section 2, contributes a northward pointing magnetic field to the equatorial plane of the magnetotail with a relative maximum strength at  $y = 0$  for a constant  $x$  position. The axially

symmetric ring current magnetic field, behaving like a dipole at large distances (see Figure 3.1), provides an additional small northward contribution which behaves similarly. The magnetic field contribution resulting from the present cross-tail currents do not depend on the  $y$  coordinate; thus, the magnetic flux passing through the equatorial plane is still greater at the center rather than the flanks of the magnetotail. To remedy this situation and get the total equatorial flux pattern to resemble the average observed pattern [Fairfield, 1986], we introduce a  $y$  dependence to the cross-tail current. This dependence will cause the cross-tail current to provide its largest negative flux contributions to the center, i.e., near  $y = 0$ , of the near-earth portion of the equatorial plane.

We can transform the vector field and include this  $y$  dependence while preserving the divergence-free condition by multiplying our cross-tail current magnetic field, which has only  $x$  and  $z$  components, with any function of  $y$ . This method is actually a very rudimentary type of vector field distortion transformation which allows one to self-consistently alter field component functions while maintaining  $\nabla \cdot \mathbf{B} = 0$ . The method was introduced by Voigt [1981] to stretch the nightside field lines of the vacuum dipole configuration into a more tail-like arrangement, thereby including distributed cross-tail currents. The procedure was elegantly generalized by Stern [1987a] for use with arbitrary coordinate systems and applications are discussed in several contexts, including magnetic field modeling (see also Section 5.1 of Voigt and Wolf [1988]).

Requiring symmetry about the  $x$ - $z$  plane and restraining the cross-tail current to flow between, yet not through the equatorial magnetopause boundaries at  $y = \pm R$ , leads to the even function

$$F(y) = \cos(\pi y/2R) e^{-(y/\Delta y)^2} \quad (4.23)$$

where  $R$  is the magnetotail radius and  $\Delta y$  is a characteristic distance for changes in the  $y$  direction.

The components of the magnetic field due to the total cross-tail current are obtained by summing the contributions from the  $n_s$  segments used to construct the tail current and performing the stretch transformation utilizing equation (4.23). The cross-tail current magnetic field components are

$$B_{\text{tail},x} = F(y) \sum_{i=1}^{n_s} B_x^{(i)}(x, z)$$

$$B_{\text{tail},y} = 0 \quad (4.24)$$

$$B_{\text{tail},z} = F(y) \sum_{i=1}^{n_s} B_z^{(i)}(x, z)$$

in units of nT, where the segment component magnetic field values come from equations (4.12) and (4.13). Note that the  $y$  component is equal to zero.

The north-south field orientation can be illustrated, as in Figure 4.2, by looking at  $B_{\text{tail},z}$  in the equatorial plane for  $\psi = 0^\circ$ . Earthward of the point where the  $z$  component changes sign, the function is negative with a maximum magnitude near the current sheet inner edge. Tailward of this point the field reaches peak values of only a few nT before decreasing. Well beyond our range of interest, i.e., in the far magnetotail near  $x = -350 R_E$ , there is a sharp peak due to edge effects where the current sheet ends. As will be demonstrated in Section 5, the location of the sign change and locations and magnitudes of the minimum and maximum contributions of  $B_{\text{tail},z}$  are easily controlled with the input parameters.

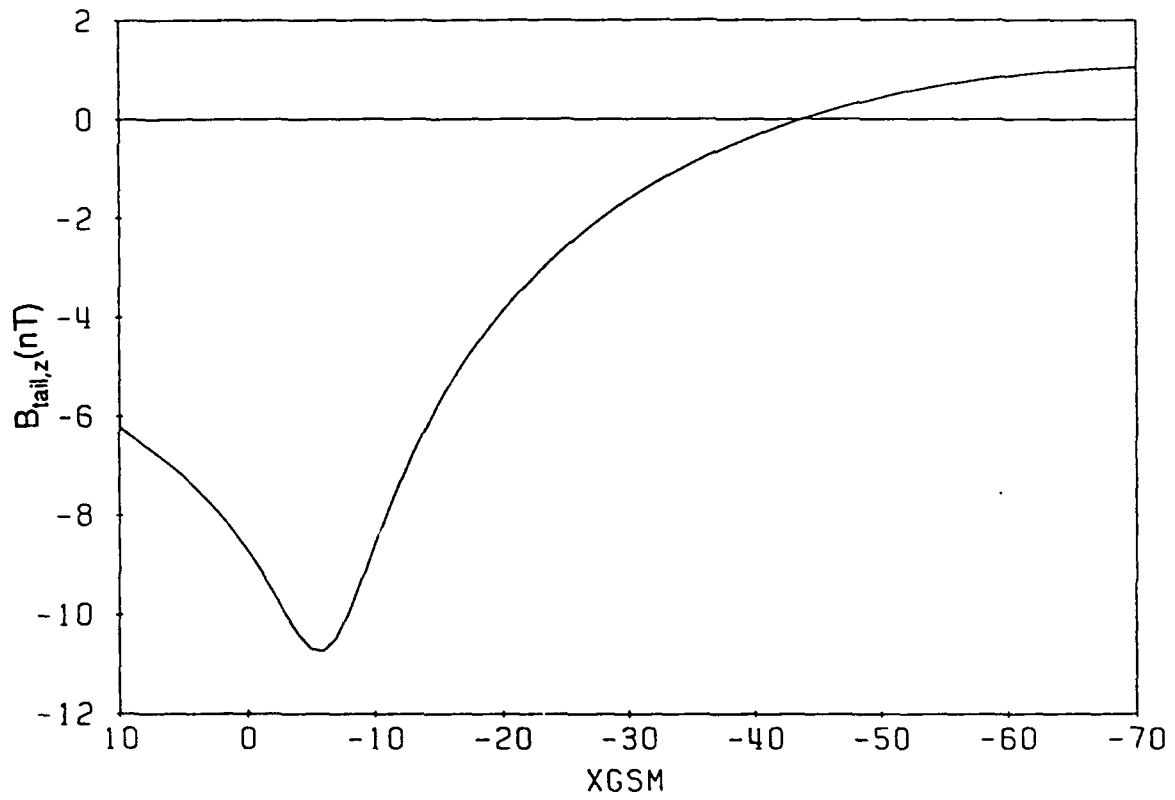


Fig. 4.2. The function  $B_{tail,z}$ , equation (4.24), plotted along the x axis for  $\psi = 0^\circ$ ,  $s_I = 6.1 R_E$ ,  $B_I = 4.0$  nT,  $[B_c/B_I] = 0.25$ , and  $\delta = 3.5 R_E$ .



The influence on the magnetic field of tilting the Earth's dipole field and bending the cross-tail current sheet can be seen in Figure 4.3, which plots contours of constant magnetic field strength in the midnight meridian for  $\psi = 0^\circ$  and  $35^\circ$ . The curvature of the current in the  $x$ - $z$  plane distorts the symmetry found in the untilted case most effectively near the inner edge. The field strength is strongest near the current sheet inner edge and contributes substantially to the lobe field strength. The cross-tail current magnetic field is directed basically earthward and tailward for positions above and below the current sheet, respectively, so it enhances the magnetic field strength of the lobes.

This is the first time in a semi-empirical representation that the cross-tail current sheet has been given such a curvature. Previous dipole tilt dependent cross-tail current representations of this nature have simply shifted the entire current sheet in the  $\pm z$  direction without considering that the hinging of the sheet must take place smoothly over a finite distance. This feature proves to be beneficial when considering magnetic field direction and magnitude close to the inner edge, e.g., the interpretation of magnetic field data depends very sensitively on the assumed location of a satellite relative to the current sheet.

The function  $F(y)$  decreases the magnitude of both magnetic field components as we move into the tail flanks, forcing them to zero at  $y = \pm R$ . Figures 4.2 and 4.3 can be scaled by this function to get field magnitudes for other  $y$  positions. This transformation method is also employed in the cross-tail current models of Tsyganenko and Usmanov [1982] and Tsyganenko [1987]; however, their  $y$  dependence allows currents to flow indefinitely in the  $\pm y$  direction.

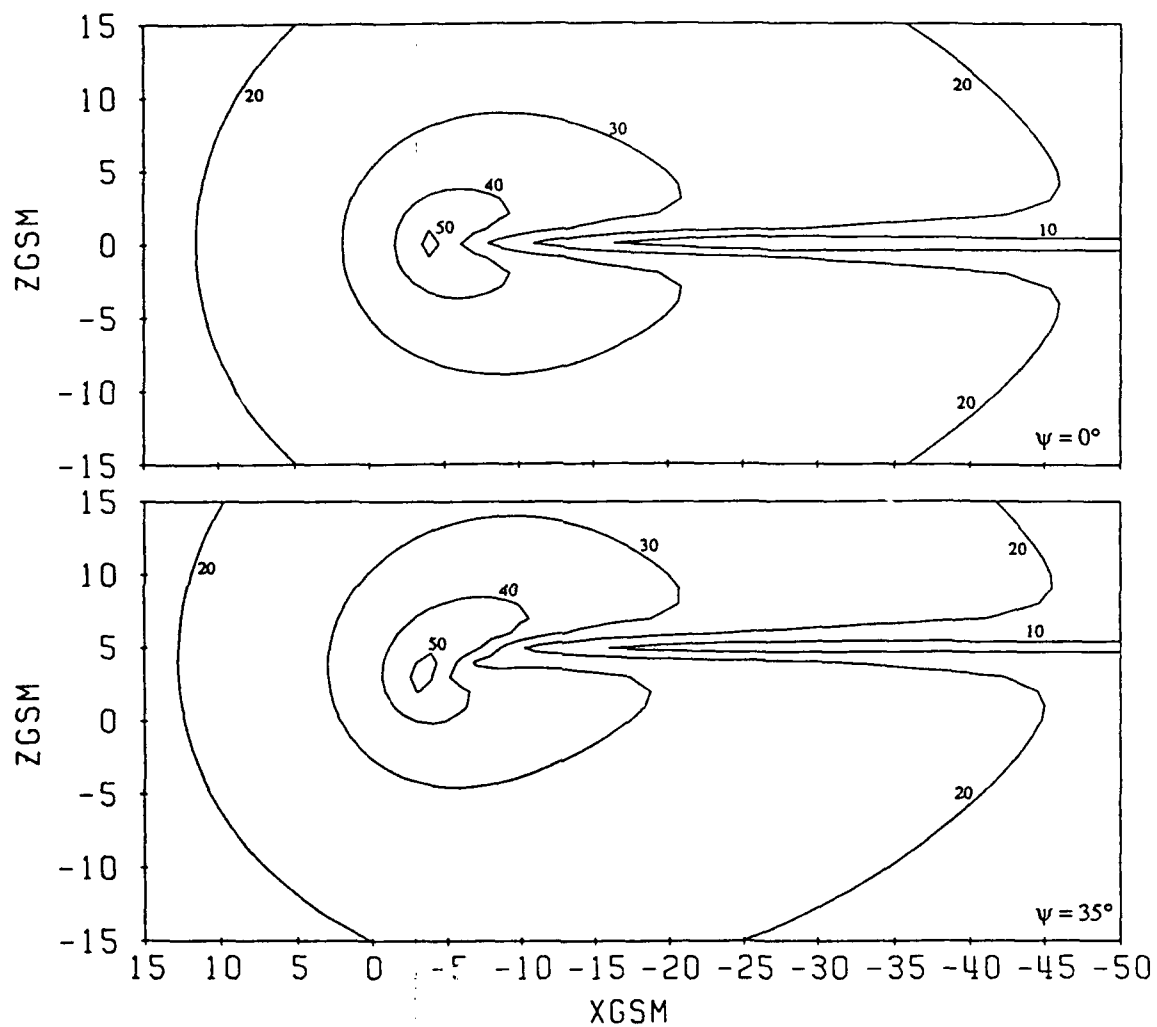


Fig. 4.3. Contours of constant cross-tail current magnetic field magnitude (nT) in the noon-midnight meridian plane for  $\psi = 0^\circ$  and  $35^\circ$  in the upper and lower panels, respectively. The parameter are from CDAW-6 magnetic field simulation time label 8. The CDAW-6 parameter sets are discussed in Section 8.

#### 4.4. Cross-Tail Current

The cross-tail current components, as derived from equations (4.12), (4.13), (4.23) and (4.24) using equation (3.1), are

$$J_{\text{tail},x} = \frac{1}{\mu_0} \frac{dF(y)}{dy} \sum_{i=1}^{n_z} B_z^{(i)}(x, z) \quad (4.25)$$

$$J_{\text{tail},y} = \frac{1}{\mu_0} F(y) \sum_{i=1}^{n_z} \left[ \frac{\partial B_x^{(i)}(x, z)}{\partial z} - \frac{\partial B_z^{(i)}(x, z)}{\partial x} \right] \quad (4.26)$$

$$J_{\text{tail},z} = \frac{1}{\mu_0} \frac{dF(y)}{dy} \sum_{i=1}^{n_z} B_x^{(i)}(x, z) \quad (4.27)$$

where the total cross-tail current is obtained, as is the total magnetic field, by summing up the contributions from the individual segments.

The partial derivative expressions needed for equation (4.26) are

$$\begin{aligned} \frac{\partial B_x^{(i)}(x, z)}{\partial z} = & \frac{an_x - bm_x}{a^{3/2}} \left[ \frac{z - z_n}{ax_n^2 + bx_n + c} - \frac{z - z_f}{ax_f^2 + bx_f + c} \right] + \left[ \frac{S}{2a^{1/2}} + \frac{Mm_x}{a^{3/2}} \right] L(x, z) + \\ & \frac{4a(ap_x - cm_x) - 2b(an_x - bm_x)}{a^{3/2}(4ac - b^2)} G_x(x, z) + \frac{T(x, z) H_x(x, z)}{a^{3/2}(4ac - b^2)^{3/2}} \end{aligned} \quad (4.28)$$

$$\frac{\partial B_z^{(i)}(x, z)}{\partial x} = \frac{an_z - bm_z}{a^{3/2}} \left[ \frac{x - x_n}{ax_n^2 + bx_n + c} - \frac{x - x_f}{ax_f^2 + bx_f + c} \right] + \left[ \frac{-S}{2a^{1/2}} + \frac{m_z}{a^{3/2}} \right] L(x, z) + \frac{4a(ap_z - cm_z) - 2b(an_z - bm_z)}{a^{3/2}(4ac - b^2)} G_z(x, z) + \frac{T(x, z) H_z(x, z)}{a^{3/2}(4ac - b^2)^{3/2}} \quad (4.29)$$

The functions  $L(x, z)$  and  $T(x, z)$  are from equations (4.14) and (4.15), the coefficients  $M, S, n_x, m_x, p_x, n_z, m_z, p_z, a, b,$  and  $c$  are defined in equations (4.4), (4.5), and (4.9) through (4.11), and the remaining undefined functions  $G_x(x, z), G_z(x, z), H_x(x, z),$  and  $H_z(x, z)$  are given by

$$G_x(x, z) = - \frac{M(4ac - b^2) + (2ax_n + b)[2a(z - z_n + Mx_n) + Mb]}{[4ac - b^2 + (2ax_n + b)^2]} + \frac{M(4ac - b^2) + (2ax_f + b)[2a(z - z_n + Mx_n) + Mb]}{[4ac - b^2 + (2ax_f + b)^2]} \quad (4.30)$$

$$H_x(x, z) = (4ac - b^2)[2a^2(B_n - Sx_n) - 4am_x(z - z_n + Mx_n) - a(Sb - 2Mn_x) - 4Mbm_x] - 2[2a(ap_x - cm_x) - b(an_x - bm_x)][2a(z - z_n + Mx_n) + Mb] \quad (4.31)$$

$$G_z(x, z) = \frac{(4ac - b^2) + (2ax_n + b)(2ax + b)}{[4ac - b^2 + (2ax_n + b)^2]} + \frac{(4ac - b^2) + (2ax_f + b)(2ax + b)}{[4ac - b^2 + (2ax_f + b)^2]} \quad (4.32)$$

$$H_z(x, z) = (4ac - b^2)[2a^2(-B_n + Sx_n) - 4am_zx + a(Sb + 2n_z) - 4bm_z] - 2[2a(ap_z - cm_z) - b(an_z - bm_z)](2ax + b) \quad (4.33)$$

The magnitude of the current passing through the noon-midnight meridian in the equatorial plane,  $J_{\text{tail},y}$ , is plotted in Figure 4.4 for a variety of tail strengths ranging from quiet to very strong. In each case, the current peaks near the current sheet inner edge and tapers off following the exponential decrease in filament strength describe by equation (4.22). The steepness of the function at the inner edge increases as  $\delta$  decreases (e.g.,  $\delta = 3.5 R_E$  and  $1.0 R_E$  for the bottom and top curves, respectively) and also corresponds to a thinning of the current sheet. These functions retain their shape at positions other than  $y = 0$  and change only by the scaling factor of equation (4.23).

Figure 4.5 illustrates contours of constant current density in the midnight meridian for  $\psi = 35^\circ$ . Note that the current density decreases very quickly as we move into the tail lobes, insuring that they remain relative current free. Also note that the current distribution bends or hinges very smoothly in the x-z plane. The direction of current flow across the magnetotail is illustrated in the next two figures.

Figure 4.6 illustrates how current flowing in the +y direction intensifies as it passes through the center of the tail and weakens again as it flairs out into the flanks. This spreading of current is consistent with the observed thickening of the plasma sheet in those same areas. The pattern within the circular boundary retains its shape and shifts vertically following the motion of the plasma sheet for configurations with non-zero dipole tilt angles. Figure 4.7 shows current traces in the equatorial plane. The traces are spaced along the x axis to reflect the relative current intensity with smaller gaps indicating regions of higher current density. Current streams almost straight across the far magnetotail and gradually bends around the Earth in the nearer regions. This curvature

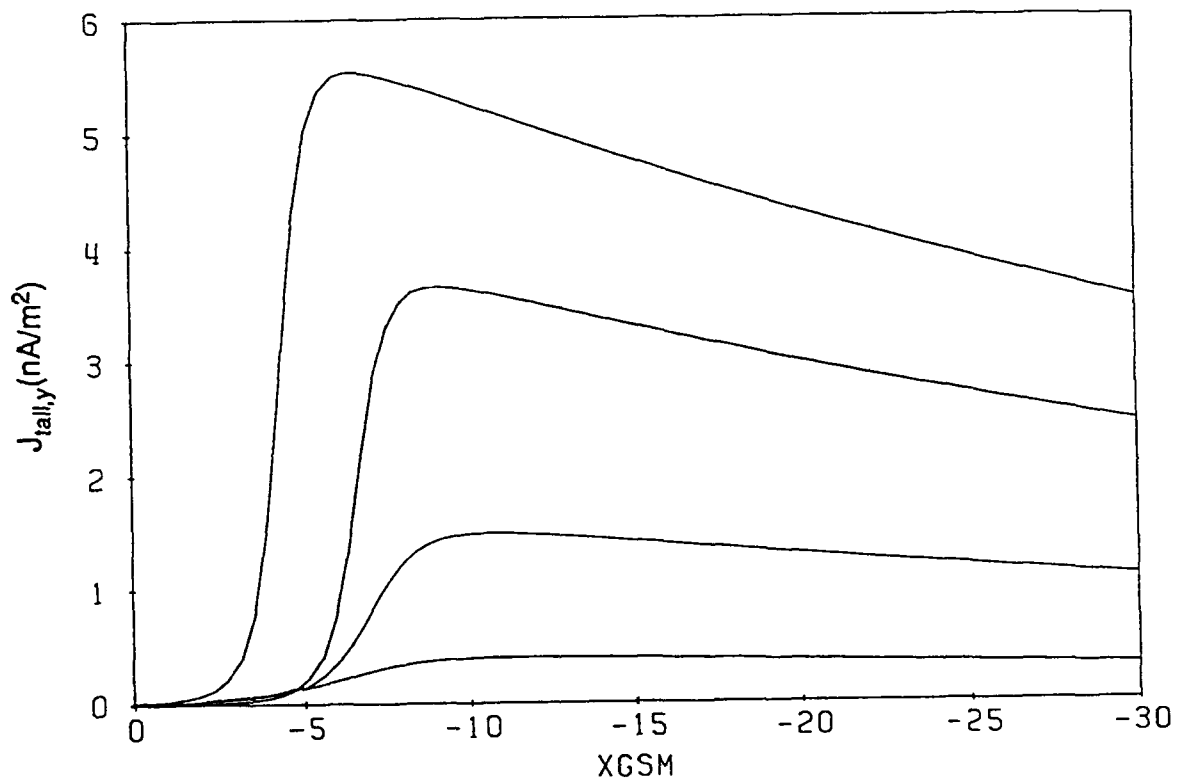


Fig. 4.4. Examples of the cross-tail current strength  $J_{\text{tail},y}$ , equation (4.26), plotted along the x axis. The lowest curve corresponds to Figure 4.2 while the remaining curves correspond, in ascending order, to CDAW-6 magnetic field simulation time labels 2, 3, and 7, respectively.

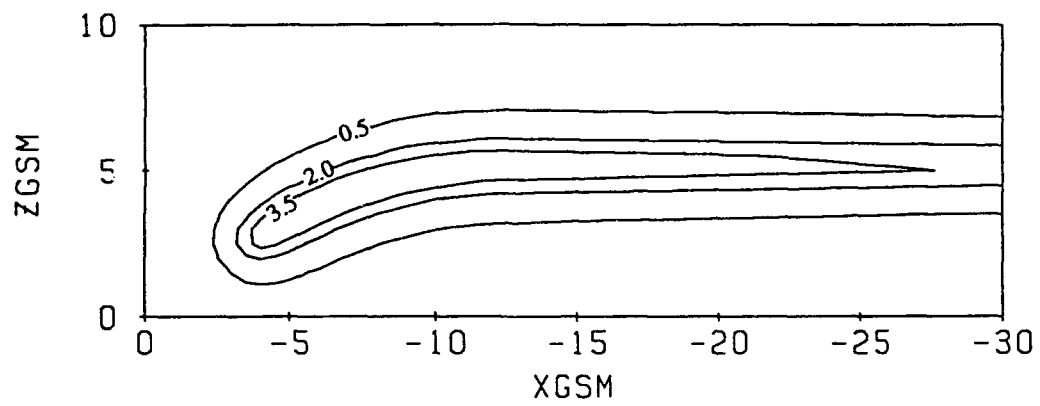


Fig. 4.5. Contours of constant cross-tail current density ( $\text{nA/m}^2$ ) in the x-z plane for  $\psi = 35^\circ$  corresponding to the magnetic field contours in the bottom panel of Figure 4.3.

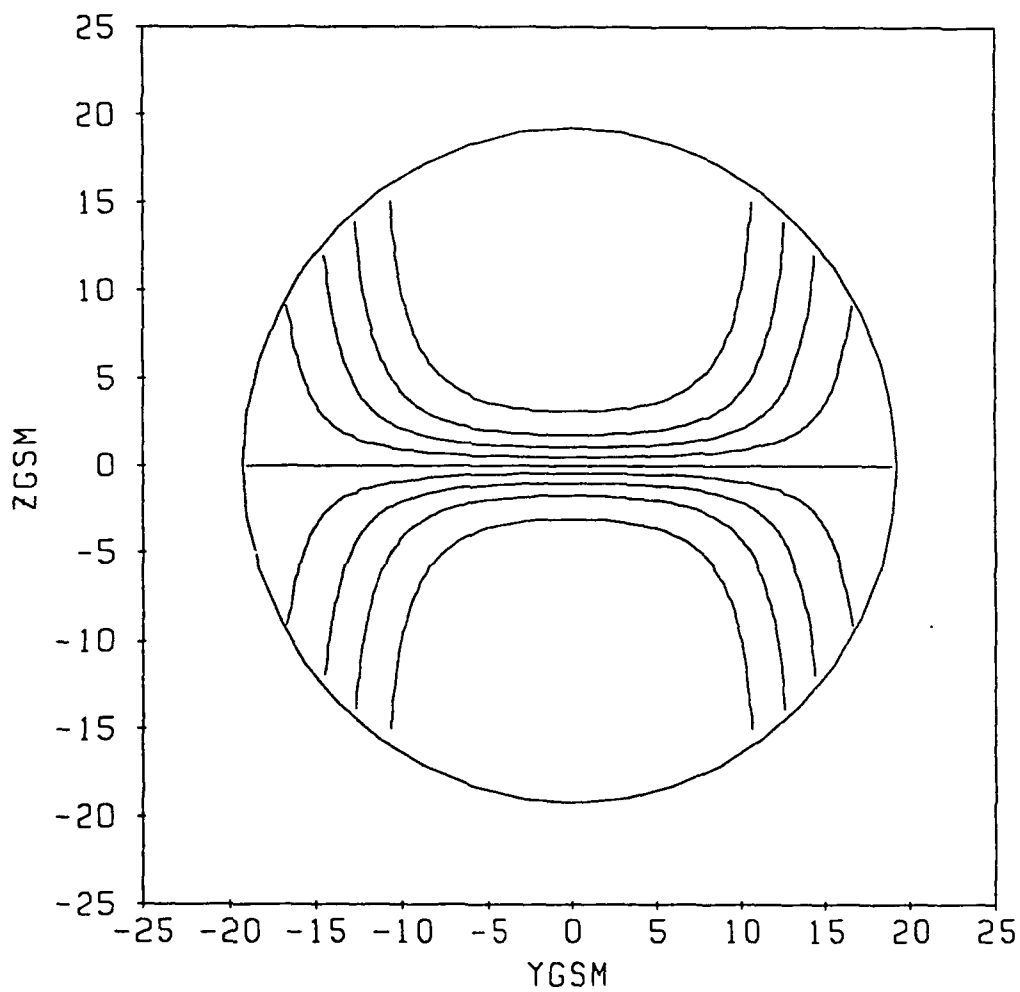


Fig. 4.6. Cross-tail current trace projection in the y-z plane at  $x = -8 R_E$  for  $\psi = 0^\circ$ . Current flows in the +y direction, becoming compressed as it passes through the magnetotail center. Input parameters are  $r_o = 10.5 R_E$ ,  $s_I = 6.0 R_E$ ,  $B_I = 6.0$  nT,  $[B_o/B_I] = 0.19$ ,  $\Delta y = 12.0 R_E$ , and  $\delta = 2.7 R_E$ .



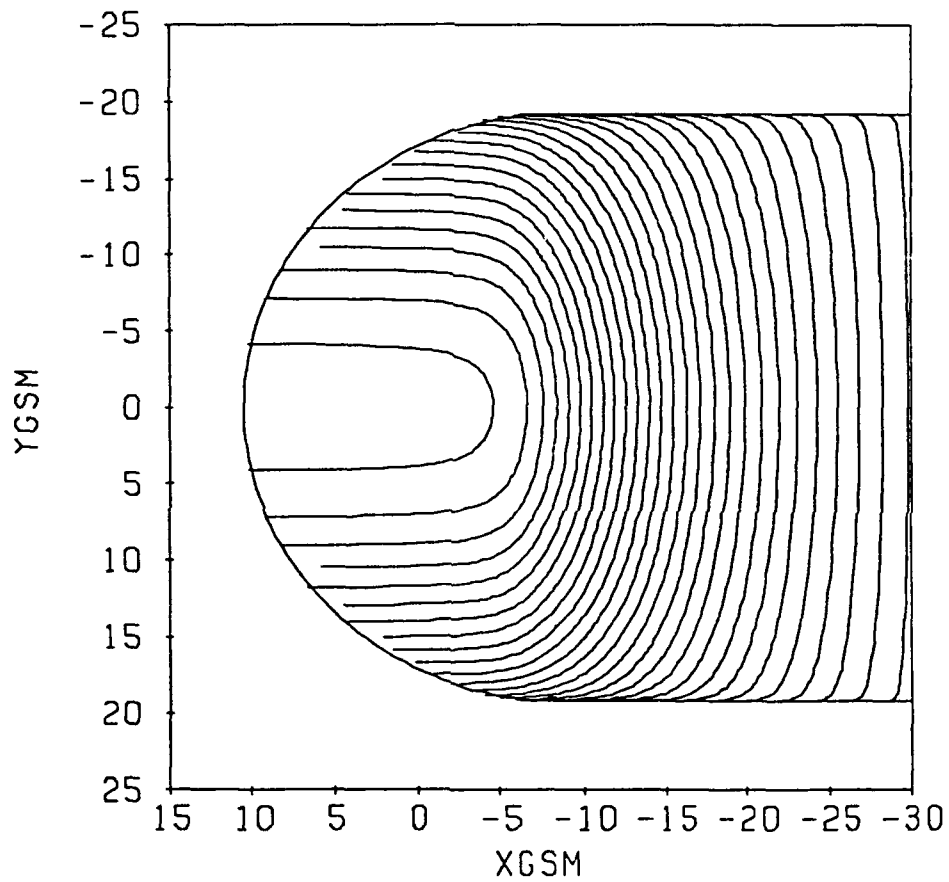


Fig. 4.7. Cross-tail current traces in the equatorial plane using the same parameters used in Figure 4.6. Current flows almost straight across the far magnetotail in the +y direction and wraps around the Earth in the near magnetotail. The traces are spaced along the x axis to reflect the relative current density with the smaller gaps indicating higher densities.

enables the cross-tail current to join continuously with the outer portion of the ring current. The cross-tail current is prevented from passing through the equatorial magnetopause boundary at  $y = \pm R$  owing to its  $y$  component being directly proportional to  $F(y)$  of equation (4.23). The straight line portions on the dayside do not represent significant current flow as the current strength decreases quickly toward the Earth from the current sheet inner edge, see Figure 4.4.

#### 4.5. Comments

There are several useful advantages gained with this cross-tail current representation. First, a high degree of flexibility has been incorporated as both the cross-tail current intensity profile (4.22) and the current sheet placement function (4.17), which controls the unique flexing of the current sheet, can be arbitrary functions of the distance along the magnetotail. The segment construction technique employed makes this possible. Second, the input parameters are physical in nature and are, as we will see, easily adjusted to accommodate a large range of magnetospheric conditions. Third, even though the current sheet does not flex in the  $y$ - $z$  plane, we will demonstrate that the shape and position of the resulting magnetic neutral sheet is very realistic. And finally, the flexible design of the cross-tail current enables us to make simple modifications to the westward current formulation in Section 7. The result is that we acquire the ability to simulate the reconfiguration or "collapse" of the magnetotail field that accompanies magnetospheric substorms.

The physical parameters needed to drive the cross-tail current model are the dipole tilt angle  $\psi$ , the tail radius  $R$ , the radial distance from the Earth to the current sheet inner edge  $s_1$ , the inner edge filament strength  $B_1$ , the ratio of current strength in the far tail to

that of the inner edge  $[B_0/B_1]$ , the scaling length  $\Delta y$ , and the characteristic half-thickness of the tail filaments  $\delta$  (also the half-thickness of the current sheet). A method for selecting values for these input parameter, as well as for those of the vacuum configuration and ring current, is outlined in the next section.

## 5. Input Parameter Selection

### 5.1. Introduction

If magnetic field data describing many different magnetospheric locations during a relatively short time interval were available, then we could search for the set of input parameters which best represent that state of the magnetosphere. The number of satellites required for such a task would be extremely prohibitive, so we must look elsewhere for a viable input parameter selection method.

One established approach incorporates vast reservoirs of data collected over long time periods that have been sorted according to a general magnetic activity index such as  $K_p$ . These bins of data are used to select sets of coefficients and parameters to model the various activity states of the magnetosphere [e.g., Sugiura and Poros, 1973; Olson and Pfitzer, 1974; Hedgecock and Thomas, 1975; Mead and Fairfield, 1975; Tsyganenko and Usmanov, 1982; Tsyganenko, 1987]. The major drawback of this approach is that it produces only average magnetic field configurations and cannot represent the diversity of states which contributed to the average state, i.e., the magnetopause, ring, and cross-tail current systems can each undergo large variations while the combined system might be categorized by a single activity index.

To facilitate modeling such diverse configurations, we develop a procedure which relies on three initial magnetospheric input parameters, the magnetopause stand-off distance  $r_0$ , the magnetic activity index  $D^{st}$ , and the midnight equatorward boundary of

the diffuse aurora  $\Lambda_0$ . The remaining unspecified input parameters are determined either through established direct relationships to these three parameters or by selecting values which best describe the nominal magnetospheric configuration as it is presently understood. If more detailed information about a specific configuration is available, such as magnetic field magnitudes in the equatorial plane, then the following procedure can easily be modified to incorporate the additional physical constraints. We begin with the parameters for the vacuum dipole configuration which define the dimensions of the magnetosphere and provides the dipole shielding magnetic field.

## 5.2. Vacuum Dipole Parameters

The magnetopause stand-off distance varies between approximately 7 and 14  $R_E$  while the average value is about 11  $R_E$ . These values are based on the cumulative observational efforts of Patel and Dessler [1966], Meng [1970], Fairfield [1971], and Ness [1972]. The magnetotail radius, as measured between  $x = -20$  and  $-40 R_E$ , has an observed minimum value of 17  $R_E$  [Wolfe et al., 1966], an average value of 20  $R_E$  [Behannon, 1970], and an observed maximum value of 27  $R_E$  [Baker and Stone, 1977]. A rough average of observational results from this same range, as provided in the extensive compilation of magnetotail dimension studies by Sibeck et al. [1986], also supports the idea that the average radius is approximately 20  $R_E$ .

Assuming there is a positive correlation between the stand-off distance and the magnetotail radius, we get an expression relating the two quantities by pairing together their respective maximum, average, and minimum values and assuming that all intermediate combinations lie on a curve containing those three points. Requiring that the stand-off distances  $r_0 = 7, 11, \text{ and } 14 R_E$  correspond to the magnetotail radii  $R = 17, 20,$

and  $27 R_E$ , respectively, leads to the expression

$$R = r_o^2(0.2262) - r_o(3.321) + (29.17) \quad \text{for } 7 R_E \leq r_o \leq 14 R_E \quad (5.1)$$

Our initial vacuum dipole configuration [Voigt, 1981], with its magnetopause surface currents, can now be completely specified by supplying only the dipole tilt angle  $\psi$  and the stand-off distance  $r_o$ .

The dipole tilt angle  $\psi$  can be readily calculated as a function of time but is set equal to zero during the parameter selection process. If not measured directly, the distance  $r_o$  can be estimated using various methods. These include doing pressure balance calculations involving solar wind parameters [e.g., Fairfield, 1985], using correlations with magnetic activity indices such as Kp and D<sup>st</sup> [e.g., Patel and Dessler, 1966; Meng, 1970; Rudneva and Feldstein, 1970; Feldstein, 1972; Su and Konradi, 1975], or using a correlation with dayside equatorial magnetic field strengths [Roederer, 1970].

### 5.3. Ring Current Parameters

The quantity  $\Delta B$ , defined as the observed magnetic field magnitude minus the magnitude of a reference geomagnetic field (which in this instance is the dipole field), is highly dependent on the character of the ring current flux contributions. We will select ring current input parameters ( $B_+$ ,  $B_-$ ,  $\rho_+$ , and  $\rho_-$ ) which maximize our chances of producing  $\Delta B$  profiles similar to the observed average profiles. For this model,  $\Delta B$  profiles typical of the observed average profile along the x axis, as displayed in Figure 5.1, must result from the sum of the equatorial flux contributions of the magnetopause dipole shielding current (Fig. 2.4), the ring current (Fig. 3.2), and the cross-tail current (Fig. 4.2). For dipole tilt angle  $\psi = 0$ , the value of  $\Delta B$  along the x axis can be written as

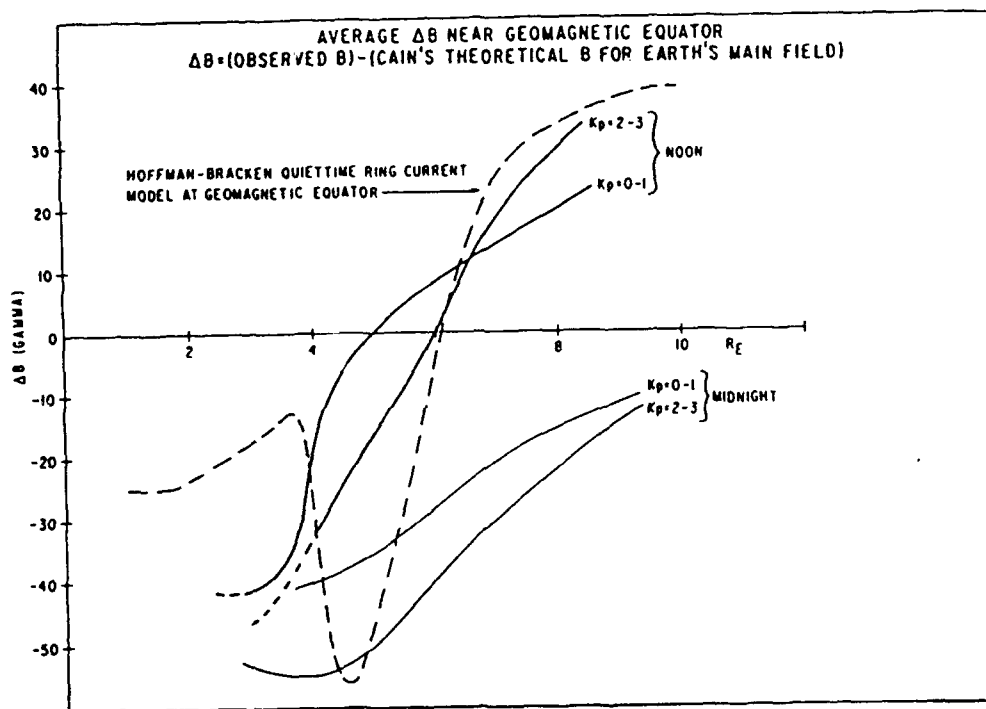


Fig. 5.1. The observed average  $\Delta B$  profiles near the geomagnetic equator for the Kp ranges 0-1 and 2-3 as functions of radial distance in the noon and midnight meridians (from Sugiura et al., 1971).

the sum of the magnetic z components of the contributing sources, thus

$$\Delta B_{x\text{-axis}} = B_{rc,z} + B_{tail,z} + B_{cfd,z} \quad (5.2)$$

The first step is to use information about the observed average  $\Delta B$  profiles to write  $B_{rc,z}$  in terms of  $B_{tail,z}$ ,  $B_{cfd,z}$ , and the  $D^{st}$  index for selected positions along the x axis.

The magnetic activity  $D^{st}$  is a measure of the worldwide deviation from quiet day values of the magnetic field H component (parallel to the magnetic dipole axis and positive northward) at mid-latitude ground stations. An illustration of the method and stations used to calculate  $D^{st}$  is given by Burton et al. [1975]. We will assume that the measured values of  $D^{st}$  directly reflect the changes in the H component at the magnetic equator. It should be noted that a frequently neglected critical point regarding the  $D^{st}$  index is that in addition to reflecting dynamic changes in the ring current, it also reflects changes in the cross-tail and magnetopause currents.

Sugiura [1973] has shown that the minimum field depression near the equatorial plane lies between the geocentric distances 2.3 and 3.6  $R_E$  and its value in nT can be represented by the expression  $\Delta B_{min} = -45 + (0.83) D^{st}$ . The distribution is basically symmetric about the Earth and tends to recover to more positive values at lesser distances (see Figure 5.1). Although this last expression was determined using data from magnetically quiet times, we will use it to represent all activity levels as there is no analogous expression for active times. This procedure is reasonable because there is a positive correlation between  $D^{st}$  and geomagnetic activity, i.e., the Kp index. If we use this expression in equation (5.2) to describe the expected  $\Delta B$  values at  $x = \pm 3 R_E$  then the desired ring current contribution at these same locations,  $B_{rc,z}(\pm 3)$ , can be written as

$$B_{rc,z}(\pm 3) = -45 + 0.83 D^{st} - B_{tail,z}(\pm 3 \text{ ave}) - 247 \times 10^{(-0.1169)r_o} \quad (5.3)$$



The quantity  $B_{\text{tail},z}$  has been replaced by  $B_{\text{tail},z}(\pm 3 \text{ ave})$ , an average of the estimated cross-tail current magnetic field contributions at  $x = \pm 3 R_E$ , and  $B_{\text{cfd},z}$  has been replaced by an exponential function, which represents the average dipole shielding contribution for these same locations as a function of the stand-off distance. The dipole shielding contribution, with  $7 R_E \leq r_o \leq 14 R_E$ , can assume values ranging from +38 to +6 nT. The estimated values of  $B_{\text{tail},z}(\pm 3 \text{ ave})$  we use are -5, -15, -30, and -45 nT to depict weak, moderate, strong, and extremely strong cross-tail currents contributions, respectively. At the end of this procedure the chosen value for  $B_{\text{tail},z}(\pm 3 \text{ ave})$  can be compared to the final cross-tail strength to see if the model  $D^{\text{st}}$  value matches the input  $D^{\text{st}}$  value.

Our next  $\Delta B$  evaluation point is located on the Earth's surface. To quantify the magnitude of the  $\Delta B$  recovery toward Earth we need an estimate for  $\Delta B$  on the Earth's surface for quiet conditions, i.e., when  $D^{\text{st}} \approx 0$ . The quiet time ring current contribution to the magnetic H component at the Earth's surface is estimated to be -21 nT, with -9 nT coming from ring current protons with energies greater than 97 keV [Hoffman and Bracken, 1965] and -12 nT resulting from ring current protons and electrons with energies less than 50 keV [Frank, 1967]. Our vacuum dipole configuration, using an average stand-off distance of  $11 R_E$ , provides a dipole shielding contribution of +13 nT, while a weak to moderate cross-tail current, as quoted above, provides -5 to -15 nT. The sum of these individual contributions gives us an estimated  $\Delta B$  which ranges between -13 and -23 nT for  $x = \pm 1 R_E$  during quiet times. This estimate is a very rough one as the actual stand-off distance and cross-tail current strength can vary greatly while  $D^{\text{st}}$  remains positive or near zero. The estimate does, however, agree with a Su and Konradi [1975] estimate that  $\Delta B$  recovers to -19 nT when  $D^{\text{st}} = 0$ . Using the latter estimate allows us to write  $\Delta B = -19 + D^{\text{st}}$  for  $x = \pm 1 R_E$ . If we put this expression in equation (5.2) to

describe the expected  $\Delta B$  values at  $x = \pm 1 R_E$  then the desired ring current contribution,  $B_{rc,z}(\pm 1)$ , can be written as

$$B_{rc,z}(\pm 1) = -19 + D^{st} - B_{tail,z}(\pm 3 \text{ ave}) - 247 \times 10^{(-0.1169)r_o} \quad (5.4)$$

where  $B_{tail,z}$  and  $B_{cfd,z}$  of (5.2) have been replaced by the same terms used to get equation (5.3). This can be done because both the dipole shielding and cross-tail current contributions change relatively little between  $x = \pm 3 R_E$  (see Figures 2.4 and 4.2).

An additional condition, to be used as a guide for controlling the width of the ring current distribution, can be determined from the noon  $Kp = (2-3)$  curve of Figure 5.1. The value of  $\Delta B$  changes sign at  $x = +6 R_E$  so equation (5.2) can again be utilized, this time with  $\Delta B = 0$ . This results in an expression for the desired value of  $B_{rc,z}(+6)$ , namely

$$B_{rc,z}(+6) = -B_{tail,z}(+6) - 70580 r_o^{3.4129} \quad (5.5)$$

where  $B_{tail,z}(+6)$  is an estimate of the cross-tail current contribution at  $x = +6 R_E$  and the remaining term is  $B_{cfd,z}$  expressed as a function of the stand-off distance for the same position. The values for  $B_{tail,z}(+6)$  are -5, -10, -20, and -30 nT, corresponding to a cross-tail current which is weak, moderate, strong, and extremely strong, respectively.

While equation (5.5) is most appropriate for average condition, i.e., when  $Kp$  is in the 2-3 range, it can be used to qualitatively check the ring current contribution for other activity levels in the following way. The zero point of the  $\Delta B$  curve tends to move outward on the dayside with higher activity levels, therefore, we should expect  $B_{rc,z}$  at  $x = +6 R_E$  to be less than  $B_{rc,z}(+6)$  when  $Kp$  is above average and greater than  $B_{rc,z}(+6)$

when conditions are very quiet.

The ring current contribution at  $x = 0$  is determined by extrapolating along the line containing the desired ring current values  $B_{rc,z}(\pm 1)$  and  $B_{rc,z}(\pm 3)$  from equations (5.4) and (5.3), such that

$$B_{rc,z}(0) = \frac{3B_{rc,z}(\pm 1) - B_{rc,z}(\pm 3)}{2} = B_+ + B_- \quad (5.6)$$

where  $B_+$  and  $B_-$  are the ring current parameters representing the positive and negative contributions to  $B_{rc,z}$  at the origin, respectively (see equation (3.6)). The ring current parameter selection procedure can now be detailed.

The magnetic index  $D^{st}$ , the magnetopause stand-off distance  $r_m$ , and an estimate of the required cross-tail current strength, i.e., weak, moderate, strong, or extremely strong, are substituted into equations (5.3) and (5.4). The results of those two equations, along with the initial guess that  $B_- = 0$  nT, are combined with equation (5.6) to get  $B_+$ . The best combination of radii,  $\rho_+$  and  $\rho_-$ , for that  $B_-$  value are found as described below. The quality of the fits tend to peak for a certain range of  $B_-$  then degrades as  $B_-$  becomes more negative. Moving in steps of -10 nT, the value of  $B_-$  is decreased until the best overall fit is found.

The best combination of radii for a particular  $B_-$  value are determine by scanning through the allowable combinations of  $\rho_+$  and  $\rho_-$  by changing each in steps of  $0.1 R_E$  for values up to  $10 R_E$  while remembering that  $\rho_-$  must always be greater than  $\rho_+$ . The combination of radii which brings us closest (i.e., gives the best least squares fit) to the desired values of equations (5.3) and (5.4) is retained. Equation (5.5) can also be included in this process or just used for qualitative comparison when the value of  $Kp$  is far from the average. Now that the ring current parameters are set, we search next for the

cross-tail current parameters.

#### 5.4. Cross-tail Current Parameters

The cross-tail current parameters to be determined are the distance to the plasma sheet inner edge  $s_I$ , the magnetic filament strength at the inner edge  $B_I$ , the ratio of the far tail filament strengths to that of the inner edge filament  $[B_f/B_I]$ , the characteristic filament half-thickness  $\delta$ , and the characteristic distance for changes in the  $y$  direction  $\Delta y$ . These parameters will be determined once for the case with  $\psi = 0$  and held fixed for all dipole tilt angles. We will specify these parameters in a prescribed order starting with the plasma sheet inner edge location.

The nightside equatorward auroral boundary of electron precipitation is connected via magnetic field lines to the plasma sheet inner edge [Vasyliunas, 1968, 1970; Chase, 1969; Lassen, 1974; Winningham et al., 1975; Lui et al., 1977]. The existence of this mapping relationship indicates that a quantitative connection might be established between the plasma sheet inner edge position  $s_I$  and the midnight equatorward auroral boundary latitude  $\Lambda_0$ . This can be done by taking advantage of their mutual dependence on geomagnetic activity. First, the auroral boundary moves equatorward with increasing geomagnetic activity as measured by  $K_p$  [Lui et al., 1975; Sheehan and Carovillano, 1978] and its equatorward position is linearly related to  $K_p$  [Slater et al., 1980; Gussenhoven et al., 1981, 1983]. Second, there is also an established connection between the plasma sheet inner edge position and  $K_p$  [e.g., Mauk and McIlwain, 1974; Freeman, 1974; Kivelson et al., 1979; Horwitz et al., 1986].

To get a  $K_p$  dependent expression for the midnight equatorward auroral boundary we average the 0000-0100 MLT range and 2300-2400 MLT range results of

Gussenhoven et al. [1983], giving

$$\Lambda_o = 66.95 - (2.03)Kp \quad (5.7)$$

Using data obtained within the 1500-2400 MLT range, Horwitz et al. [1986] determined that the 100 eV electron plasma sheet inner edge is linearly related to Kp such that  $s_I = 7.97 - (0.82)Kp$ . An alternative expression,  $s_I = 6.90 - (0.57)Kp$ , is from Kivelson et al. [1979] and comes from evaluating the top equation of their Table 1 for the midnight meridian. Both expressions were selected as being typical of the results presented in their respective works. By assuming that the average of these two expressions more adequately represents the typical functional dependence, we have

$$s_I = 7.44 - (0.70)Kp \quad (5.8)$$

and using equation (5.7) to eliminate Kp in (5.8) gives

$$s_I = (0.34)\Lambda_o - 15.64 \quad (5.9)$$

where the equatorward auroral boundary at local midnight  $\Lambda_o$  is in degrees of magnetic dipole latitude and  $s_I$  is in  $R_E$ . This expression illustrates how, on average, earthward movement of the plasma sheet inner edge is tied to the equatorward motion of the midnight auroral boundary. We should also note that this relationship makes  $\Lambda_o$  the most critically sensitive of our initial input parameters as small variations in the inner edge location have a dramatic effect on the magnetic field configurations.

The next three parameters,  $B_I$ ,  $[B_c/B_I]$ , and  $\delta$ , are selected such that the model magnetic field in the midnight meridian fulfills three basic requirements. First, the

surface point on the Earth corresponding to the midnight equatorward boundary of the diffuse aurora,  $(-\cos\Lambda_o, 0, \sin\Lambda_o)$ , maps magnetically to the midnight location of the plasma sheet inner edge in the equatorial plane  $(-s_I, 0, 0)$ . Second, the magnetic field along the x axis, as given by the component  $B_{T,z}$ , generally remains positive and decreases monotonically tailward [e.g., Behannon, 1970; Fairfield, 1986]. And finally, if the formation of a minimum in  $B_{T,z}$  cannot be avoided, as will occur when extreme tail field stretching is occurs just prior to the onset of a substorm, the minimum should be kept as shallow as possible. This last point is included as an attempt to kept the tail configurations in line with the average observational picture. It should be noted, however, that some steady state magnetotail calculations [e.g., Hau et al., 1989] predict the existence of a  $B_{T,z}$  minimum in the near tail.

Experience with the model indicates that the inner edge filament strength can assume values as large as  $B_I = 20$  for extremely stretched tail configurations, and values as small as  $B_I \approx 1$  for extremely weak cross-tail currents. The final value will be kept as small as possible to minimize the total cross-tail current. This is done under the postulation that the most likely configuration of the magnetosphere corresponds to the lowest possible energy state and thus the least amount of cross-tail current.

The inner edge filament strength selection procedure starts with an initial assumption for  $B_I$ . Next, a search for an appropriate combination of  $[B_c/B_I]$  and  $\delta$  is conducted and if the three midnight meridian requirements can be satisfied then all three parameters are set. If the magnetic field mapping overshoots (undershoots) the inner plasma sheet boundary then  $B_I$  is increased (decreased) slightly and we repeat the procedure as necessary.

The parameters  $[B_c/B_I]$  and  $\delta$ , indicating the fraction of the inner edge filament strength found in the far tail filaments and the magnetic filament half-thickness,

respectively, are determined simultaneously using information about their combined effect on magnetic field stretching and the  $B_{T,z}$  distribution down the tail axis.

Table 5.1 demonstrates the effect that these two parameters have of  $B_{\text{tail},z}$  along the magnetotail central axis and can be used as a selection guide. The relative locations and sizes of the minimum and maximum values of  $B_{\text{tail},z}$  (see Figure 4.2), along with the location of the functions zero point, are provided for different parameter combinations in Table 5.1. As  $\delta$  decreases, the location of the function's zero and maximum points move earthward while the maximum and minimum values both increase in magnitude. In addition, as  $[B_c/B_T]$  decreases, the function's zero and maximum points also move inward while the maximum value increases and the minimum value becomes more shallow. The net effect is that field line stretching is enhanced when either  $[B_c/B_T]$  increases or  $\delta$  decreases. These trends correspond to increasing the tail current and thinning of the plasma sheet, respectively.

The quantities in Table 5.1 are for a current sheet, as described in Section 4, which extends more than  $350 R_E$  tailward of the Earth. Although it is unrealistic to quote model magnetic field values at such distant locations, we should note that the presence of current in the far magnetotail does influence the flux distribution close to the Earth. The extended current sheet helps us fulfill our mapping criteria more easily.

The final cross-tail current parameter,  $\Delta y$ , is determined by utilizing the work of Fairfield [1979, 1986] which illustrates that, for all activity levels, the magnetic field strength in the flanks of the equatorial plane is greater than that in the magnetotail center for distances  $x = -10$  to  $-33 R_E$ . We divide the equatorial region between  $x = -20$  and  $-40 R_E$  into three regions of equal width in  $y$  and determine the average field strength for each region. The ratio of the average field strength in the flanks to the average that in the magnetotail center is maximized by adjusting  $\Delta y$  and generally reaches values between 1

TABLE 5.1. The quantities  $x_{\text{zero}}$ ,  $x_{\text{max}}$ ,  $B_{\text{max}}$ , and  $B_{\text{min}}$ , from the function  $B_{\text{tail},z}(x,0,0)$ , vs.  $[B_c/B_I]$  and  $\delta$ . The quantities indicate where the function is equal to zero, the location of its maximum value, and the maximum and minimum values, respectively ( $x_{\text{min}} \approx -0.5$  for all cases). They are calculated using  $B_I = 1$ ,  $s_I = 0$ , and  $\psi = 0$  and grouped vertically in descending order starting with  $x_{\text{zero}}$ . Distances are measured along the x axis in  $R_E$  and magnetic field strengths are in nT. To get actual x positions add  $-s_I$  to the distances given. Field strengths can be obtained by multiplying the given strength by  $B_I$ . Field line stretching in the magnetotail increases with increasing  $[B_c/B_I]$  and decreasing  $\delta$ .

$[B_c/B_I]$	$\delta = 0.5$	1.0	1.5	2.0	2.5	3.0	3.5	4.0	4.5	5.0
0.01	-8.5	-9.0	-9.5	-9.5	-10.0	-10.5	-10.5	-11.0	-11.0	-11.5
	-29.5	-30.0	-30.5	-31.5	-33.5	-34.5	-35.0	-35.5	-36.0	-36.5
	0.7	0.7	0.7	0.6	0.6	0.6	0.6	0.6	0.6	0.6
	-2.8	-2.4	-2.1	-1.9	-1.7	-1.6	-1.4	-1.3	-1.2	-1.2
0.10	-18.5	-19.0	-19.5	-20.0	-20.5	-20.5	-21.0	-21.5	-22.0	-22.0
	-55.0	-55.5	-56.0	-56.0	-56.5	-56.5	-57.0	-57.5	-58.0	-59.0
	0.6	0.6	0.6	0.6	0.5	0.5	0.5	0.5	0.5	0.5
	-3.6	-3.2	-2.9	-2.6	-2.4	-2.3	-2.1	-2.0	-1.9	-1.8
0.20	-29.0	-29.5	-30.0	-30.5	-31.0	-31.5	-32.0	-32.5	-33.0	-33.5
	-80.5	-81.0	-81.0	-81.0	-81.0	-81.0	-81.0	-81.5	-81.5	-81.5
	0.5	0.4	0.4	0.4	0.4	0.4	0.4	0.4	0.4	0.4
	-4.0	-3.6	-3.3	-3.0	-2.8	-2.7	-2.5	-2.4	-2.3	-2.2
0.30	-42.5	-43.0	-43.5	-44.5	-45.0	-45.5	-46.0	-46.5	-47.5	-48.0
	-87.5	-87.5	-87.5	-87.5	-87.5	-87.5	-87.5	-87.5	-87.5	-87.5
	0.3	0.3	0.3	0.3	0.3	0.3	0.3	0.3	0.3	0.3
	-4.4	-3.9	-3.6	-3.4	-3.2	-3.0	-2.8	-2.7	-2.6	-2.5
0.40	-62.0	-63.0	-63.5	-64.5	-65.0	-66.0	-66.5	-67.5	-68.0	-69.0
	-90.5	-90.5	-90.5	-90.5	-91.0	-91.0	-91.0	-91.5	-91.5	-91.5
	0.2	0.2	0.1	0.1	0.1	0.1	0.1	0.1	0.1	0.1
	-4.7	-4.3	-3.9	-3.7	-3.5	-3.3	-3.1	-3.0	-2.9	-2.8



and 2. Recreating this type of equatorial flux distribution is only possible because, while the initial vacuum configuration has positive  $B_{T,z}$  throughout the equator with maximum values at the magnetotail center (see Figure 2.5), the cross-tail current contributes negative flux earthward of  $x = -s_I + x_{zero}$  (see Table 5.1) with the largest magnitudes also at the center of the tail.

### 5.5. Comments

The specific magnetic field configurations generated using this procedure are designed to represent the most likely magnetospheric state for a given initial input parameter set. They result from a combination of both very specific and general criteria and are selected in a very specific order according to their relative importance. This process enables us to generate sequences of static configurations which change in a predictable and realistic manner in response to variations of the initial parameter inputs.

A three parameter characterization of the Earth's magnetosphere obviously offers more flexibility than one based on only a single parameter such as  $K_p$ . The real advantage comes from the fact that it enables us to tailor magnetic field models for investigations involving dynamic processes such as ring current development and magnetic field line stretching in the magnetotail. An example of this type of investigation is discussed in Section 8, where this procedure is used to construct a set of magnetic field models to simulate the behavior of the magnetosphere during a magnetically active time period.

We should note that this procedure imposes artificial constraints on the output of the ring and cross-tail currents as it does not include contributions from magnetopause shielding currents for the ring and cross-tail current fields. To introduce these additional

fields, an automatic shielding method similar to the one used for the dipole field would have to be developed to accommodate the iterative style of parameter selection. An initial estimate of their flux contributions to the equatorial plane would then have to be made and included in equations (5.3)-(5.5) as is now done for the cross-tail current.

The relative amount of change this would bring to the resulting current systems is small for the ring current and inner portions of the cross-tail current. This is due to the fact that magnetopause boundary violations are dominated by contributions from the dipole field, thus its shielding field within the magnetospheric cavity also dominates. This can be seen in Figure 5.2, which compares the model component magnetic field contributions normal to the magnetopause along the noon-midnight meridian. It is along this meridian that the normal component reaches its maximum values. With proper shielding the positive flux through the equatorial plane would increase, thus enhancing the contribution from the dipole shielding already in place. This would require strengthening of both the ring and cross-tail currents to match the requisite  $\Delta B$  profile. Fortunately, the increased current levels would also be needed to meet the magnetic field mapping constraint, as it is by decreasing the equatorial flux levels that we promote field line stretching. Now that an input parameter selection procedure has been established, we can begin to look at the behavior of the system as a whole.

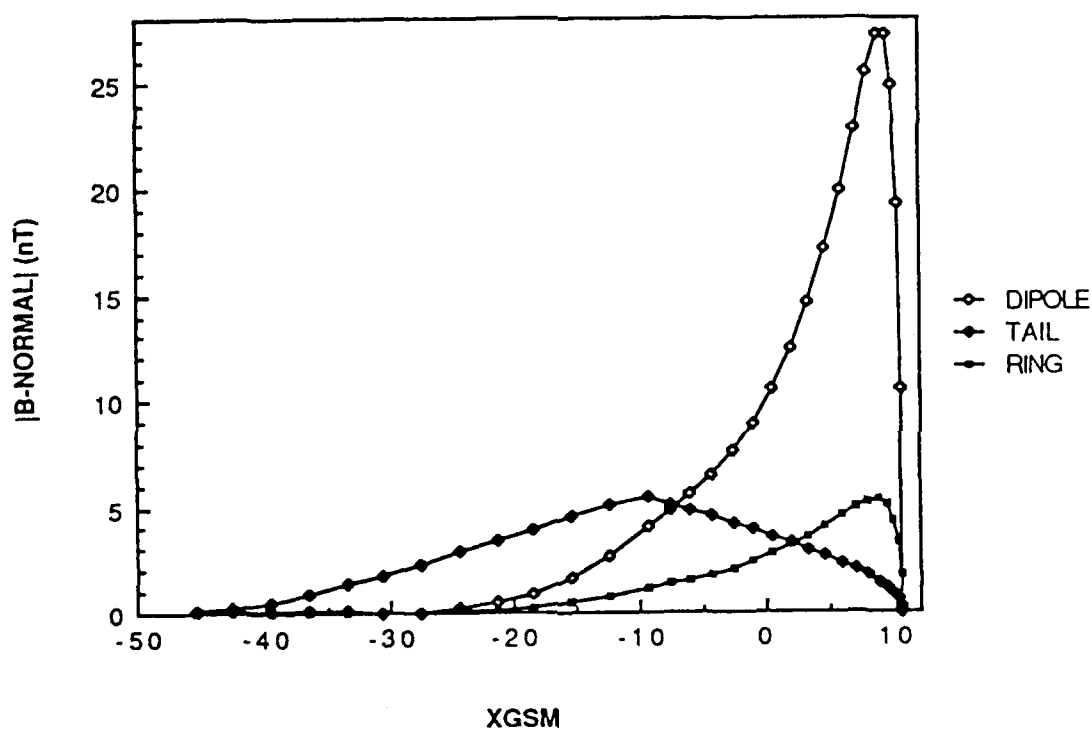


Fig. 5.2. Magnitude of the magnetic field component normal to the magnetopause in the noon-midnight meridian as a function of corresponding position along the x axis for the dipole, ring current, and cross-tail current of a moderately stretched configuration. The subsolar point is at  $x = +10.5 R_E$ , the Earth is at  $x = 0 R_E$ , and the cylindrical portion of the tail begins at  $x = -8.7 R_E$ .

## 6. Integration of the Model Components: The Nominal Magnetosphere

### 6.1. Introduction

Various characteristics of our vacuum configuration were illustrated in Section 2, namely, the magnetic field mapping and equatorial flux distribution as they varied with the dimensions of the magnetopause and the behavior of the neutral sheet surface as it flexes with changing dipole tilt angle. With the subsequent development of the ring and cross-tail currents, we are now ready to investigate the impact of these currents on the magnetic field mapping and magnetic flux distribution of the nominal magnetosphere (a detailed look at the motion of the neutral sheet is left for Section 8). We can also look at the model's sensitivity to changing input parameters.

### 6.2. Total Magnetic Field and Current

Our first full magnetic field model example is designed to represent what might be considered a typical or average configuration when viewed with respect to the range of possible input parameters  $r_o$ ,  $D^{st}$ , and  $\Lambda_o$  used in the selection procedure of Section 5. The chosen stand-off distance  $r_o = 10.5 R_E$  is near the average value, the magnetic activity index  $D^{st} = -20$  nT is representative of moderately quiet conditions, and the equatorward latitude of the diffuse auroral precipitation  $\Lambda_o = 64^\circ$  corresponds to a  $K_p \leq$

2. With these initial inputs and an estimate that a "weak" cross-tail current (i.e., see equations 5.3 and 5.4) is required to achieve the desired mapping (see equation 5.9), our selection procedure yields a parameter set that specifies the configuration in Figure 6.1. This can be compared with the vacuum configurations of Section 2. Note that the most equatorward field line in the noon-midnight meridian view, for this and all subsequent figures of this type, emanates from  $60^\circ$  as opposed to the  $66^\circ$  latitude value used in Figure 2.1. The change is made to better illustrate the more inflated field line structures to be encountered when including additional current systems.

The most obvious changes from the vacuum state are the more inflated field lines of the inner magnetosphere, the tailward stretching of the nightside field, and the penetration of field lines through the magnetopause boundary owing to the unshielded internal currents. The lower panel of Figure 6.1 reveals that some of the curves connecting points mapped from constant latitudes are no longer closed as they are in the vacuum case (see Figure 2.2) indicating again that flux has escaped our boundary. While the inner contours are enlarged and retain their basically dipolar character, field lines mapping from higher latitudes are drawn farther tailward preferentially at longitudes near local midnight. This can be attributed to the  $y$  dependence of the cross-tail current which enables it to weaken toward the tail flanks.

A dipole-tilted version of the same model with  $\psi = 25^\circ$  is shown in Figure 6.2. If the working definition for "cusp" location is qualified for this presentation to be the latitude dividing field lines which bend tailward or sunward just before impacting the magnetopause, then the northern hemisphere cusp position moves to a higher latitude when the dipole tilts. This behavior is also found in the vacuum case (see lower panel of Figure 2.1). It should also be noted that the neutral sheet has been raised above the equatorial plane and sustains its position with distance down the tail, whereas in the

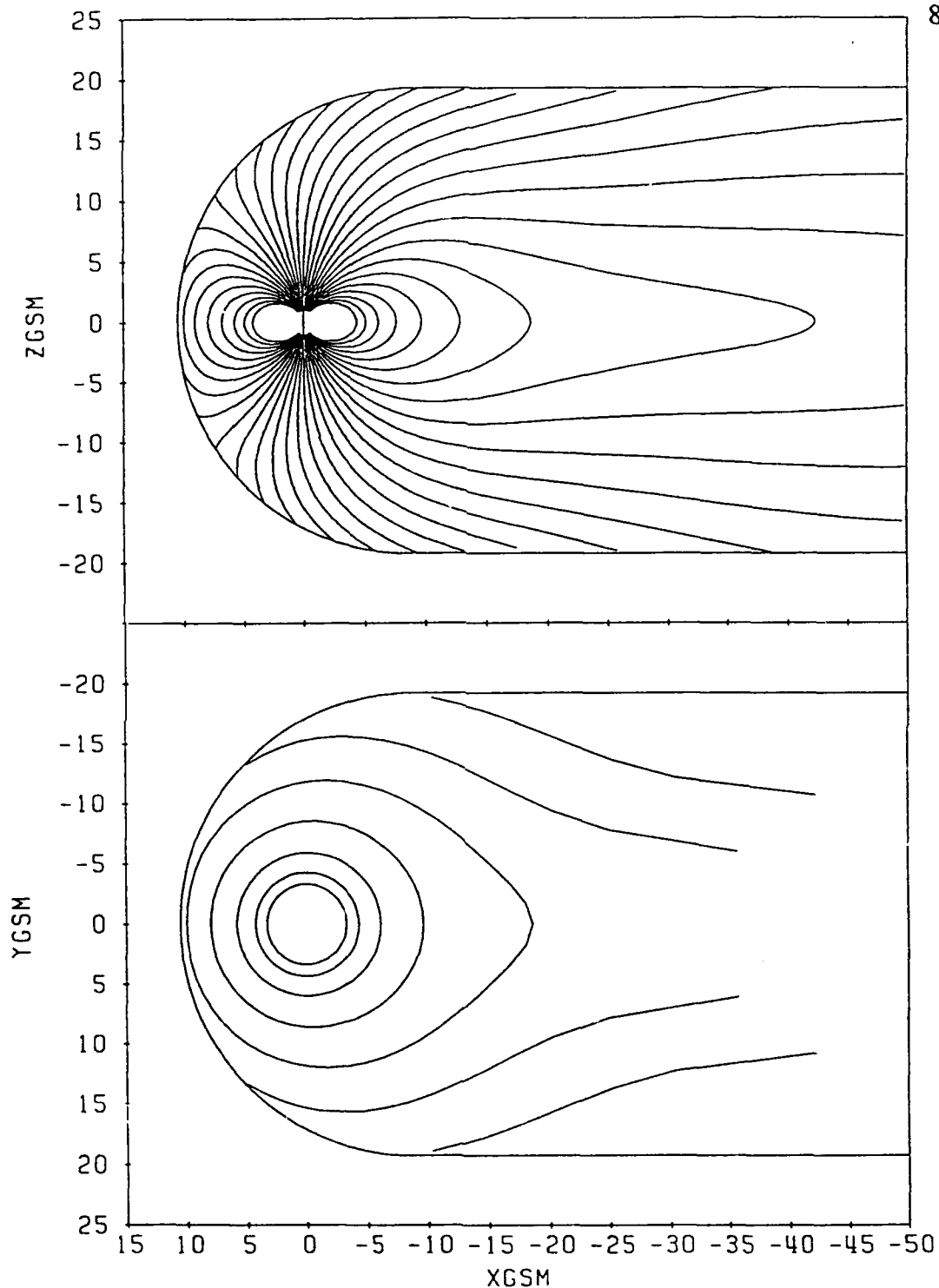


Fig. 6.1. Magnetic field lines in the noon-midnight meridian mapped from  $60^\circ$  latitude in steps of  $2^\circ$  for  $\psi = 0^\circ$  (upper panel) and corresponding equatorial mappings from rings of constant latitude (lower panel) with inner most ring mapping from  $56^\circ$  latitude. Successive contours are separated by  $+4^\circ$  of latitude. Input parameters are  $r_0 = 10.5 R_E$ ,  $s_1 = 6.1 R_E$ ,  $B_I = 4.0$  nT,  $[B_\phi/B_I] = 0.25$ ,  $\Delta y = 9.0 R_E$ ,  $\delta = 3.5 R_E$ ,  $B_- = -310.0$  nT,  $B_+ = 272.7$  nT,  $\rho_- = 2.8 R_E$ , and  $\rho_+ = 2.1 R_E$ .

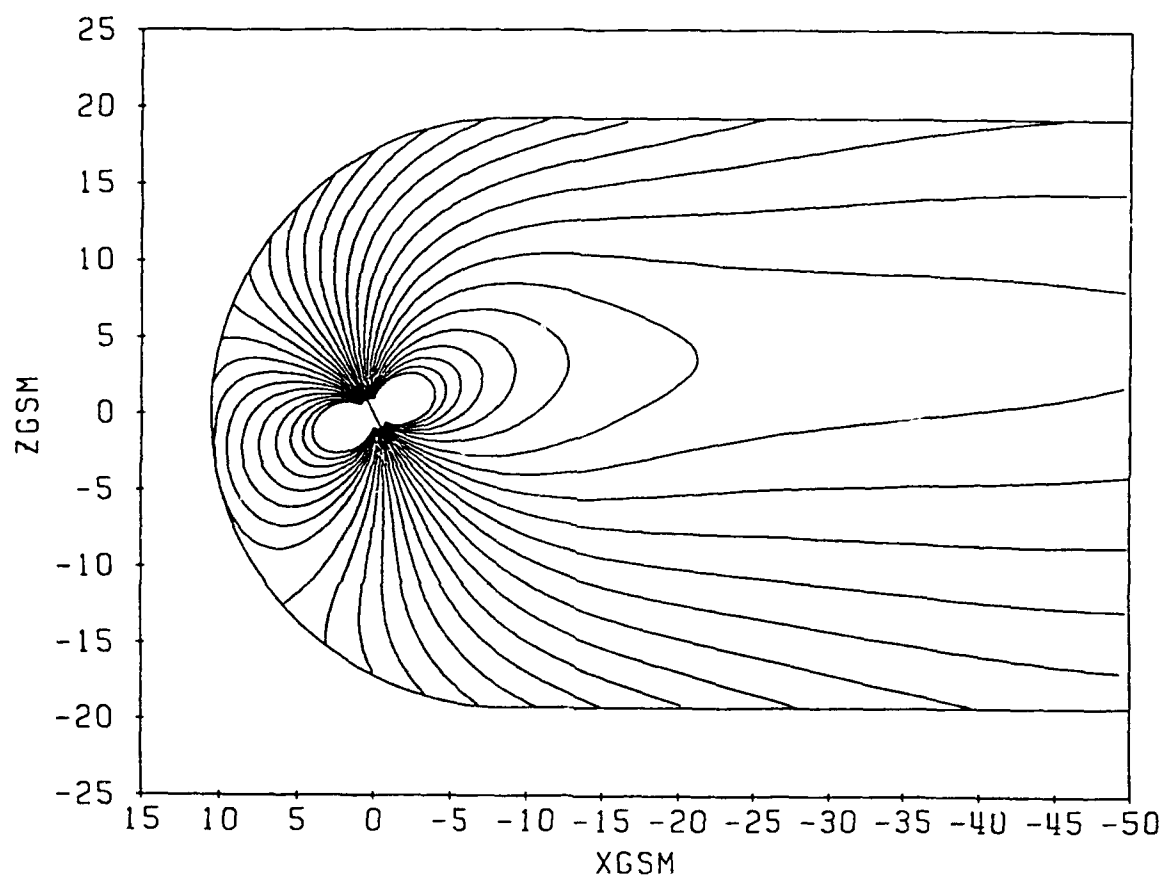


Fig. 6.2. Magnetic field lines in the noon-midnight meridian corresponding to Figure 6.1 with  $\psi = 25^\circ$ .

vacuum case it returned quickly to the that same plane. A discussion of neutral sheet behavior is provided in Section 8.

The relative contributions to the tailward stretching of field lines from the individual current systems are illustrated in Figure 6.3. The addition of only the ring current to the vacuum configuration helps to extend field lines from about  $60^\circ$  latitude and higher by only a few Earth radii (curve 2). In contrast, the cross-tail current alone in combination with the vacuum field affects latitudes above approximately  $68^\circ$ , but the stretching is much more dramatic and changes equatorial mapping distances by many  $R_E$  (curve 3). Incorporating both current systems reveals the complementary interaction required to achieve the final state (curve 4). The ring and cross-tail currents each have their own latitudinal zones of influence and combining them results in a multiplying effect with the net displacement of field lines being greater than the sum of displacements due to the individual current components.

The current components also make very different contributions to the equatorial magnetic field strength. The comparison of the equatorial contours of Figures 6.4 and 2.5 can be used to make this point. The inner most contours, i.e., those for 150 and 80 nT, have shifted earthward in Figure 6.4 as the ring and cross-tail currents both provide negative (i.e., southward) field contributions in that region. Beyond a radial distance of about  $10 R_E$  (see Figure 3.1) the ring current contribution is positive and is actually larger than the negative cross-tail contribution in some regions. The result is that for  $y \geq \pm 10 R_E$ , the contours have shifted outward and tailward with the net addition of flux. The central portions of the tail, out to about  $x \approx -40 R_E$ , is dominated by negative contributions from the tail current and the contours shift earthward. Beyond that distance the tail contribution switches to become positive (see Table 5.1) and the contours, e.g., for 0.5 nT, shifts tailward.



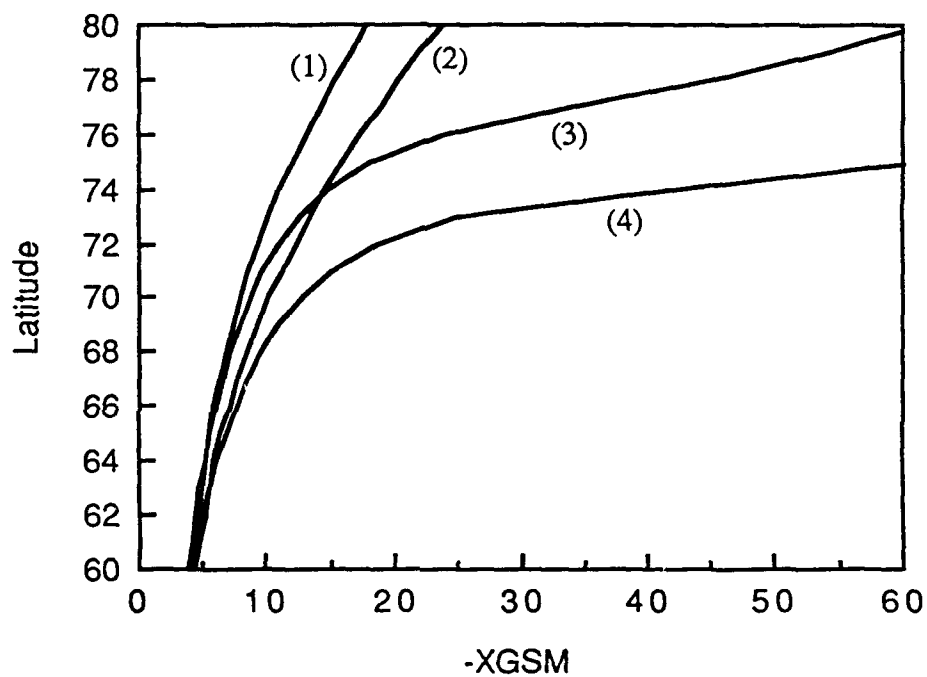


Fig. 6.3. Midnight latitudes as a function of equatorial mapping position with  $\psi = 0^\circ$  corresponding to (1) the vacuum field, (2) the vacuum field plus the ring current, (3) the vacuum field plus the cross-tail current, and (4) all components of the Figure 6.1 configuration.

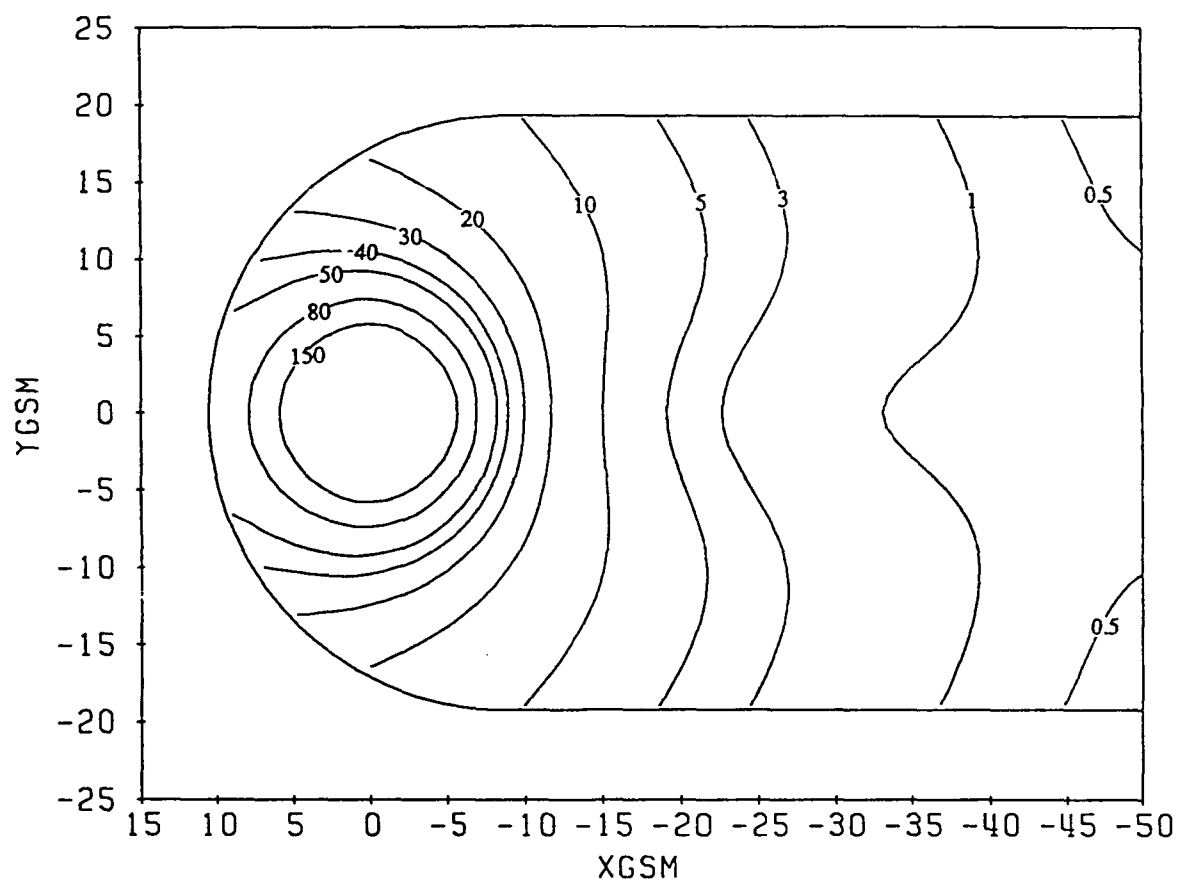


Fig. 6.4. Contours of constant magnetic field magnitude (nT) in the equatorial plane corresponding to Figure 6.1.

A main point to notice about the net distribution is that more flux passes through the flanks between  $x = -15$  to  $-40 R_E$  than through the center of the magnetotail at those same distances, in agreement with the observational trends [Fairfield, 1979, 1986], and that most of the model configurations calculated using our selection procedure contain this flux characteristic. Also, the values of  $B_{T,z}$  down the center of the magnetotail match well with the average values determined by Behannon [1970], which decrease from  $\approx 3.5$  nT to  $\approx 1.0$  nT over the distance range  $x = -20$  to  $-50 R_E$ .

The currents producing these field changes are illustrated in Figure 6.5. The top panel contains the current density profile for the equatorial plane at midnight and shows a moderately weak cross-tail current sheet, which matches our original tail strength estimate, merging continuously with the westward portion of ring current. Below this we have the current flow pattern in the equatorial plane showing the cross-tail current bending around the Earth and smoothly joining with the ring currents. The radial location of the eastward flowing current, which completely encircles the Earth, is indicated by the incomplete current traces.

While the inner ring current flows in closed circular paths, the outer portions intersect the magnetopause boundary. If the magnetic field and current were calculated self-consistently, then adiabatic particles contributing to the current would flow along the paths described by the magnetic field contours of Figure 6.4. These contours are similar but do differ noticeably from the model current patterns. The current flow across the magnetotail viewed in the x-y plane is similar to the pattern shown in Figure 4.6, with the current becoming compressed as it passes through the center of the tail.

An example of current densities in the noon-midnight meridian plane for a tilted dipole configuration is provided in Figure 6.6. The near-earth region is dominated by the westward current which envelops the interior eastward portion of the ring current. Both

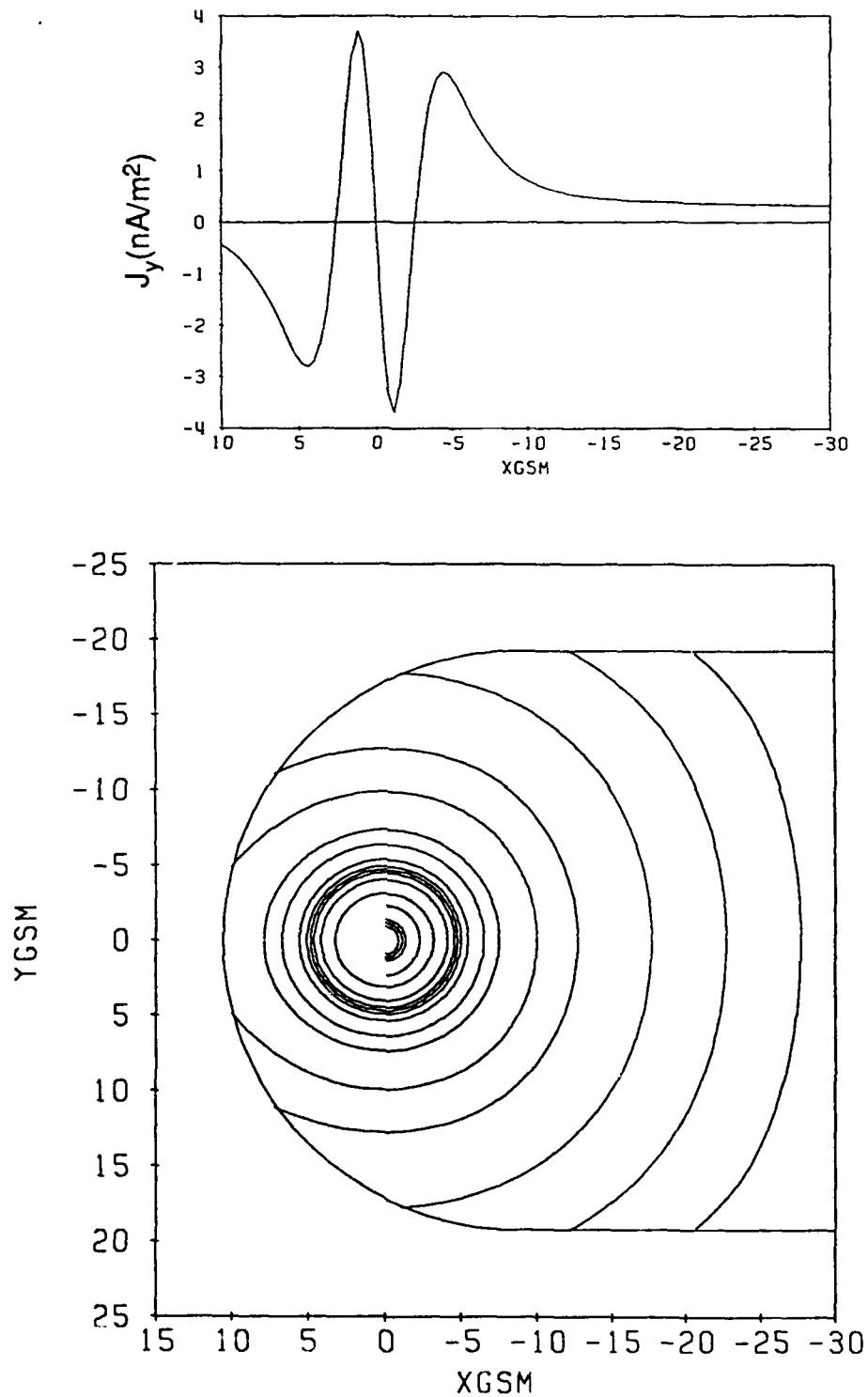


Fig. 6.5. Combined ring and cross-tail current,  $J_y$ , as a function of distance along the x axis (upper) and corresponding equatorial current traces (lower) for the configuration of Figure 6.1. The current traces are grouped according to the current intensity along the x axis with more closely spaced traces corresponding to stronger current regions. The eastward portion of the ring current follows a roughly circular path and is denoted by the incomplete traces closest to Earth.

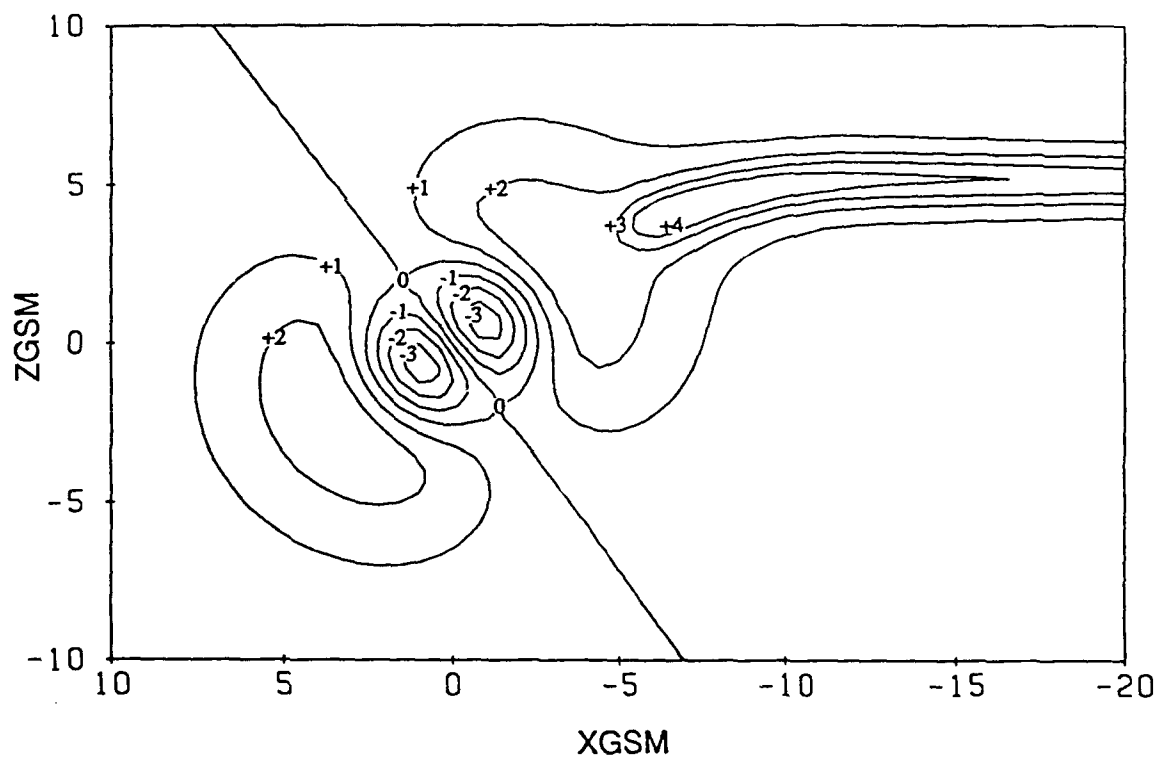


Fig. 6.6. Contours of constant current density ( $\text{nA/m}^2$ ) passing through the noon-midnight meridian for  $\psi = 35^\circ$ . Eastward and westward traveling current is marked negative and positive, respectively. This figure combines the ring current of Figure 6.1 with the cross-tail current of CDAW-6 time label 4.

ring current components tilt to remain symmetric about the dipole axis. The cross-tail current sheet gradually bends farther away from the dipole equatorial plane to become parallel with the x-y plane. These current densities compare favorably with those from some of the self-consistent calculations [e.g., Sozou and Windle, 1969] and the figure can be contrasted, for example, with Figure 10 of Tsyganenko [1987], which includes neither an eastward current source nor the flexing of the current sheet in the x-z plane.

### 6.3. Input Parameter Sensitivity

The inflation of the inner magnetosphere and the tailward stretching of field lines can be accomplished in one or more of the following ways. The net magnetic flux of the inner region can be decreased by increasing the ring current strength. This is accomplished either by making the sum ( $B_+ + B_-$ ) more negative or by increasing  $\rho_-$  relative to  $\rho_+$ . The cross-tail current can increase field line stretching if the inner edge strength  $B_I$  is increased, the inner edge position  $s_I$  is decreased, the ratio [ $B_c/B_I$ ] is increased, or the characteristic plasma sheet thickness  $\delta$  is decreased. By increasing  $\Delta y$ , the cross-tail current can influence a broader width of the magnetotail and more effectively draw tailward field lines originating from dawn and dusk longitudes.

The range of values used for the ring current parameters  $B_-$  and  $B_+$  can be exemplified by the variations in the magnetic index  $D^{st}$ , which can assume values from several tens of nT positive to several hundred nT negative, as their sum is related to the value of this index (see equations 5.3, 5.4, and 5.6). The radii  $\rho_+$  and  $\rho_-$  are generally less than  $5 R_E$  and most often in the 2 to  $3 R_E$  range.

The scope of the cross-tail current parameter values encountered when modeling extremely quiet to extremely stretched and magnetically active configurations are as

follows: ( $3 R_E \leq s_I \leq 8 R_E$ ), ( $1 \text{ nT} \leq B_I \leq 20 \text{ nT}$ ), ( $0.1 \leq [B_c/B_I] \leq 0.4$ ), ( $5 R_E \leq \Delta y \leq 15 R_E$ ), and ( $0.5 R_E \leq \delta \leq 5.0 R_E$ ). While  $s_I$  and  $B_I$  control the general extent to which midnight meridian field lines are stretched, the fine tuning of the equatorial flux levels (i.e., the avoidance of negative  $B_{T,z}$ , control of the depth of minima in  $B_{T,z}$ , and the final field mapping characteristics) is controlled by  $[B_c/B_I]$  and  $\delta$ .

Figure 6.7 illustrates the effect these two parameters have on field line mapping. The configuration of Figure 6.1 was altered by substituting different values for  $[B_c/B_I]$  and  $\delta$  into the parameter list. The equatorial latitude is given as a function of equatorial mapping position in the upper and lower panels, respectively. It is obvious from both this figure and Table 5.1 that the value of the ratio  $[B_c/B_I]$  is much more critical than the current sheet thickness  $\delta$  for both field line mapping and magnetic flux distribution along the center of the magnetotail. This is owing to the fact that decreasing  $\delta$  concentrates the current closer to the corresponding magnetic field filaments (equation 4.1) but does not change the total current of the filament (or the system), whereas varying the ratio  $[B_c/B_I]$  does change the total current content of the system.

Figures 6.8, 6.9, and 6.10 illustrate the range of possible configuration types and represent what might be termed "quiet", "intermediate", and "stretched" states of the magnetosphere, respectively. The corresponding configurations with  $\psi = 25^\circ$  appear in Figure 6.11. These examples all have the same magnetopause dimensions so they can be used to illustrate the internal parameter changes required to move the model through these various stages.

The progression from one state to the next requires that the ring current gradually strengthens, the current sheet moves earthward, the inner edge current sheet intensity increases, the ratio  $[B_c/B_I]$  decreases, and the current sheet thins. Note that in this sequence, the ratio  $[B_c/B_I]$  gets smaller as  $B_I$  increases. This indicates that much of the

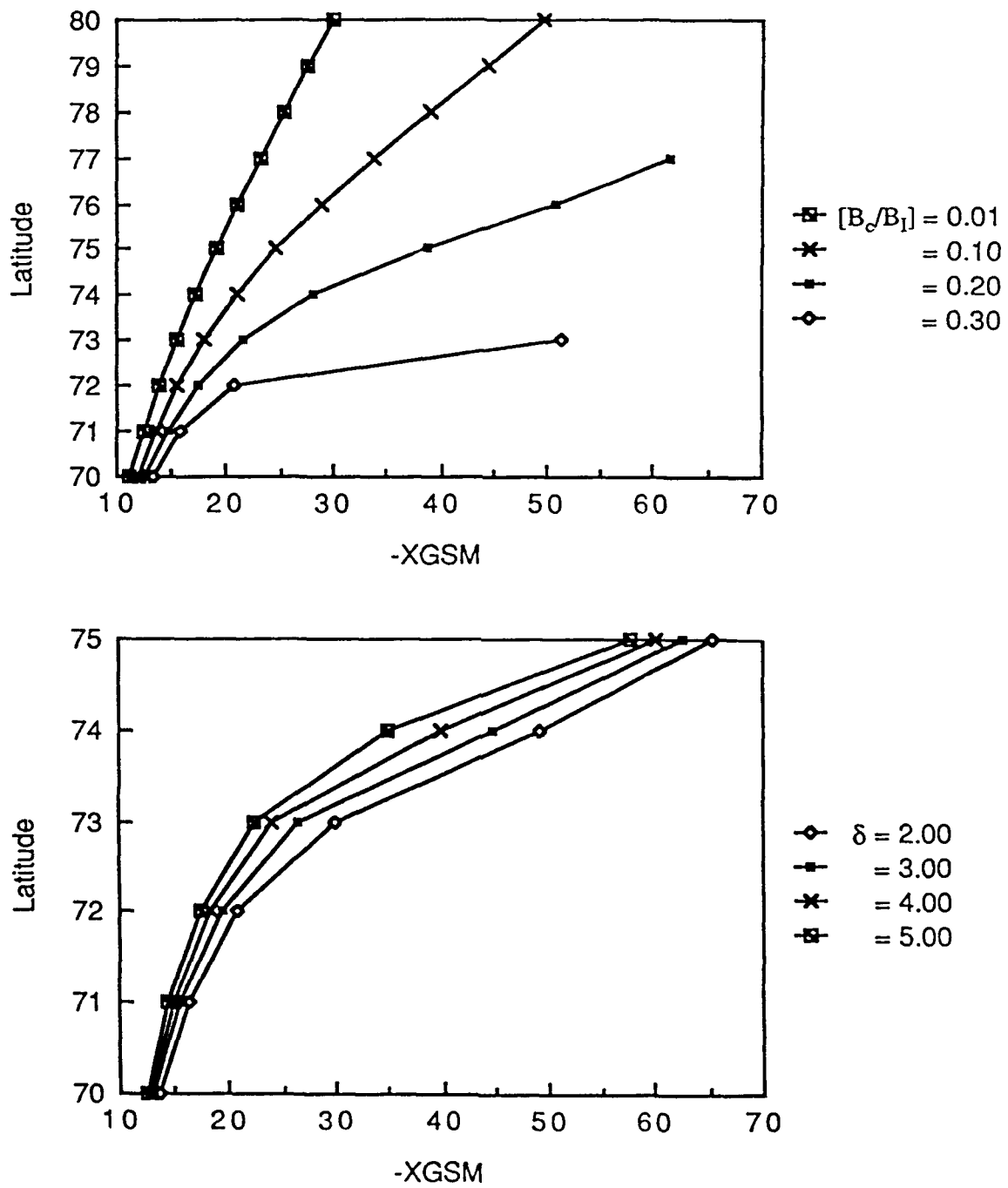


Fig. 6.7. Midnight latitudes as a function of equatorial mapping position for the parameter set of Figure 6.1 with substituted values for  $[B_0/B_1]$  and  $\delta$ .



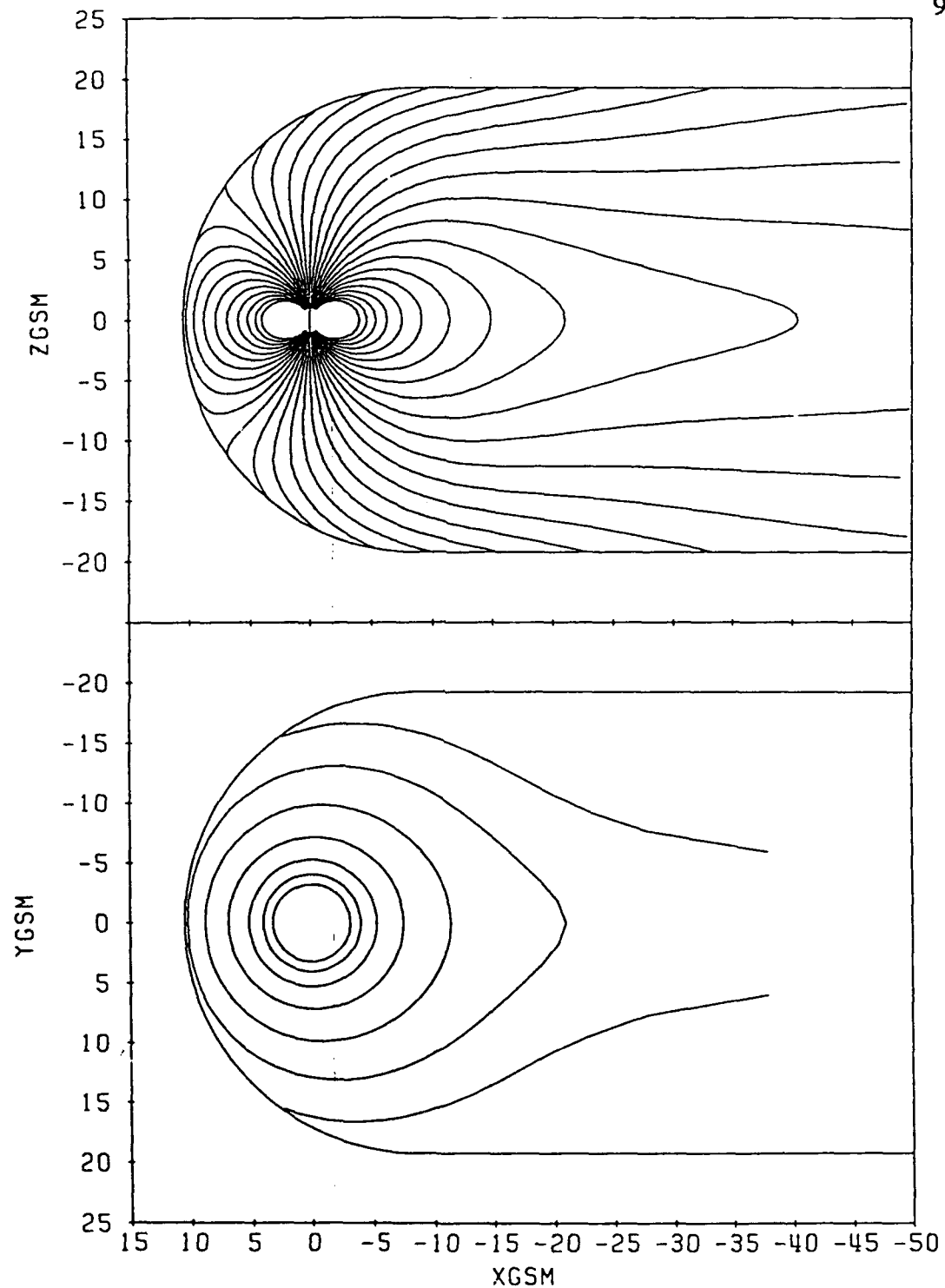


Fig. 6.8. Magnetic field lines in the noon-midnight meridian (upper panel) and corresponding equatorial mappings from rings of constant latitude (lower panel) for a "quiet" configuration with input parameters  $\psi = 0^\circ$ ,  $r_0 = 10.5 R_E$ ,  $s_I = 7.5 R_E$ ,  $B_I = 2.5$  nT,  $[B_c/B_I] = 0.25$ ,  $\Delta y = 9.0 R_E$ ,  $\delta = 3.5 R_E$ ,  $B_- = -110.0$  nT,  $B_+ = 105.0$  nT,  $\rho_- = 2.8 R_E$ , and  $\rho_+ = 2.2 R_E$ .

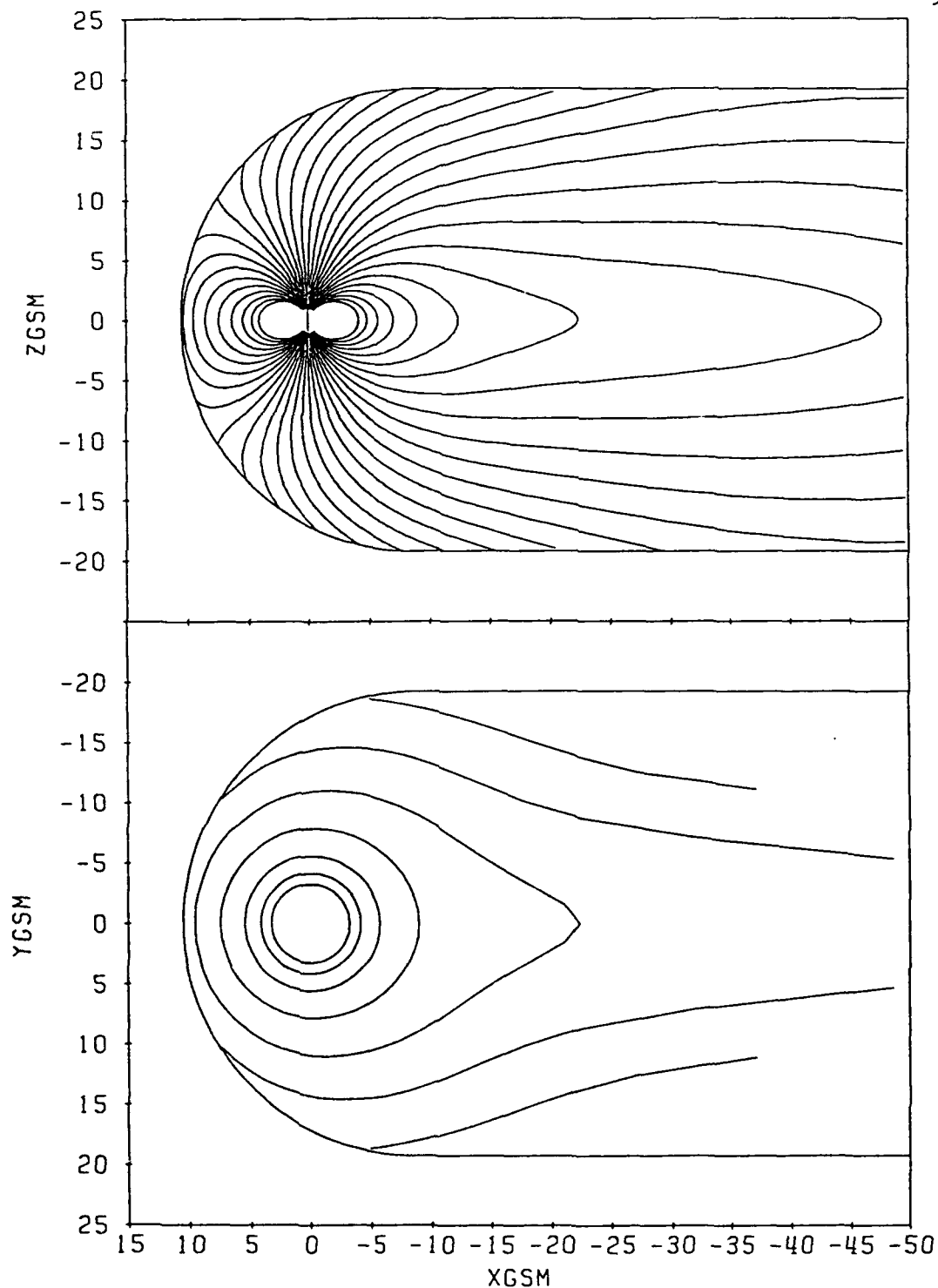


Fig. 6.9. Magnetic field lines in the noon-midnight meridian (upper panel) and corresponding equatorial mappings from rings of constant latitude (lower panel) for an "intermediate" configuration with input parameters  $\psi = 0^\circ$ ,  $r_o = 10.5 R_E$ ,  $s_I = 6.0 R_E$ ,  $B_I = 6.0$  nT,  $[B_o/B_I] = 0.19$ ,  $\Delta y = 9.0 R_E$ ,  $\delta = 2.7 R_E$ ,  $B_- = -170.0$  nT,  $B_+ = 163.0$  nT,  $\rho_- = 2.8 R_E$ , and  $\rho_+ = 2.0 R_E$ .

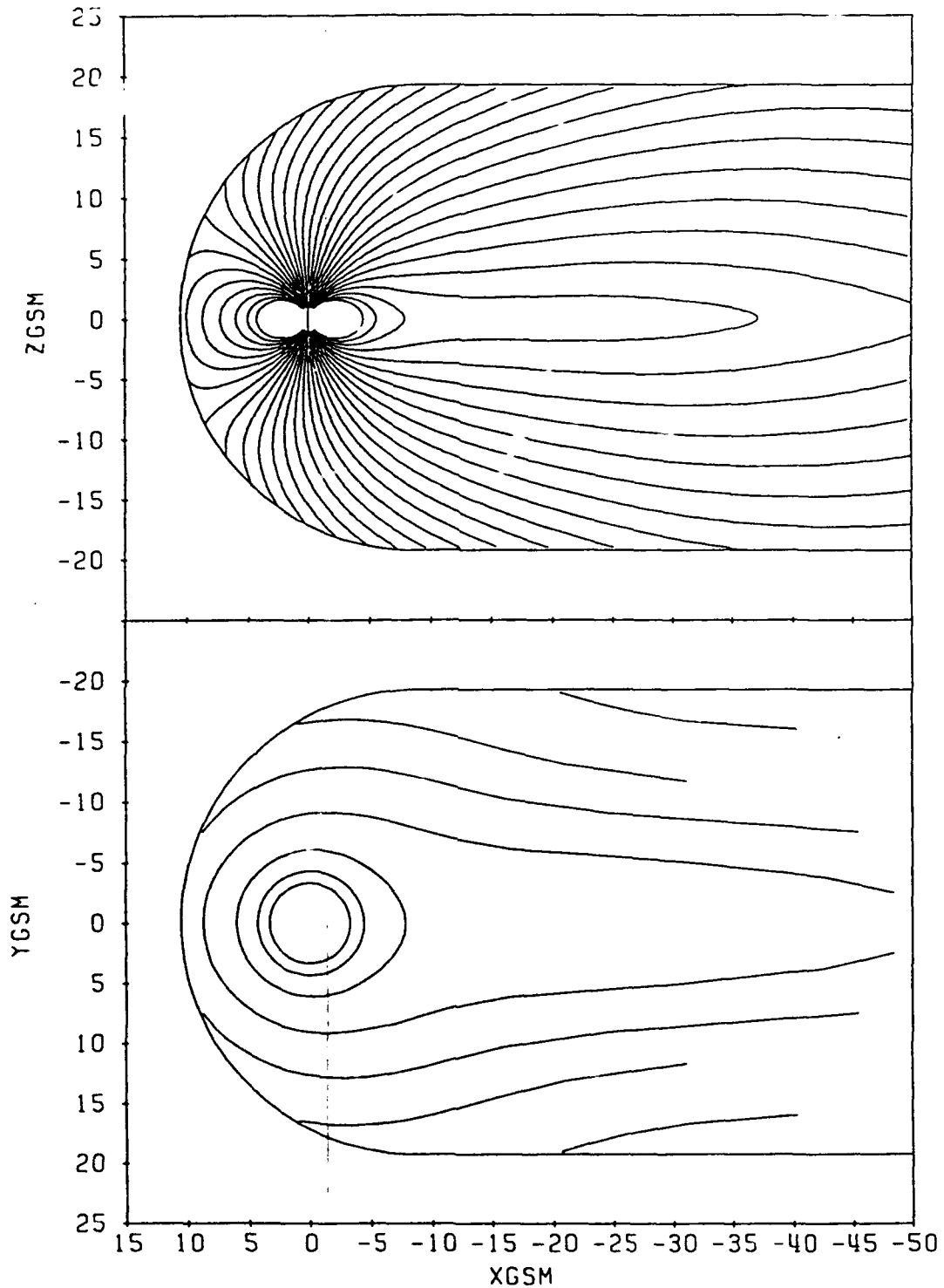


Fig. 6.10. Magnetic field lines in the noon-midnight meridian (upper panel) and corresponding equatorial mappings from rings of constant latitude (lower panel) for a "stretched" configuration with input parameters  $\psi = 0^\circ$ ,  $r_0 = 10.5 R_E$ ,  $s_I = 5.0 R_E$ ,  $B_I = 15.0$  nT,  $[B_c/B_I] = 0.17$ ,  $\Delta y = 8.0 R_E$ ,  $\delta = 1.0 R_E$ ,  $B_- = -240.0$  nT,  $B_+ = 230.0$  nT,  $\rho_- = 2.8 R_E$ , and  $\rho_+ = 2.0 R_E$ .

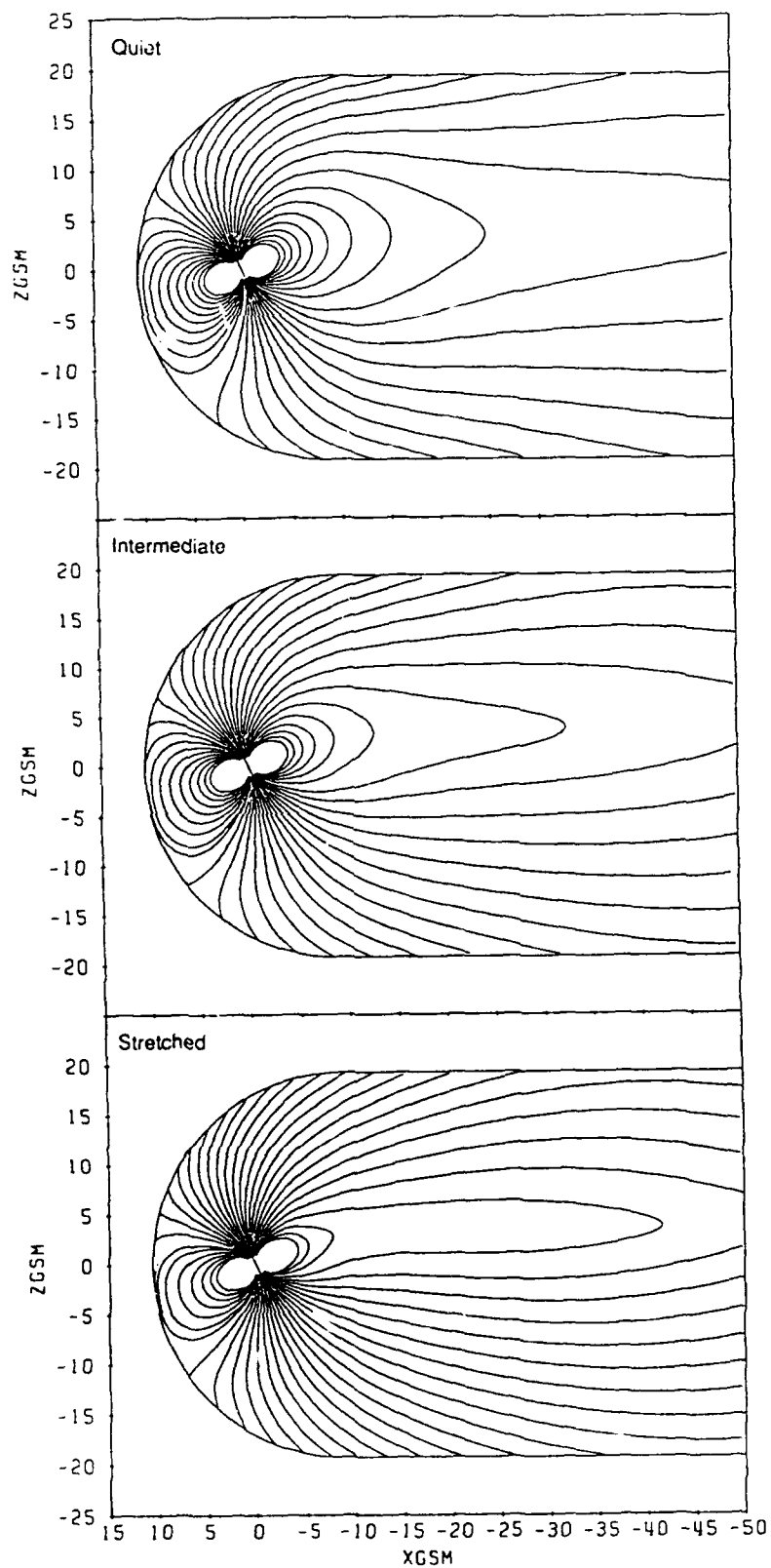


Fig. 6.11. Magnetic field lines in the noon-midnight meridian with  $\psi = 25^\circ$  for the "quiet", "intermediate", and "stretched" configurations of Figures 6.8, 6.9, and 6.10.

additional current build-up is concentrated near the current sheet inner edge as is necessary to keep  $B_{T,z}$  positive in the equatorial plane. The parameter  $\Delta y$  changes very little in this sequence because the cross-tail current  $y$  dependence, from equation (4.23), is closely tied to the radius of the magnetotail. The positive flux provided by our vacuum configurations needs to be eroded over a decreasing region as the magnetotail radius decreases. More variation in this parameter will be seen in Section 8 as the magnetopause stand-off distance is changed in the CDAW-6 magnetic field simulation.

As we progress from the quiet to the stretched model the inner region becomes more inflated, as can be seen in the lower panels of Figures 6.8, 6.9, 6.10, as magnetic flux is gradually drawn tailward and spread throughout the tail. The magnetic fields strength over the poles also becomes more concentrated as the region of open field lines expands. The tail lobe field lines become more rounded as the stretching progresses and the cross-tail current field dominates the configuration. The dipole-tilted versions of Figure 6.11 again demonstrate how the neutral sheet is lifted above the equatorial plane.

A comparison of the field line mapping behavior of the vacuum configuration and our three representative magnetospheric states is provided in Figure 6.12. In all but the vacuum case there seems to be a latitude at which there is a large jump in equatorial mapping distance. This critical latitude drops as we move from the quiet to the stretched configuration and has values of approximately  $78^\circ$ ,  $72^\circ$ , and  $65^\circ$ . This jump in mapping distance reflects the increased tailward displacement of equatorial magnetic flux with increased activity.

The magnetic field strength of the tail lobes is also highly correlated with geomagnetic activity [Behannon, 1970; Caan et al. 1973; Meng and Anderson, 1974]. Increased rate of reconnection and transport of dayside flux to the tail and an increase in solar wind pressure contribute to increased lobe field strengths and the stronger tail

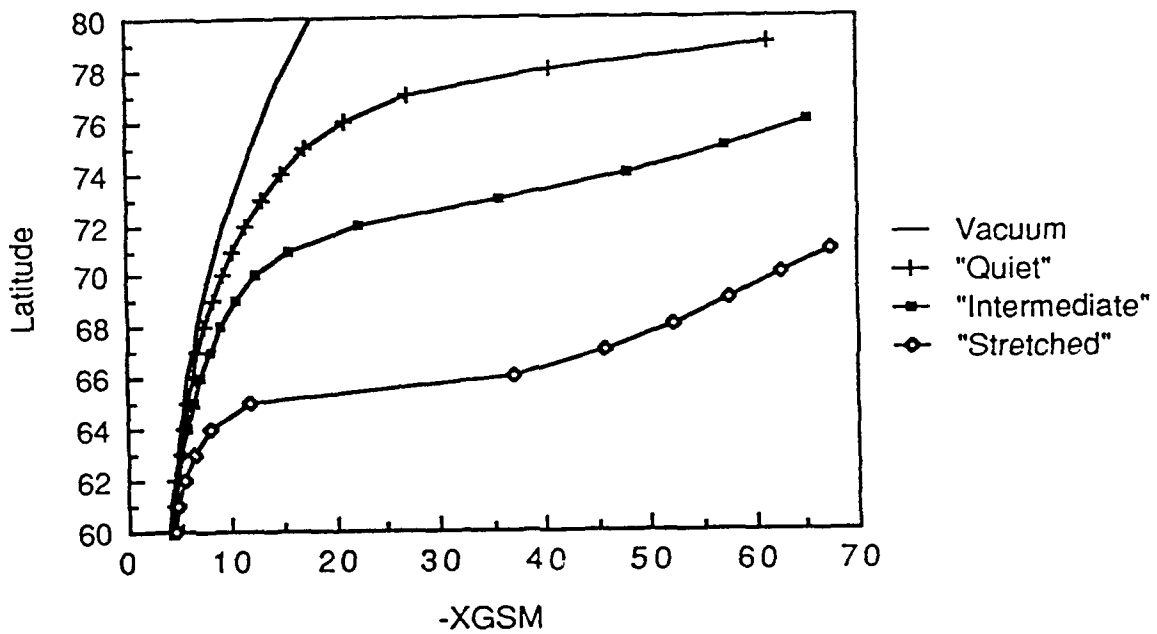


Fig. 6.12. Midnight latitudes as a function of equatorial mapping position with  $\psi = 0^\circ$  for the "quiet", "intermediate", and "stretched" configurations of Figures 6.8, 6.9, and 6.10, and the corresponding vacuum configuration with the same stand-off distance.

currents needed to support them. Our three examples, which correspond to varying magnetospheric activity states, also reflect this trend in lobe field strength as is shown in the upper panel of Figure 6.13.

The quiet configuration corresponds to very low activity levels, i.e.,  $K_p \approx 0$ , and has a relatively weak cross-tail current and its lobe field magnitudes are just slightly larger than that of the vacuum configuration. The intermediate configuration corresponds most closely with the average activity state, i.e.,  $K_p \approx 2$ , and compares well with the observations of Behannon [1970], shown in the lower panel, and similar observations reported by Mihalov and Sonett [1968]. The stretched configuration includes very strong lobe fields and represents a very high activity state, i.e.,  $K_p \geq 5$  (see Rothwell [1986] for an empirical relationship between the magnetic activity index  $K_p$  and the tail lobe field strength).

A configuration similar to this stretched case with even higher lobe field strengths and corresponding to an even higher activity state of the magnetosphere, i.e., with  $K_p \approx 7$ , is discussed in the next section in connection with the reconfiguration of the magnetotail during substorms.

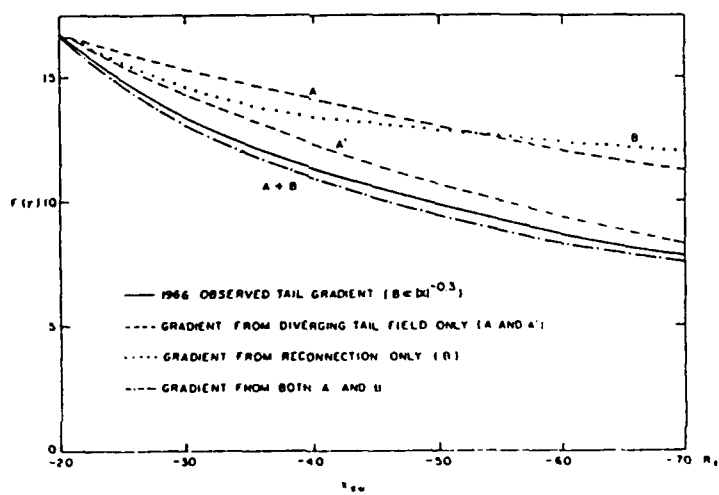
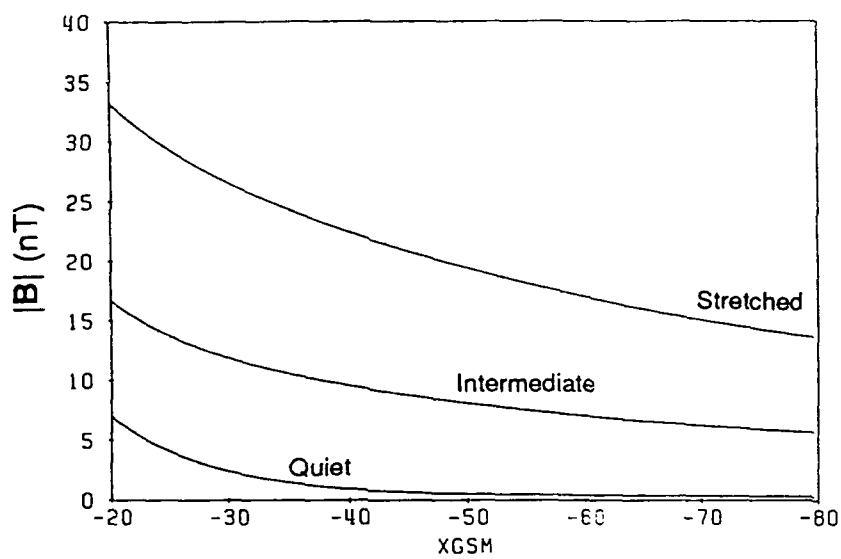


Fig. 6.13. Magnetotail lobe field strength along the line defined by  $(x, y = 0 R_E, z = 10 R_E)$  for the "quiet", "intermediate", and "stretched" configurations of Figures 6.8, 6.9, and 6.10 (upper panel). Observed magnetotail lobe field strength (solid curve) from Behannon [1970] for  $K_p \leq 2$  and  $|z| \geq 2 R_E$ .



## 7. Reconfiguration of the Geomagnetic Tail During Magnetospheric Substorms

### 7.1. Introduction

An important dynamic process involved in the interchange of energy between the solar wind, the magnetosphere, and the ionosphere is the magnetospheric substorm. Dayside magnetospheric field lines interconnected with the IMF are swept to the nightside by the solar wind and contribute to increased field strengths in the magnetotail. During this "growth" phase of the substorm, the tail field becomes more stretched and the cross-tail current intensifies as more and more solar wind energy is deposited in the tail in the form of magnetic flux. Starting at a critical point called the "expansion onset", perhaps coincident with magnetic reconnection and the formation of a neutral line in the near tail, energy is rapidly dissipated and the magnetotail undergoes a dramatic reconfiguration of its magnetic field structure (see e.g., McPherron [1979] for a review of substorm phenomena and a discussion of the possible expansion onset triggering mechanisms).

The reconfiguration requires the redirection of some of the westward traveling cross-tail current up into the postmidnight auroral ionosphere, eventually to return to the tail on the premidnight side [e.g., McPherron et al., 1973; Nagai, 1982; Takahashi et al., 1987; Lui et al., 1988]. It is this diversion of current and the resulting magnetic field perturbations which we would like to simulate. To do this we must first review some

observational information pertaining to the growth and subsequent expansion onset during a substorm.

During the growth phase, the increase in the cross-tail current can cause the geosynchronous equatorial field around local midnight to decrease by about 15 nT, as seen by Sauvaud et al. [1987], or even well over 50 nT as noted by Kokubun and McPherron [1981] and Barfield et al. [1985]. This decrease in  $B_{T,z}$  leads to a more tail-like field structure and is associated with thinning of the near-earth current sheet [Fairfield and Ness, 1970; Pytte and West, 1978]. This thinning seems to be accompanied by inward motion of the inner edge of the plasma sheet [Shelley et al., 1971] as particles move earthward to regions with higher flux densities trying to conserve their first adiabatic invariant.

The substorm onset and plasma sheet expansion for the inner region are basically simultaneous [Fairfield et al., 1981a]. The field becomes more dipolar in this region as field lines snap earthward to regain their pre-storm character [Nishida and Fujii, 1976; Pytte and West, 1978]. This process seems to be limited to the center portion of the tail, i.e., between  $y \approx \pm 5 R_E$  [Arnoldy and Moore, 1983; Lopez et al., 1988]. Also, the sudden earthward transport of magnetic flux is associated with the injection of energetic particles into the nightside geosynchronous region [e.g., Kivelson et al., 1979; Lyons and Williams, 1980; Mauk and Meng, 1987].

While plasma sheet thinning might occur before the onset inside of  $15 R_E$ , beyond that distance dramatic thinning occurs closer to the time of the onset [Akasofu et al., 1971; Hones et al., 1971; Aubry et al., 1972; Nishida and Fujii, 1976; Huang et al., 1987] and might result from the tailward loss of plasma on those plasma sheet field lines that have reconnected at the neutral line [Hones, 1977]. As with the dipolarization of the inner regions, this thinning is also limited to the center portions of the magnetotail

[Hones, 1979; Hones and Schindler, 1979; Fairfield et al., 1981b]. This thinning also occurs in conjunction with the magnetic field becoming even more tail-like as indicated by reductions in  $B_{T,z}$  [Fairfield et al., 1981b]. The magnitude of the field in the tail lobes also decreases in conjunction with the substorm onset as the flaring angle of the magnetotail decreases [Caan et al., 1975, 1978].

## 7.2. Disruption Current and Geomagnetotail Field Collapse

The simulation of the disruption of the cross-tail current is accomplished by superimposing our westward cross-tail current with an eastward current of lesser magnitude flowing across a narrower width of the tail. The magnetic field resulting from this new current is determined using the same magnetic filament and segment structure method described in Section 4 for the westward current.

The strength of the filaments representing the final cross-tail current along the midnight meridian,  $B(s)$ , is given by the sum of the eastward and westward filament contributions, such that

$$B(s) = B_e(s) + B_w(s) \quad (7.1)$$

where  $B_e(s)$  represents eastward current and  $B_w(s)$ , from equation (4.22), represents the westward current. In order to control the amount of westward current diverted, the filament strength profile representing the eastward current is expressed as a negative fraction of the filament strength characterizing the original westward current. This insures that the net current will always flow westward through the midnight meridian. The expression is

$$B_e(s) = -B_w(s) \frac{(f_w - 1)}{2} [\tanh\{\kappa(s - s_I - \sigma)\} - \tanh\{-\kappa\sigma\} - 2] \quad (7.2)$$

where  $s$  indicates the position along the curve defining the current sheet placement,  $s_I$  is the distance to the inner edge,  $f_w$  is the fraction of westward current remaining at the midnight inner edge,  $\sigma$  is approximately equal to the distance from the inner edge which is altered by the addition of eastward current, and  $\kappa$  determines how quickly the eastward current contribution dies off around the distance  $s = s_I + \sigma$ . We set  $\kappa = 0.4 (R_E)^{-1}$  for all examples presented here. This effectively reduces the relative amount of eastward current from 90% to 10% of its maximum value over a distance of  $5 R_E$ . Note that  $B_w(s)$  is defined to be zero earthward of the current sheet inner edge. Put more simply, equation (7.2) indicates that the westward current strength is reduced to roughly a constant fraction  $f_w$  of its initial strength for a distance  $\sigma$  from the inner edge. With an exponential function representing the westward current, the majority of the newly introduced eastward current will be located near the inner edge.

The  $y$  dependence for the eastward current has the same form as that of the westward current with  $\Delta y$  replaced by  $\Delta y_e$  in equation (4.23). The parameter  $\Delta y_e$  is always kept smaller than  $\Delta y$  for the westward current to insure that the total current always flows westward and that the flanks of the magnetotail remain relatively unchanged.

The input parameters are selected with  $\psi = 0^\circ$  and reflect the observational trends noted above. The parameters  $f_w$  and  $\sigma$  are selected in combination to produce a specific geosynchronous magnetic field recovery, e.g., an increase of 10-20 nT in  $B_{T,z}$  at the equator, as well as to insure that the magnetic field is positive everywhere in the equatorial plane.

There are two parameter space regions which can satisfy this last requirement. The

first region has  $f_w \approx 1.0$  and  $\sigma$  equal to only a few  $R_E$  and corresponds to a small fraction of current being diverted from near the inner edge of the current sheet. The second region is where  $f_w$  is appreciably less than 1.0 and  $\sigma$  is large, e.g., greater than  $30 R_E$ . This corresponds to a larger fraction of current being diverted from a much longer portion of the current sheet. If the midnight geosynchronous magnetic field z component is to recover substantially as is typical, i.e., increase by 10-20 nT, then the larger values of  $\sigma$  found in the second parameter region are required. This is consistent with the idea that the source of diverted current is generally outside of the geosynchronous region [Nagai, 1982]. Values for the quantity  $\Delta y_e$  are chosen such that only the center portion of the magnetotail, between  $y \approx \pm 5 R_E$ , is influenced by the diversion of current [Arnoldy and Moore, 1983; Lopez et al., 1988]. This leaves the field of the flanks relatively unchanged.

The specific magnetotail reconfiguration example discussed in this section belongs to the sequence of magnetospheric configurations designed to simulate the CDAW-6 magnetospheric substorm event discussed in Section 8 (see McPherron and Manka, [1985] and other authors in that same issue). The stretched and collapsed tail fields correspond to the key event times or "time labels" 5 and 6, respectively.

Our model pre-onset configuration (see the upper panel of Figures 7.1 and 7.2) results from the inward motion, intensification, and thinning of the cross-tail current. The increase of current is seen especially near the current sheet inner edge. These changes correspond to the growth phase described above and include a reduction in  $B_{T,z}$  and the rotation of the magnetic field direction from being fairly dipolar to more tail-like in the inner regions. The tailward stretching of magnetic field lines occurs at all distances down the tail and is predominate in the center portion of the tail's width. The configuration is now changed by the addition of the eastward disruption current.

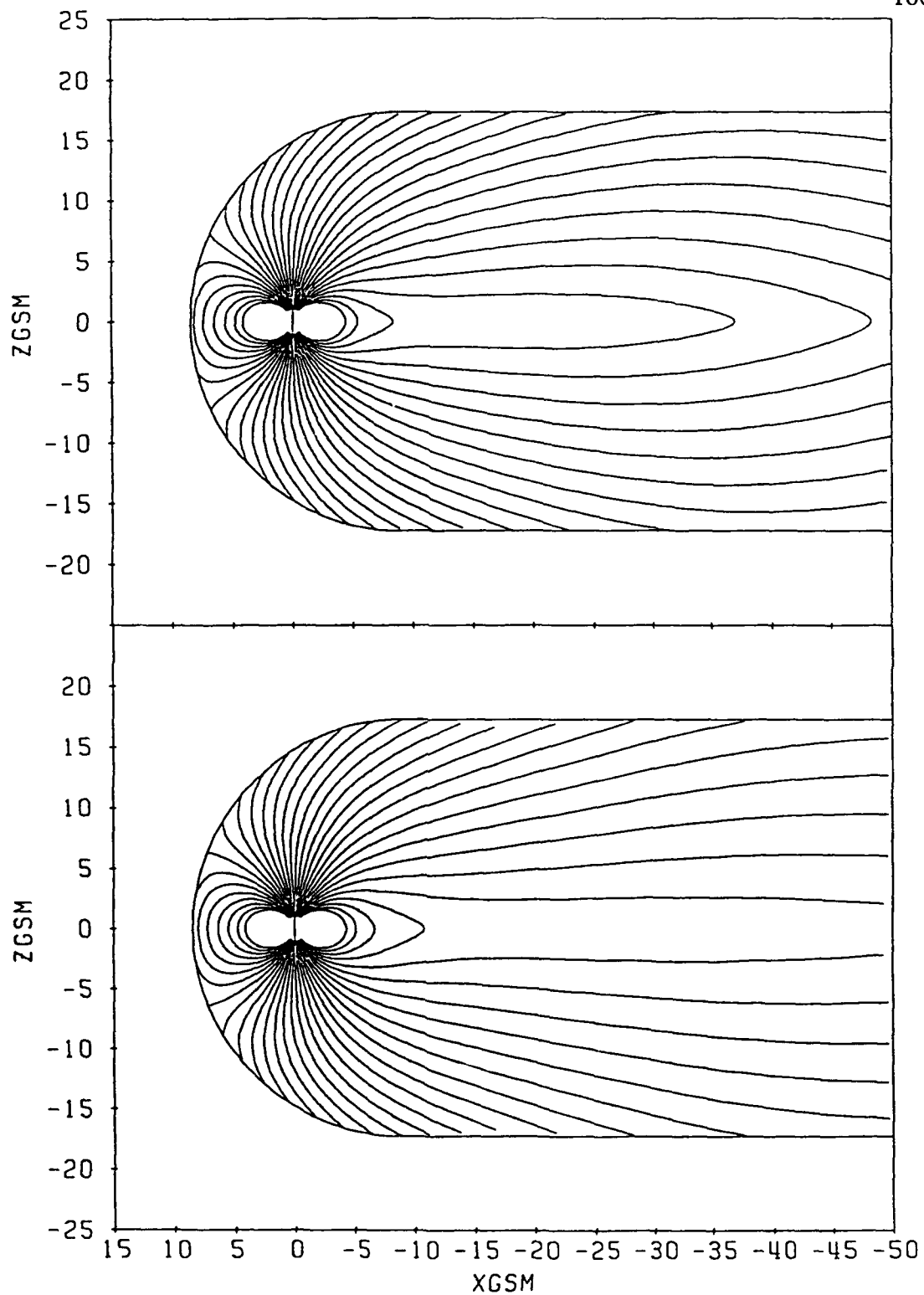


Fig. 7.1. Magnetic field lines in the noon-midnight meridian for CDAW-6 time labels 5 (upper) and 6 (lower) representing the stretched and collapsed configurations, respectively.

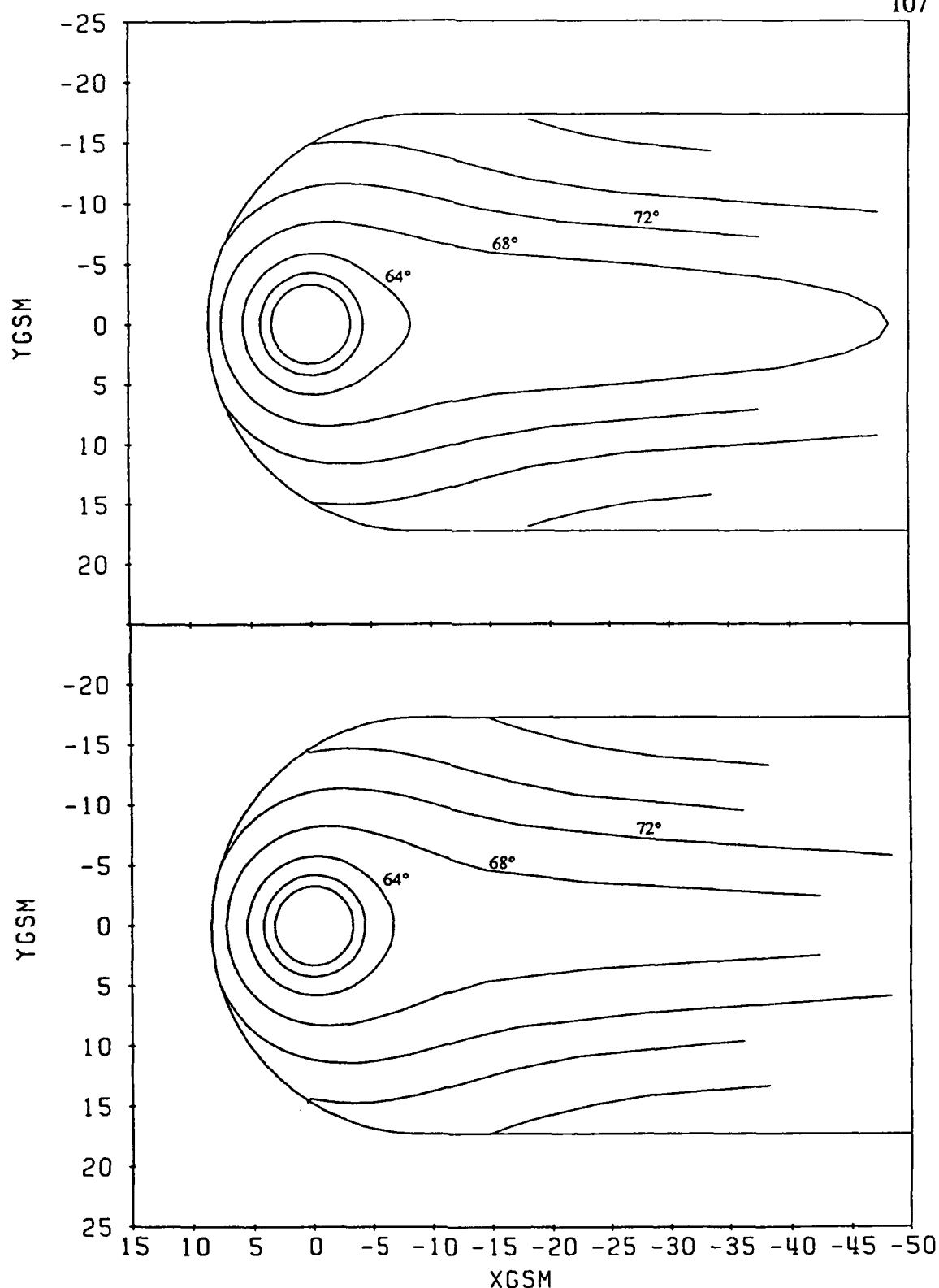


Fig. 7.2. Mapping of the magnetic field to the equatorial plane from rings of constant latitude corresponding to the cases in Figure 7.1.

Current passing across the near tail as viewed in the  $y$ - $z$  plane (see Figure 7.3), which normally only becomes compressed near the middle of the tail (upper panel), diverges slightly as it weakens and passes through the midnight meridian for the current disruption case (lower panel). A similar spreading of current can be seen in the  $x$ - $y$  plane (see Figure 7.4) as current is diverted both earthward and tailward of the disruption region near the inner edge of the current sheet. These two figures represent an exaggerated displacement of current as almost all of the current in the first  $5 R_E$  of the current sheet was diverted. The collapsed configuration represented in all of the other figures in this section resulted from diverting about 30% of the current in the first  $45 R_E$  of the current sheet. With such an extended region being affected, the displacement of current flow lines is much less evident than in the examples of Figures 7.3 and 7.4.

The change in equatorial magnetic field strength at midnight, which occurs between the configurations shown in the upper and lower panels of Figures 7.1 and 7.2, is provided in Figure 7.5. The total magnetic field has recovered and increased by over 15 nT near geosynchronous distance as  $B_{\text{tail},z}$  became less negative. Beyond  $x \approx -20 R_E$  the total field strength decreased as  $B_{\text{tail},z}$  decreased also. Both of these changes are consistent with the diversion of current from the inner edge of the current sheet. The redistribution of magnetic flux is also very significant to field line mapping behavior.

The magnetic field became more dipolar in the near tail as field lines collapsed inward, e.g., in Figure 7.1 the field line emanating from  $66^\circ$  latitude (the fourth line crossing the equatorial plane on the nightside) moved in from  $x \approx -37 R_E$  to  $x \approx -11 R_E$ . In contrast, the decrease in flux beyond  $x \approx -20 R_E$  helped the field lines from the higher latitudes map to more distant equatorial points as the far tail became even more stretched. This change in mapping behavior is better quantified in Figure 7.6, which reveals that the transition between field lines becoming more dipolar and more tail-like occurs between



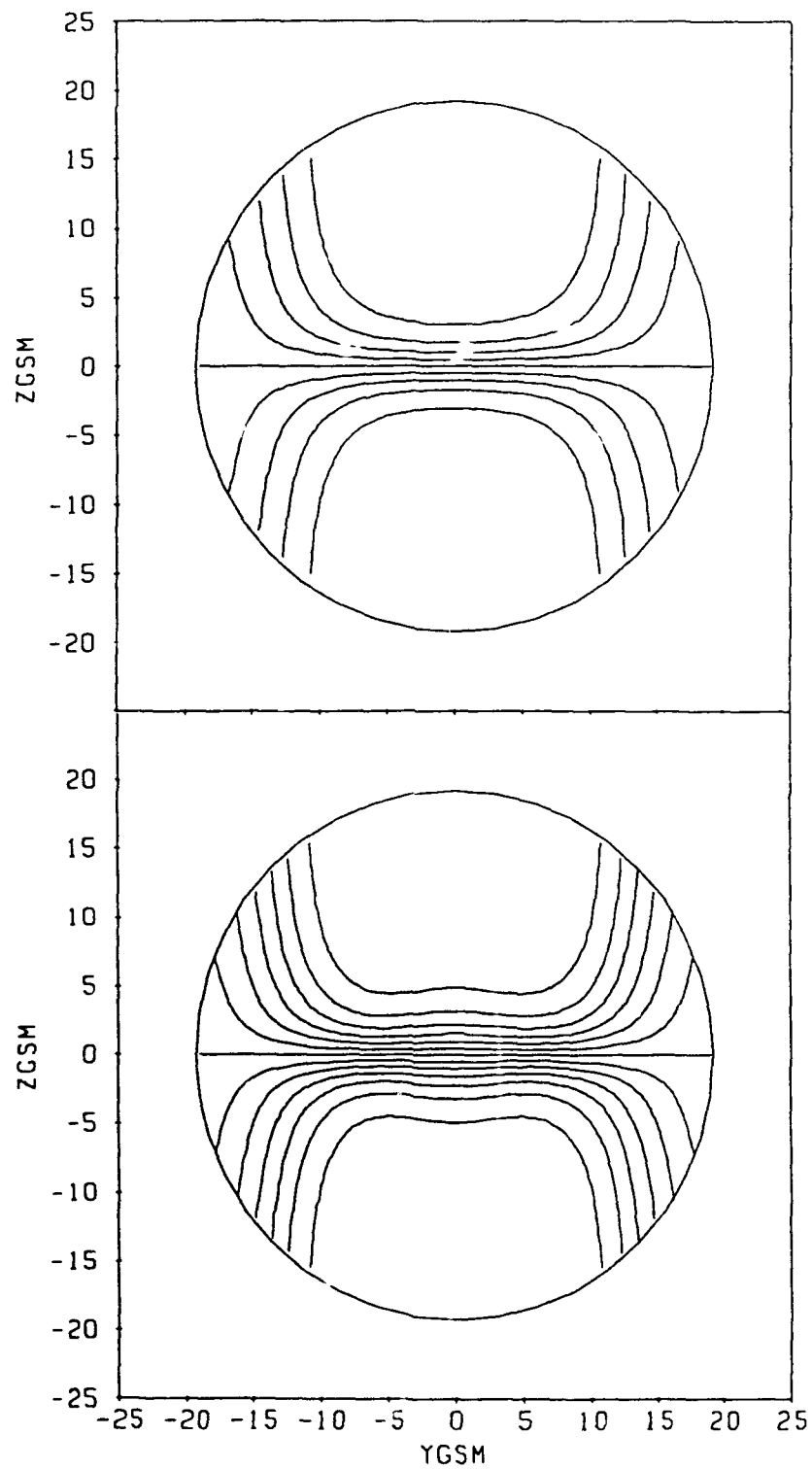


Fig. 7.3. Cross-tail current trace projections in the  $y$ - $z$  plane at  $x = -8 R_E$  for a regular (upper) and disrupted (lower) current sheet. The cross-tail current parameters are the same as those used in Figure 4.6 with the additional of the collapse parameters  $f_w = 0.0$ ,  $\sigma = 5.0 R_E$ , and  $\Delta y_c = 5.0 R_E$  for the lower panel.

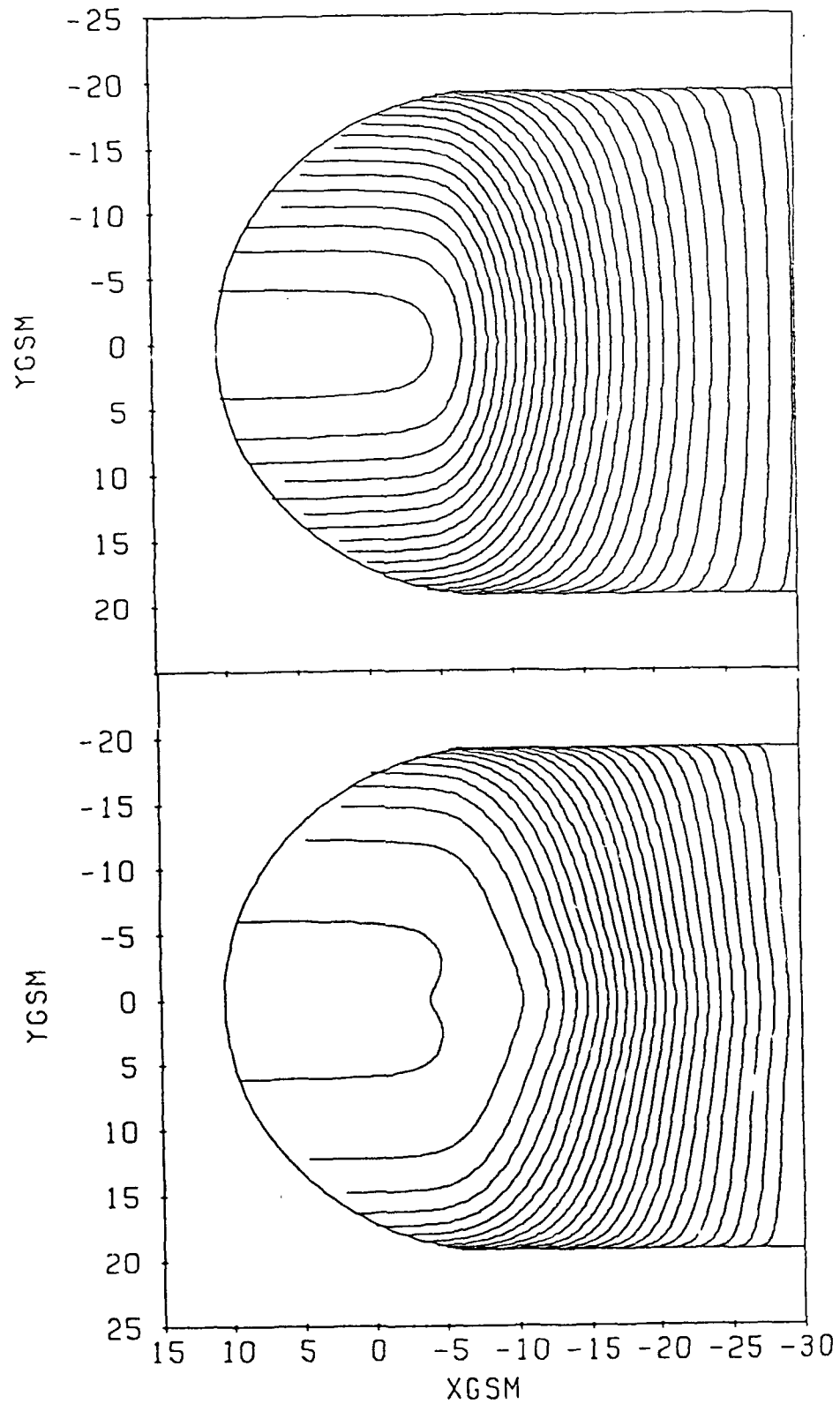


Fig. 7.4. Cross-tail current traces in the equatorial plane for the regular (upper) and disrupted (lower) current sheet represented in Figure 7.3.

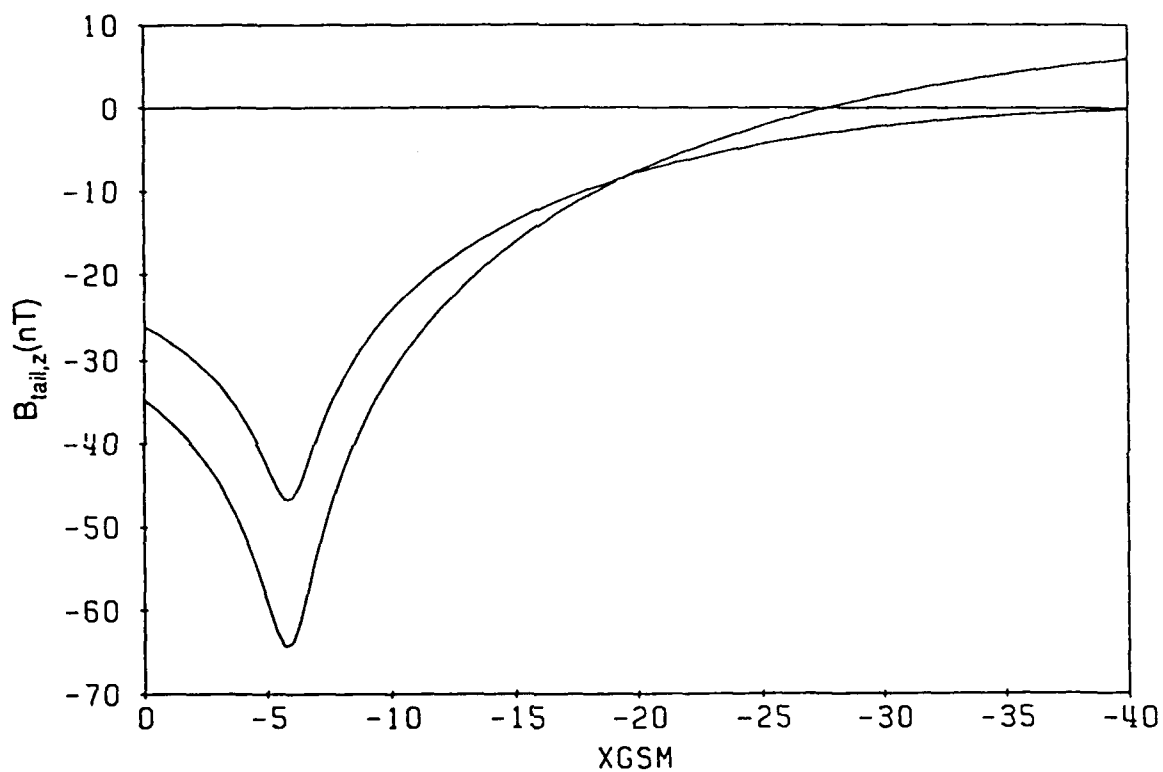


Fig. 7.5. Cross-tail current magnetic field contributions,  $B_{\text{tail},z}$ , plotted along the x axis for CDAW-6 time labels 5 and 6, representing the stretched and collapsed magnetotail, respectively. The stretched configuration has the deeper minimum near the current sheet inner edge ( $x = -5.86 R_E$ ).

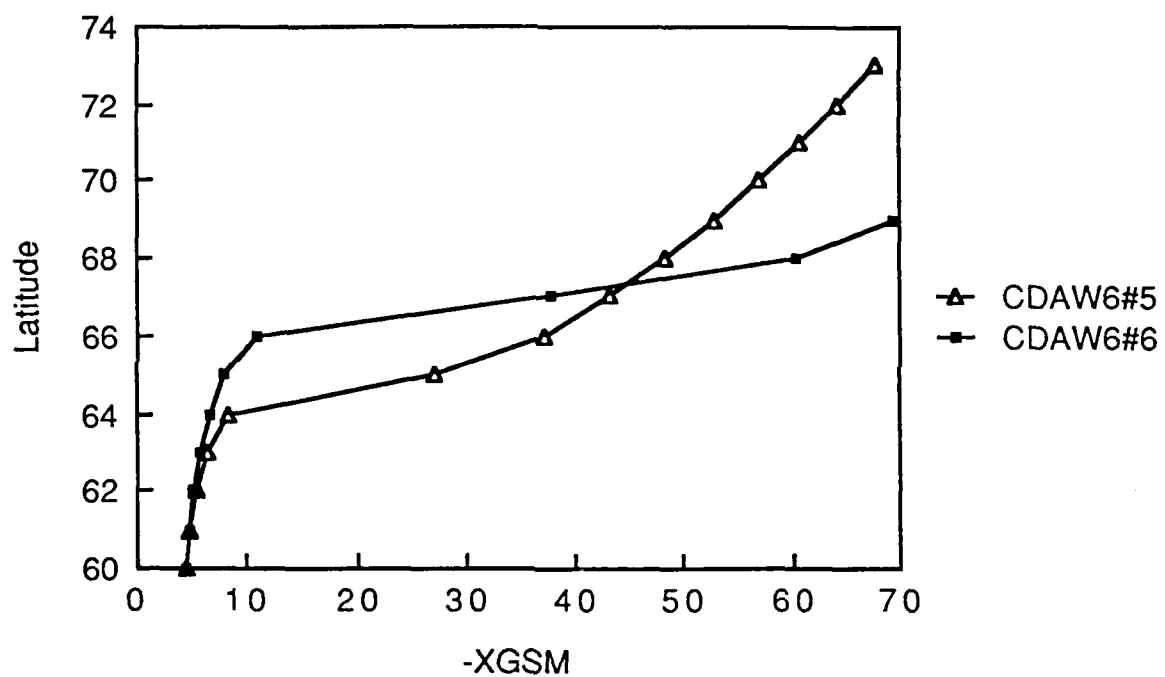


Fig. 7.6. Midnight latitude as a function of equatorial mapping location for CDAW-6 time labels 5 and 6.

67° and 68° latitude. It is also apparent that tail lobe field lines moved closer to the equatorial plane beyond distances of 15 to 20  $R_E$ , indicating that the plasma sheet became compressed or thinned in that region.

The equatorial range of these effects is further clarified in Figure 7.2. Both the dipolarization of the inner tail regions ( $x > -20 R_E$ ) and the further stretching of the field in the far tail region, corresponding to plasma sheet thinning, are limited to the center portions of the magnetotail while the flanks are left relatively unchanged. Notice that while the mapping locations of points representing 64° and 68° latitude changed, the equatorial positions corresponding to 72° latitude in the flanks has not changed. This was accomplished by keeping  $\Delta y_e$  smaller than the corresponding parameter for the westward traveling current  $\Delta y$ .

The disruption of current at onset starts near the midnight meridian and propagates toward the flanks during the expansion phase [Nagai et al., 1983]. This causes a delay between the dipolarization of the fields near midnight and those toward the flanks. Taking this into consideration, the collapsed configuration seems most representative of the moment when the dipolarization of the midnight geosynchronous region is complete. This happens just before the recovery of the far tail plasma sheet occurs. The field configurations of Figure 7.1, in fact, show a striking resemblance to portions A and C of Baker's [1984] Figure 12, which are field line schematics of the magnetosphere just prior to onset and just before substorm recovery.

### 7.3. Comments

Although there have been estimates using very simple two dimensional models that the disruption and diversion of cross-tail current can account quantitatively for the

observed magnetic field reconfiguration [Lui, 1978; Kaufman, 1987], this model provides the first detailed representation of this type of magnetotail magnetic field reconfiguration in three dimensions.

The reconfiguration of the Earth's magnetotail during the expansion phase of magnetospheric substorms, as modeled here, agrees well with the magnetic field observations reviewed in the introduction of this section. One shortfall of the present method is that field aligned currents do not make it all the way to the ionosphere, but curve back into the tail much sooner, thus they do not fit the usual concept of Birkeland currents. Also, due to the method used to introduce the  $y$  dependencies in the tail model, the tail cannot reproduce the expected perturbations of the magnetic  $y$  component that real Birkeland currents produce on the ground and in the inner magnetosphere [e.g., Nagai, 1987]. This last point might be partially remedied by the introduction of an asymmetric ring current as discussed in Section 3.

## 8. Physical Comparisons

### 8.1. Introduction

To this point we have concentrated on specific aspects of the model such as equatorial magnetic flux levels and magnetic field mapping characteristics. To better illustrate the average behavior of the model on broader spatial scales and also demonstrate the flexibility available to represent very diverse configurations, we present three types of physical comparison between the model and observations.

First, we simulate the magnetic field development of the CDAW-6 event of March 22, 1979, an extensively studied moderate magnetic storm. A brief review of this exercise will demonstrate that driving the model with only three initial input parameters, namely  $r_0$ ,  $D^{st}$ , and  $\Lambda_0$ , leads to both a reasonable sequence of behavior for the ring and cross-tail currents and general agreement with observational geosynchronous magnetic flux densities. For a detailed summary and interpretation of the event see McPherron and Manka [1985] as well as other papers in that special issue. In the second comparison, we reconfirm the appropriateness of our cross-tail current sheet formulation by exploring the three dimensional behavior of the shape and position of the neutral sheet surface as it changes with the tilting of the Earth's dipole. Studying the character of the neutral sheet is one of the best ways to evaluate the dipole tilted configurations. The final comparison centers on the average observational  $\Delta B$  profiles which were used extensively during model development. Similarities in changes of profile behavior with general magnetic

activity are noted between the model and observations.

## 8.2. CDAW-6 Magnetic Field Simulation

The input parameter selection procedure of Section 5 and the magnetotail reconfiguration procedure of Section 7 were used to construct seventeen different magnetic field configurations to represent selected times extending over a ten hour period of the CDAW-6 magnetic storm event of March 22, 1979. The times represented were chosen to coincide with critical events such as storm sudden commencement (SSC) and substorm onset. They were also selected to coincide with changes in the magnetosphere as inferred by variations in  $D^{st}$ , the stand-off distance, and IMF polarity.

The initial input parameters are the stand-off distance  $r_o$ , the magnetic index  $D^{st}$ , and the latitude of the midnight auroral equatorward boundary  $\Lambda_o$ . The dipole tilt angle, which varied by about  $\pm 10^\circ$  during the event, was held constant at  $\psi = 0^\circ$ . The assigned simulation time labels, the universal time (UT), and the initial input parameters are listed in Table 8.1. The choice of simulation times and the values for  $r_o$ ,  $D^{st}$ , and  $\Lambda_o$  were provided by G.-H. Voigt and R. A. Wolf (private communication). These values were used to generate the ring and cross-tail current model parameters listed in Table 8.2 for all time labels except 6 and 14, which represent the collapse of the magnetotail and were developed using the method described in Section 7. All of the magnetic field mappings from the midnight latitude  $\Lambda_o$  to the current sheet inner edge position at  $(-s_i, 0, 0)$  were achieved within  $0.05 R_E$ .



TABLE 8.1. Initial Input Parameters for the CDAW-6 Magnetic Field Simulation

Label	UT	Comment	$r_o(R_E)$	$D^{st}(nT)$	$\Lambda_o(deg)$
1	600	Pre-SSC	10.58	+13.53	66.28
2	826	Storm Sudden Commencement	7.83	+43.20	66.28
3	1000	-	7.83	+43.20	65.25
4	1020	IMF turns Southward	8.93	+32.56	64.72
5	1054 - $\epsilon$	Maximum Stretching	8.45	+16.61	62.51
6	1054 + $\epsilon$	Collapse	-	-	-
7	1130	-	8.10	-15.30	59.22
8	1206	-	8.45	-24.41	58.82
9	1243	-	8.77	-18.34	59.77
10	1310	IMF turns Southward	8.71	-13.78	60.72
11	1340	-	8.64	-9.22	60.73
12	1407	-	8.61	-16.82	60.73
13	1436 - $\epsilon$	Maximum Stretching	7.58	-22.14	60.13
14	1436 + $\epsilon$	Collapse	-	-	-
15	1515	-	7.62	-39.61	59.80
16	1550	-	7.68	-57.08	59.27
17	1600	-	8.50	-60.88	59.14

TABLE 8.2. Model Parameters for the CDAW-6 Magnetic Field Simulation. Note: Equation (7.6) pre-dates the CDAW-6 exercise and different  $s_I$  vs.  $\Lambda_o$  relations were used. For labels 1-6,  $s_I = (0.31)\Lambda_o - 13.21$  and for labels 7-17,  $s_I = (0.36)\Lambda_o - 16.94$

Label	$s_I$	$B_I$	$[B_o/B_I]$	$\Delta y$	$\delta$	$B_-$	$B_+$	$\rho_-$	$\rho_+$
1	7.00	4.3	0.25	15.0	2.0	-105.0	117.2	3.2	2.1
2	7.01	8.3	0.20	12.5	2.0	-50.0	75.9	4.0	1.6
3	6.69	12.0	0.15	10.0	1.2	-50.0	75.9	4.0	1.6
4	6.53	12.7	0.15	10.0	1.0	-50.0	72.0	4.0	1.6
5	5.86	17.5	0.14	7.5	0.8	-230.0	221.6	2.9	2.1
6	*	-	-	-	-	-	-	-	-
7	4.38	15.0	0.15	7.5	1.0	-400.0	354.5	2.7	2.1
8	4.24	15.0	0.15	7.5	1.0	-490.0	437.1	2.6	2.1
9	4.58	15.0	0.15	7.5	1.0	-390.0	345.8	2.7	2.1
10	4.92	15.0	0.15	7.5	1.0	-380.0	340.4	2.7	2.1
11	4.92	15.0	0.15	7.5	1.0	-540.0	504.9	2.6	2.2
12	4.92	17.0	0.14	7.5	1.0	-500.0	466.4	2.5	2.2
13	4.71	17.0	0.14	7.5	1.0	-570.0	522.9	2.5	2.1
14	**	-	-	-	-	-	-	-	-
15	4.59	15.0	0.15	7.5	2.0	-840.0	774.3	2.4	2.1
16	4.40	11.0	0.20	10.0	2.0	-700.0	615.9	2.5	2.1
17	4.35	11.0	0.20	10.0	2.0	-680.0	597.9	2.5	2.1

\* Same input as Label 5 plus  $f_w = 0.7$ ,  $\sigma = 45.0$ ,  $\Delta y_e = 5.0$

\*\* Same input as Label 13 plus  $f_w = 0.8$ ,  $\sigma = 35.0$ ,  $\Delta y_e = 5.0$

### 8.2.1. *Simulation Overview*

The simulation begins at 0600 UT with a relatively quiet configuration having an average magnetopause stand-off distance (label 1). Both the ring and cross-tail currents are weak and  $D^{\text{st}}$  is positive. At 0826 UT there is a storm sudden commencement as enhanced solar wind pressure suddenly reduces the magnetopause stand-off distance by almost  $3 R_E$  (label 2). This results in a large positive change in  $D^{\text{st}}$ , a slight cross-tail current increase, and inward motion of the ring current as defined by the quantity  $\rho_o$  of equation 3.8. The configurations for the first two time labels are illustrated in Figures 8.1 and 8.2 and are included to illustrate the dramatic field line mapping changes accompanying the sudden commencement. A decrease in the stand-off distance lessens the stretching of tail field lines in the vacuum case (see Figure 2.3), yet there is extensive stretching in the midnight region after the compression. This is due to the doubling of the inner edge cross-tail current needed to fulfill the midnight mapping requirement.

By 1000 UT the latitude of the midnight equatorward aurora has shifted equatorward more than a degree while the other initial inputs maintained their values (label 3). Further tail field stretching is induced to satisfy this new mapping requirement. This intensifies, thins, and brings the current sheet earthward while the ring current remains quiet. At 1020 UT the IMF turns southward, the stand-off distance increases and  $\Lambda_o$  drops again (label 4). The ring current does not change, but the current sheet thins and shifts earthward again as field lines continue to be pulled down the tail.

The greatest degree of tail stretching leading up to the first substorm onset occurs at 1054 UT (label 5), by which time the midnight aurora has dropped an additional  $2^\circ$  from the previous time label. Note once again that  $\Lambda_o$  is the most crucial and sensitive of the initial input parameters determining the current sheet configuration. The current sheet inner edge is built up to its maximum strength and the ring current has moved in slightly

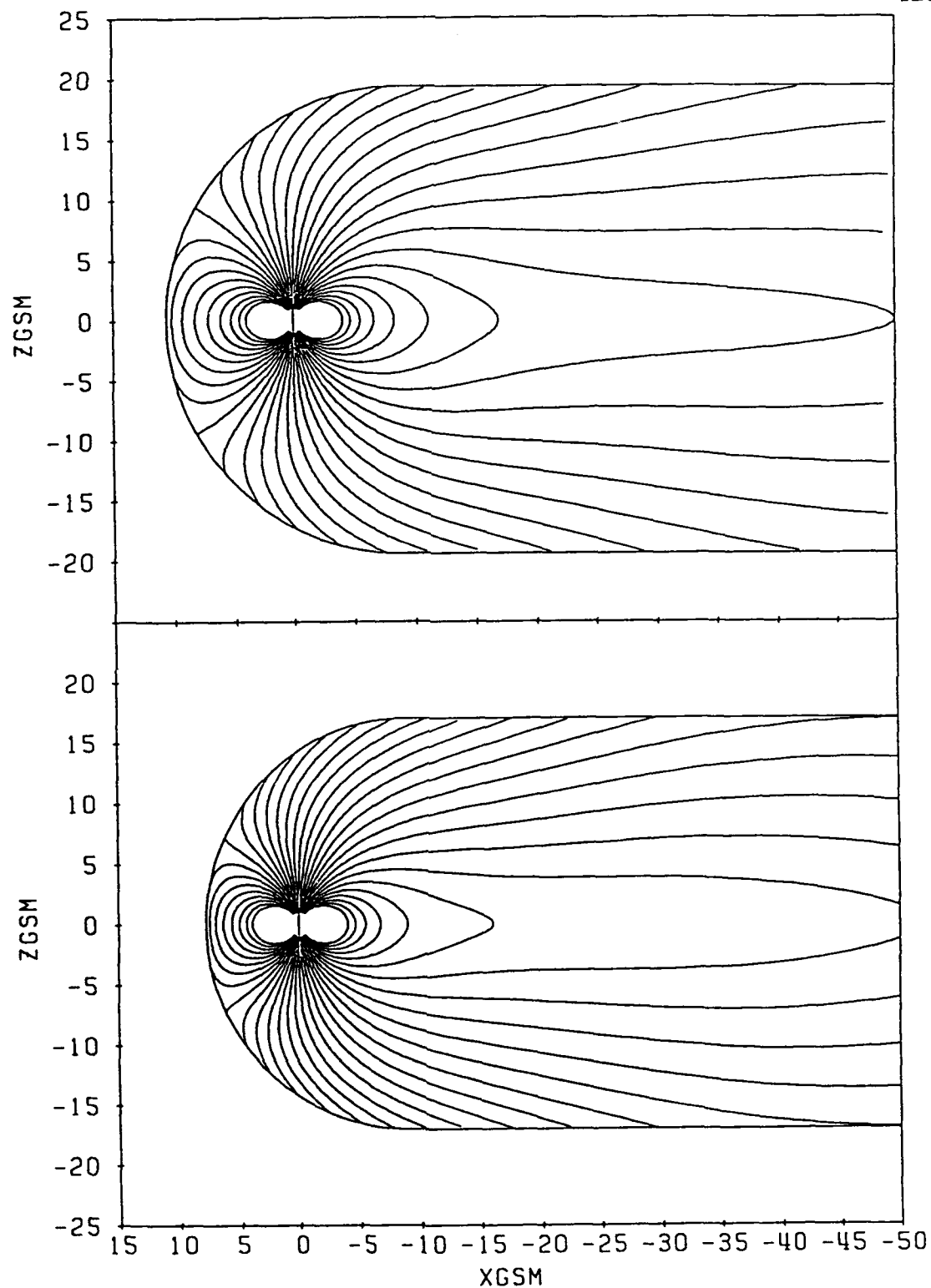


Fig. 8.1. Magnetic field lines in the noon-midnight meridian for CDAW-6 time labels 1 (upper) and 2 (lower) representing the transition occurring at substorm sudden commencement due to enhanced solar-wind pressure.

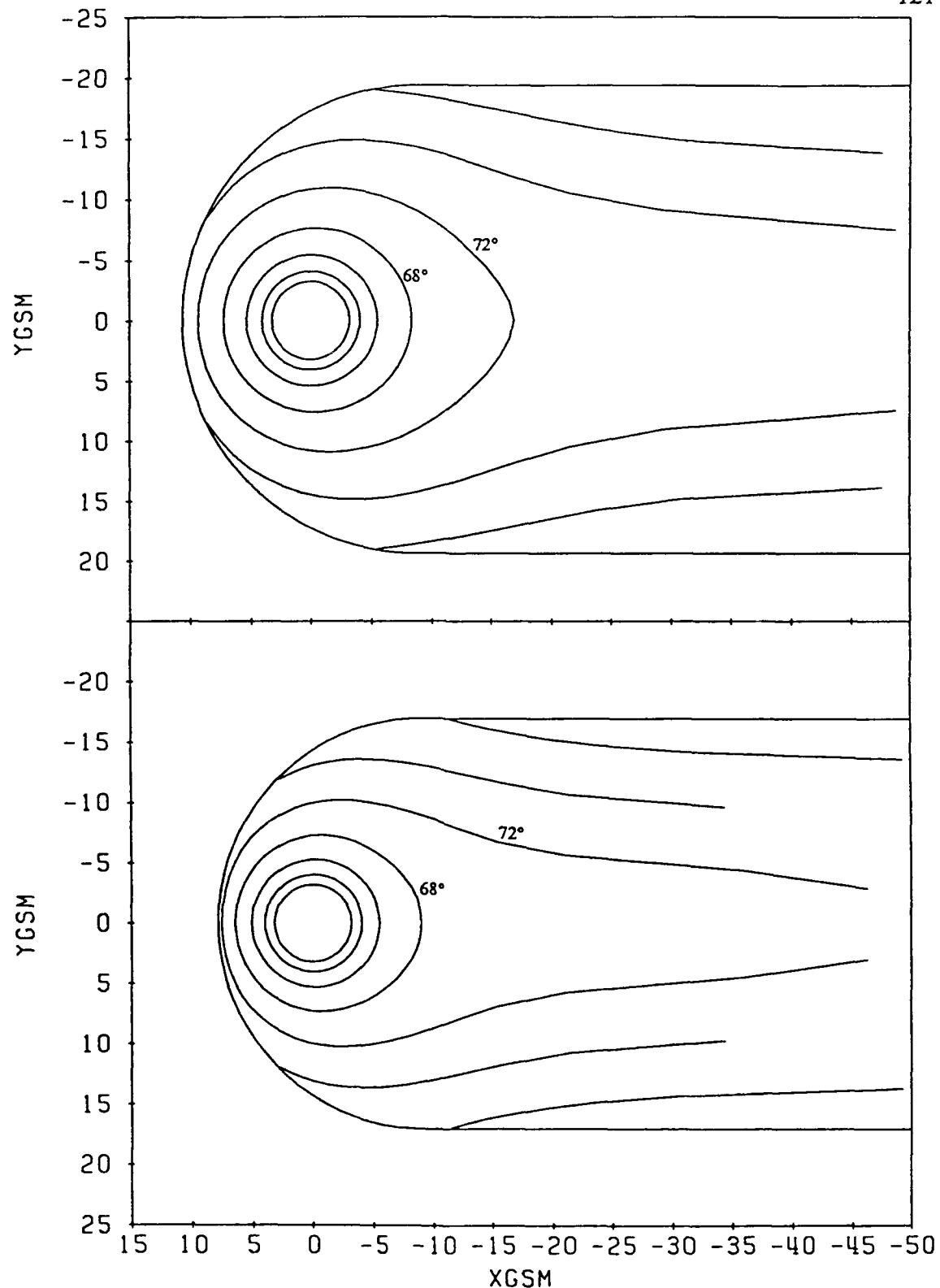


Fig. 8.2. Mapping of the magnetic field to the equatorial plane from rings of constant latitude for CDAW-6 time labels 1 (upper) and 2 (lower) corresponding to Figure 8.1.

showing a very minor increase in strength. Within the next few minutes, by 1054+ $\epsilon$  UT, the magnetic field of the tail is reconfigured as it collapses after the onset of the substorm (label 6). This process was discussed in detail in Section 7 and the configurations corresponding to time labels 5 and 6 are illustrated in Figures 7.1 and 7.2. A recovery of 15-20 nT in the midnight geosynchronous  $B_{T,z}$  component is provided [Barfield et al., 1985] and promotes a more dipolar field near the Earth while collapsing the rest of the tail. This field collapse is restricted to the region of the magnetotail between  $y \approx \pm 5 R_E$ .

With the collapse configuration being a modified version of the previous magnetospheric state, the model reveals its most dynamics changes in the 1130 UT configuration (label 7). It is at this time that the largest changes in the ring current are first noticed. At some point between the collapse and the 1130 UT configuration the ring current strengthened dramatically and made a large earthward jump ( $\approx 0.5 R_E$ ). The current sheet also shifted earthward more than an Earth radius. These changes in the model resulted from a 30 nT decrease in  $D^{st}$  and a  $3^\circ$  decrease in the midnight equatorward auroral latitude. In subsequent configurations, the ring current relaxes and moves slowly outward until the IMF turns southward once again at 1310 UT and additional magnetotail stretching commences. This inward motion of the ring current during substorms and the slow outward motion during recovery is indicative of the substorm process [e.g., Hamilton et al., 1988].

The developments surrounding the second substorm follow a pattern very similar to those of the first one except that the ring current formed during the first event is present throughout. The tail current intensifies and moves inward once again leading to more tail stretching (labels 11-13). The second collapse (label 14), which produced a recovery of 7 nT in the geosynchronous midnight equatorial z component, results from less current diversion than in the first collapse. It is also followed by the inward motion and

strengthening of the ring current (label 15). With no midnight geosynchronous satellite coverage for this second event, a clear substorm signature was not observed [Barfield et al., 1985]. The strength of the ring current present throughout this second event is demonstrative of  $D^{st}$  remaining negative for the rest of the event.

The increase of the magnetic field strength in the lobes during the growth phase of the first substorm causes the magnetotail to flare. The boundary of the magnetotail enlarges until onset, when the flaring reduces dramatically [Fairfield, 1985]. It is interesting to note that, while our model has a magnetotail of fixed radius, the loss of flux due to the violation of magnetopause boundary conditions actually helps simulate the flaring of the tail during this event.

The magnetic activity during this event was high with  $K_p = 6-$  for time labels 3 through 7 and  $K_p = 7-$  for the remainder of the event. As commented on in Section 5, it is this type of higher activity state that is most likely to produce cross-tail currents stronger than the estimates used to determine the ring current parameters. This indicates that the final  $\Delta B$  distribution will be more negative than initially called for in equations (5.3) to (5.5) and reminds us that the parameter selection procedure was developed using observational information corresponding to weak or moderate conditions. We can conclude that the actual dependence of the  $\Delta B$  profiles on the  $D^{st}$  index for high activity states must obviously differ from that for weak and moderately active states.

### *8.2.2. Comparison with Magnetic Field Data*

We now present a comparison between the model output and data from three geosynchronous satellites for a time period surrounding the first substorm of the CDAW-6 event, namely from 1020 to 1220 UT. The purpose of this comparison is to demonstrate that the model configurations, which were generated from a limited set of

initial input parameters, provide reasonable magnetic flux densities. The observational information presented here, the magnetic field data and the satellite positions, is from the combined works of McPherron and Manka [1985], Barfield et al. [1985], and Baker et al. [1985].

To simplify the investigation, the satellite locations at 1100 UT were used to give a rough estimate of their positions for the entire interval of interest. This means that the satellites' maximum deviation from the model locations used corresponds to about  $20^\circ$  of longitude or roughly  $2.3 R_E$  along a satellite orbital path. Note once again that the dipole tilt angle was held fixed at  $\psi = 0^\circ$ .

The GEOS 2 satellite was on the dayside near 1330 LT at magnetic latitude  $-2^\circ$ . This position corresponds to the point  $x = 6.2 R_E$ ,  $y = 2.3 R_E$ , and  $z = -0.2 R_E$  in the model's GSM coordinate system. GOES 2 was near 0400 LT at magnetic latitude  $+9.6^\circ$  and GOES 3 was closer to the midnight meridian near 0145 LT at magnetic latitude  $+4.5^\circ$ . These points corresponding to  $x = -3.3 R_E$ ,  $y = -5.7 R_E$ , and  $z = 1.0 R_E$  for GOES 2 and  $x = -6.0 R_E$ ,  $y = -2.8 R_E$ , and  $z = 0.5 R_E$  for GOES3. The magnetic field observations from these three satellites are given in Figure 8.3 in the dipole VDH coordinate system. The magnetic V component is parallel to the dipole equatorial plane and points radially outward from Earth. The H component is parallel to the magnetic dipole axis and is positive northward. The D component is orthogonal to both of these and is positive in the eastward direction.

As a point of interest, there are several important magnetic field features revealed in these plots that help to characterize the CDAW-6 event. The most dramatic dayside field change recorded by GEOS 2 is the sudden increase in the H component at 0826 UT, which corresponds to the sudden compression of the magnetopause due to increased solar wind pressure. The solar wind pressure then drops just as suddenly slightly after



MARCH 22, 1979

125

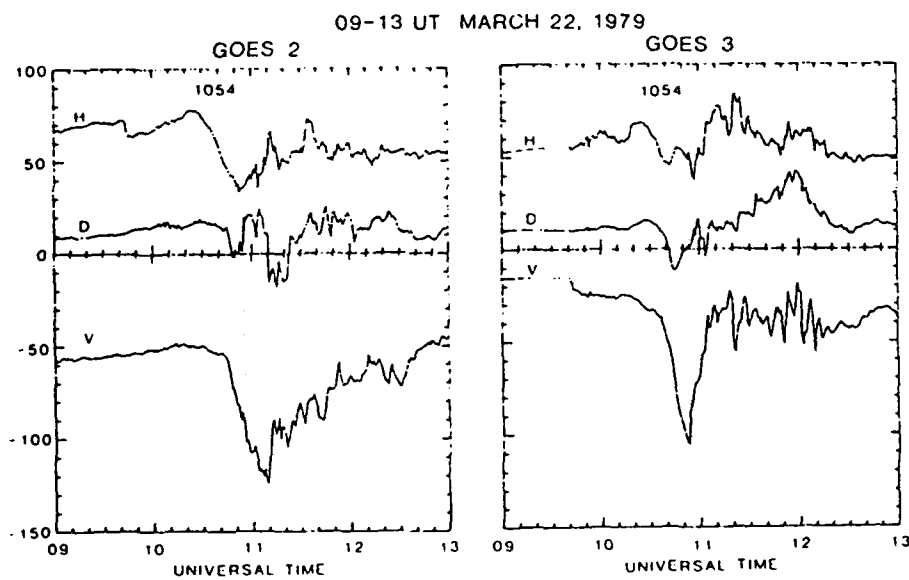
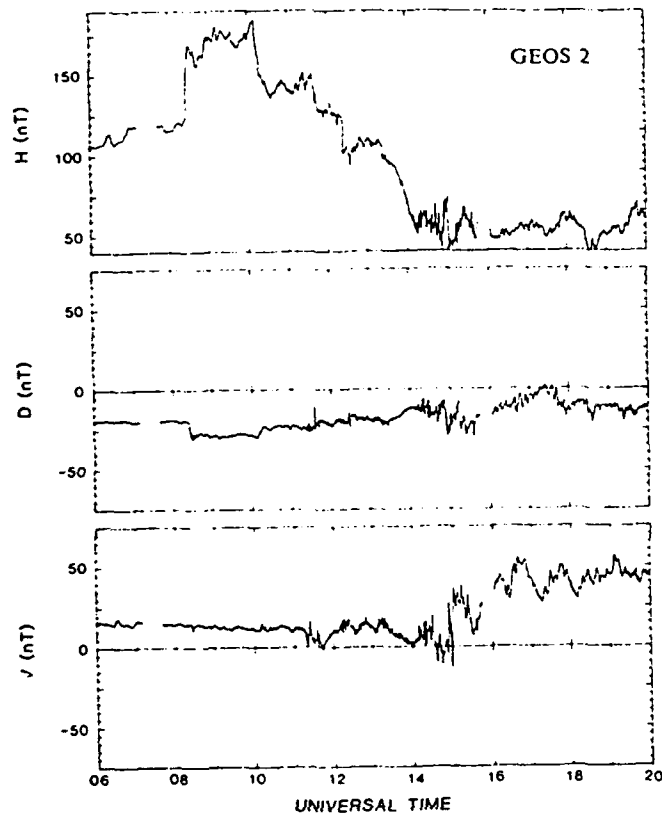


Fig. 8.3. GEOS 2 and GOES 2 and 3 magnetic field observations (nT) at geosynchronous orbit for the CDAW-6 event of March 22, 1979 [McPherron and Manka, 1985]. GEOS 2 (1330 LT) was on the dayside near local noon and GOES 2 (0400 LT) and GOES 3 (0145 LT) were in the magnetotail in the early morning hours.

1000 UT, with the southward turning of the IMF, and the dayside field magnitude decreases as the stand-off distance enlarges in response.

A classic nightside substorm signature was recorded by GOES 3 near the center of the magnetotail. The field strengthens and grows more tail-like (decreasing H and a large negative deflection in V) until the onset at 1054 UT. The field at GOES 3 completes its return to a more dipolarized state by 1110 UT (H increases and V decreases in magnitude). The major magnitude changes are mainly attributable to the fluctuations of the V component. The GOES 2 satellite is farther from the midnight meridian and goes through similar changes, but records its most tail-like features after GOES 3 does and shows a recovery which is less abrupt. This delay has been related to the expansion of the current diversion region both eastward and westward from the point of initial onset [e.g., Nagai et al., 1983].

The magnetic field magnitudes from the CDAW-6 models representing simulation labels 4 through 8 and the observations for these same times are listed in Table 8.3. The maximum stretched configuration (label 5) corresponds to the substorm onset at 1054 UT and the collapsed configuration (label 6) corresponds with the completion of the dipolarization of the field at GOES 3 at 1110 UT. In general, the agreement is much better on the nightside.

A systematic difference is evident in the dayside GEOS 2 data comparison with the model underestimating the field strength. There are two factors which contribute to this difference. First, with the boundary violations due to the ring current following a similar pattern to those of the dipole field (see Figure 5.2), a ring current shielding field would contribute positive flux preferentially to the sunward portions of the equatorial plane in a manner similar to the dipole shielding contributions (see Figure 2.4). This would increase the dayside flux in the model and bring it in closer agreement with the

observations. Second, the strong tail currents needed to meet the nightside mapping requirement contribute substantial flux to the dayside equator at this location. Proper shielding would once again help this situation. Fortunately, the combination of having small stand-off distances and requiring extreme tail field stretching means that these cross-tail current are some of the strongest to be encountered with this model. We note also that in both the observations and the model simulation, the variations in the dayside flux levels do not seem to correspond to any specific changes in the nightside flux levels.

TABLE 8.3. CDAW-6 magnetic field magnitudes (nT) from the model and observations for 5 time labels surrounding the first substorm (model value/ observational value). The substorm onset UT 1054 corresponds to the model UT 1054-ε. The completion of the dipolarization of the field at GOES3 occurred at UT 1110 and corresponds to the model UT 1054+ε.

Label	UT	GEOS 2 ( 1330 LT )	GOES 2 (0400 LT )	GOES 3 (0145 LT )
4	1020	120 / 150	95 / 92	73 / 70
5	1054	120 / 140	92 / 100	64 / 115
6	1110	124 / 140	95 / 140	72 / 75
7	1130	127 / 140	96 / 100	80 / 75
8	1206	120 / 130	95 / 90	79 / 78

The model results for the GOES 3 satellite location near midnight match the observations well in total magnitude for all times except 1054 UT. The GOES 3 magnetic V component decreases by more than 70 nT from its value at 1020 UT while the model manages a modest 10 nT decrease of that same component. Both the model and observational H components decrease by 15 nT. The net result is that the observations indicate that the field was stronger by more than 50 nT and the configuration even more tail-like than the model indicates.

An encouraging note to add is that a check of the model output at a position only 1  $R_E$  above the specified 1054 UT location of the GOES 3 satellite reveals that the field strength increases quickly to 95 nT. Applying a similar procedure to the other time labels does not improve the agreement. This indicates that the model can provide the strong increases in the magnetic V component, but in this case the current sheet was not thin enough to produce such strong fields so close to the equatorial plane.

A similar phenomena occurred involving the GOES 2 satellite observation out near 0400 LT. The model output matches well with the GOES 2 satellite observations for all times except 1110 UT. Again, the time label in question corresponds to a large decrease in the magnetic V component and the most stretched configuration for that location.

The results of this very rough and limited comparison indicate that the model is capable of producing reasonable patterns of magnetic flux at geosynchronous altitudes, especially on the nightside. They also indicate that proper shielding of the ring and cross-tail currents would improve the models ability to produce the observed flux levels.

Several important points must be emphasized regarding this CDAW-6 magnetic field simulation. First, although the flux levels before and after the onset are very close in magnitude in both the model configurations and the observations, the model cross-tail current reached peak strength and weakened slightly while the ring current started out

very weak and grew dramatically during the sequence. Second, the complementary behavior of these two current systems, which represents a transport of energy to the inner magnetosphere, was generated by only three initial input parameters and depicts a physically reasonable sequence of development for both current systems. And finally, the often extreme combinations of input parameters represented in this simulation characterize the diversity of the possible model configurations. There were, for example, highly stretched tail configurations in compressed magnetospheres with weak ring currents and tail field collapses with and without a strong ring current present, all of which existed under different midnight equatorial mapping constraints.

### 8.3. Shape and Position of the Neutral Sheet

The addition of the ring and cross-tail currents has dramatically altered the shape and position of the magnetic neutral sheet when compared with that of the vacuum configuration of Figure 2.6. As illustrated in Figure 8.4, the neutral sheet bends smoothly away from the dipole equatorial plane to become parallel to the x-y plane in the midnight meridian and shows no tendency to return to that plane with distance down the tail as it does in the vacuum case. These curves generally agree with the expected midnight meridian neutral sheet positions shown in Figure 4.1, which were derived by combining the average observations inside of  $8.8 R_E$  [Fairfield et al., 1987] with those beyond  $15 R_E$  [Fairfield, 1980; Gosling et al., 1986]. They differ in that the neutral sheet bends away from the dipole equatorial plane slightly earlier than expected with the obvious additional trend that the separation occurs closer to Earth for weaker cross-tail currents and larger tilt angles.

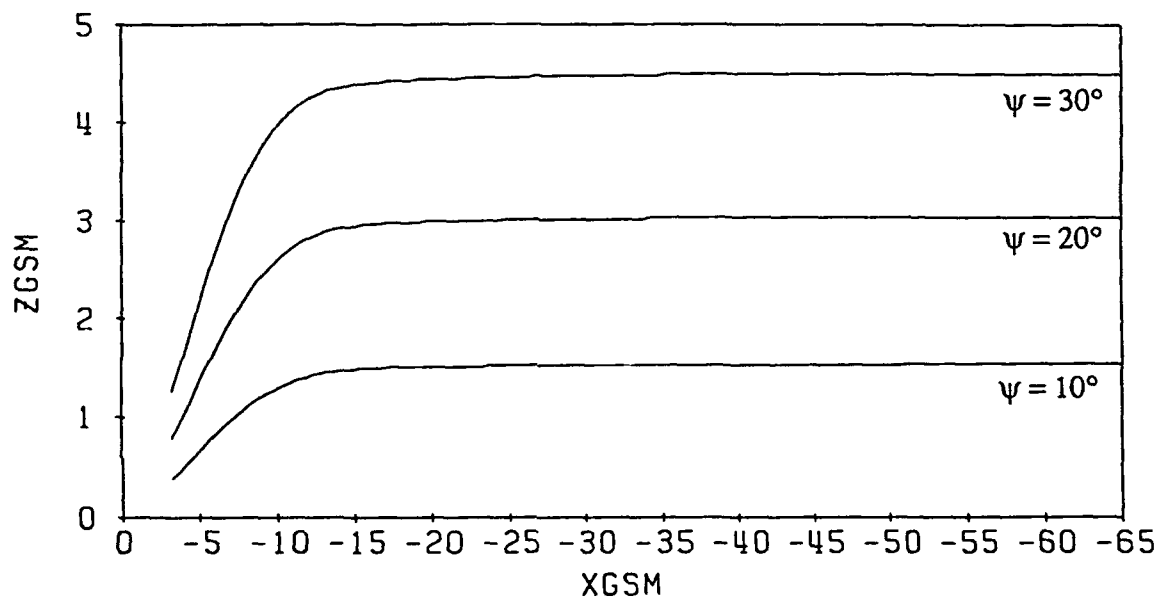


Fig. 8.4. Neutral sheet position in the midnight meridian plane with  $\psi = 10^\circ$ ,  $20^\circ$ , and  $30^\circ$  for CDAW-6 time label 8. Note that different scales are used for the x and z axes. Compare with expected neutral sheet position illustrated in Figure 4.1. The neutral sheet is defined as the surface where  $B_{T,x} = 0$ .

This discrepancy could be partially remedied by increasing the present "hinging" distance from  $H_d = 9.0 R_E$  [Gosling et al., 1986] to  $H_d = 10.5 R_E$  [Fairfield, 1980; Dandouras, 1988]. This would lift the flat portion of the neutral sheet farther from the equatorial plane while keeping it closer to the dipole equatorial plane in the inner magnetosphere. It could also be altered by introducing a flat current sheet representation [e.g., Tsyganenko, 1987], but this would introduce unphysical currents in the near tail and further detract from the idea that the neutral sheet and plasma sheet should roughly coincide to promote pressure balance throughout the magnetotail.

The behavior of the neutral sheet with distance down the tail is illustrated in Figure 8.5. The neutral sheet dips below the equatorial plane in the flanks at closer distances and gradually flattens out with increased distance as the influence of the dipole field weakens and the cross-tail current begins to dominate. At greater distances, the neutral sheet is shifted in the same direction across the entire width of the tail. Once again, the center portion of the neutral sheet remains elevated at all distances.

These basic trends are in agreement with the magnetohydrostatic equilibrium calculations of Voigt [1984] and support the notion that although the neutral sheet dips below the equatorial plane in the flanks at the middle tail distances [e.g., Fairfield, 1980; Dandouras, 1988], the neutral sheet may approach the equatorial plane in the flanks at greater distances [e.g., Russell and Brody, 1967]. Thus it supports the more physically reasonable notion that the neutral sheet cannot have the same shape along its entire length.

Although our cross-tail current does not flex in the  $y$ - $z$  plane following the neutral sheet behavior, the  $y$  dependence of the cross-tail current, originally adjusted to satisfy equatorial magnetic flux distribution requirements, allows the fields of the vacuum configuration to influence the position of the neutral sheet in the flanks. The flattening of the neutral sheet with distance down the tail is naturally accentuated by stronger cross-tail

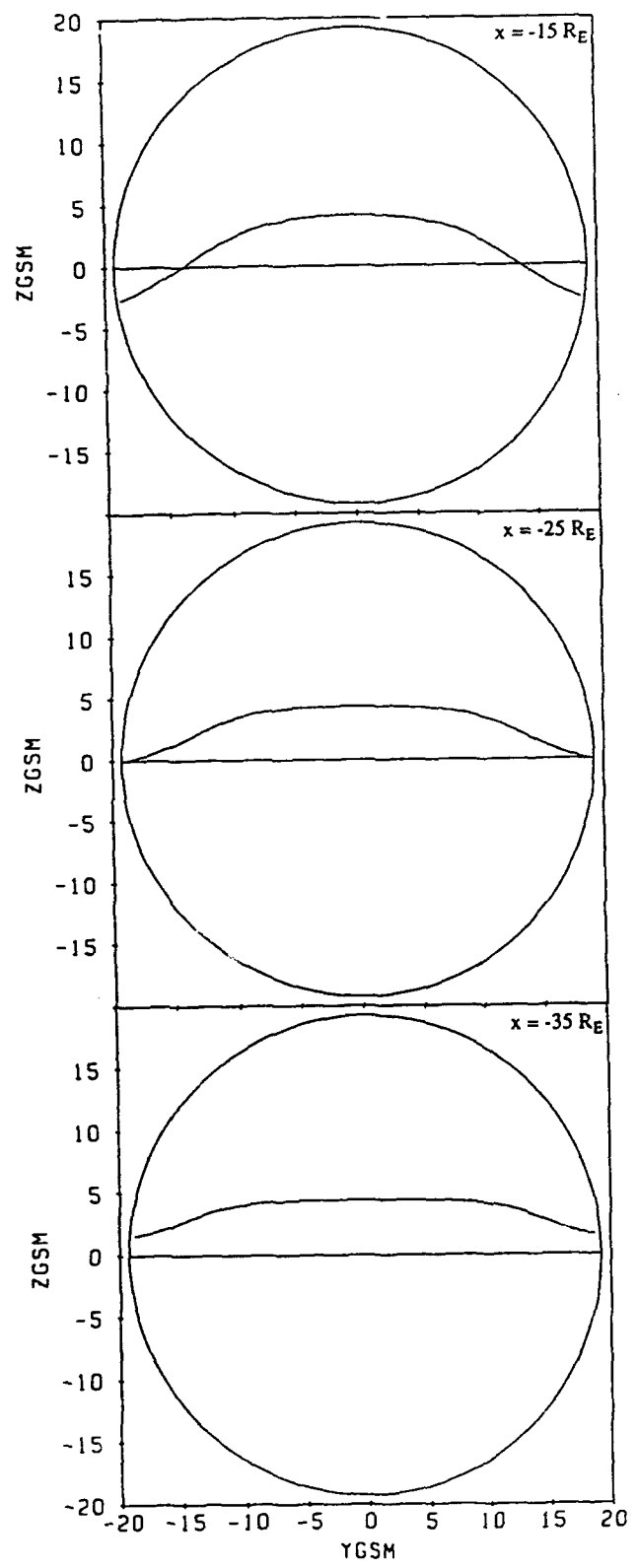


Fig. 8.5. Neutral sheet position in the y-z plane at  $x = -15, -25,$  and  $-35 R_E$  for the configuration introduced in Figure 6.1 with  $\psi = 30^\circ$ .



currents. A current sheet which remained stronger in the flanks, but flexed in the y-z plane with the neutral sheet, would have a better chance of approximating pressure balance in the magnetotail. We should also be reminded that in a self-consistent model the plasma sheet shape and the magnetopause shape are closely connected [Birn, 1979], and that we have introduced additional currents without considering possible consequences to magnetopause shape.

The evidence provided here indicates that the model produces physically reasonable configurations when the dipole is tilted as both the shape and position of the model magnetic neutral sheet are in general agreement with the average observed neutral sheet behavior. This, in turn, reflects well on the method used to formulate the cross-tail current sheet.

#### 8.4. $\Delta B$ Profiles

The quantity  $\Delta B$ , which is defined as the observed magnetic field magnitude minus the magnitude of a reference field intensity, has been useful for investigating the nature of magnetic fields originating from current sources external to the Earth. Profiles of this quantity are very helpful for both designing and evaluating magnetic field models as reproduction of the observed profiles provides a strong indication that a model possesses some realism (see the review by Walker [1976] for commentary on the  $\Delta B$  profiles of some of the earlier magnetic field models). We begin with a review of the observed  $\Delta B$  topology and the changes accompanying increased geomagnetic activity.

The observational profiles for quiet ( $K_p = 0-1$ ) and slightly disturbed ( $K_p = 2-3$ ) conditions obtained by OGO 3 and 5 satellites are provided in Figures 8.6 and 8.7, for the noon-midnight and dawn-dusk meridians, respectively. We will adopt the

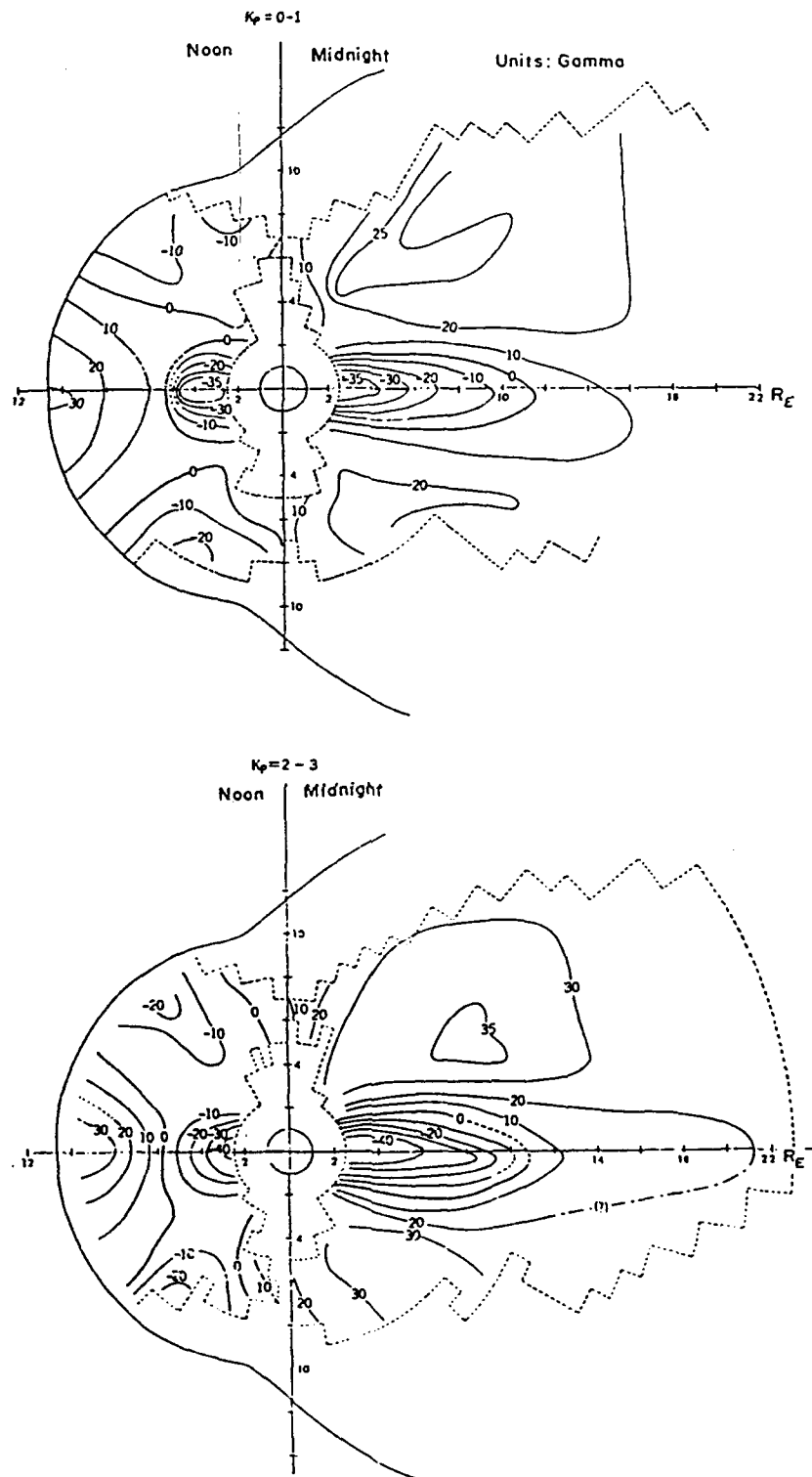


Fig. 8.6. Observational contours of constant  $\Delta B$  (nT) in the noon-midnight meridian plane for  $K_p = 0-1$  (upper) and  $K_p = 2-3$  (lower) from Sugiura and Poros [1973]. The blank areas bounded by broken lines indicate regions where the data was either not available or considered unreliable.

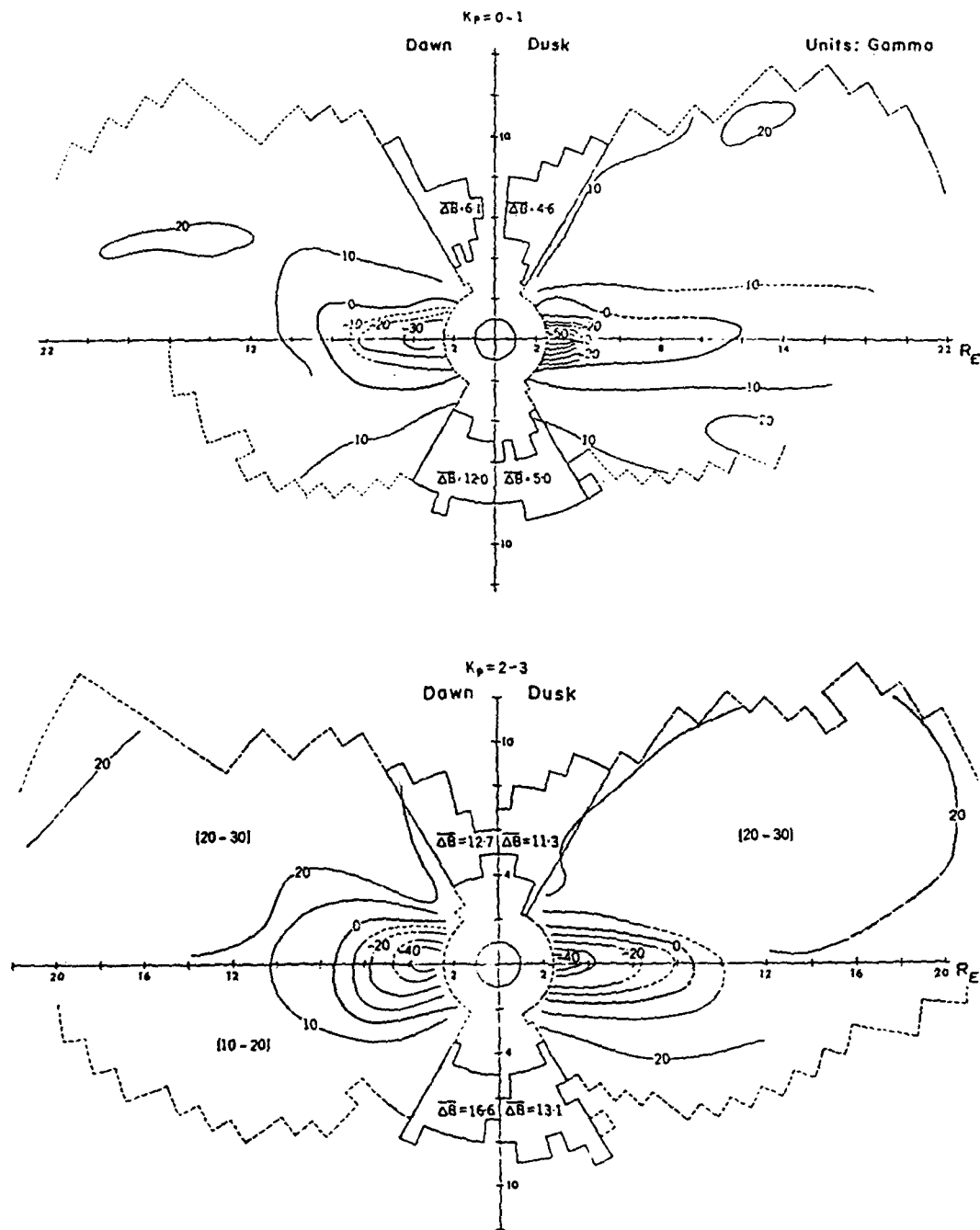


Fig. 8.7. Observational contours of constant  $\Delta B$  (nT) in the dawn-dusk meridian plane for  $K_p = 0-1$  (upper) and  $K_p = 2-3$  (lower) from Sugiura and Poros [1973].

classification scheme used by Sugiura [1972] for both the observational and model  $\Delta B$  topology and briefly summarize here his review of the observations.

The noon-midnight meridian plane can be divided into four basic regions: (A) the equatorial  $-\Delta B$  encircling the Earth, (B) the nightside  $+\Delta B$  that surrounds the nightside portion of Region A, (C) the two separate  $-\Delta B$  regions in the noon meridian at middle to high latitudes, and (D) the  $+\Delta B$  region about the equator in the noon meridian. Moving from the noon meridian toward the dawn-dusk meridian, Region A expands and Region C disappears while Region D merges with Region B in the dawn-dusk meridian. Sugiura [1972] also notes that the dawn-dusk asymmetry of the contours being stretched out more on the dusk side is probably a real effect as the same tendency holds for different activity levels.

The changes in the observational  $\Delta B$  profile with increased magnetic activity are as follows. There tends to be an enhancement of the negative values of Region A, particularly in the midnight meridian, and the positive values of Region B and the polar cap area also increase in magnitude. Region C expands and can become connected to the dayside equatorial Region A which compresses the extent of the intensified Region D sunward.

Before looking at the model  $\Delta B$  profile, we note that all of the examples presented use the same stand-off distance and the equatorial flux contribution due to dipole shielding is that given in Figure 2.5. This allows us to concentrate on the development of the ring and cross-tail current contributions to  $\Delta B$ . The reference field is the Earth's dipole and does not affect the comparison as it is the difference field that is of interest. Also, emphasis has not been placed on duplicating a  $\Delta B$  profile associated with any particular activity level, as we are interested in comparing the basic model  $\Delta B$  topology as it evolves within the set of example configurations.

The noon-midnight equatorial asymmetry of Region A also appears in the model due to the combined contributions of the ring and cross-tail currents and is shown in Figure 8.8. This plot is most appropriately compared with the  $K_p = 2-3$  curve of the observational plot of Figure 5.1. Both noon and midnight minima occur at radial distances of  $3-4 R_E$  [Sugiura, 1973], while the profile recovers to less negative values toward the Earth [Su and Konradi, 1975]. The depth of the nightside minimum is greater than that of the dayside minimum and the dayside values change sign near  $6 R_E$  while the nightside values remain negative beyond  $10 R_E$  with the difference being attributable to the cross-tail current. The approximate magnitude of the field depressions in the inner region is easily controlled by the ring current which, as noted in Section 5, is closely tied to the  $D^{st}$  index.

The  $\Delta B$  contours in the noon-midnight and dawn-dusk meridian planes for four very different model configurations are shown in Figures 8.9 and 8.10, respectively. These include the vacuum case and three other configurations which range from depicting an extremely quiet magnetosphere to a very active or stretched magnetosphere. This series of magnetospheric states demonstrates the strong influence of growing ring and cross-tail currents.

If the observational plots for  $K_p = 0-1$  and  $2-3$  of Figures 8.6 and 8.7 were to be fit into the model example sequence according to activity level, they would fit most appropriately on either side of the "intermediate" configuration which corresponds to  $K_p \approx 2$ . The "stretched" configuration probably corresponds to  $K_p \geq 5$  and the "quiet" configuration represents only a slight modification of the vacuum case. We stress again that the observational plots represent average contours derived from thousands of data points taken over a time period of greater than one year, while the model examples represent quite specific configurations.

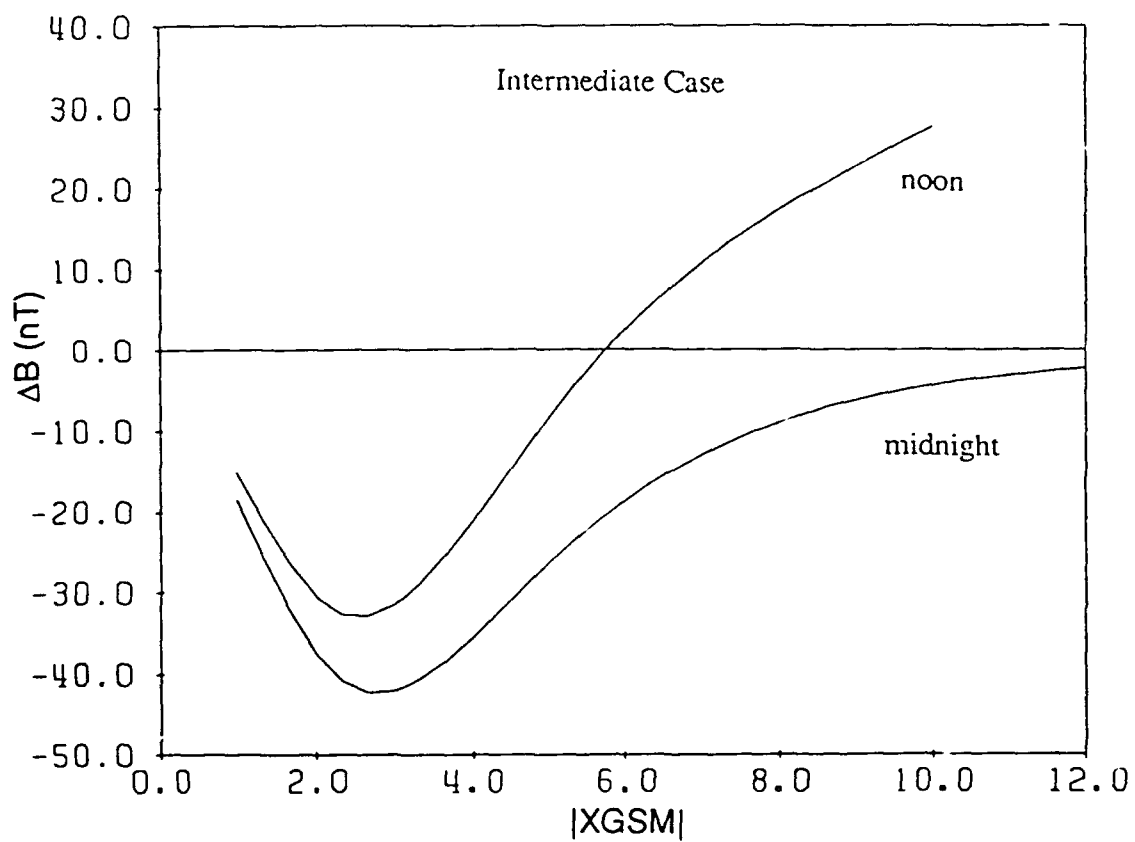


Fig. 8.8. Model  $\Delta B$  as a function of position along a folded noon-midnight x axis for the "intermediate" configuration introduced in Figure 6.9. Compared most appropriately with the observational  $K_p = 2-3$  curve of Figure 5.1.

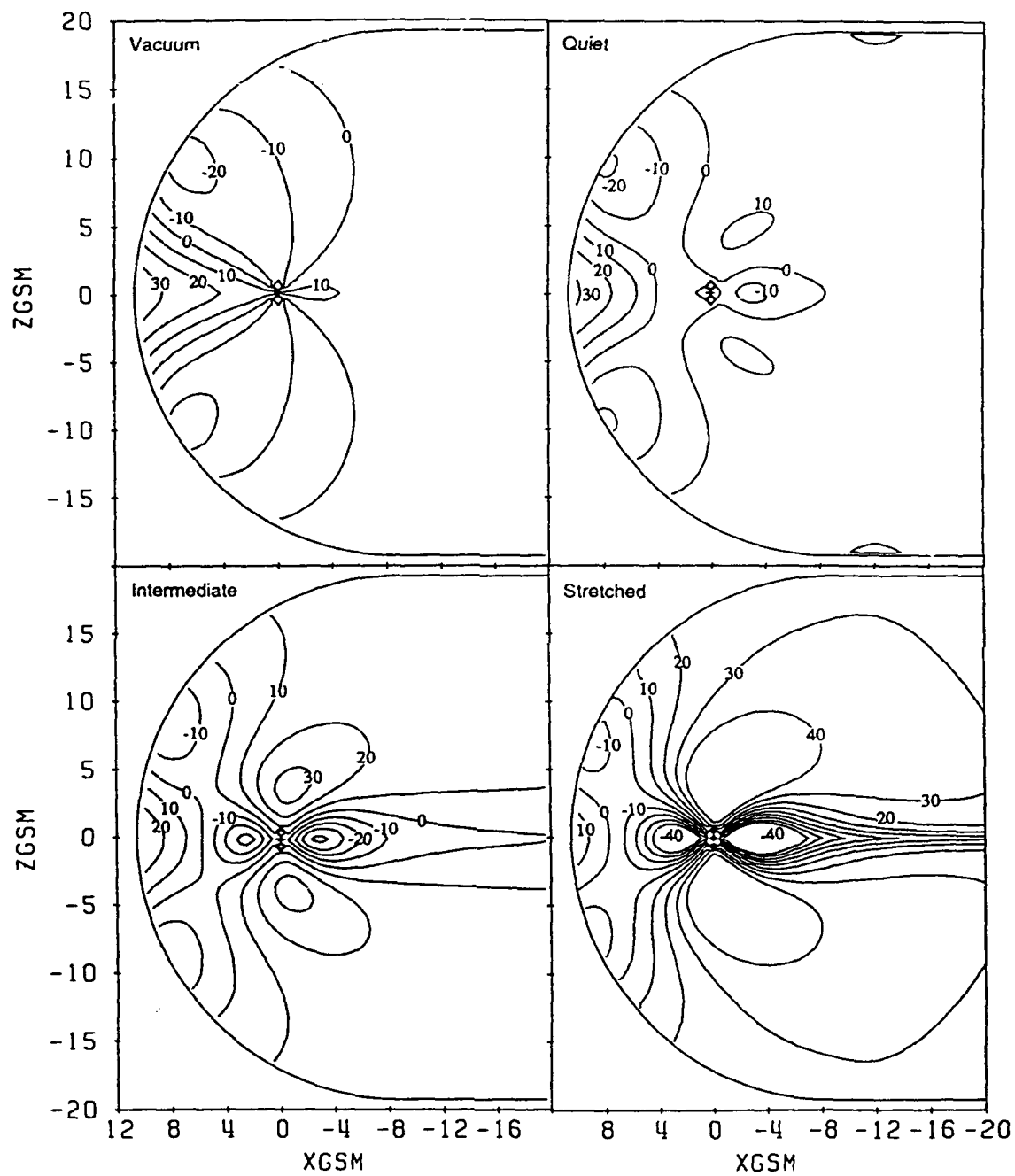


Fig. 8.9. Model contours of constant  $\Delta B$  (nT) in the noon-midnight meridian plane for the "quiet", "intermediate", and "stretched" configurations (Figures 6.8, 6.9, and 6.10) and the corresponding vacuum configuration. The contours are symmetric about the x axis and are plotted in steps of 10 nT.

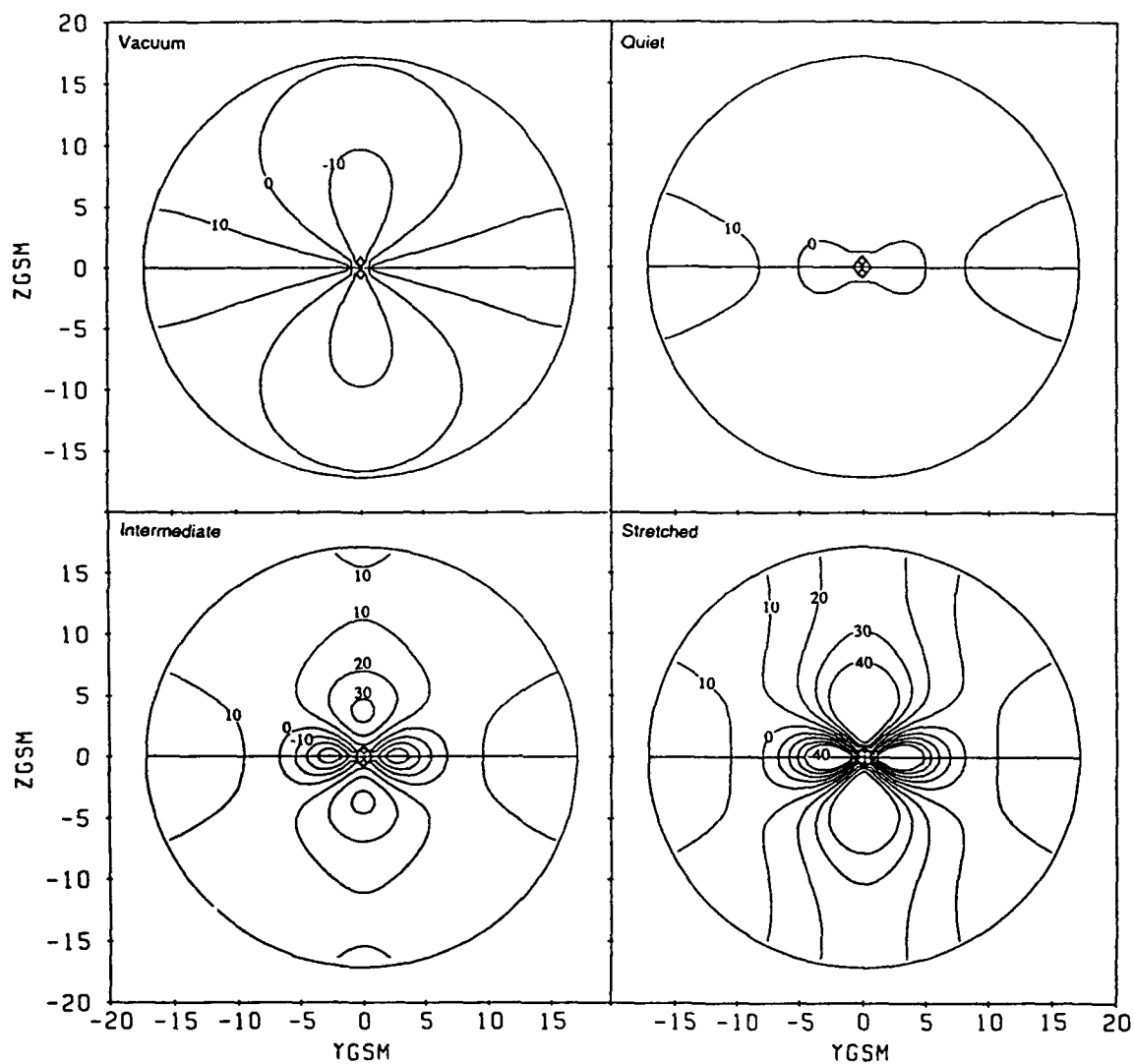


Fig. 8.10. Model contours of constant  $\Delta B$  (nT) in the dawn-dusk meridian plane for the "quiet", "intermediate", and "stretched" configurations (Figures 6.8, 6.9, and 6.10) and the corresponding vacuum configuration. The contours are symmetric about both the y and z axes and are plotted in steps of 10 nT.



All of the observed  $\Delta B$  regions, as classified by Sugiura, exist with varying degrees of  $\Delta B$  intensity in the non-vacuum model examples. The lower panels of Figures 8.9 and 8.10 provide the best illustration of this fact. The model ring current and cross-tail current combine to produce the noon-midnight asymmetry of Region A. This region grows as we move toward the dawn-dusk meridian to join the extended midnight part of that same region. The vacuum configuration, of course, has no additional internal currents and therefore lacks a Region A. The increased tail fields in the tail lobe portions of Region B are related to the cross-tail current while the increased positive values over the poles are also enhanced by the ring current. Region C is related to the cusp region where magnetopause currents, in this case owing to the shielding of the dipole field, diminish field magnitudes. Region C is localized at middle and high latitudes near the noon meridian. Region D at noon is dominated by the positive equatorial flux from the magnetopause shielding field and weakens as it wraps around to the flanks of the dawn-dusk meridian and continues down the tail flanks. In the dawn-dusk meridian it is clear that Region D comes in contact with Region B.

There are also noticeable model trends which are different from those of the observations. The model nightside equatorial values remain negative to greater distances. This indicates that the cross-tail current of the average observed configurations might be relatively more intense near the current sheet inner edge and therefore boost the  $\Delta B$  values more in the  $x = -10$  to  $-20 R_E$  range. Also, the intensity peak in the model lobe Region B tend to be centered over the poles and sunward of the observed peaks which occur 5 to 10  $R_E$  back in the lobes.

The evolution of the  $\Delta B$  pattern from one model example to the next can also be compared with the observed changes with magnetic activity. Starting with the vacuum configuration, we can see the influence of the dipole shielding field. Equatorial flux

levels are enhanced while the region over the poles and sunward toward the cusps experiences a reduction of field strength as the dipole shielding and dipole magnetic fields oppose each other. With the addition of a ring and cross-tail current to form the "quiet" configuration, the  $-\Delta B$  values of Region A make themselves evident and the positive values of Region B increase while Regions C and D are each compressed into smaller volumes.

The transition between successive model states reveals trends in the development of the  $\Delta B$  contours as both the ring and cross-tail currents are strengthened. Region A expands and the  $-\Delta B$  values intensify to accentuate the noon-midnight asymmetry. Note that the sharp contour features in the midnight equatorial plane of Region A in the "stretched" configuration could never appear in the averaged observations due to data averaging and the tilting of the Earth's dipole. The  $+\Delta B$  values of Region B intensify as the lobe field increases with larger tail currents and the pole regions (most noticeable in dawn-dusk view) are also intensified by the boosted ring current. Region C is compressed and shifts to lower latitudes following the motion of the cusp but still joins with the dayside portion of Region A. The earthward boundary of Region D moves sunward as that region is also compressed. Due to the constant stand-off distance used for these examples and the lack of magnetopause shielding for the added currents, there is no change in the magnetopause shielding field so the compression of the Regions C and D is not accompanied by intensification of  $\Delta B$  values as seems to be the case with the observations.

The great similarities between the basic  $\Delta B$  topology of these model examples and that of the time-averaged observations, as well as between the respective changes associated with increased geomagnetic activity (or stronger ring and cross-tail currents), indicate that the model behaves reasonably well over a broad spatial range.

## 9. Summary and Conclusions

A highly flexible tilt-dependent magnetic field model of the Earth's magnetosphere was constructed. Analytic representations for the ring and cross-tail currents were combined with the vacuum magnetic field model of Voigt [1981], a fully shielded dipole within a fixed magnetopause geometry, to form a semi-empirical representation capable of describing many diverse magnetospheric configurations. The resulting magnetic field strictly satisfies the condition  $\nabla \cdot \mathbf{B} = 0$ .

While the model is applicable over a very large spatial region, its strength lies in the ability to represent the inner portions of the magnetosphere, thus points very close to the magnetopause boundary or in the very distant tail are less well represented. Principle improvements to the model, which would both increase the accuracy and extend the spatial range of validity, include the proper shielding of the ring and cross-tail currents and a method for representing field aligned currents.

Highlights of the physical characteristics and capabilities of the magnetospheric magnetic field model can be summarized as follows.

1. Use of the Voigt [1981] vacuum field allows for the adjustment of the dipole shielding field with variations in magnetopause dimensions. It also influences greatly the shape and position of the neutral sheet as it varies with dipole tilt angle.

2. The ring current consists of nested eastward and westward flowing current distributions which tilt with and remain axially symmetric about the magnetic dipole axis. It provides a simple method for precisely controlling the inflation of the inner

magnetosphere. Despite the fact that the ring current is not generated self-consistently with the total magnetic field, it is very similar to current distributions determined in that way.

3. The model can represent cross-tail currents which have their position and current intensity in the midnight meridian plane described by arbitrary functions of the distance down the magnetotail. This allows for the flexing of the current sheet in the near tail and eliminates edge effects which result from flat current sheet representations. This is the first semi-empirical current sheet to flex in such a physical way. The inner current sheet bends around the Earth to become contiguous with the ring current and thickens toward the flanks of the magnetotail. The current sheet thickness can be controlled to allow the lobes to remain relatively current free.

4. Nominal model configurations are completely specified by four initial physical input parameters, the dipole tilt angle, the magnetopause stand-off distance, the geomagnetic index  $D^{st}$ , and the midnight equatorward boundary of the diffuse aurora. These parameters are used to automatically determine the relative position and strength of both the ring and cross-tail currents and provide for a diverse array of configurations including many degrees of magnetotail field stretching. This multi-parameter process allows many different combinations of ring and tail currents to exist simultaneously under conditions which would normally be characterized by a single geomagnetic activity index.

5. The unique combination of magnetic field sources provide reasonable magnetic flux levels in both the lobes and the equatorial plane and can reproduce the specific observed equatorial feature that flux densities are higher in the flanks than they are near the center of the magnetotail.

6. The disruption of the near-earth cross-tail current sheet and the collapse of the midnight field region, which occur during magnetospheric substorms, can be

represented. This includes the classic dipolarization of the near-earth field and the thinning of the far-tail field with both phenomena begin confined to the midnight tail region. This is the first time a detailed representation of this type of magnetotail magnetic field reconfiguration has been included in a three-dimensional semi-empirical representation.

7. A physically reasonable sequence of magnetospheric configurations can be generated using only sets of observable initial input parameters and a special magnetotail collapse procedure. This was demonstrated with a magnetic field simulation of the CDAW-6 event which described the motion, growth, and decay of the ring and cross-tail currents in a manner consistent with the observations. Geosynchronous magnetic flux densities were also in general agreement with observations from the event.

8. The shape and position of the neutral sheet change with the tilt of the Earth's dipole in a manner consistent with the results of both equilibrium calculations and observations.

9. The validity of the model over an extended three-dimensional range is confirmed by a favorable comparison of model and observational  $\Delta B$  topologies and their evolution with changes in geomagnetic activity.

A final comment is in order regarding this model's place in the hierarchy of existing magnetospheric models. There are two basic approaches which represent the extremes in large scale modeling of the Earth's magnetosphere. The first is the physical approach of MHD models which attempt to include self-consistent plasma physical processes. The second approach is basically a descriptive one and results in purely empirical models. This semi-empirical model stresses equally the physical representation of both the magnetic fields and the currents and can represent many diverse states of the

magnetosphere while relying on only physical input parameters. This combination of traits facilitates the investigation of the physical relationship between the input parameters and the development of the magnetospheric fields and currents. From this point of view, this work brings us a step closer to a physical modeling approach and represents a significant advance in magnetospheric description.

## References

- Akasofu, S.-I., J. C. Cain, and S. Chapman, The magnetic field of the quiet-time proton belt, *J. Geophys. Res.*, 67, 2645-2647, 1962.
- Akasofu, S.-I., E. W. Hones, Jr., M. D. Montgomery, S. J. Bame, and S. Singer, Association of magnetotail phenomena with visible auroral features, *J. Geophys. Res.*, 76, 5985-6003, 1971.
- Arnoldy, R. L., and T. E. Moore, Longitudinal structure of substorm injections at synchronous orbit, *J. Geophys. Res.*, 88, 6213-6220, 1983.
- Aubry, M. P., M. G. Kivelson, R. L. McPherron, C. T. Russell, and D. S. Colburn, Outer magnetosphere near midnight at quiet and disturbed times, *J. Geophys. Res.*, 77, 5487-5502, 1972.
- Baker, D. N., and E. C. Stone, The relationship of energy flow at the magnetopause to geomagnetic activity, *Geophys. Res. Lett.*, 4, 395-398, 1977.
- Baker, D. N., Particle and field signatures of substorms in the near magnetotail, in *Magnetic Reconnection in Space and Laboratory Plasma*, *Geophys. Monogr. Ser.*, 30, ed. by E. W. Hones, Jr., 193-202, AGU, Washington, D. C., 1984.
- Baker, D. N., T. A. Fritz, R. L. McPherron, D. H. Fairfield, Y. Kamide, and W. Baumjohann, Magnetotail energy storage and release during the CDAW 6 substorm analysis intervals, *J. Geophys. Res.*, 90, 1205-1216, 1985.
- Balsiger, H., On the composition of the ring current and the plasma sheet and what it tells about the sources of these hot plasmas, in *High-Altitude Space Physics*, ed. by B. Hulqvist and T. Hagfors, 313-333, Plenum Press, New York, 1983.
- Bame, S. J., J. R. Asbridge, H. E. Felthaus, E. W. Hones, Jr., and I. B. Strong, Characteristics of the plasma sheet in the earth's magnetotail, *J. Geophys. Res.*, 72, 113-129, 1967.
- Bame, S. J., R. C. Anderson, J. R. Asbridge, D. N. Baker, W. C. Feldman, J. T. Gosling, E. W. Hones, Jr., D. J. McComas, and R. D. Zwickl, Plasma regimes in the deep geomagnetic tail: ISEE 3, *Geophys. Res. Lett.*, 10, 912-915, 1983.
- Barfield, J. N., C. S. Lin, and R. L. McPherron, Observations of magnetic field perturbations at GOES 2 and GOES 3 during the March 22, 1979, substorms: CDAW 6 analysis, *J. Geophys. Res.*, 90, 1289-1295, 1985.
- Behannon, K. W., Mapping of the earth's bow shock and magnetic tail by Explorer 33, *J. Geophys. Res.*, 73, 907-930, 1968.
- Behannon, K. W., Geometry of the geomagnetic tail, *J. Geophys. Res.*, 75, 743-753, 1970.

- Bird, M. K., and D. B. Beard, The self-consistent geomagnetic tail under static conditions, Planet. Space Sci., 20, 2057-2072, 1972.
- Birn, J., R. Sommer, and K. Schindler, Self-consistent theory of the quiet magnetotail in three dimensions, J. Geophys. Res., 82, 147-154, 1977.
- Birn, J., Self-consistent magnetotail theory: general solution for the quiet tail with vanishing field-aligned currents, J. Geophys. Res., 84, 5143-5152, 1979.
- Birn, J., and E. W. Hones, Jr., Three-dimensional computer modeling of dynamic reconnection in the geomagnetic tail, J. Geophys. Res., 86, 6802-6808, 1981.
- Birn, J., and K. Schindler, Self-consistent theory of three-dimensional convection in the geomagnetic tail, J. Geophys. Res., 88, 6969-6980, 1983.
- Bowling, S. B., The influence of the direction of the geomagnetic dipole on the position of the neutral sheet, J. Geophys. Res., 79, 5155-5158, 1974.
- Burton, R. K., R. L. McPherron, and C. T. Russell, An empirical relationship between interplanetary conditions and  $D^{st}$ , J. Geophys. Res., 80, 4204-4214, 1975.
- Caan, M. N., R. L. McPherron, and C. T. Russell, Solar wind and substorm-related changes in the lobes of the geomagnetic tail, J. Geophys. Res., 78, 8087-8096, 1973.
- Caan, M. N., R. L. McPherron, and C. T. Russell, Substorm and interplanetary magnetic field effects on the geomagnetic tail, J. Geophys. Res., 80, 191-194, 1975.
- Caan, M. N., R. L. McPherron, and C. T. Russell, The statistical signature of magnetospheric substorms, Planet. Space Sci., 26, 269-279, 1978.
- Cahill, L. J., Jr., Inflation of the inner magnetosphere during a magnetic storm, J. Geophys. Res., 71, 4505-4519, 1966.
- Carovillano, R. L., and G. L. Siscoe, Energy and momentum theorems in magnetospheric processes, Rev. Geophys. Space Phys., 11, 289-353, 1973.
- Chase, L. M., Evidence that the plasma sheet is the source of auroral electrons, J. Geophys. Res., 74, 348-350, 1969.
- Coleman, P. J., Jr., and W. D. Cummings, Stormtime disturbance fields at ATS 1, J. Geophys. Res., 76, 51-62, 1971.
- Dandouras, J., On the average shape and position of the geomagnetic neutral sheet and its influence on plasma sheet statistical studies, J. Geophys. Res., 93, 7345-7353, 1988.
- Davies, C. M., A simple time-dependent solution of the geomagnetic ring-current problem, Geophys. J. R. Astro. Soc., 50, 23-28, 1977.



- Eastman, T. E., L. A. Frank, W. K. Peterson, and W. Lennartsson, The plasma sheet boundary layer, J. Geophys. Res., 89, 1553-1572, 1984.
- Fairfield, D. H., and N. F. Ness, Configuration of the geomagnetic tail during substorms, J. Geophys. Res., 75, 7032-7047, 1970.
- Fairfield, D. H., Average and unusual locations of the earth's magnetopause and bow shock, J. Geophys. Res., 76, 6700-6716, 1971.
- Fairfield, D. H., On the average configuration of the geomagnetic tail, J. Geophys. Res., 84, 1950-1958, 1979.
- Fairfield, D. H., A statistical determination of the shape and position of the geomagnetic neutral sheet, J. Geophys. Res., 85, 775-780, 1980.
- Fairfield, D. H., R. P. Lepping, E. W. Hones, Jr., S. J. Bame, and J. R. Asbridge, Simultaneous measurements of magnetotail dynamics by IMP spacecraft, J. Geophys. Res., 86, 1396-1414, 1981a.
- Fairfield, D. H., E. W. Hones Jr., and C.-I. Meng, Multiple crossings of very thin plasma sheet in the earth's magnetotail, J. Geophys. Res., 86, 11189-11200, 1981b.
- Fairfield, D. H., Solar wind control of magnetospheric pressure (CDAW 6), J. Geophys. Res., 90, 1201-1204, 1985.
- Fairfield, D. H., The magnetic field of the equatorial magnetotail from 10 to 40  $R_E$ , J. Geophys. Res., 91, 4238-4244, 1986.
- Fairfield, D. H., Structure of the geomagnetic tail, in Magnetotail Physics, ed. by A. T. Y. Lui, 23-33, The Johns Hopkins University Press, Baltimore, 1987.
- Fairfield, D. H., M. H. Acuna, L. J. Zanetti, and T. A. Potemra, Magnetic field of equatorial midnight: AMPTE/CCE observations at  $R < 8.8 R_E$ , J. Geophys. Res., 92, 7432-7442, 1987.
- Feldstein, Y. I., Auroras and associated phenomena, in Solar-Terrestrial Physics, Part 3, ed. by Dyer, 152-191, D. Reidel, Dordrecht, Holland, 1972.
- Feldstein, Y. I., V. Y. Pisarsky, N. M. Rudneva, and A. Grafe, Ring current simulation in connection with interplanetary space conditions, Planet. Space Sci., 32, 975-984, 1984.
- Frank, L. A., On the extraterrestrial ring current during geomagnetic storms, J. Geophys. Res., 72, 3753-3767, 1967.
- Frank, L. A., Relationship of the plasma sheet, ring current, trapping boundary, and plasmopause near the magnetic equator and local midnight, J. Geophys. Res., 76, 2265-2275, 1971.
- Freeman, J. W.,  $K_p$  dependence of the plasma sheet boundary, J. Geophys. Res., 79, 4315-4317, 1974.

- Fukushima, N., and Y. Kamide, Partial ring current models for worldwide geomagnetic disturbances, Rev. Geophys. Space Phys., 11, 795-853, 1973.
- Gosling, J. T., D. J. McComas, M. F. Thomsen, S. J. Bame, and C. T. Russell, The warped neutral sheet and plasma sheet in the near-earth geomagnetic tail, J. Geophys. Res., 91, 7093-7099, 1986.
- Gussenhoven, M. S., D. A. Hardy, and W. J. Burke, DMSP/F2 electron observations of equatorward auroral boundaries and their relationship to magnetospheric electric fields, J. Geophys. Res., 86, 768-778, 1981.
- Gussenhoven, M. S., D. A. Hardy, and N. Heinemann, Systematics of the equatorial diffuse auroral boundary, J. Geophys. Res., 88, 5692-5708, 1983.
- Hamilton, D. C., G. Gloeckler, F. M. Ipavich, W. Studemann, B. Wilken, and G. Kremser, Ring current development during the great geomagnetic storm of February 1986, J. Geophys. Res., 93, 14343-14355, 1988.
- Harel, M., R. A. Wolf, P. H. Reiff, R. W. Spiro, W. J. Burke, F. J. Rich, and M. Smiddy, Quantitative simulation of a magnetospheric substorm, 1, Model logic and overview, J. Geophys. Res., 86, 2217-2241, 1981.
- Hau, L.-N., R. A. Wolf, G.-H. Voigt, and C. C. Wu, Steady state magnetic field configurations for the earth's magnetotail, J. Geophys. Res., 94, 1303-1316, 1989.
- Hedgecock, P. C., and B. T. Thomas, HEOS observations of the configuration of the magnetosphere, Geophys. J. R. Astr. Soc., 41, 391-403, 1975.
- Hilmer, R. V., and G.-H. Voigt, The effects of a magnetic  $B_y$  component on geomagnetic tail equilibrium, J. Geophys. Res., 92, 8660-8672, 1987.
- Hoffman, R. A., and P. A. Bracken, Magnetic effects of the quiet-time proton belt, J. Geophys. Res., 70, 3541-3556, 1965.
- Hoffman, R. A., and P. A. Bracken, Higher-order ring currents and particle energy storage in the magnetosphere, J. Geophys. Res., 72, 6039-6049, 1967.
- Hoffman, R. A., Particle and field observations from Explorer 45 during the December 1971 magnetic storm period, J. Geophys. Res., 78, 4771-4777, 1973.
- Hones, E. W., Jr., S.-I. Akasofu, S. J. Bame, and S. Singer, Poleward expansion of the auroral oval and associated phenomena in the magnetotail during auroral substorms, 2., J. Geophys. Res., 76, 8241-8257, 1971.
- Hones, E. W., Jr., Substorm processes in the magnetotail: Comments on 'On hot tenuous plasmas, fireballs, and boundary layers in the earth's magnetotail' by L. A. Frank, K. L. Ackerson, and R. P. Lepping, J. Geophys. Res., 82, 5633-5640, 1977.
- Hones, E. W., Jr., Transient phenomena in the magnetotail and their relation to substorms, Space Science Review, 23, 393-410, 1979.

- Hones, E. W., Jr., and K. Schindler, Plasma flow during substorms: A survey with IMP 6 and IMP 8 satellites, J. Geophys. Res., 84, 7155-7169, 1979.
- Hones, E. W., Jr., D. N. Baker, S. J. Bame, W. C. Feldman, J. T. Gosling, D. J. McComas, R. D. Zwickl, J. A. Slavin, E. J. Smith, and B. T. Tsurutani, Structure of the magnetotail at 220  $R_E$  and its response to geomagnetic activity, Geophys. Res. Lett., 11, 5-7, 1984.
- Horwitz, J. L., S. Mentee, J. Turnley, J. L. Burch, J. D. Winningham, C. R. Chappell, J. D. Craven, L. A. Frank, and D. W. Slater, Plasma boundaries in the inner magnetosphere, J. Geophys. Res., 91, 8861-8882, 1986.
- Huang, C. Y., L. A. Frank, and T. E. Eastman, Observations of plasma distributions during the coordinated data analysis workshop substorms of March 31 to April 1, 1979, J. Geophys. Res., 92, 2377-2384, 1987.
- Kaufman, R. L., Substorm currents: Growth phase and onset, J. Geophys. Res., 92, 7471-7486, 1987.
- Kivelson, M. G., S. M. Kaye, D. J. Southwood, The physics of plasma injection events, in Dynamics of the Magnetosphere, ed. by S.-I. Akasofu, 385-405, D. Reidel, Dordrecht, Holland, 1979.
- Kokobun, S., and R. L. McPherron, Substorm signatures at synchronous altitude, J. Geophys. Res., 86, 11265-11277, 1981.
- Kosik, J. C., A quantitative model of the ring current magnetic field region, accepted by J. Geophys. Res., March 1989.
- Lassen, K., Relation of the plasma sheet to the nighttime auroral oval, J. Geophys. Res., 79, 3857-3858, 1974.
- Lopez, R. E., A. T. Y. Lui, D. G. Sibeck, R. W. McEntire, L. J. Zanetti, T. A. Potemra, and S. M. Krimigis, The longitudinal and radial distribution of magnetic reconfigurations in the near-earth magnetotail as observed by AMPTE/CCE, J. Geophys. Res., 93, 997-1001, 1988.
- Lui, A. T. Y., C. D. Anger, and S.-I. Akasofu, The equatorward boundary of the diffuse aurorae and auroral substorms as seen by the ISIS 2 auroral scanning photometer, J. Geophys. Res., 80, 3603-3614, 1975.
- Lui, A. T. Y., D. Venkatesan, C. D. Anger, A.-I. Akasofu, W. J. Heikkila, J. D. Winningham, and J. R. Burrows, Simultaneous observations of particle precipitations and auroral emissions by the ISIS 2 satellite in the 19-24 MLT sector, J. Geophys. Res., 82, 2210-2226, 1977.
- Lui, A. T. Y., Estimates of current changes in the geomagnetotail associated with a substorm, Geophys. Res. Lett., 5, 853-856, 1978.
- Lui, A. T. Y., R. W. McEntire, and S. M. Krimigis, Evolution of the ring current during two geomagnetic storms, J. Geophys. Res., 92, 7459-7470, 1987.

- Lui, A. T. Y., R. E. Lopez, S. M. Krimigis, R. W. McEntire, L. J. Zanetti, and T. A. Potemra, A case study of magnetotail current sheet disruption and diversion, Geophys. Res. Lett., 15, 721-724, 1988.
- Lyons, L. R., and D. J. Williams, A source for the geomagnetic storm main phase ring current, J. Geophys. Res., 85, 523-530, 1980.
- Lyons, L. R., and D. J. Williams, Trapping regions and currents due to trapped particles, in Quantitative Aspects of Magnetospheric Physics, Geophysics and Astrophysical Monographs, 23, ed. by B. M. McCormac, 28-55, D. Reidel, Dordrecht, Holland, 1984.
- Mauk, B. H., and C. E. McIlwain, Correlation of Kp with the substorm-injected plasma boundary, J. Geophys. Res., 79, 3193-3196, 1974.
- Mauk, B. H., and C.-I. Meng, Plasma injection during substorms, Physica Scripta, T18, 128-139, 1987.
- McPherron, R. L., Substorm related changes in the geomagnetic tail: The growth phase, Planet. and Space Sci., 20, 1521-1539, 1972.
- McPherron, R. L., G. K. Parks, D. S. Colburn, and M. D. Montgomery, Satellite studies of magnetospheric substorms on August 16, 1968, 2. Solar wind and outer magnetosphere, J. Geophys. Res., 78, 3054-3061, 1973.
- McPherron, R. L., Magnetospheric substorms, Rev. Geophys. Space Phys., 17, 657-681, 1979.
- McPherron, R. L., and R. H. Manka, Dynamics of the 1054 UT March 22, 1979, substorm event: CDAW 6, J. Geophys. Res., 90, 1175-1190, 1985.
- Mead, G. D., and D. H. Fairfield, A quantitative magnetospheric model derived from spacecraft magnetometer data, J. Geophys. Res., 80, 523-534, 1975.
- Meng, C.-I., Variation of the magnetopause position with substorm activity, J. Geophys. Res., 75, 3252-3254, 1970.
- Meng, C.-I., and J. D. Mihalov, On the diamagnetic effect of the plasma sheet near 60 R<sub>E</sub>, J. Geophys. Res., 77, 4661-4669, 1972.
- Meng, C.-I., and K. A. Anderson, Magnetic field configuration in the magnetotail near 60 R<sub>E</sub>, J. Geophys. Res., 79, 5143-5153, 1974.
- Mihalov, J. D., and C. P. Sonnett, The cislunar geomagnetic tail gradient in 1967, J. Geophys. Res., 73, 6837-6841, 1968.
- Murayama, T., Spatial distribution of energetic electrons in the geomagnetic tail, J. Geophys. Res., 71, 5547-5557, 1966.
- Nagai, T., Observed magnetic substorm signatures at synchronous altitude, J. Geophys. Res., 87, 4405-4417, 1982.

- Nagai, T., D. N. Baker, and P. R. Higbie, Development of substorm activity in multiple-onset substorms at synchronous orbit, J. Geophys. Res., 88, 6994-7004, 1983.
- Nagai, T., Field-aligned currents associated with substorms in the vicinity of synchronous orbit 2. GOES 2 and GOES 3 observations, J. Geophys. Res., 92, 2432-2446, 1987.
- Ness, N., Review of magnetic field observations, in Earth's Magnetospheric Processes, ed. by B. M. McCormac, 189-199, D. Reidel, Dordrecht, Holland, 1972.
- Nishida, A., and K. Fujii, Thinning of the near-earth ( $10\sim 15 R_E$ ) plasma sheet preceding the substorm expansion phase, Planet. Space Sci., 24, 849-853, 1976.
- Olson, W. P., A model of the distributed magnetospheric currents, J. Geophys. Res., 79, 3731-3738, 1974.
- Olson, W. P., and K. A. Pfitzer, A quantitative model of the magnetospheric magnetic field, J. Geophys. Res., 79, 3739-3748, 1974.
- Parker, E. N., Newtonian development of the dynamical properties of ionized gases of low density, Phys. Rev., 107, 924-933, 1957.
- Patel, V. L., and A. J. Dessler, Geomagnetic activity and size of magnetospheric cavity, J. Geophys. Res., 71, 1940-1942, 1966.
- Pytte, T., and H. I. West, Jr., Ground-satellite correlations during presubstorm magnetic field configuration changes and plasma sheet thinning in the near-earth magnetotail, J. Geophys. Res., 83, 3791-3804, 1978.
- Roederer, J. G., in Dynamics of Geomagnetically Trapped Radiation, Physics and Chemistry in Space, 2, ed. by J. G. Roederer and J. Zahringer, 26-27, Springer-Verlag, New York, 1970.
- Rothwell, P. L., An empirical relationship between  $K_p$  and the tail lobe magnetic field, J. Geophys. Res., 91, 9012-9016, 1986.
- Rudneva, N. M., and Y. I. Feldstein, Distance to the subsolar point of the magnetosphere boundary as a function of the magnetic activity, Geomagn. Aeron. Engl. Tran., 10(5), 635-638, 1970.
- Russell, C. T., and K. I. Brody, Some remarks on the position and shape of the neutral sheet, J. Geophys. Res., 72, 6104-6106, 1967.
- Sauvaud, J. A., J. P. Treilhou, A. Saint-Marc, J. Dandouras, H. Reme, A. Korth, G. Kremser, G. K. Parks, A. N. Zaitzev, V. Petrov, L. Lazutine, and R. Pellinen, Large scale response of the magnetosphere to a southward turning of the interplanetary magnetic field, J. Geophys. Res., 92, 2365-2376, 1987.
- Skopke, N., A study of self-consistent ring current models, Cosmic Electrodyn., 3, 330-348, 1972.

- Sheehan, R. E., and R. L. Carovillano, Characteristics of the equatorward auroral boundary near midnight determined from DMSP images, J. Geophys. Res., **83**, 4749-4754, 1978.
- Shelley, E. G., R. G. Johnson, and R. D. Sharp, Plasma-sheet correction velocities inferred from electron-flux measurements at geosynchronous altitude, Radio Sci., **6**, 305-313, 1971.
- Sibeck, D. G., G. L. Siscoe, J. A. Slavin, R. P. Lepping, Major flattening of the distant geomagnetic tail, J. Geophys. Res., **91**, 4223-4237, 1986.
- Siscoe, G. L., and N. U. Crooker, On the partial ring current contribution to D<sup>st</sup>, J. Geophys. Res., **79**, 1110-1112, 1974.
- Siscoe, G. L., A quasi-self-consistent axially symmetric model for the growth of a ring current through the earthward motion from a pre-storm configuration, Planet. Space Sci., **27**, 285-295, 1979.
- Slater, D. W., L. L. Smith, and E. W. Klecknes, Correlated observations of the equatorward diffuse auroral boundary, J. Geophys. Res., **85**, 531-542, 1980.
- Slavin, J. A., B. T. Tsurutani, E. J. Smith, D. E. Jones, and D. G. Sibeck, Average configuration of the distant ( $\leq 220 R_E$ ) magnetotail: Initial ISEE-3 magnetic field results, Geophys. Res. Lett., **10**, 973-976, 1983.
- Slavin, J. A., E. J. Smith, D. G. Sibeck, D. N. Baker, R. D. Zwickl, and S.-I. Akasofu, An ISEE-3 study of average and substorm conditions in the distant magnetotail, J. Geophys. Res., **90**, 10875-10895, 1985.
- Smith, P. H., and R. A. Hoffman, Ring current particle distributions during the magnetic storms of December 16-18, 1971, J. Geophys. Res., **78**, 4731-4737, 1973.
- Sozou, C., and D. W. Windle, A self consistent ring current in the earth's dipole field, Planet. Space Sci., **17**, 375-387, 1969.
- Speiser, T. W., and N. F. Ness, The neutral sheet in the geomagnetic tail: Its motion, equivalent currents, and field line connection through it, J. Geophys. Res., **72**, 131-141, 1967.
- Speiser, T. W., and T. G. Forbes, Explorer 34 magnetic field measurements near the tail current sheet and auroral activity, Astrophys. and Space Sci., **77**, 409-442, 1981.
- Spiro, R. W., and R. A. Wolf, Electrodynamics of convection in the inner magnetosphere, in Magnetospheric Currents, Geophys. Monogr. Ser., **28**, ed. by T. A. Potemra, 247-259, AGU, Washington, D. C., 1984.
- Stening, R. J., and D. E. Winch, Night-time geomagnetic variations at low latitudes, Planet. Space Sci., **35**, 1523-1539, 1987.
- Stern, D. P., Tail modeling in a stretched magnetosphere 1. Methods and transformations, J. Geophys. Res., **92**, 4437-4448, 1987a.

- Stern, D. P., Modeling of the magnetosphere, Reviews of Geophysics, 25, No. 3, 523-527, 1987b.
- Su, S.-Y., and A. Konradi, Magnetic field depressions at the earth's surface calculated from the relationship between the size of the magnetosphere and the  $D^{st}$  values, J. Geophys. Res., 80, 195-199, 1975.
- Sugiura, M., B. G. Ledley, T. L. Skillman, and J. P. Heppner, Magnetospheric field distortions observed by Ogo 3 and 5, J. Geophys. Res., 76, 7552-7565, 1971.
- Sugiura, M., The ring current, in Critical Problems of Magnetospheric Physics, ed. by E. R. Dyer, 195-209, IUCSTP Secretariat c/o National Academy of Sciences, Washington, D. C., 1972.
- Sugiura, M., Quiet time magnetospheric field depression at 2.3-3.6  $R_E$ , J. Geophys. Res., 78, 3182-3185, 1973.
- Sugiura, M., and D. J. Poros, A magnetospheric field model incorporating the OGO 3 and 5 magnetic field observations, Planet. Space Sci., 21, 1763-1773, 1973.
- Takahashi, K., L. J. Zanetti, R. E. Lopez, R. W. McEntire, T. A. Potemra, and K. Yumoto, Disruption of the magnetotail current sheet observed by AMPTE/CCE, Geophys. Res. Lett., 14, 1019-1022, 1987.
- Tascione, T. F., H. W. Kroehl, R. Creiger, J. W. Freeman, Jr., R. A. Wolf, R. W. Spiro, R. V. Hilmer, J. W. Shade, and B. A. Hausman, New ionospheric and magnetospheric specification models, Radio Science, 23, 211-222, 1988.
- Tsurutani, B. T., J. A. Slavin, E. J. Smith, R. Okida, and D. E. Jones, Magnetic structure of the distant geotail -60 to -220  $R_e$ : ISEE-3, Geophys. Res. Lett., 11, 1-4, 1984.
- Tsyganenko, N. A., and A. V. Usmanov, Determination of the magnetospheric current system parameters and development of experimental geomagnetic field models based on data from IMP and HEOS satellites, Planet. Space Sci., 30, 985-998, 1982.
- Tsyganenko, N. A., Global quantitative models of the geomagnetic field in the cislunar magnetosphere for different disturbance levels, Planet. Space Sci., 35, 1347-1358, 1987.
- Vasyliunas, V. M., A survey of low-energy electrons in the evening sector of the magnetosphere with Ogo 1 and Ogo 3, J. Geophys. Res., 73, 2839-2884, 1968.
- Vasyliunas, V. M., Low energy particle fluxes in the geomagnetic tail, in Polar Ionosphere and Magnetospheric Processes, ed. by G. Skavli, 25-47, Gordon and Breach, New York, 1970.
- Voigt, G.-H., A three-dimensional analytical magnetospheric model with defined magnetopause, Z. Geophys., 38, 319-346, 1972.

- Voigt, G.-H., A mathematical magnetospheric field model with independent physical parameters, Planet. Space Sci., 29, 1-20, 1981.
- Voigt, G.-H., The shape and position of the plasma sheet in earth's magnetotail, J. Geophys. Res., 89, 2169-2179, 1984.
- Voigt, G.-H., Magnetospheric equilibrium configurations and slow adiabatic convection, in Solar Wind-Magnetospheric Coupling, ed. by Y. Kamide and J. A. Slavin, 233-273, Terra Scientific, Tokyo, 1986.
- Voigt, G.-H., and R. A. Wolf, Quasi-static magnetospheric MHD processes and the "ground state" of the magnetosphere, Reviews of Geophysics, 26, 823-843, 1988.
- Walker, R. J., An evaluation of recent quantitative magnetospheric magnetic field models, Rev. Geophys. Space Phys., 14, 411-427, 1976.
- Walker, R. J., Quantitative modeling of planetary magnetospheric magnetic fields, in Quantitative Modeling of Magnetospheric Processes, Geophys. Monogr. Ser., 21, ed. by W. P. Olson, 9-34, AGU, Washington, D. C., 1979.
- Walker, R. J., and D. J. Southwood, Momentum balance and flux conservation in model magnetospheric magnetic fields, J. Geophys. Res., 87, 7460-7466, 1982.
- Williams, D. J., and G. D. Mead, Nightside magnetosphere as obtained from trapped electrons at 1100 kilometers, J. Geophys. Res., 70, 3017-3029, 1965.
- Williams, D. J., Ring current composition and sources: An update, Planet. Space Sci., 29, 1195-1203, 1981.
- Williams, D. J., The earth's ring current: Present situation and future thrusts, preprint of review presented at the Sixth International Symposium on Solar-Terrestrial Physics, Toulouse, France, 30 June-5 July 1986.
- Williams, D. J., Ring current and radiation belts, Reviews of Geophysics, 25, No. 3, 570-578, 1987.
- Willis, D. M., and R. J. Pratt, A quantitative model of the geomagnetic tail, J. of Atmospheric and Terrestrial Physics, 34, 1955-1976, 1972.
- Winningham, J. D., F. Yasuhara, S.-I. Akasofu, and W. J. Heikkila, The latitudinal morphology of 10-eV to 10-keV electron fluxes during magnetically quiet and disturbed times in the 2100-0300 MLT sector, J. Geophys. Res., 80, 3148-3171, 1975.
- Wolfe, J. H., R. W. Silva, and M. A. Myers, Observations of the solar wind during the flight of Imp 1, J. Geophys. Res., 71, 1319-1340, 1966.



Appendix G

## ABSTRACT

### PARTICLE FLUXES AT GEOSYNCHRONOUS ORBIT AND IN THE PLASMA SHEET DURING A SUBSTORM: IMPLICATIONS FOR ADIABATIC CONVECTION

by

Bonnie A. Hausman

Energetic particles are injected into the geosynchronous-orbit region of the Earth's magnetosphere during events called magnetospheric substorms. This injection process has been investigated using the Magnetospheric Specification Model (MSM), which is a set of computer algorithms that is being developed for the U.S. Air Force. Using time-dependent models of the magnetospheric electric and magnetic fields, the code follows the ExB and gradient/curvature drifts of ions and electrons of differing energies from each grid point within the modeling region. With allowance made for precipitation loss, the flux at each grid point is calculated from the initial and boundary condition fluxes, which are estimated from other observations.

We used the data from the geomagnetic storm of March 22, 1979 to test the model's accuracy. Particle populations at the tailward boundary were estimated from ISEE-1 and -2 observations in the plasma sheet and the requirement of force balance in the magnetotail. The magnetic- and electric-field model outputs were tailored to match the data for the event. Major results of comparing predicted and observed geosynchronous particle fluxes are as follows:

1. The model's predictions as to when freshly injected ions and electrons should

arrive at various locations at the geosynchronous orbit are in good agreement with observations.

2. However, the model tends to overestimate the magnitudes of the geosynchronous fluxes, unless special algorithms are invoked to limit the predicted values. If one assumes adiabatic drift of particles from the plasma sheet to the geosynchronous orbit region, with reasonable allowance for precipitation loss, one obtains substorm fluxes that are about a factor of ten too high. This implies the existence of a powerful loss process that operates during a substorm on particles drifting between the middle plasma sheet and geosynchronous-orbit region.

## TABLE OF CONTENTS

ABSTRACT .....	ii
ACKNOWLEDGEMENTS.....	iv
TABLE OF CONTENTS .....	v
I. INTRODUCTION	
A. General Magnetosphere Description .....	1
B. Substorms .....	5
C. Ring Current Injection .....	8
D. Models and Results .....	10
II. ADIABATIC MODELING OF THE INNER MAGNETOSPHERE	
A. Assumptions Used and Region Modeled .....	11
III. STRUCTURE OF THE MAGNETOSPHERIC SPECIFICATION MODEL	
A. General Philosophy .....	15
B. Electric Field Model .....	17
C. Magnetic Field Model .....	22
D. Particle Tracer Model .....	25
E. Boundary Plasma Condition .....	29
F. Initial Plasma Condition .....	35
IV. TESTING THE MODEL USING THE CDAW6 EVENT	
A. General Description of Event .....	38
B. Model Inputs .....	40
1. Magnetic Field Model .....	40
2. Electric Field Model .....	42
3. Boundary Plasma Condition .....	44
4. Initial Plasma Condition .....	47

C. Model Results .....	52
D. Interpretation and Implication .....	56
V. CONCLUSION	
A. Summary of Results .....	62
B. Possibilities for Further Study .....	63
APPENDIX A: Derivation of Electron Flux in Terms of Model Parameters .....	64
REFERENCES .....	66

## I. INTRODUCTION

### A. General Magnetosphere Description

The interaction of the supersonic solar wind with the earth's intrinsic dipole magnetic field defines a region of space called the magnetosphere, as shown in figure 1.1. The force of the solar wind is balanced by the earth's magnetic field and the pressure of the magnetospheric plasma at the magnetopause. Upstream, a collisionless shock is formed, the bow shock. At this point, the solar wind becomes thermalized and subsonic, and it flows around the magnetopause as magnetosheath plasma. Also associated with the solar wind-magnetosphere interaction are a number of boundary layers which contain magnetosheath-like particles with flows in the anti-sunward direction such as the low latitude boundary layer, polar cusp, and plasma mantle.

The solar wind plasma is considered to be a perfect conductor so that the interplanetary magnetic field (IMF) is carried outward from the sun with the plasma (frozen in flux). At the magnetopause these field lines can merge with those of the earth's magnetic field, with the rate of magnetic merging depending on the orientation of the IMF and being strongest when the fields are anti-parallel (southward IMF). These field lines and their associated plasma are then swept back by streaming plasma until they reconnect in the distant nightside tail region. The oppositely-directed magnetic field from the north and south poles are separated by a 'neutral' sheet where the magnetic field is small; the neutral sheet contains a cross-tail current associated with the magnetic field reversal. The neutral sheet is surrounded by a region of closed field lines which contain hot plasma called the plasma sheet. The magnetic reconnection in the magnetotail energizes particles from the lobe and mantle and accelerates them earthward within the plasma sheet. The bulk flow of the plasma across open field lines implies an  $E = -v \times B$  electric field oriented in the dawn to dusk direction. This electric field gives rise to a sunward plasma drift in the inner magnetosphere along the closed field lines of the

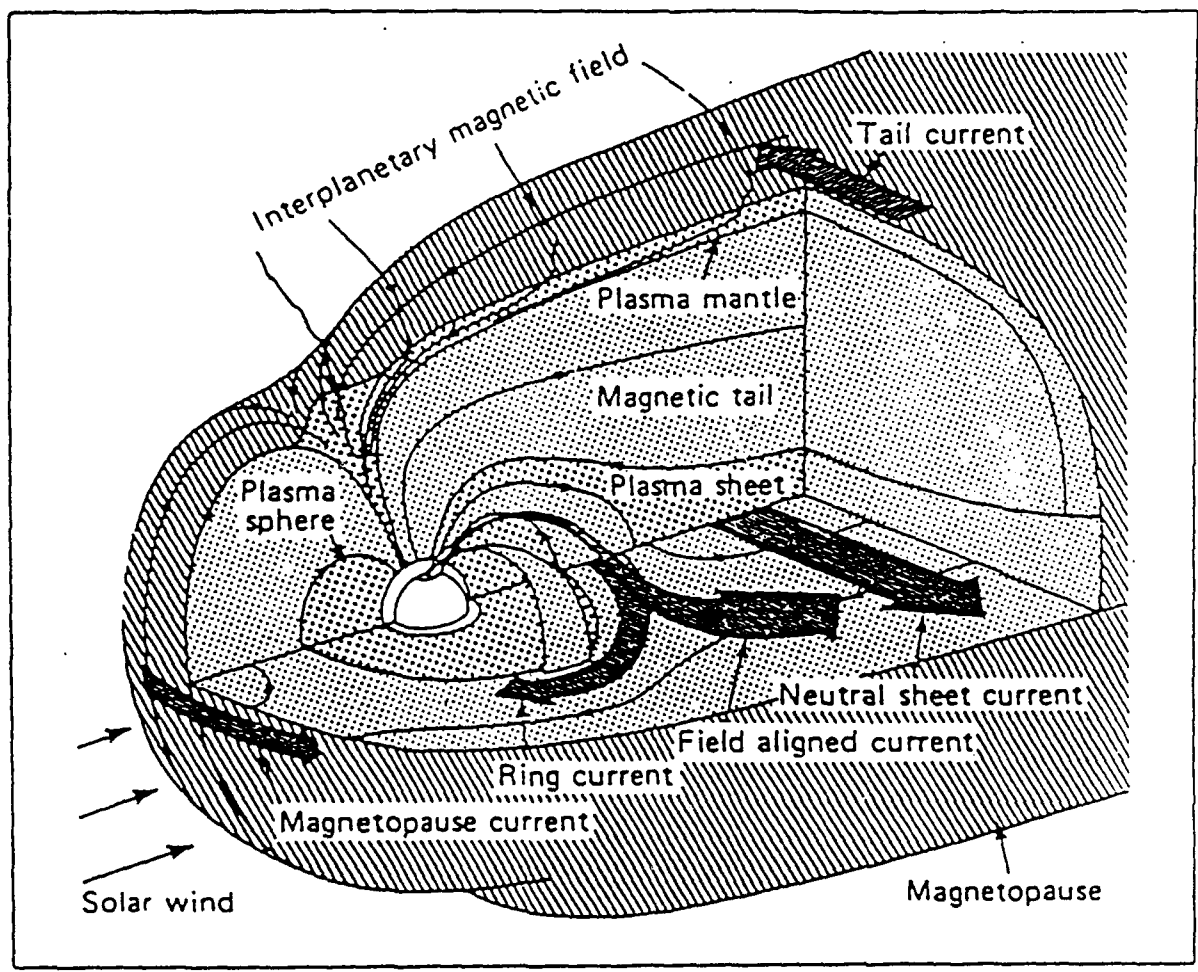


Figure 1.1 Cartoon of major magnetospheric plasma regions and currents.

plasma sheet. Other plasma which has not been trapped on closed field lines will simply be lost down the tail.

Within the closed portion of the magnetosphere the plasma drifts are a complicated pattern resulting from competing processes. The magnetic field becomes more dipolar and stronger close to the earth, and the plasma in the inner magnetosphere also gradient-curvature drifts along with the  $E \times B$  drift. This drift, however, separates the particles, with the electrons drifting towards dawn and ions towards dusk. As the higher energy particles gradient-curvature drift more quickly, there is an energy diffusive boundary called the Alfvén layer, with the lower energy particles drifting closer to the earth than the higher energy ones. However, the picture isn't this simple. If the particles precipitate at the strong pitch angle scattering rate (particles scattered in and out of the loss cone many times in one bounce), there exists a precipitation flow boundary, at which the convection time scales of particles are equal to the precipitating time scales so that particles are precipitated and do not enter further into the magnetosphere regardless of their drift orbit (Southwood and Wolf, 1978). This is also an energy diffusive boundary as more energetic particles have shorter lifetimes and are depleted upstream. Also, the electrons are precipitated at a higher rate because the more massive ions have a longer bounce time. There is an additional eastward drift due to the corotation electric field; which adds to the gradient/curvature drifts of the electrons. The ions gradient/curvature drift in the opposite sense, leading to a far more complicated drift pattern.

Assuming that field lines are equipotentials, the magnetospheric convection electric fields can be mapped into the ionosphere with the resulting ionospheric electric field normal to these equipotentials as shown in Figure 1.2(b) (Chiu et. al., 1984). The horizontal ionospheric currents shown in Figure 1.2(c) are divided into 2 components, the Pedersen current along the direction of the electric field, and the Hall current. The Hall and Pedersen currents result from the fact that the ionospheric plasma is far denser



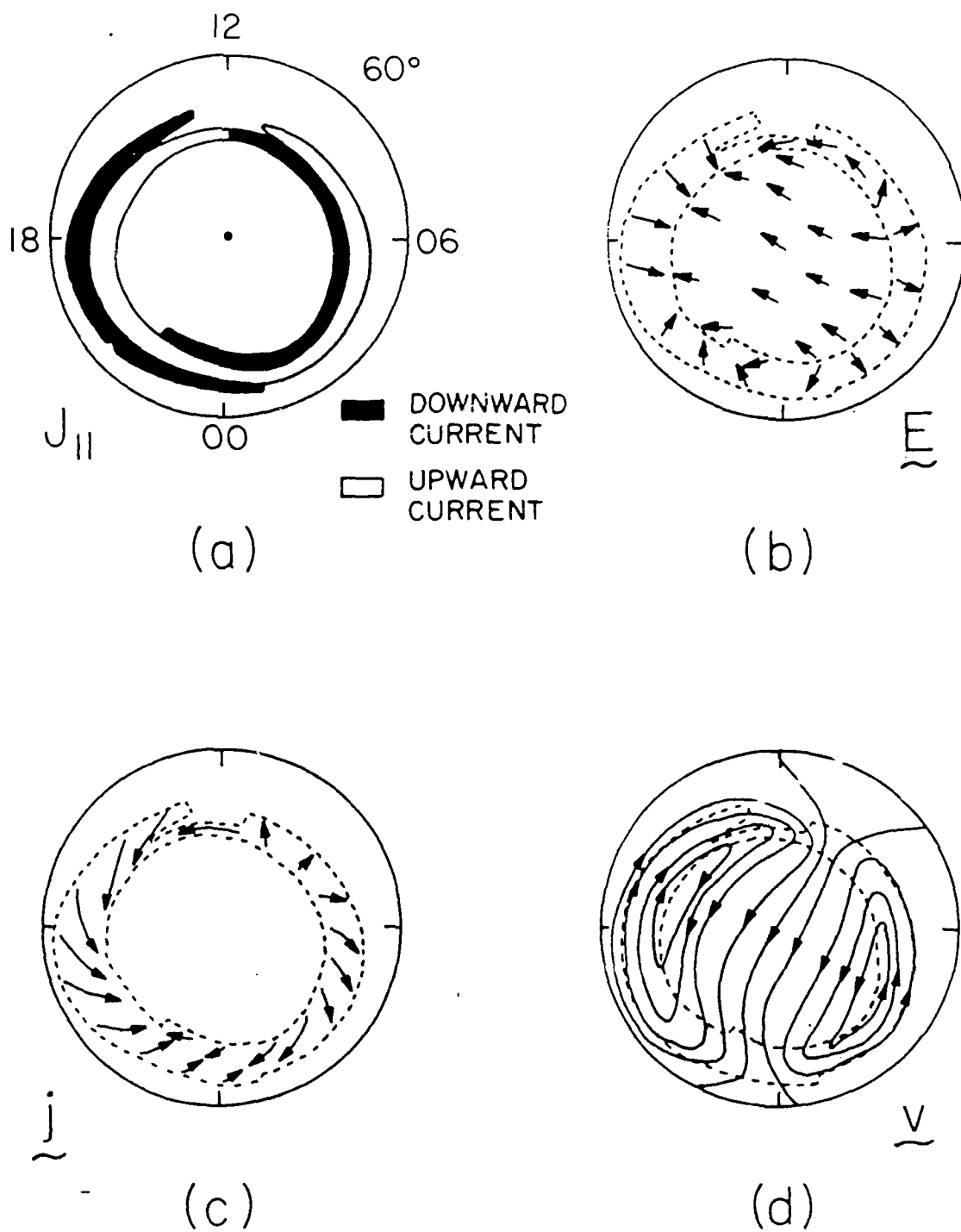


Figure 1.2 Sketch of the typical patterns of (a) Birkeland current (Iijima and Potemira, 1978), (b) electric fields, (c) horizontal ionospheric current, and (d)  $E \times B$ -drift velocity. Polar cap currents are not shown.

than that of the magnetosphere and the drifts are no longer collisionless. The collisions, principally between the charged particles and the ionospheric neutrals, give rise to different  $E \times B$  drift rates for the electrons and ions and a Hall current that flows in the  $-E \times B$  direction; the collisions also result in a Pedersen current that flows in the direction of  $E$ . The average location of sheets of magnetic-field-aligned currents is shown in Figure 1.2(a). The poleward Region 1 currents flow down into the ionosphere at dawn and out of the ionosphere at dusk. These field lines map generally to outer-magnetospheric field lines or at times to the solar wind. The Region 2 currents flow up from the dawn ionosphere and down into the dusk ionosphere, along field lines connected to the inner plasma sheet.

#### B. Substorms

Variations in solar wind velocity or density or both can produce time changes in the solar wind-magnetosphere interaction. One dramatic result is the magnetospheric substorm. Even the definition of what constitutes a substorm has been disputed; I have used the definition of Rostoker et al. (1980), which seemed to represent a consensus and extended that made earlier by Akasofu (1968). Rostoker et al. (1980) named the following defining characteristics.

- 1) The onset is signalled by explosive increases in auroral luminosity in the midnight sector.
  - 2) The entire substorm encompasses the time during which the current in the auroral electrojets increases and then returns to the previous level. This is typically 1-3 hours.
  - 3) A substorm may include one or more intensifications of the westward electrojet; each associated with a Pi2 micropulsation burst and westward travelling surge.
  - 4) The region of discrete auroras moves poleward and westward (poleward bulge).
  - 5) The bulge reaches the maximum latitudinal extent and then begins to retreat
- The start of the Pi2 bursts mark the expansion phase, with the recovery phase beginning

when the poleward bulge has reached its maximum.

The exact mechanisms involved in the substorm are unclear. Two major models center on the boundary layer and near-earth magnetic reconnection. The x-line magnetic reconnection models base their interpretation on data observed in the magnetotail plasma sheet rather than ionospheric phenomena and they constitute the most popular opinion at the moment. The first comprehensive review of this theory is by Russell et al. (1973). The model proposes that there exists a growth phase during which magnetic flux from the dayside magnetosphere is transferred to the tail and stored there. As this phase progresses, the magnetic field in the near tail increases and the currents strengthen and move earthward. The plasma sheet thins as the magnetic field becomes more and more stretched. The expansion phase begins when a near-earth neutral line forms. The neutral line then moves down the tail and the plasma sheet re-expands. This scenario was refined by Hones (1979); in his picture, a series of field lines undergoes reconnection during the growth phase and form a plasmoid, a collection of unconnected field lines which eventually moves down the tail carrying the plasma with it. Figure 1.3 shows Hones' cartoon sequence of substorm evolution (Hones, 1979).

One boundary layer model (Rostoker et al., 1987) claims that the central plasma sheet never exhibits tailward flows even during substorms. Instead, the essential dynamics of the substorm occur in the plasma sheet boundary layer. They theorize that an increase in energy from the solar wind increases momentum shear between the sunward flowing central plasma sheet and the anti-sunward low-latitude boundary layer. The intense discrete aurora are caused by the growth of a Kelvin-Helmholtz instability between the two regions. Another variation of the boundary layer model, the thermal catastrophe model (Smith et al., 1986; Goertz et al., 1989), proposes that the resonant absorption of Alfvén waves by the plasma sheet boundary layer is a source of energy to heat the plasma sheet particles. At a critical point, which depends on the incident wave

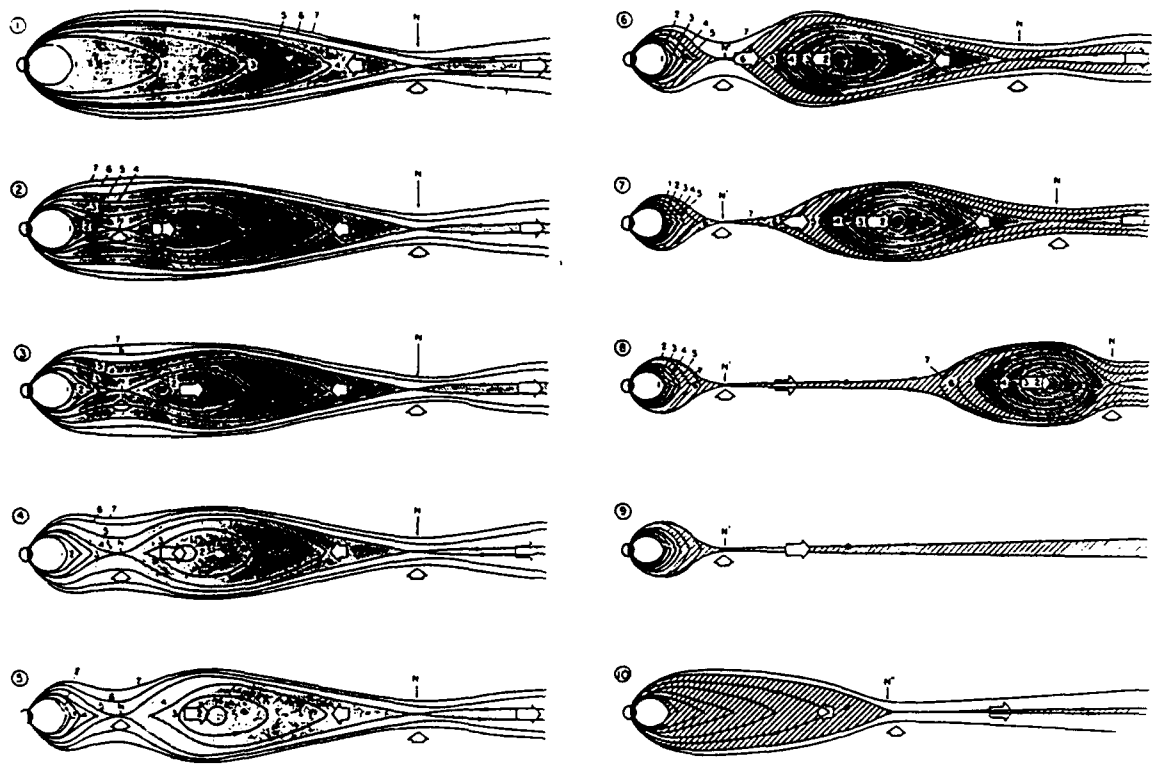


Figure 1.3 Schematic representation of changes of the magnetotail plasma sheet that are thought to occur during substorms.

spectra and amplitudes, the heating becomes too rapid for the excess energy to be convected to the central plasma sheet so that the plasma sheet temperature rises dramatically and the substorm expansion phase begins.

Two other models (Kan et al., 1988; Rothwell et al., 1988) concentrate on the role of the ionosphere, and assume that substorm onset is a consequence of enhanced magnetospheric convection. Kan has developed an Alfvén-wave reflection model which proposes that enhanced magnetosphere-ionosphere coupling creates Alfvén waves moving toward the ionosphere. These waves, which are reflected by the ionosphere and bounce between conjugate hemispheres, propagate the convection electric field between the ionosphere and magnetosphere. As convection increases, the field-aligned currents carried by these waves increases and leads to the ionospheric signature of substorm onset: a sudden brightening of an auroral arc.

### C. Ring Current Injection

One of the most dramatic signals that a magnetic storm is in progress is the large decrease in the magnetic field at low latitudes caused by an increase in the strength of the ring current. Using geosynchronous satellite data, DeForest and McIlwain (1971) noted the appearance of hot magnetospheric particles at geosynchronous orbit after substorms. Depending on the location of the satellite, frequently the most energetic ions arrived at the satellite first, with lower energies arriving later. There are several theories to explain how the magnetospheric particles are injected earthward. McIlwain (1974), using empirical models of the electric and magnetic fields, was able to reproduce the energy dispersion by injecting particles near local midnight then following their subsequent  $E \times B$  and gradient/curvature drift. The energy dispersion is due to the fact that higher energy particles gradient/curvature drift faster. The particles are energized by some unidentified process and arrive at an 'injection boundary' at substorm onset. After the injection the particles drift in the quasi-static convection electric and magnetic fields.

In contrast, the Alfvén layer models (Kaye and Kivelson, 1979) theorize that an enhanced convection electric field moves the previous quiet time Alfvén boundaries earthward to produce enhanced fluxes at geosynchronous orbit. When the boundary shifts the satellite will see an increase in some energy channels but not all because the boundary itself does not contain all energies. However, the model does not explain dispersionless injections and is sensitive to the choice of initial conditions assumed for the magnetospheric electric field.

Moore et al. (1981) have used results from 2 geosynchronous satellites to modify the Alfvén-layer model. They have included the effects of particle loss by precipitation and conclude that the boundary motion is actually the precipitation flow boundary. The injection is from a compression wave produced by a partial tail collapse outside of synchronous orbit. The wave front interacts with the precipitating flow boundary to push it earthward and the satellite detects the hot Maxwellian plasma sheet particles behind the boundary. The steepening of this wave as it moves toward less dense plasma could account for the energy dispersionless structure of the observed injection.

Another theory of ring current generation is simply that an enhanced convection electric field drives the plasma sheet inward on the nightside. Harel et al. (1981a, 1981b), using the Rice Convection Model, have shown that the inner edge of the higher energy ions drifts earthward more quickly at dusk than the lower energy ions or the electrons. This results in the energy dispersion at geosynchronous orbit as observed by DeForest and McIlwain without having to include any other mechanism. However, Wolf (1987) points out that any theory needs to take into account the large transient electric fields which occur during a substorm. These include the westward induction and potential electric fields created by the collapse of the midnight-region magnetic field lines at substorm onset. The collapse would also result in an eastward potential electric field across the earthward edge of the collapse region because the inner edge of the plasma

sheet is closer to the earth at midnight. It is also important to consider the ionospheric response to these fields through changes in the structure and intensity of the Birkeland currents.

#### D. Models and Results

One objective of computer simulation is, of course, to use theory to attempt to replicate reality. Substorms represent a challenge to accurately model the time-dependent changes of the electric and magnetic fields, which in turn change charged particle distributions, which further change the electric and magnetic fields and so on. The simulations should either match the data or help us to understand the physical process if they don't. Often there are several competing processes and no simple model can completely explain the results. The Magnetospheric Specification Model represents an attempt to simplify the self-consistent calculations of the Rice Convection Model. It is not a smaller version of the Rice Convection Model, but a new program. A description of the model, a comparison of the output to data and the implications are discussed in the following chapters.

## II. ADIABATIC MODELING OF THE INNER MAGNETOSPHERE

### A. Assumptions Used and Region Modeled

In the Magnetospheric Specification Model, detailed magnetospheric-particle traces are performed in a modeling region that lies within the inner and middle magnetosphere. Specifically this includes 1) on the dayside, the region earthward and equatorward of the magnetopause and its boundary layers, and 2) on the nightside, the inner part of the plasma sheet. The boundaries of the modeling region are parallel to the magnetic field. The following assumptions are made:

- 1) The convection velocities are substantially subsonic.
- 2) The bounce time for plasma sheet particles is short compared to the convection time.
- 3) The plasma sheet particles have an isotropic distribution.
- 4) The magnetic- and electric-field configurations can be estimated with sufficient accuracy from pre-computed B-field and E-field models.

From observed data (Huang and Frank, 1986), the first 3 assumptions are reasonable for the inner plasma sheet particles. The fourth assumption frees us from the difficult problem of trying to model the three dimensional convection and the magnetic structure simultaneously.

Given assumption 1, the inertial term in the momentum equation becomes negligible and we can neglect the propagation of MHD waves in the magnetosphere. The bulk motion of the plasma is then just the  $E \times B$  and gradient and curvature drifts. Although the formulas for bounce-averaged drift have been derived elsewhere (Northrup, 1963, Roederer, 1970), the following derivation follows the one by Dr. R. A. Wolf (1988).

If we assume that the particle's drift perpendicular to the field lines is much slower than the bounce along the field line (assumption 2), we can derive a bounce-averaged drift formula for the motion of the intersection of the particle's guiding center field line



with some reference surface (Roederer, 1970). Neglecting the dipole tilt of the magnetic field, we define the surface where  $\mathbf{B}$  is always perpendicular to the field lines as the magnetic equatorial plane. For ease of calculation, we choose to follow the motion of the intersection of the field line with this plane so that

$$\bar{\mathbf{B}}_e(\bar{\mathbf{x}}_e) = B_e(\bar{\mathbf{x}}_e) \hat{z}$$

Because of the slow drift time we can, for a given magnetic field configuration, define the kinetic energy of a particle of charge  $q$  and given adiabatic invariants  $\mu$  and  $J$  as

$$E_k = \frac{1}{2} m v_{\perp}^2 + \frac{1}{2} m v_{\parallel}^2 = E_k(\bar{\mathbf{x}}_e, \mu, J) \quad (2.1)$$

where  $\bar{\mathbf{x}}_e$  = equatorial crossing point of the magnetic field line

The rate of change in the total energy ( $E_T$ ) over time is

$$\frac{dE_T(\mathbf{x}, t)}{dt} = \frac{\partial E_T}{\partial t} + (\bar{\mathbf{v}} \cdot \nabla) E_T \quad (2.2)$$

Assuming that the particle drifts in a static electric and magnetic field, the total energy is conserved such that

$$(\bar{\mathbf{v}} \cdot \nabla) E_T = 0 \quad (2.3)$$

The total energy stored within the magnetic and electric fields includes the kinetic energy given by equation 2.1 and the electrostatic potential energy  $qV$ . The energy equation becomes

$$(\bar{\mathbf{v}}_{EBe} + \bar{\mathbf{v}}_{GCe}) \cdot \nabla_e [ qV(\bar{\mathbf{x}}_e) + E_k(\bar{\mathbf{x}}_e, \mu, J) ] = 0 \quad (2.4)$$

where  $\mathbf{v}_{EBe}$  = equatorial  $\mathbf{E} \times \mathbf{B}$  drift velocity

$\mathbf{v}_{GCe}$  = bounce averaged gradient/curvature drift velocity

$V$  = electrostatic potential at  $\mathbf{x}_e$

$\nabla_e$  = 2 dimensional gradient operator in the equatorial plane

The assumption that particles  $\mathbf{E} \times \mathbf{B}$  drift is equivalent to the assumption of a perfect conductor.  $\mathbf{E} \times \mathbf{B}$ -drifting particles remain frozen to the field line and do not diffuse. Since the bounce-averaged  $\mathbf{E} \times \mathbf{B}$ -drift velocity follows the movement of the field lines to

which these particles are attached, the drift requires no average of a particle's motion over a bounce length. On the magnetic equatorial plane the motion becomes

$$\bar{\mathbf{E}} + \bar{\mathbf{v}} \times \bar{\mathbf{B}} = 0 \quad (2.5)$$

$$\mathbf{v}_\perp = \mathbf{v}_{E\bar{B}_e} = \frac{\bar{\mathbf{E}}_e \times \mathbf{B}(\bar{\mathbf{x}}_e) \hat{\mathbf{z}}}{|\mathbf{B}(\bar{\mathbf{x}}_e)|^2} = \frac{\hat{\mathbf{z}} \times \nabla_e V_e(\bar{\mathbf{x}}_e)}{\mathbf{B}(\bar{\mathbf{x}}_e)} \quad (2.6)$$

For equation 2.4 to be satisfied for any arbitrary  $V_e(\mathbf{x}_e)$  including  $V_e(\mathbf{x}_e) = 0$

$$\bar{\mathbf{v}}_{GCe} \cdot \nabla_e E_k(\bar{\mathbf{x}}_e, \mu, J) = 0 \quad (2.7)$$

$$\bar{\mathbf{v}}_{GCe} = C \hat{\mathbf{z}} \times \nabla_e E_k(\bar{\mathbf{x}}_e, \mu, J) \quad (2.8)$$

Subtracting equation 2.7 from equation 2.4, using the  $\mathbf{v}_{E\bar{B}_e}$  and  $\mathbf{v}_{GCe}$  formulas, and solving for the scalar  $C$ , we obtain the drift formula

$$\bar{\mathbf{v}}_{GCe} = \frac{\hat{\mathbf{z}}}{q} \frac{\nabla_e E_k(\bar{\mathbf{x}}_e, \mu, J)}{|\mathbf{B}(\bar{\mathbf{x}}_e)|} \quad (2.9)$$

Under the assumption of lossless convection, we can derive an invariant density  $\eta$ , the number of particles per unit magnetic flux. The law of conservation of particles mapped to the equatorial plane becomes

$$\frac{\partial(\eta B_e)}{\partial t} + \nabla_e \cdot (\eta B_e \bar{\mathbf{v}}_e) = 0 \quad (2.10)$$

where  $\mathbf{v}_e = \mathbf{v}_{E\bar{B}_e} + \mathbf{v}_{GCe}$

Using equations 2.6 and 2.9 and rearranging gives

$$B_e \left( \frac{\partial}{\partial t} + \bar{\mathbf{v}}_e \cdot \nabla_e \right) \eta + \eta \frac{\partial B_e}{\partial t} + \eta \nabla_e \cdot [\bar{\mathbf{E}}_e \times \hat{\mathbf{z}} + \nabla_e E_k \times \hat{\mathbf{z}}] = 0 \quad (2.11)$$

using Faraday's law and vector identities yields

$$\left[ \frac{\partial}{\partial t} + \bar{\mathbf{v}}_e \cdot \nabla_e \right] \eta = 0 \quad (2.12)$$

so that the number of particles per unit magnetic flux is conserved.

Assuming adiabatic compression of an ideal monatomic gas and an isotropic particle

distribution with no significant energy loss during the scattering, the kinetic energy per particle (with  $\gamma = 5/3$ ) is

$$E_k(\bar{x}_e, \lambda) = \lambda [\Xi(\bar{x}_e)]^{-2/3} \quad (2.13)$$

where  $\Xi(x_e)$  is an effective confining volume and  $\lambda$  is invariant along the drift path.

From equation 2.12 for the invariant density, we know that an assembly of particles will forever occupy the same unit of magnetic flux as the one with which they initially started. If  $\eta$  is conserved and the number of particles is conserved (no loss), then the magnetic flux contained in the confining volume must be conserved. By defining our initial confining volume to be one unit of magnetic flux, the effective confining volume is then simply the flux tube volume per unit magnetic flux. The kinetic energy per particle is then

$$E_k(\bar{x}_e, \lambda) = \lambda \left[ \int \frac{ds}{B} \right]^{-2/3} \quad (2.14)$$

where  $\lambda$  is invariant along the drift path. The bounce average gradient-curvature drift formula becomes (Wolf, 1988)

$$\bar{v}_{GCe} = \frac{\lambda \hat{z} \times \nabla_e \left[ \int \frac{ds}{B} \right]^{-2/3}}{qB(\bar{x}_e)} \quad (2.15)$$

### III. STRUCTURE OF THE MAGNETOSPHERIC SPECIFICATION MODEL

#### A. General Philosophy

The Magnetospheric Specification Model was developed as an on-line, real-time program for use in the Space Forecast Center operated by the Air Weather Service of the U.S. Air Force. It is intended to help the Center personnel to perform their mission to provide information, particularly during magnetospheric disturbances, to "customers" who operate spacecraft. The output of the model includes (but is not limited to):

- 1) Fluxes of electrons and ions in the inner plasma sheet and the geosynchronous orbit region.
- 2) Energy fluxes and characteristic energies of the electrons and ions precipitated into the ionosphere.

The most sophisticated type of theoretical inner-magnetosphere/ionosphere model is exemplified by the Rice Convection Model (RCM). However, the Air Force requirement for near-real time data output and the relatively slow run-time of the RCM made it unsuitable for Air Force operational use. Also, the RCM input parameters require some scientific experience which may not be available to the Forecast Personnel.

With these constraints in mind we dropped the self-consistent treatment and have separate ionospheric electric field and magnetospheric magnetic field models to trace particles in the magnetosphere equatorial plane (Figure 3.1). The magnetic field model provides the mapping between the two regions with the condition that the equatorward edge of the auroral zone in the ionosphere maps to the inner edge of the plasma sheet in the magnetospheric equatorial plane. To optimize the accuracy of the modelled geosynchronous fluxes, geosynchronous orbit data will be used to adjust plasma and initial boundary conditions. A specific description of the model and plasma regions follows.

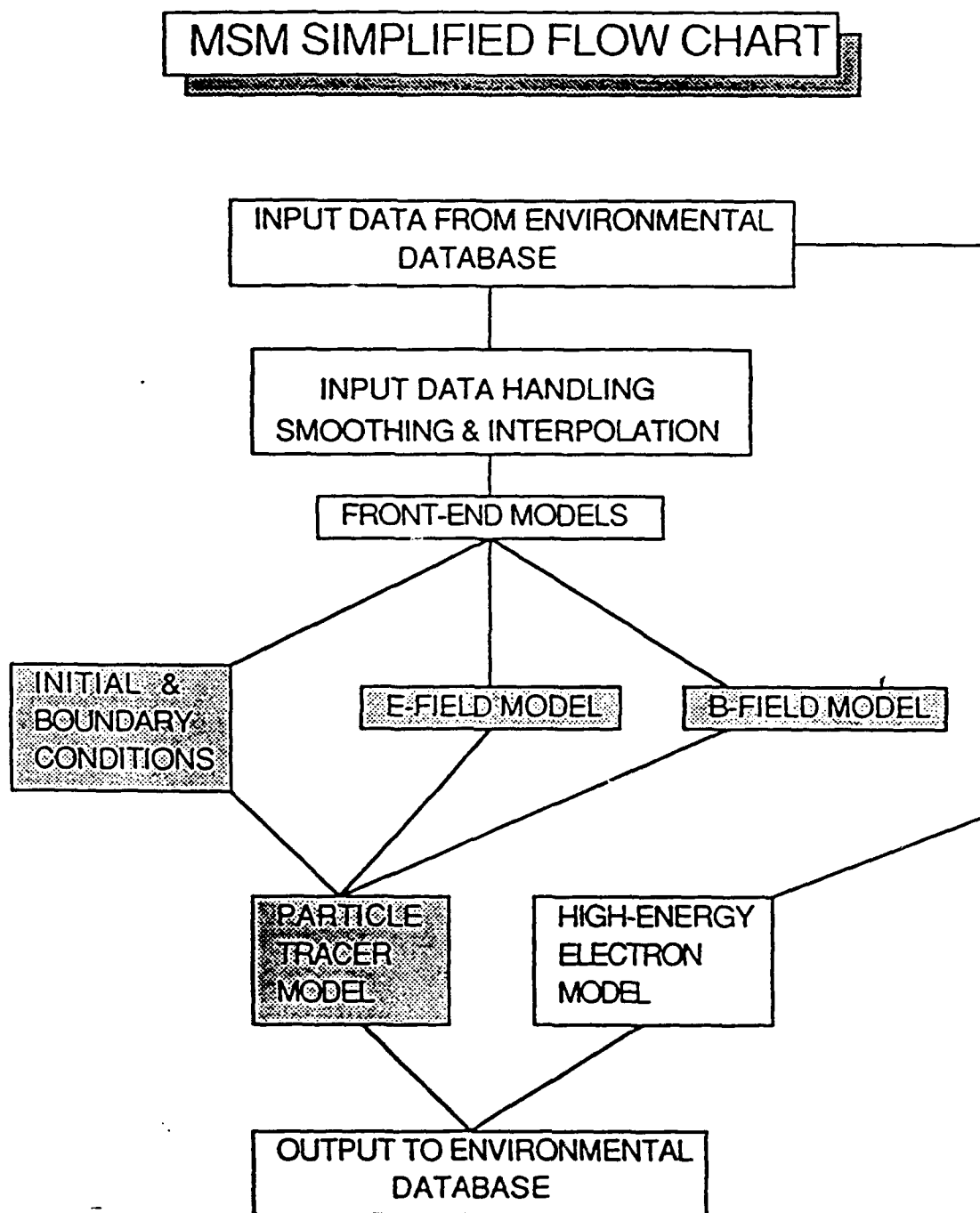


Figure 3.1 Structure of the Magnetospheric Specification Model.

## B. Electric Field Model

The electric field model was designed and implemented by Dr. R. A. Wolf. The equations and figures in this section are from analysis he has done on ionospheric electric field and from runs of the Rice Convection Model with Dr. R. W. Spiro. The model is divided into 4 regions as shown in Figure 3.2. Inputs include cross polar cap potential, polar cap pattern type, and the latitude of the equatorward edge of the diffuse aurora at midnight. The calculations are done in several steps. First, the boundary of each region is determined. Then the potential distribution on each boundary is calculated. The potential distribution is calculated in each region, in a sequence that guarantees continuity of the normal derivative  $\partial V/\partial n$  at each boundary.

### Boundary Calculation

1) Boundary 3, which is the equatorward edge of the main auroral-electric field region (also known as the "shielding layer"), is located according to the following assumptions

- i) it coincides with the equatorward edge of auroral precipitation at local midnight;
- ii) it is  $1^\circ$  higher in latitude at local dawn and dusk than at local midnight;
- iii) for local noon, we add the offset determined by Gussenhoven et al (1983) with "Kp" estimated from the midnight latitude.

The total potential drop across the boundary is calculated from the observed motion of the equatorward edge of the aurora.

2) Boundary 2 is approximately the equatorward edge of the region 1 currents and corresponds to the outer boundary of the particle-trace calculation. Mapped to the magnetospheric equatorial plane, this boundary maps to:

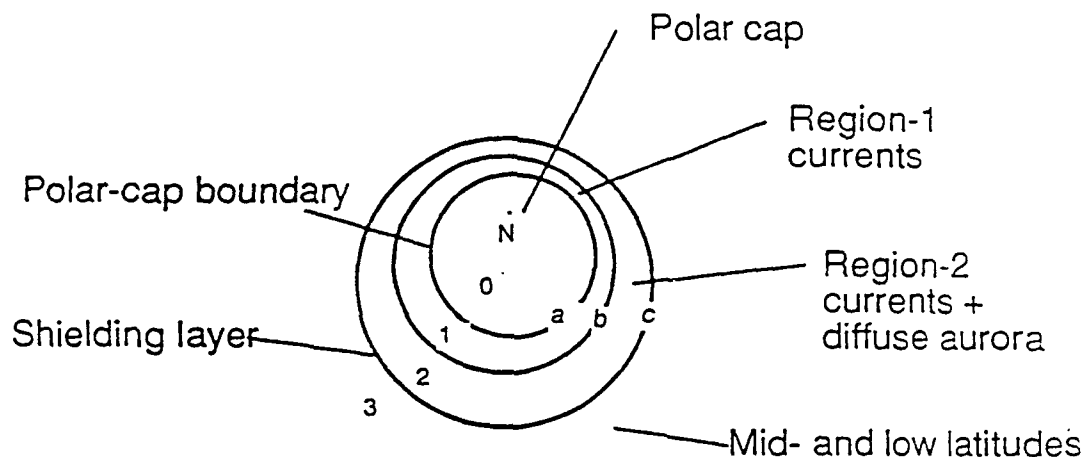
0.95  $r_{\text{standoff}}$  at noon

1.40  $r_{\text{standoff}}$  at dawn and dusk

2.00  $r_{\text{standoff}}$  at midnight

## ELECTRIC-FIELD MODEL

### REGIONS:



### APPROACHES USED IN THE VARIOUS REGIONS:

- Region 0: Heppner/Maynard/Rich empirical model, with adjustable total potential drop and polar-cap size. Different patterns are used for different IMF orientations.
- Region 3: Analytic formula based on experience with RCM and comparisons with data. Most important input parameter is the penetration potential, which is estimated from the motion of the equatorward edge of the diffuse aurora.
- Region 2: Analytic form representing classic sunward flow region of auroral zone.
- Region 1: Fitting formula that fits smoothly to regions 0 and 2. Total potential drop across region 1 estimated from Heppner/Maynard/Rich patterns.

Figure 3.2 Electric-Field model regions.

Using the field-line traces from each magnetic field mark time, the ionospheric latitudes of the noon, dawn, dusk and midnight points are located and are fit to an ellipse, which is described by four parameters A, B, DX, and DY; the first two being the axes measured noon-midnight and dawn-dusk, and the last two locating the center of the ellipse relative to the geomagnetic pole. To calculate the potential across the boundary, we use the Heppner-Maynard (H-M) empirical model (Heppner and Maynard, 1987; Rich and Maynard, 1989). The choice of pattern type depends on the IMF direction and strength. The seven classifications are:

<u>Model Parameter</u>	<u>H-M designation</u>	<u>IMF</u>
1	A	$B_y \leq 0, B_z < 0$
2	BC	$B_y > 0, B_z < 0$
3	DE	$B_y \ll 0, B_z < 0$
4	BCP	$B_y > 0, B_z \text{ weak} > 0$
5	BCPP	$B_y > 0, B_z \text{ strong} > 0$
6	DEP	$B_y < 0, B_z \text{ weak} > 0$
7	DEPP	$B_y < 0, B_z \text{ strong} > 0$

From the computed Heppner-Maynard polar cap potential patterns, we have estimated the location of the polar cap boundary ( $B=1$ ) and the equatorward edge of the region 1 currents ( $B=2$ ) for each of the 7 patterns such that the 'electric field reversal region' lies between these 2 ellipses near dawn and dusk. Ellipses defining boundaries 1 and 2 were drawn on each of the seven published Heppner-Maynard (1987) patterns; and the parameters describing each ellipse ( $A_{HM}, B_{HM}, DX_{HM}, DY_{HM}$ ) were scaled from the drawing. For a given point ( $x=\theta \cos \phi, y=\theta \sin \phi$ ) in the ionosphere, we can define a corresponding point ( $X_{HM}, Y_{HM}$ ) in the Heppner-Maynard pattern using simple scaling formulas that force ellipse 2 on the Heppner-Maynard pattern to coincide with ellipse 2 derived from the real-time observations.



3) Boundary 1 is defined to be the poleward edge of the electric-field reversal region or approximately the poleward edge of the region 1 currents. The difference between the  $A_{HM}$ ,  $B_{HM}$ ,  $DX_{HM}$ , and  $DY_{HM}$  values for ellipses 1 and 2 indicates the latitudinal width of the electric field reversal region, as a function of local time, in the Heppner-Maynard model. We locate boundary 1 in the real-time potential distribution by using the corresponding Heppner-Maynard width, scaled using the same procedure as for boundary 2. The potential across the boundary is calculated using the Heppner-Maynard model and the procedure described for boundary 2.

#### Potential Calculations within the Regions

1) Region 3 represents mid and low latitude electric fields. These electric fields result partly from the motion of the neutral atmosphere across the Earth's magnetic field and partly from direct penetration of auroral-zone electric fields to low latitudes. The electric-field effects of quiet-time winds are reasonably well understood (Richmond and Roble, 1987) but the effects of time-varying winds are not. However, there is evidence that during magnetically disturbed times there is a strong link between the auroral and equatorial electric fields (Nishida, 1968, a, b). This was further studied by Gonzales et al (1979) and Kelley et al (1979) who concluded that rapid changes in the magnetospheric convection can cause immediate effects on the equatorial electric fields. They conjectured that the perturbations are caused by the penetration of the convection field before the shielding charges can move to cancel the field. According to Rice Convection Model results from simulations of prompt low latitude electric field effects (Spiro et al., 1988), the patterns can be parametrized by

$$V_{p3}(\theta, \phi) = \langle V(t) \rangle + F(t) \sin^p \theta \sum_m a_m \sin [m(\phi - \phi_0(\theta))] \quad (3.1)$$

where  $F(t)$  is the overall strength of electric field penetration of the shielding layer at time  $t$ .

To estimate the direct penetration of the magnetospheric electric field we use the equatorward boundary of the auroral zone electron precipitation. Assuming that the equatorward edge represents the inner boundary of the plasma sheet, we follow the motion of the ionospheric mapping point of the electrons that lie on that boundary.

This formulation involves several assumptions:

- a) We are neglecting the potential drop across the dusk side rapid-flow trough region compared to the potential drop along the shielding layer.
- b) We are assuming that the precipitation lifetime is not too short compared to the time scale which the boundary moves. If the precipitation is so strong that the equatorward edge becomes a precipitation boundary rather than a convection boundary, then this procedure will underestimate the strength of the penetration electric field.
- c) *The meridional motion of the inner edge occurs on a time scale that is small compared to the particle drift time so that the motion of the inner edge can be equated to the motion of an individual inner edge particle.*

2) Region 2 includes the region 2 magnetic field-aligned currents (Iijima and Potemra, 1976) and the diffuse aurora. To assure continuity across the shielding layer, we simply add an auroral-zone field to a smoothed extrapolation of the potential used in the low latitudes (region 3).

$$V_2(\theta, \phi) = V_{low,x}(\theta, \phi) + V_{az}(\theta, \phi) \quad (3.2)$$

where  $V_{low,x}(\theta, \phi)$  is a smoothed extrapolation of the region 3 potential for the low latitude and an analytic form for the auroral zone potential which takes into account the auroral-zone contribution to the potential at boundary b and a function to represent the Harang discontinuity.

3) Region 1 contains the region 1 field aligned currents. The potential function has been designed to transition smoothly between Regions 0 and 2 and assumes that for a given local time, the latitudinal dependence of the potential is expressible in a 4-term power series. The coefficients are determined by the condition that  $V$  and its normal derivative must be continuous at both the poleward and equatorward boundaries of region

4) Region 0 is the polar cap. The potential is scaled from the Heppner-Maynard model.

### C. Magnetic Field Model

As the model has already been described fully elsewhere (Hilmer, 1989), I will only briefly review the program. The model was designed to strike a compromise between ideal equilibrium MHD model where the  $j \times B$  and  $\nabla P$  forces are balanced and the empirical models available. The blend of the Tsyganenko and Usmanov (1982) empirical model, the analytic model by Voigt (1981), and additional work by Hilmer (1989) on the ring and tail current structures was used in constructing the magnetic field program for the MSM. The equations in this section are from these sources.

The magnetic field is assumed to be a sum of 4 different current structures

$$B_d = \text{earth's main field} \quad (3.3)$$

$$B_{rc} = \text{field of ring current} \quad (3.4)$$

$$B_{tail} = \text{field of cross tail current} \quad (3.5)$$

$$B_{cf} = \text{field of Chapman-Ferraro currents} \quad (3.6)$$

$$B_{total} = B_d + B_{rc} + B_{tail} + B_{cf}$$

The magnetopause is assumed to be a discontinuity with zero normal component of the magnetic field

$$\bar{n} \cdot (B_d + B_{cf}) = 0 \quad (3.7)$$

The magnetic field caused within the magnetosphere by currents flowing in the magnetopause discontinuity can be derived from a scalar potential

$$B_{cf} = -\nabla \phi_{cf} \quad (3.8)$$

Putting equation (3.8) into equation (3.7) results in a boundary condition

$$\frac{\partial \phi_{cf}}{\partial n} = + n \cdot B_d \quad (3.9)$$

and the potentials must also solve Laplace's equation

$$\nabla^2 \phi_{cf} = 0 \quad (3.10)$$

The details of the expansion of the Chapman-Ferraro potentials and the explicit solutions of the magnetic field values are in Voigt (1981).

The ring current contribution  $B_{rc}$  was originally taken from the axially symmetric ring current derived by Tsyganenko and Usmanov (1982). They introduce the magnetic vector potential  $A = (0, A_\phi, 0)$

$$A_\phi = C\rho (\rho^2 + z^2 + 4\rho_0^2)^{-3/2} \quad (3.11)$$

where the addition of the  $\rho_0$  term is the only change from the dipolar coordinates and eliminates the singularity at the origin of the coordinate system. At large distances the potential approaches that of a pure dipole, which is a current free field. The majority of

the current is contained within  $(\rho^2 + z^2)^{1/2} < 2\rho_0$  where  $\rho_0$  is the characteristic radius. To better replicate observed data, Dr. R. V. Hilmer (1989) has improved this algorithm to include the current contributions from both the eastward and westward components of the ring current and their characteristic radii.

The cross tail current field  $B_{tail}$  is based on the Tsyganenko and Usmanov (1982) model. To avoid the mathematical discontinuities that arise from attempting to model the current systems as infinitely thin sheets, they introduce a system of superpositions of an infinite number of straight current filaments lying in the equatorial plane parallel to the y axis. Each filament has an axially symmetric current so that the magnetic field simply varies with radial distance R. The variation in the magnetic field is then

$$dB = \frac{\frac{R}{D}}{1 + \left[\frac{R}{D}\right]^2} = \frac{D[(x-x_0)^2 + z^2]^{1/2}}{(x-x_0)^2 + z^2 + D^2} \quad (3.12)$$

where  $D$  = scale half thickness of the filament.

A linear function of current per unit length  $I(x_0)$  is introduced and the x and z components of the magnetic field are integrated from  $x_n$  = inner edge to  $x_f$  = outer edge of the current slab. The magnetic field of a filament has no y-dependence; however to produce the "bending" of the current lines in the near tail dawn and dusk sectors, a factor  $f(y)$  is appended to the  $B_x$  and  $B_z$  integrations.

Dr. R. V. Hilmer and Dr. G.-H. Voigt have introduced several improvements to this scheme. The magnetic field dependence has been extended in 2 dimensions so that

$$dB = F(x,z,x_0,z_0) \text{ radial dependence of the field at } (x,z) \text{ from a} \\ \text{single filament at } (x_0,z_0)$$

This allows much greater flexibility in choosing the position and intensity functions for the current sheet as functions of both x and z. The total current then becomes the sum of

the  $n$  segments for which functions have been defined.

The second modification is that the model allows for the interruption of the cross tail currents and subsequent magnetic field collapse during a substorm onset, an observed feature of the substorm process. The model's flexibility also includes the ability to input the area over which the disturbance takes place.

#### D. Particle Tracer Model

The particle tracer model was designed by Dr. R. W. Spiro, and Figure 3.3 shows how the program is implemented. As derived in Chapter 2, the gradient-curvature and ExB drifts of the ions and electrons are traced by the formula

$$v_D = \frac{E \times B}{B^2} + \frac{\lambda}{q} \frac{\nabla \cdot (\int ds/B)^{-2/3} \times B}{B^2} \quad (3.13)$$

where  $\lambda$  = energy invariant

$(\int ds/B)$  = flux tube volume

which uses the fact that for a given  $\lambda$ , the number of particles per unit magnetic flux  $\eta$ , is constant along a drift path (Harel et al., 1981), except for the effects of loss. Including loss, we write

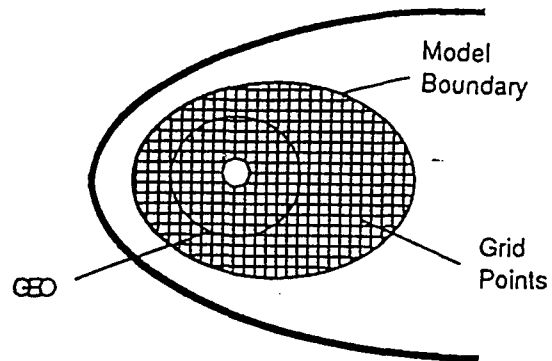
$$\left[ \frac{\partial}{\partial t} + v_D \cdot \nabla \right] \eta = - \frac{\eta}{\tau} \quad (3.14)$$

where  $\tau$  is the loss lifetime. A fourth order Runge-Kutta scheme with self-adjusting time step follows each particle's position in time. The geosynchronous satellite data available is not used explicitly in the formulation, but is used to improve the initial and boundary conditions of the plasma.

Beginning with electric and magnetic field output for a given time ( $t=t_1$ ), a particle

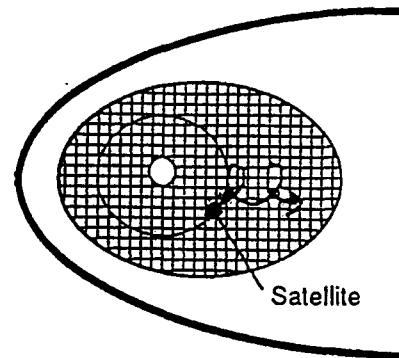
### Particle Tracing & Invariant-Density Computation Sequence

1. Assume the distribution function at all grid points at the start time (initial condition) and at all boundary grid points for all times (boundary condition).



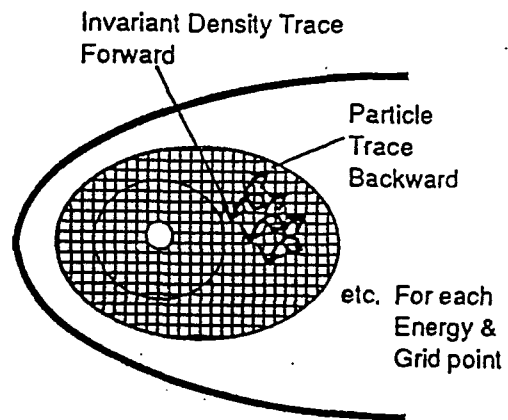
2. If satellite particle data are available, trace particles of each energy from the observation point back to the boundary, or until the model start time is reached.

3. Assuming that invariant density is constant along each trajectory, except for loss, adjust boundary and initial conditions to improve agreement with satellite data.



4. If results are available from a previous MSM run, adjust initial condition toward consistency with those results.

5. To compute the distribution function at  $t_1 > t_0$ , trace particles backward in time from every grid point from  $t_1$  to  $t_0$ , or to the boundary, whichever is reached first. Interpolate to find the invariant density at that point. Calculate invariant density at grid point at  $t_1$  by assuming that invariant density is constant along the drift path, except for loss.



6. Continue this process forward in time as long as necessary.

Figure 3.3 Particle-Tracer model structure.

from each grid point for each energy is traced backward in time until it crosses either the spatial or time boundary ( $t=t_0$ ). Using the initial and boundary  $\eta$  values, we interpolate to find the invariant density at that point. From equation 3.14 the invariant density, corrected for loss, can be calculated for time  $t_1$ . The computed invariant density for each energy and species for time  $t_1$  then becomes the new 'initial' condition for the next mark time  $t_2$ . The method of tracing a single particle back to its initial location and then using the invariance of  $\eta$  to move the ensemble of particles forward in time overcomes the problem of following small objects with a finite grid structure.

Precipitation due to pitch angle scattering is the major loss mechanism within the program. (We have not included charge exchange.) Scattering rates are difficult to predict accurately as they depend on the amplitude of the scattering wave, which may be determined by non-linear plasma interactions. However, by assuming strong pitch angle scattering we can obtain an approximate upper limit to the precipitation rate. This process assumes that particles have their pitch angles scattered on each bounce by an amount large compared to the width of the loss cone and can lead to a further simplification that the particle distribution function is isotropic and becomes a function of energy only, not distance along the field line. The rate at which particles of energy  $E$  are lost from a flux tube of unit magnetic flux is given by (Wolf, class notes)

$$\dot{N} = \left[ \frac{2}{B_i} \right] \left[ \frac{n}{2} \right] \left[ \frac{1}{2} \left[ \frac{2E}{m} \right]^{1/2} \right] \quad (3.15)$$

where  $(2/B_i)$  = effective loss area for flux tube

$(n/2)$  = number of downward moving particles

$(2E/m)^{1/2}$  = velocity of particles

Using  $\eta = n \int ds/B$



$$\frac{1}{\tau_{\text{full}}} = \frac{f}{n} = \left[ \frac{E}{2m} \right]^{1/2} \left[ B_i \int \frac{ds}{B} \right]^{-1} \quad (3.16)$$

where  $\tau_{\text{full}}$  is the loss lifetime for strong pitch angle scattering.

Specifically within the program, Dr. R. A. Wolf has developed an algorithm to compute the loss rate:

$$\frac{D\eta(t)}{\eta(t)} = \frac{-f_0 \eta(t) G(t)}{\tau_{\text{full}}(x(t))} \quad (3.17)$$

where

$$G = 1 - \frac{\eta_{\text{eq}}(x(t))}{\eta(t)} \quad \text{for } \eta(t) > \eta_{\text{eq}}(x(t)) \quad (3.18a)$$

$$G = 0 \quad \text{for } \eta(t) < \eta_{\text{eq}}(x(t)) \quad (3.18b)$$

$\tau_{\text{full}}$  = described in equation 3.16

$\eta_{\text{eq}}$  = equilibrium invariant density; set equal to the initial  $\eta$

$f_0$  = the assumed overall efficiency of pitch angle scattering

The function  $f_0$  depends on both the particle type and energy. From runs using the Rice Convection Model, the efficiency of the ions of all energies is estimated as

$$f_0 = 0.1$$

From the empirical estimates of Schumaker et al. (1988), the efficiency for all but the highest energy electrons is set at

$$f_0 = 1/3 \quad \text{during magnetically quiet times}$$

$$f_0 = 2/3 \quad \text{during magnetically active times}$$

Our highest energy electron channel corresponds to approximately 40 keV at

geosynchronous orbit. Electrons of this energy are affected mostly by electromagnetic waves and suffer very little pitch angle scattering on the nightside where total plasma density is low at synchronous orbit. However, these particles go into strong pitch angle scattering on the dayside as the flux tubes fill with cold plasma and the particles go into resonance with whistlers. We implement this in the program with the function

$$f_0 = \max(0, \cos(\phi))$$

where  $\phi$  = local time angle with 0 at noon.

#### E. Boundary Plasma Condition

The plasma boundary condition of the model calculation was set to balance the plasma sheet particle pressure with the magnetic field lobe pressure at 20 Re. The equatorial energy density at  $x = -20$  Re and local midnight is set equal to 1.5 times the lobe magnetic pressure:

$$u(-20,0,0) = 1.5 \times \left[ \frac{B^2}{8\pi} \right] \frac{\text{ergs}}{\text{cm}^3} \quad (3.19)$$

The energy per particle in terms of the model parameters is

$$E = |\lambda| \times VM \quad (3.20)$$

with  $VM = [ds/B]^{-2/3}$ , so that the total particle energy density is

$$u = C \sum n_s \times \lambda_s \times VM = C \sum \eta_s \times VM^{3/2} \times \lambda_s \times VM \quad (3.21)$$

With the conversion factor  $C$  between the model parameters of (eV-nT / Weber-Re) to the magnetic energy in ergs/cm<sup>3</sup> the equation becomes

$$u = (2.508 \times 10^{-34} \text{ ergs/cm}^3) \times \sum_s \eta_s |\lambda_s| \times VM^{5/2} \quad (3.22)$$

Summing over the ions and electrons, the equation becomes

$$u = (2.508 \times 10^{-34} \text{ ergs/cm}^3) \times \eta_{\text{tot}} \times (\langle |\lambda_i| \rangle + \langle |\lambda_e| \rangle) \times VM^{5/2} \quad (3.23)$$

where  $\eta_{\text{tot}}$  is the total density per unit magnetic flux of either the electrons or ions.

Requiring that the particle pressure balance the lobe magnetic pressure (equations 3.19 and 3.23) gives  $\eta_{\text{tot}}$  as

$$\eta_{\text{tot}} = \frac{1.5 \times \left[ \frac{B^2}{8\pi} \right]}{(2.508 \times 10^{-34} \text{ ergs/cm}^3) \times (\langle |\lambda_i| \rangle + \langle |\lambda_e| \rangle) \times VM^{5/2}} \quad (3.24)$$

Using known temperatures of ions ( $T_i$ ), electrons ( $T_e$ ), and the model flux tube volume at the position that the measurements were taken, the energy invariants of each species can be calculated:

$$\lambda_{kT_i} = \frac{kT_i}{VM} \quad \left| \lambda_{kT_e} \right| = \frac{kT_e}{VM} \quad (3.25)$$

The program currently computes the density for 16 ion energy channels ( $K=1-16$ ) and 16 electron channels ( $K=17-32$ ). From the assumption that the particle distributions are maxwellian, we choose to model particles up to  $8kT$ ; particles beyond this energy carry an insignificant fraction of the current or energy. We assign one-third of our energy channels to energies less than  $1.13kT$ . (Half the number density is below  $1.13kT$  and  $1/2$  above  $1.13kT$ ). We use unequal energy spacings ( $x$ ) but equal levels in  $y$  such that

$$x = E/kT = r(e^y - 1) \quad (3.26)$$

$$y \text{ for ions} \quad y(K) = (K-0.5) \times y_{\text{max}}/16 \quad (3.27a)$$

$$y \text{ for electrons} \quad y(K) = (K-16.5) \times y_{\text{max}}/16 \quad (3.27b)$$

$$ALAM(K) = \pm x(K) \times \lambda_{kTj} \quad (3.28)$$

where  $j='e'$  for electrons,  $j='i'$  for ions

Given the  $\lambda_{kTi}$  and  $\lambda_{kTe}$  we can compute for each energy species  $k$ , the density at the back boundary at midnight ( $\eta_k$ ) by the following:

Assuming a Maxwellian at the boundary,  $\eta_k$  is generally given by

$$\eta_k = \left( \int \frac{ds}{B} \right) \times \int_{E_{min,k} < E < E_{max,k}} d^3v f_k(v) = C \int_{E_{min}}^{E_{max}} E^{1/2} e^{-E/kT} dE \quad (3.29)$$

where  $E_{min}$  and  $E_{max}$  are, respectively, the lower and upper limits of the energy range corresponding to species  $k$ , and  $C$  is a normalization constant that is independent of the species index  $k$  but depends on mass. For a given point on the boundary, we can transform the right-most integral in (3.29) to an integral over  $\lambda$ :

$$\eta_k = D \int_{|\lambda|_{min,k}}^{|\lambda|_{max,k}} |\lambda|^{1/2} \exp\left[-\frac{|\lambda|}{\lambda_{kT}}\right] d|\lambda| \quad (3.30)$$

where  $D$  is another normalization constant that is independent of  $k$ . We approximate the integral over the single energy channel  $k$  as follows:

$$\eta_k = D' \left[ \{|\lambda|_{max,k}\}^{3/2} - \{|\lambda|_{min,k}\}^{3/2} \right] \exp\left[-\frac{|ALAM(K)|}{\lambda_{kT}}\right] \quad (3.31)$$

The lower-limit  $|\lambda|$  values for species  $k$  are given by

$$|\lambda|_{\min,k} = 0 \quad \text{for } k=1 \text{ or } 17 \quad (3.32a)$$

$$|\lambda|_{\min,k} = \frac{[|\text{ALAM}(K-1)| + |\text{ALAM}(K)|]}{2} \quad \text{otherwise} \quad (3.32b)$$

The upper-limit  $|\lambda|$  values for species  $k$  are given by

$$|\lambda|_{\max,k} = |\lambda|_{\min,k} \left\{ 1 + \frac{3\lambda_{kT}}{2|\lambda|_{\min,k}} \left[ 1 + \frac{\lambda_{kT}}{2|\lambda|_{\min,k}} \right] \exp \left[ \frac{(|\text{ALAM}(K)| - |\lambda|_{\min,k})}{\lambda_{kT}} \right] \right\}^{2/3} \quad (3.33a)$$

for  $k = 16$  or  $32$  and

$$|\lambda|_{\max,k} = \frac{[|\text{ALAM}(K)| + |\text{ALAM}(K+1)|]}{2} \quad \text{otherwise} \quad (3.33b)$$

for other  $k$  values. (The complicated form (3.33a) is chosen such that, the highest energy  $k$ -values give good estimates of the integral all the way to infinity).

We assume that the sum of the invariant density over the energy channels of each species is equal and choose the normalization constant  $D'$  so that

$$\sum_{k=1}^{16} \eta_k = \eta_{\text{tot}} \quad (3.34a)$$

and

$$\sum_{k=17}^{32} \eta_k = \eta_{\text{tot}} \quad (3.34b)$$

To represent the substorm-associated plasma sheet depletion we decrease the density by multiplying out boundary value  $\eta_{\text{base}}$  by a factor

$$\exp(-f_{\text{FP}}) \quad (3.35)$$

where  $f_{\text{FP}} = 0$  before substorm onset

$$f_{Fp} = \ln(x) \text{ after substorm onset}$$

The program originally ran with  $\alpha=2$  under the assumption that 1/2 of the particles were accelerated earthward during the substorm process and the other 1/2 were ejected tailward and out of our modelling region. However, densities at geosynchronous orbit were a factor of 5 too high so that further study was done to analyze the effect of increasing the depletion factor. Some results of this are shown in the next chapter.

The back boundary also includes the effect of the finite width of the magnetotail source region as presented by Kivelson and Spence (1988). Given that finite energy particles gradient and curvature drift from the same point in the source region at differing rates and assuming the low-latitude boundary layer is a negligible source of plasma sheet particles, at a given point in the magnetosphere there are 2 particle populations: 1) high energy particles which have drifted from a source region relatively close to the point and 2) low energy particles which have drifted from the far tail. You therefore get a depletion in the high energy particles closer toward the earth, and our model back boundary is inhomogenous in local time (See Figure 3.4). To implement this in the model, Dr. Wolf has developed the following scheme. We define:

$$V_{\text{outside}} = V_{\text{max}} \text{ for ions}$$

$$V_{\text{outside}} = V_{\text{min}} \text{ for electrons}$$

where  $V_{\text{max}}$  and  $V_{\text{min}}$  are the maximum and minimum electrostatic energy over the entire grid.  $W_{\text{extra}}$  is set equal to the maximum electrostatic potential energy of a particle of species  $K$  in the magnetosphere ( $\text{sign} \times V_{\text{outside}}$ ) minus the total energy of a particle at point  $p$

$$W_{\text{extra}} = \text{Sign}(\text{ALAM}(K)) \times (V_{\text{outside}} - V_p) - |\text{ALAM}(K)| \times VM_p \quad (3.36)$$

When  $W_{\text{extra}}$  is substantially negative, the total energy of the particle at point  $p$  is much greater than the magnetospheric electrostatic potential energy and the density is decreased to reflect the reduced population of the energetic particles. To smooth the transition, the

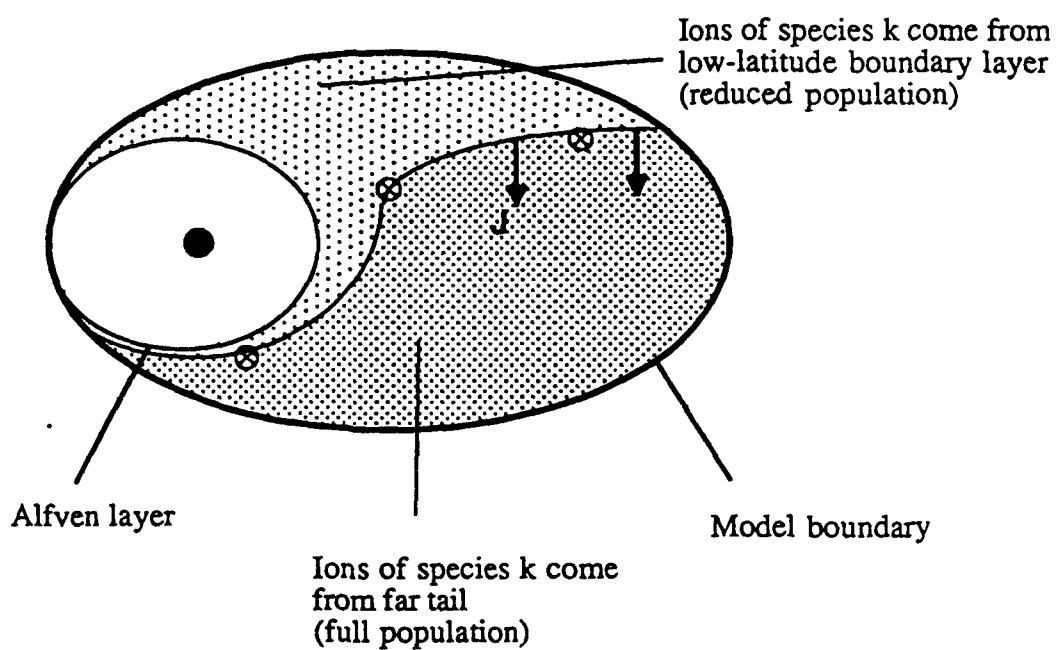


Figure 3.4 Inhomogenous boundary plasma condition.

width of the change is spread out over a few gridpoints using the form

$$\Delta V = \frac{2(V_{\max} - V_{\min})}{(J_{\max} - J_{\text{WRAP}})} \quad (3.37)$$

where  $J_{\max}$  = the maximum number of gridpoints in local time

$J_{\text{WRAP}}$  = the number of 'wrap-around' points in the local time grid.

The depletion factor ( $f_{Kp}$ ) is set as

$$f_{Kp} = \frac{f_{Kp\max}}{1 + \exp\left[\frac{W_{\text{extra}}}{\Delta V}\right]} \quad (3.38)$$

where  $F_{Kp\max} = \ln(10) =$  the maximum assumed effect of a factor of 10.

The total reduction in density for the substorm and inhomogenous boundary conditions becomes

$$\eta_p = \eta_{\text{base}} \times \exp(-f_{Kp} - f_{Fp}) \quad (3.39)$$

#### F. Initial Plasma Condition

The plasma sheet ions and electrons are assumed to have a maxwellian distribution. We recognize that the higher energy particles have a power law dependence, but by using the geosynchronous orbit data to modify the initial conditions we hope to correct the errors that occur in using the maxwellian distribution. For the present version of the model we use 30-45 Kev electron fluxes measured by the 1977-077 and 1976-059 spacecraft which corresponds to the highest electron energy channel in the program (EETA(32)). See Appendix A for a complete derivation of the flux in terms of the model parameters. The resulting expression is:



$$\left[ \frac{d^2J}{dEd\Omega} \right]_{\text{cm}^{-2}\text{s}^{-1}\text{eV}^{-1}\text{ster}^{-1}} = 7.392 \times 10^{-16} \frac{|\text{ALAM}(K)|^{1/2} \times \text{VM} \times \text{EETA}(K)}{|\lambda_{k\text{max}} - \lambda_{k\text{min}}|} \quad (3.40)$$

where  $\text{ALAM}(K)$  = energy channel  $K$  in units of  $\text{eV}(\text{Re}/nT)^{2/3}$

$\text{VM}$  = flux tube volume

$\text{EETA}(K)$  = computed density per unit flux tube volume for energy channel  $K$

$\lambda_{k\text{max}}$  = computed using equation (3.33a) of the last section

$\lambda_{k\text{min}}$  = computed using equation (3.32b) of the last section

Using appropriate geosynchronous satellite flux data and program values for  $\text{ALAM}$ ,  $\text{VM}$ ,  $\lambda_{k\text{max}}$ , and  $\lambda_{k\text{min}}$ , we can calculate the density at geosynchronous orbit ( $\text{EETA}(32)$ ). Taking the ratio of this density to the calculated density at the boundary will give the decrease in density between the two points.

$$\frac{\text{EETA (geosynchronous)}}{\text{EETA (boundary)}} = \text{factor} \quad (3.41)$$

Assuming a power law dependence on geocentric distance  $r$  and that all energy components have the same radial dependence, the power coefficient can be calculated

$$\frac{\text{EETA (geosynchronous)}}{\text{EETA (boundary)}} = \text{factor} = \left[ \frac{6.6 \text{ Re}}{\text{boundary at local midnight}} \right]^p \quad (3.42)$$

$$p = \frac{\log \text{factor}}{\log \left[ \frac{6.6 \text{ Re}}{\text{boundary at local midnight}} \right]} \quad (3.43)$$

The total density ( $\eta_{\text{tot}}$ ) is then recomputed:

$$\eta_{\text{tot}}(r) = \eta_{\text{boundary}} \times \left[ \frac{r}{\text{boundary at local midnight}} \right]^p \quad (3.44)$$

Using the initial density value of species K at midnight ( $\eta_p$ ), the initial condition becomes for each grid point I,J

$$EETA_{\text{initial}}(K,I,J) = \left[ \frac{\eta_p(\text{midnight})}{\eta_{\text{boundary}}} \right] \left[ \frac{r}{\text{boundary at local midnight}} \right]^p \quad (3.45)$$

where  $\eta_p(\text{midnight})$  refers to the initial value at gridpoint I,J of energy K.

#### IV. TESTING THE MODEL USING THE CDAW6 EVENT

##### A. General Description of Event

The Coordinated Data Analysis Workshop #6 (CDAW6) focused its effort on understanding the physical processes which control the flow of energy from the solar wind through the magnetosphere and the eventual release through magnetospheric substorms. The participants studied the first of 2 large substorms which occurred on March 22, 1979. Preceded by a day of quiet conditions both in the solar wind and the magnetosphere, a storm sudden commencement was observed at 0826UT followed by the onset of the expansive phase of the first substorm at 1054UT. The ready availability of a large data set and numerous papers (see Journal of Geophysical Research volume 90, February 1985 for most of them) made it a natural candidate for the preliminary testing of the model's capabilities.

Figure 4.1 is a summary of solar wind plasma parameters at IMP-8 (located slightly to the duskside of the bow shock) and the AE magnetic activity index published as Figure 2 in the overview paper by McPherron and Manka (1985). The major features of these data include:

- 1) An interplanetary shock arrives at IMP-8 at 0821:20UT, as indicated by an increase in solar wind density, velocity and magnetic field strength.
- 2) At 0826UT the shock arrives at the dayside of the earth compressing the magnetosphere causing a sudden storm commencement, which can be seen as a small spike in the AE index.
- 3) The magnetic field turns southward at IMP-8 at 1008UT which begins the stretching of the magnetotail and the growth phase of the first substorm.
- 4) The first substorm expansion onset at 1054UT produced auroral zone magnetic activity (as measured by the AE index) exceeding 1000 nT.

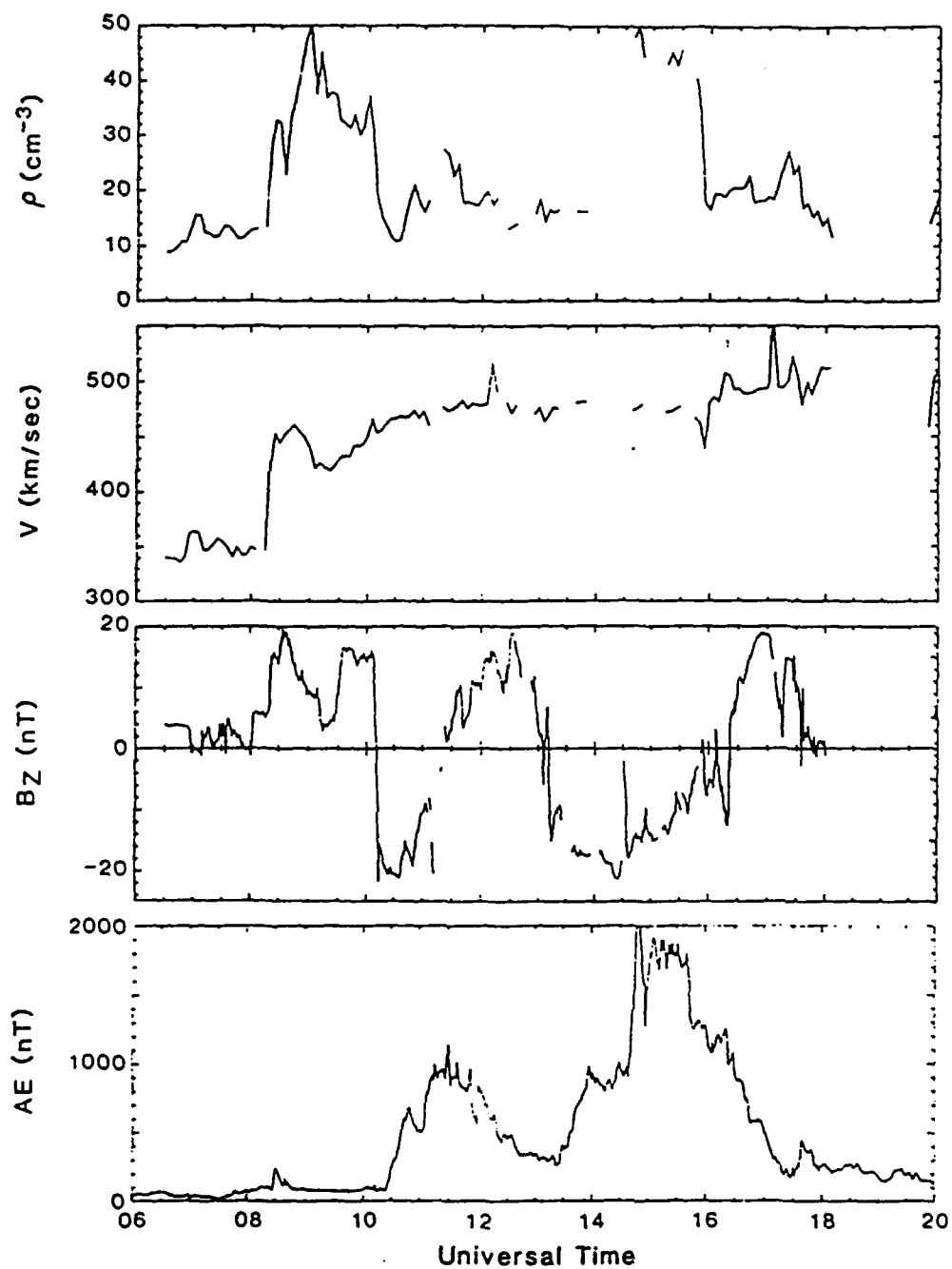


Figure 4.1 Summary of solar wind plasma parameters at IMP 8 on March 22, 1979. Top traces show 5-min averages of solar wind velocity and density. Middle trace shows 1-min values of the GSM Z component of the IMF at IMP 8. Bottom trace presents a 55-station AE index calculated at 1 min time resolution.

5) At 1122UT the IMF becomes northward at IMP-8, magnetic activity starts to decline and the recovery phase of the substorm begins.

## B. Model Inputs

### 1. Magnetic Field Model

After studying the IMF data and Dst index, Dr. G.-H. Voigt subdivided the CDAW-6 interval into 17 time labels (Table 4.1) which represent different configurations of the magnetic field during the event. The magnetic field matrices were then pre-computed for each time. The inputs to the model are

**STAND** - the magnetopause standoff distance ( $R_e$ ) from the solar wind data.

**Dst** - the standard index of ring current intensity (nT).

**Aur.Eq.Bd.** - the equatorward edge of the auroral zone at midnight (information on how this is done is in Section 2 - Electric Field Model Inputs).

**Map(E)** - the expected mapping from the Aur.Eq.Bd. (above) to the inner edge of the plasma sheet at local midnight in the equatorial plane of the magnetosphere ( $R_e$ ). This was estimated using the work by Kivelson et al.(1979), Horowitz et al. (1986), and Gussenhoven et al. (1981) who have calculated  $K_p$ -based relationships between the inner edge of the plasma sheet and the equatorward edge of the auroral zone.

From these four observable parameters, Hilmer (1989) has devised a scheme to estimate the remaining input values necessary to run the model:

**TILT** - Dipole tilt angle (set to 0.0 for the CDAW-6 event).

**HJNEAR** - Strength of the cross-tail current sheet at the inner edge.

**XNEAR** - Location of the inner edge of the model plasma sheet at local midnight ( $R_e$ ).

**HJFRAC** - Fraction of HJNEAR appearing at and beyond (XNEAR-100)  $R_e$ .  
Current intensity is constant in the far tail.

LABEL = 1	6:00	UT	Pre-Storm Sudden Commencement
LABEL = 2	8:26	UT	Storm Sudden Commencement
LABEL = 3	10:00	UT	Same as LABEL 2 but little bit more stretch
LABEL = 4	10:20	UT	IMF turns southward
LABEL = 5	10:54 - EPS		Maximum stretch just before onset of first substorm
LABEL = 6	10:54 + EPS		Collapse right after onset of substorm
LABEL = 7	11:30	UT	End of phase "gradually back to normal"
LABEL = 8	12:06	UT	Nominal phase (i.e. nominal model)
LABEL = 9	12:43	UT	Nominal phase
LABEL = 10	13:10	UT	IMF turns southward
LABEL = 11	13:40	UT	Gradual stretching period
LABEL = 12	14:07	UT	Gradual stretching period
LABEL = 13	14:36 - EPS		Maximum stretch just before onset of second substorm
LABEL = 14	14:36 + EPS		Collapse right after onset of substorm
LABEL = 15	15:15	UT	Gradually back to normal after collapse
LABEL = 16	15:50	UT	Gradually back to normal
LABEL = 17	16:00	UT	Beginning of last nominal phase

Table 4.1 Critical time labels for CDAW-6 event.

DY - Scale length for changes in tail structure along the GSM y-axis ( $R_e$ ). This applies to the westward tail current system.

DFIL - Plasma sheet thickness parameter.

BRN, BRP - Ring-current contributions ( $nT$ ) at Earth's center from the westward and eastward components, respectively ( $BRN < 0$ ,  $BRP > 0$ ).

RN, RP - Characteristic radii of the westward and eastward ring-current components, respectively.

COLLAP - Fraction of the pre-collapse midnight cross-tail current remaining in the disturbed region (from the inner edge,  $X_{NEAR}$  to  $X_{NEAR} - DELXC$ ).  $COLLAP = 1.0$  means no collapse.

DELXC - The distance from the inner edge ( $R_e$ ), along the x-axis, which is altered by the addition of eastward tail current.  $DELXC = 0.0$  means no collapse.

DYC - Scale length for changes in tail structure along the GSM y-axis ( $R_e$ ). Applies to the eastward disruption collapse current.  $DYC$  is always less than  $DY$ .  $DYC = 0.0$  means no collapse.

Table 4.2 from Dr. R. Hilmer contains a list of these parameters for the CDAW-6 event. Also listed are three output parameters:

MAP(R) - The resulting midnight equatorial mapping distance ( $R_e$ ).

RC Zero - Characteristic radius for the ring current ( $R_e$ ). The ring current changes sign at this distance and is an implied particle pressure maximum.

Min-Loc - The minimum  $|B|$  and its location in the equatorial plane at midnight.

## 2. Electric Field Model

The cross polar cap potential was calculated from the IMF data and the empirical formula suggested by Crooker et al. (1982) and presented by Reiff and Luhmann (1986)

$$\phi(kV) = 22 + 0.069 vB Q1$$

where  $Q1 = \alpha(\alpha - \cos \theta) (\alpha^2 + 1 - 2\alpha \cos \theta)^{-1/2}$  for  $\cos \theta < \alpha$

	Label	UT	Comment	Stand	Dst	Aur.Eq.Bd.	Map(E)	Map(R)	RC Zero	Min-Loc
1	1	6:00	Pre-SSC	10.58	13.53	66.28	7.01	7.00	3.56	0.72 - 36
2	2	8:26	SSC	7.83	43.20	66.28	7.01	7.01	3.21	0.81 - 26
3	3	10:00	*	7.83	43.20	65.25	6.69	6.69	3.21	1.70 - 20
4	4	10:20	IMF South	8.93	32.56	64.72	6.53	6.52	3.20	1.24 - 20
5	5	10:54	Stretched	8.45	16.61	62.51	5.86	5.83	3.04	0.50 - 17
6	6	10:54+	Collapse	8.45	16.61	62.51			3.04	0.42 - 24
7	7	11:30	Nominal	8.10	-15.30	59.22	4.38	4.33	2.51	3.16 - 21
8	8	12:06	*	8.45	-24.41	58.82	4.24	4.23	2.41	3.21 - 21
9	9	12:43	*	8.77	-18.34	59.77	4.58	4.54	2.60	2.80 - 21
10	10	13:10	IMF South	8.71	-13.78	60.72	4.92	4.94	2.66	2.48 - 20
11	11	13:40		8.64	-9.22	60.73	4.92	4.90	2.64	2.44 - 20
12	12	14:07		8.61	-16.82	60.73	4.92	4.92	2.56	2.11 - 18
13	13	14:36	Stretched	7.58	-22.14	60.13	4.71	4.72	2.42	2.90 - 20
14	14	14:36+	Collapse	7.58	-22.14	60.13			2.42	1.09 - 26
15	15	15:15	Nominal	7.62	-39.61	59.80	4.59	4.58	2.24	2.57 - 22
16	16	15:50	*	7.68	-57.08	59.27	4.40	4.40	2.14	1.49 - 26
17	17	16:00	*	8.50	-60.88	59.14	4.35	4.35	2.14	1.40 - 26

	HJNEAR	XNEAR	HJFRAC	DY	DFIL	COLLAP	DELXC	DYC	BRN	BRP	RN	RP
1	4.3	-7.00	0.25	15.0	2.0	1.0	0.0	0.0	-105.0	117.2	3.2	2.1
2	8.3	-7.01	0.20	12.5	2.0	1.0	0.0	0.0	-50.0	75.9	4.0	1.6
3	12.0	-6.69	0.15	10.0	1.2	1.0	0.0	0.0	-50.0	75.9	4.0	1.6
4	12.7	-6.53	0.15	10.0	1.0	1.0	0.0	0.0	-50.0	72.0	4.0	1.6
5	17.5	-5.86	0.14	7.5	0.8	1.0	0.0	0.0	-230.0	221.6	2.9	2.1
6	17.5	-5.86	0.14	7.5	0.8	0.7	45.0	5.0	-230.0	221.6	2.9	2.1
7	15.0	-4.38	0.15	7.5	1.0	1.0	0.0	0.0	-400.0	354.5	2.7	2.1
8	15.0	-4.24	0.15	7.5	1.0	1.0	0.0	0.0	-490.0	437.1	2.6	2.1
9	15.0	-4.58	0.15	7.5	1.0	1.0	0.0	0.0	-390.0	345.8	2.7	2.1
10	15.0	-4.92	0.15	7.5	1.0	1.0	0.0	0.0	-380.0	340.4	2.7	2.1
11	15.0	-4.92	0.15	7.5	1.0	1.0	0.0	0.0	-540.0	504.9	2.6	2.2
12	17.0	-4.92	0.14	7.5	1.0	1.0	0.0	0.0	-500.0	466.4	2.5	2.1
13	17.0	-4.71	0.14	7.5	1.0	1.0	0.0	0.0	-570.0	522.9	2.5	2.1
14	17.0	-4.71	0.14	7.5	1.0	0.8	35.0	5.0	-570.0	522.9	2.5	2.1
15	15.0	-4.59	0.15	7.5	2.0	1.0	0.0	0.0	-840.0	774.3	2.4	2.1
16	11.0	-4.40	0.20	10.0	2.0	1.0	0.0	0.0	-700.0	615.9	2.5	2.1
17	11.0	-4.35	0.20	10.0	2.0	1.0	0.0	0.0	-680.0	597.9	2.5	2.1

Table 4.2 Input parameters for B-field model for CDAW-6 interval.



$$Q_1 = 0$$

$$\text{for } \cos \theta > \alpha$$

$$\alpha = \min \left[ \frac{(4B_T B_E)^{1/2}}{60 \text{ nT}}, 1 \right]$$

$\theta$  = polar angle of the IMF

$B_T$  = projection of IMF on solar-magnetosphere y-z plane

$B_E$  = magnetic field just inside magnetopause

The polar cap pattern type was also estimated from  $B_y$  and  $B_z$  IMF data for each time label using the criteria given in chapter 3. For the CDAW-6 interval, the equatorward edge of the diffuse aurora was based on electron data from DMSP, P78, and TIROS satellites.

Table 4.3 contains the input data calculated by Dr. R. A. Wolf and used during the interval for:

VPVC - cross-polar cap potential (kV).

IPATTV - polar cap pattern type.

EDGE - equatorward edge of auroral zone at midnight.

A(L) - radius of ellipse measured in x (sunward) direction.

B(L) - radius of ellipse measured in y (duskward) direction.

DX(L) - sunward displacement of coordinate system center from pole.

DY(L) - duskward displacement of coordinate system center from pole.

### 3. Boundary Plasma Condition

The invariant temperatures ( $\lambda_{kT_e}$ ,  $\lambda_{kT_i}$ ) were estimated from data from the ISEE-2 satellite, as shown in Figure 4.2 and published as Figure 1 in Paschmann et al. (1985). The satellite moved earthward from  $\sim 14.8$  to  $\sim 13.0$  Re geocentric distance at  $\sim 0200$  local time from 1010-1200 UT. However, the published observations do not cover the entire

	1	2	3	4	5	6	7	8
1	Time	VPCV	IPATTV	EDGE	A(1)	A(2)	A(3)	B(1)
2	0 - 0826-e	24	4	66.25	15.47	16.81	21.88	15.67
3	0826+e	24	5	66.25	17.85	19.25	21.88	18.52
4	1000	24	5	65.35	18.75	20.48	22.63	18.63
5	1020	66	3	64.80	18.70	20.66	23.10	17.56
6	1054-e	137	3	62.80	20.88	22.89	24.78	19.05
7	1054+e	137	3	62.80	19.70	21.61	24.78	18.78
8	1130	130	3	59.00	20.94	22.72	27.97	20.12
9	1206	107	3	59.00	20.91	22.71	27.97	19.86
10	1243	88	3	59.90	20.77	22.61	27.21	19.39
11	1310	94	3	60.20	20.72	22.59	26.96	19.31
12	1340	135	3	60.85	20.61	22.47	26.42	19.25
13	1407	161	3	60.60	20.76	22.68	26.63	19.17
14	1436-e	156	3	60.10	21.34	23.15	27.05	20.64
15	1436+e	156	3	60.10	20.74	22.49	27.05	20.49
16	1515	144	2	59.80	20.99	22.71	27.30	20.75
17	1550	127	2	59.25	20.73	22.31	27.76	21.08
18	1600	122	2	59.25	20.33	22.02	27.76	20.19

	9	10	11	12	13	14	15	16
1	B(2)	B(3)	DX(1)	DX(2)	DX(3)	DY(1)	DY(2)	DY(3)
2	14.04	22.83	-1.00	-0.56	-1.87	-0.90	0.00	0.00
3	17.09	22.83	-1.19	-0.81	-1.87	-0.77	0.00	0.00
4	17.40	23.74	-1.54	-1.62	-2.02	-0.64	0.00	0.00
5	16.53	24.30	-1.73	-2.21	-2.10	-0.64	0.00	0.00
6	17.82	26.33	-1.96	-2.48	-2.42	-0.64	0.00	0.00
7	17.50	26.33	-1.36	-1.78	-2.42	-0.64	0.00	0.00
8	18.88	30.18	-1.08	-1.37	-3.03	-0.64	0.00	0.00
9	18.53	30.18	-1.10	-1.40	-3.03	-0.64	0.00	0.00
10	18.04	29.27	-1.27	-1.62	-2.89	-0.64	0.00	0.00
11	17.97	28.96	-1.35	-1.73	-2.84	-0.64	0.00	0.00
12	17.90	28.30	-1.35	-1.73	-2.74	-0.64	0.00	0.00
13	17.79	28.56	-1.56	-1.99	-2.78	-0.64	0.00	0.00
14	19.46	29.06	-1.20	-1.53	-2.86	-0.64	0.00	0.00
15	19.28	29.06	-0.89	-1.15	-2.86	-0.64	0.00	0.00
16	19.49	29.37	-0.68	-0.92	-2.90	-0.64	0.00	0.00
17	20.07	29.92	-0.31	-0.40	-2.99	-0.64	0.00	0.00
18	19.06	29.92	-0.48	-1.62	-2.99	-0.64	0.00	0.00

Table 4.3 Input parameters for E-field model for CDAW-6 interval.

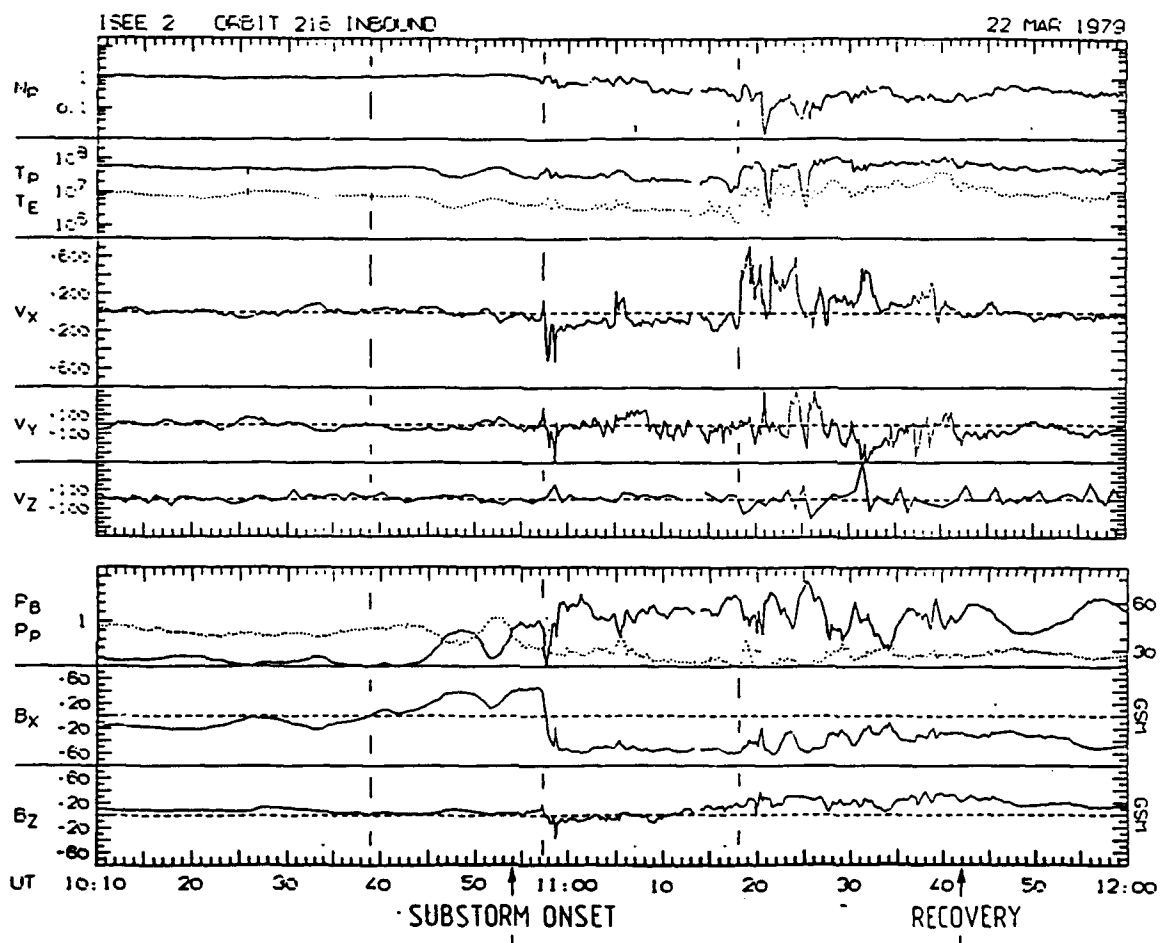


Figure 4.2 ISEE 2 plasma and magnetic field parameters for the time interval 1010-1200 UT on March 22, 1979.  $T_p$  and  $T_e$  are the ion and electron temperatures (degrees Kelvin).

time interval we want to model, so we have estimated the temperatures from the data and extrapolated to cover the rest of the event. The top of Table 4.4 shows the invariant temperatures calculated for the entire event. The headings are

Label - Time label of magnetic field model (See Table 4.1).

$t_{\text{figure}}$  - Time of ISEE-2 data point used to calculate temperature.

$r_{\text{figure}}$  - Radial distance of ISEE-2 ( $R_e$ ).

$VM_{\text{model}}$  - Flux tube volume at  $r_{\text{figure}}$  from the magnetic field model.

$T_i$  ( $^{\circ}K$ ) - Estimated ion temperature from ISEE-2 data.

$T_e$  ( $^{\circ}K$ ) - Estimated electron temperature from ISEE-2 data.

$\lambda_{kTi}$  - Calculated ion invariant temperature.

$\lambda_{kTe}$  - Calculated electron invariant temperature.

$\langle |\lambda_i| \rangle$  - average value of ion energy invariant ( $= 1.5 \times \lambda_{kTi}$ ).

$\langle |\lambda_e| \rangle$  - average value of electron energy invariant ( $= 1.5 \times \lambda_{kTe}$ ).

The bottom figure shows the value of  $\eta_{\text{tot}}$  calculated from equation 3.24 in Chapter 3 at a distance of 20  $R_e$  and local midnight. The headings are

$UT_{\text{model}}$  - the universal time of the model.

$B_{\text{lobe}}^2 / 8\pi(\text{model}(20R_e))$  - lobe magnetic pressure at 20  $R_e$  and midnight.

$VM_{\text{model}}(20R_e)$  - flux tube volume at 20  $R_e$  and midnight.

$\eta_{\text{tot}}$  - calculated total invariant density at 20  $R_e$  and midnight .

The initial invariant density for each energy channel is given by equation 3.31 in Chapter 3. A list of the energy channels ( $K$ ), invariant energy ( $ALAM(K)$ ), and boundary values at 20  $R_e$  and local midnight ( $ETAB(K)$ ) is given in Table 4.5.

#### 4. Initial Plasma Condition

The initial plasma condition is set using  $K=32$ , the highest electron energy that we model and it corresponds to  $\sim 40\text{keV}$  at geosynchronous orbit. Using the 30-45 keV electron channel of the 1977-007 and 1976-059 spacecraft we estimated the average flux

Label	t <sub>figure</sub>	r <sub>figure</sub>	VM <sub>model</sub>	T <sub>i</sub> (°K)	T <sub>e</sub> (°K)	λ <sub>kTi</sub>	λ <sub>kTe</sub>	< λ <sub>i</sub>  >	< λ <sub>e</sub>  >
1	10:26am	14.5	1.111	6.4x10 <sup>7</sup>	1.0x10 <sup>7</sup>	4960	775	7440	1162.5
2	10:26am	14.5	1.124	6.4x10 <sup>7</sup>	1.0x10 <sup>7</sup>	4908	767	7362	1150.5
3	10:26am	14.5	1.147	6.4x10 <sup>7</sup>	1.0x10 <sup>7</sup>	4810	752	7215	1128.
4	10:26am	14.5	1.121	6.4x10 <sup>7</sup>	1.0x10 <sup>7</sup>	4921	769	7381.5	1153.5
5	10:26am	14.5	1.453	6.4x10 <sup>7</sup>	1.0x10 <sup>7</sup>	3797	593	5695.5	889.5
6	10:26am	14.5	1.246	6.4x10 <sup>7</sup>	1.0x10 <sup>7</sup>	4428	692	6642	1038
7	11:50am	13.16	1.719	1.0x10 <sup>8</sup>	2.0x10 <sup>7</sup>	5015	1003	7522.5	1504.5
8	11:50am	13.16	1.730	1.0x10 <sup>8</sup>	2.0x10 <sup>7</sup>	4983	996	7474.5	1494
9	11:50am	13.16	1.649	1.0x10 <sup>8</sup>	2.0x10 <sup>7</sup>	5228	1045	7842	1567.5
10	10:26am	14.5	1.287	6.4x10 <sup>7</sup>	1.0x10 <sup>7</sup>	4287	670	6430.5	1005
11	10:26am	14.5	1.339	6.4x10 <sup>7</sup>	1.0x10 <sup>7</sup>	4120	644	6180	966
12	10:26am	14.5	1.316	6.4x10 <sup>7</sup>	1.0x10 <sup>7</sup>	4192	655	6288	982.5
13	10:26am	14.5	1.346	6.4x10 <sup>7</sup>	1.0x10 <sup>7</sup>	4099	640	6148.5	960
14	10:26am	14.5	1.296	6.4x10 <sup>7</sup>	1.0x10 <sup>7</sup>	4257	665	6385.5	997.5
15	11:50am	13.16	1.593	1.0x10 <sup>8</sup>	2.0x10 <sup>7</sup>	5412	1082	8118	1623
16	11:50am	13.16	1.642	1.0x10 <sup>8</sup>	2.0x10 <sup>7</sup>	5250	1050	7875	1575
17	11:50am	13.16	1.613	1.0x10 <sup>8</sup>	2.0x10 <sup>7</sup>	5345	1069	8017.5	1603.5

Label	UT <sub>model</sub>	B <sub>lobe</sub> <sup>2</sup> /8π(model (20R <sub>E</sub> ))	VM <sub>model</sub> (20R <sub>E</sub> )	η <sub>tot</sub>
1	0 - 0826-ε	8.049x10 <sup>-10</sup>	0.6049	1.966x10 <sup>21</sup>
2	0826+ε	20.019x10 <sup>-10</sup>	0.6050	4.940x10 <sup>21</sup>
3	1000	33.054x10 <sup>-10</sup>	0.7366	5.088x10 <sup>21</sup>
4	1020	35.461x10 <sup>-10</sup>	0.7335	5.393x10 <sup>21</sup>
5	1054-ε	65.914x10 <sup>-10</sup>	0.9300	7.178x10 <sup>21</sup>
6	1054+ε	34.808x10 <sup>-10</sup>	0.6462	3.075x10 <sup>21</sup>
7	1130	47.003x10 <sup>-10</sup>	0.8949	4.111x10 <sup>21</sup>
8	1206	49.956x10 <sup>-10</sup>	0.9148	3.912x10 <sup>21</sup>
9	1243	46.720x10 <sup>-10</sup>	0.8730	4.170x10 <sup>21</sup>
10	1310	46.792x10 <sup>-10</sup>	0.8709	5.137x10 <sup>21</sup>
11	1340	46.601x10 <sup>-10</sup>	0.8631	5.636x10 <sup>21</sup>
12	1407	55.492x10 <sup>-10</sup>	0.8923	6.069x10 <sup>21</sup>
13	1436-ε	56.765x10 <sup>-10</sup>	0.9280	5.757x10 <sup>21</sup>
14	1436+ε	43.138x10 <sup>-10</sup>	0.8166	5.799x10 <sup>21</sup>
15	1515	45.457x10 <sup>-10</sup>	0.7328	6.071x10 <sup>21</sup>
16	1550	31.912x10 <sup>-10</sup>	0.6988	4.948x10 <sup>21</sup>
17	1600	31.526x10 <sup>-10</sup>	0.6860	5.028x10 <sup>21</sup>

Table 4.4 Invariant temperature and total invariant density calculated from CDAW-6 interval.

K	ALAM(K)	ETAB(K)
1	374.80640	0.86136E+20
2	1202.52612	0.15263E+21
3	2146.50952	0.19207E+21
4	3223.09546	0.21585E+21
5	4450.89844	0.22572E+21
6	5851.17187	0.22246E+21
7	7448.13672	0.20738E+21
8	9269.42187	0.18272E+21
9	11346.53120	0.15164E+21
10	13715.41020	0.11792E+21
11	16417.03520	0.85332E+20
12	19498.16410	0.56979E+20
13	23012.07810	0.34758E+20
14	27019.57030	0.19146E+20
15	31589.98440	0.93944E+19
16	36802.38670	0.62709E+19
17	-58.56357	0.86136E+20
18	-187.89493	0.15263E+21
19	-335.39233	0.19207E+21
20	-503.60913	0.21585E+21
21	-695.45410	0.22572E+21
22	-914.24683	0.22246E+21
23	-1163.77295	0.20738E+21
24	-1448.34888	0.18272E+21
25	-1772.89771	0.15164E+21
26	-2143.03564	0.11792E+21
27	-2565.16455	0.85332E+20
28	-3046.59180	0.56979E+20
29	-3595.64160	0.34758E+20
30	-4221.81250	0.19146E+20
31	4935.93750	0.93945E+19
32	-5750.37891	0.62709E+19

Table 4.5 A list of the energy channels (K), invariant energy (ALAM(K)), and boundary values at 20 Re and local midnight (ETAB(K)).

to be  $10^{1.48} \text{ cm}^{-2}\text{s}^{-1}\text{sr}^{-1}\text{eV}^{-1}$  (See Figure 4.3). The other parameters needed to solve equation 3.40 are:

ALAM(K) - energy invariant for energy K=32; =  $-5750.4 (\text{Re}/nT)^{2/3}$

VM - magnetic flux tube volume at 6.6 Re on dawn/dusk meridian

$$= 6.82 (\text{Re}/nT)^{-2/3}$$

$\lambda_{k\text{max}}$  - defined in equation 3.33a in Chapter 3

$$= -7451.8 \text{ eV} (\text{Re}/nT)^{2/3}$$

$\lambda_{k\text{min}}$  - defined in equation 3.32b in Chapter 3

$$= -5343.2 (\text{Re}/nT)^{2/3}$$

Solving for EETA(32), the invariant density at geosynchronous orbit is

$$\text{EETA}(32) = 1.666\text{E}17$$

The invariant density for K=32 at the back boundary is given in Table 4.4 as 0.6271E19.

The initial back boundary at local midnight at 15.87 Re. Solving equation 3.42 in Chapter 3 to get the power law coefficient:

$$\frac{\text{EETA}(\text{Geosynchronous})}{\text{EETA}(\text{Boundary})} = \frac{1.666\text{E}17}{0.627\text{E}19} = 0.0266 = \left[ \frac{6.6 \text{ Re}}{15.87 \text{ Re}} \right]^p$$

$$p = 4.134$$

Previous runs have shown the 'Kivelson' effect is not important for 40 keV electrons at local midnight, and it is neglected for adjusting the  $\eta$  values. Solving equation 3.44 in Chapter 3, the revised density becomes

$$\eta_{\text{tot}}(r) = (1.966\text{E}21) \left[ \frac{r}{15.87} \right]^{4.134}$$

The initial density values for entire grid are calculated using

$$\text{EETA}_{\text{initial}}(K,I,J) = \left[ \frac{\eta_p(\text{midnight})}{1.966\text{E}21} \right] \left[ \frac{r(LJ)}{15.87} \right]^{4.134}$$

where  $\eta_p(\text{midnight})$  is the initial value for energy species K at midnight.

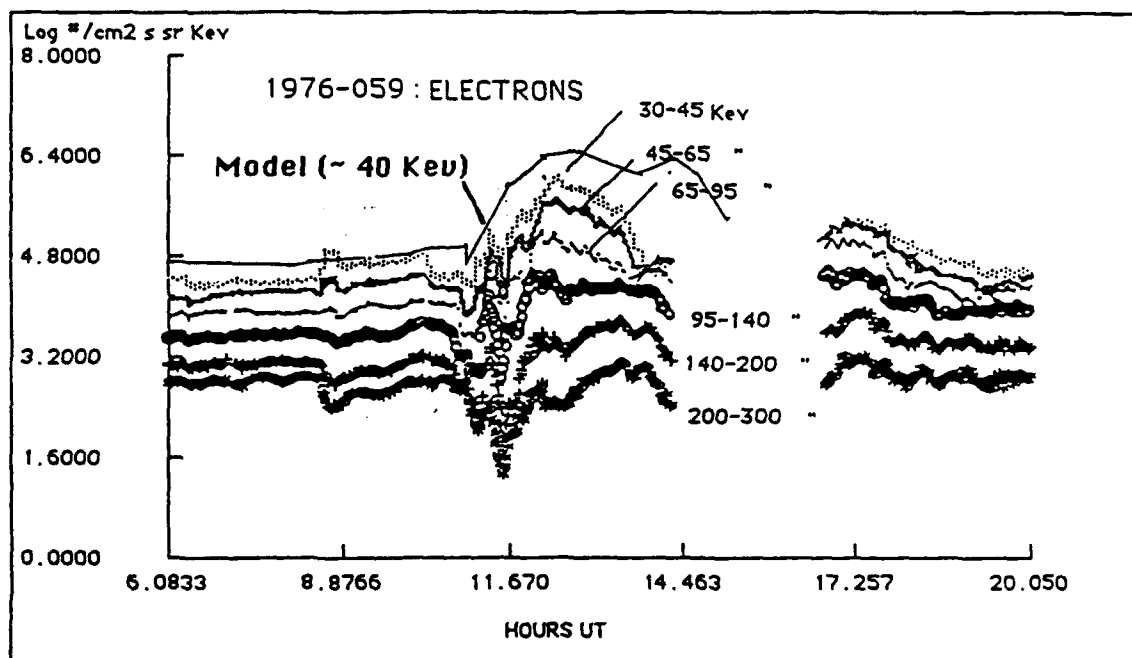
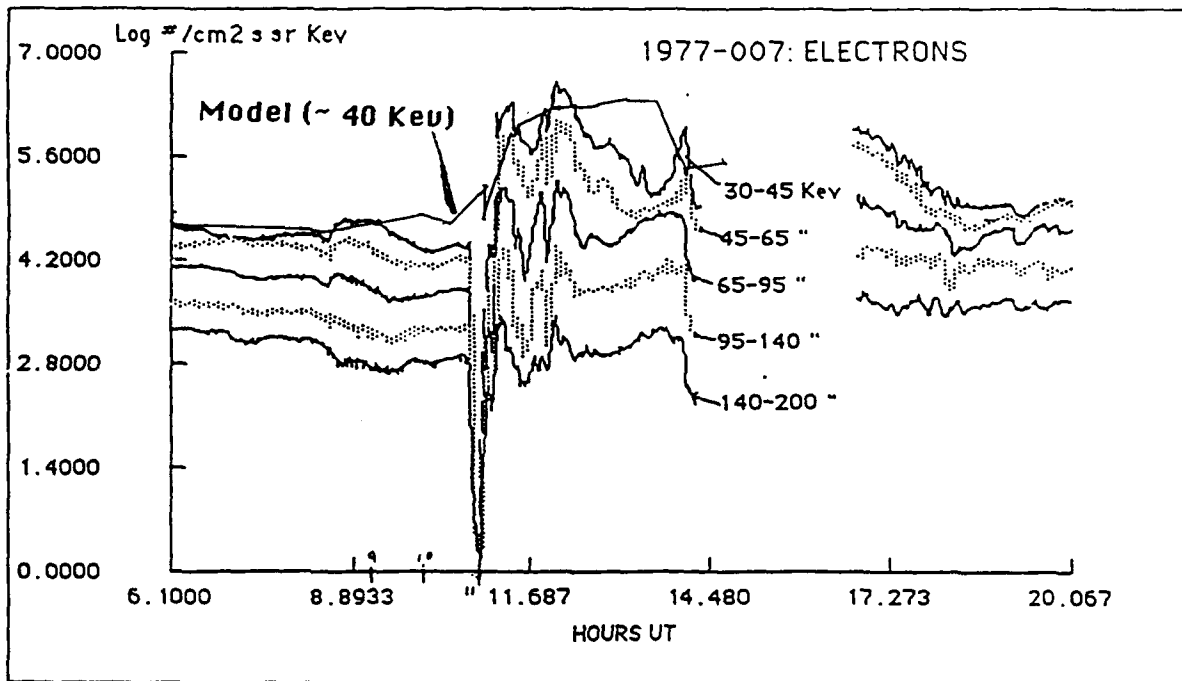


Figure 4.3 Calculated 40 keV geosynchronous electron flux values and 1977-077 and 1976-059 observed 40 keV electron flux values.



The plasma sheet depletion factor ( $f_{F_p}$ ) defined in equation 3.35 of Chapter 3 was set to 5 and was activated at the substorm onset at 10:54:01 UT.

### C. Model Results

Figure 4.4 shows the time evolution of the invariant density ( $\eta$ ) in the equatorial plane for our highest energy electrons ( $\sim 40$  keV at synchronous orbit). Figure 4.5 is a similar plot for "medium energy" ions ( $\sim 40$  keV at synchronous orbit); and Figure 4.6 represents low energy ions ( $\sim 2.5$  keV at synchronous orbit). The contours represent contours of constant  $\eta$ ; that is, constant numbers of particles per unit magnetic flux. The contours differ by a factor of  $10^{0.2}$  in density level. In the plots, the sun is to the left. The outermost contour represents approximately the outer boundary of our calculations. Some physical features include

- 1) Collapse of the magnetic field causes the inner edge of the plasma sheet near local midnight to move earthward approximately 1 Re at the onset of the expansion phase of the first substorm at 1054UT.
- 2) Electrons drift eastward after the injection, with high densities reaching local noon at approximately 1200UT.
- 3) Medium energy ions drift westward from the midnight region, leading to high densities at local noon beginning about 1200UT.
- 4) Subsequently the afternoon inner edge moves gradually earthward.

The output from the model was compared with data available from the CDAW-6 interval, which included

- 1) Available data from geosynchronous orbit
  - a) 1-16 keV ions in the afternoon sector just after noon UT (GEOS-2)
  - b) 40 keV electrons around 0200 LT at 1100UT (1977-077)
  - c) 40 keV electrons around dawn at 1100UT (1976-056)
- 2) Low orbit data

$\lambda = 5750$  electrons ( $\sim 40$  keV at synchronous orbit)

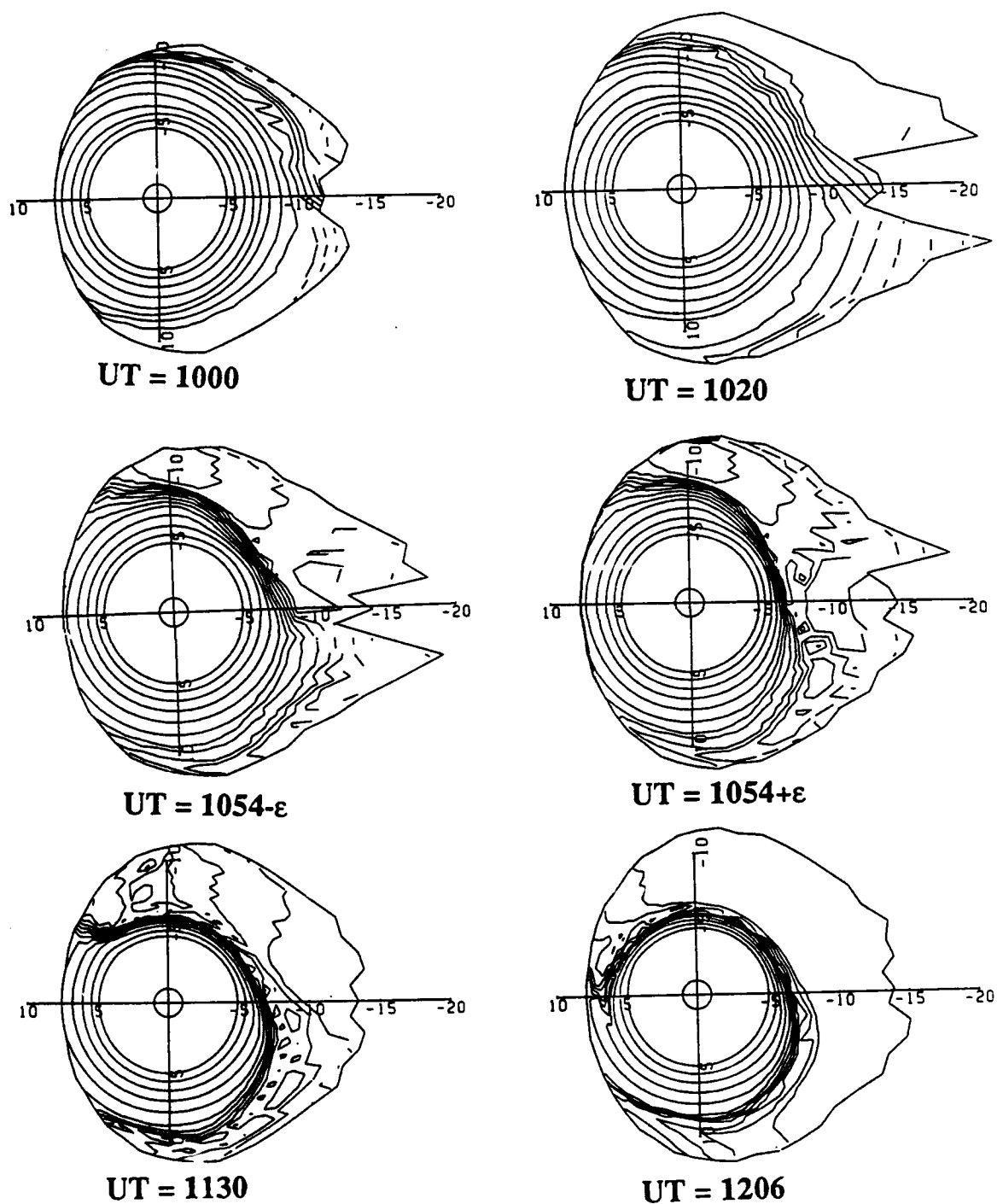


Figure 4.4 Time evolution of invariant density ( $\eta$ ) in the equatorial plan for highest energy electrons ( $\sim 40$  keV at geosynchronous).

$\lambda = 5851$  ions ( $\sim 40$  keV at synchronous orbit)

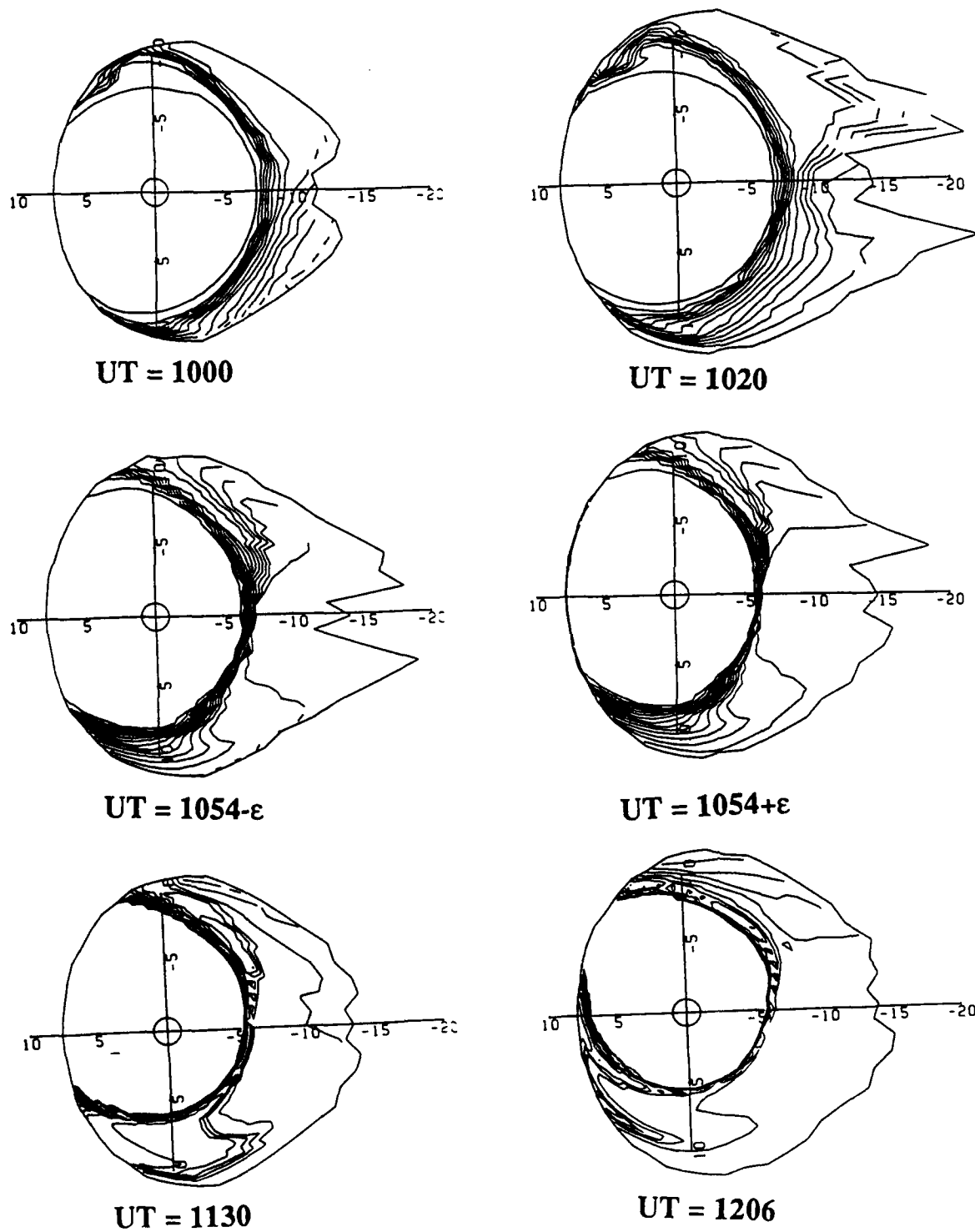


Figure 4.5 Time evolution of invariant density ( $\eta$ ) in the equatorial plan for medium energy ions ( $\sim 40$  keV at geosynchronous).

$\lambda = 375$  ions ( $\sim 2.5$  keV at synchronous orbit)

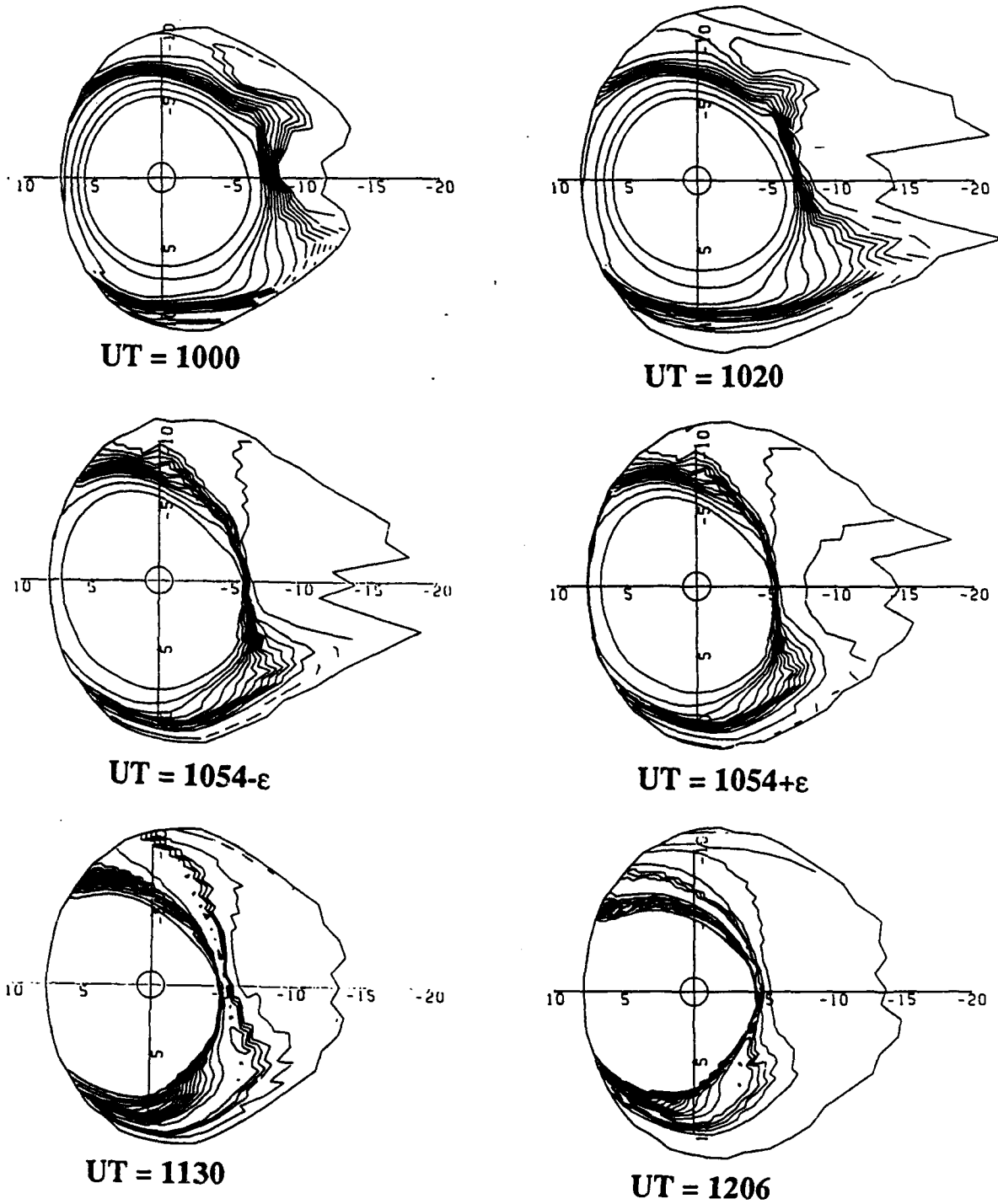


Figure 4.6 Time evolution of invariant density ( $\eta$ ) in the equatorial plan for low energy ions ( $\sim 2.5$  keV at geosynchronous).

#### a) Precipitating electron flux from DMSP

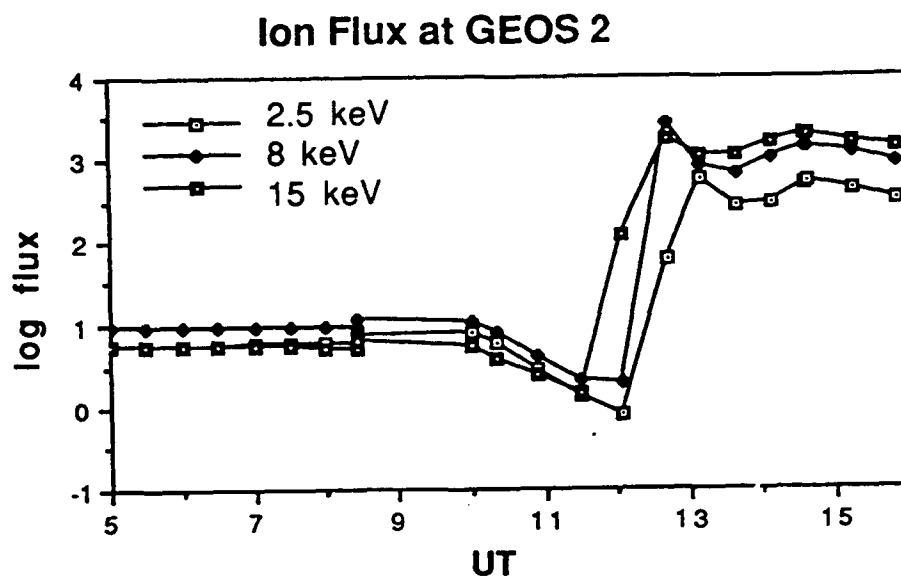
Figure 4.3 shows the electron flux measured at the geosynchronous satellites and compares them with the highest electron energy channel (K=32) in the model which corresponds to approximately 40 keV at geosynchronous orbit. The arrival times of approximately 1100UT for 1977-077 and 1130UT for 1976-059 show good agreement. However, in both cases the fluxes are too high by a factor of 2.

The ion energy channels for K=1, 2, and 3 in the model correspond approximately to geosynchronous energies of 2.5 keV, 8.0 keV, and 15.0 keV respectively. A comparison of the model ion flux with the GEOS-2 data is shown on Figure 4.7. Again the arrival times and energy dispersion are in good agreement with the 15 keV ions arriving around 1200UT, 8.0 keV ions arriving around 1230UT, and the 2.5 keV ions arriving about 1330UT. The peak fluxes show the same general tendency to be high by about a factor of 2.

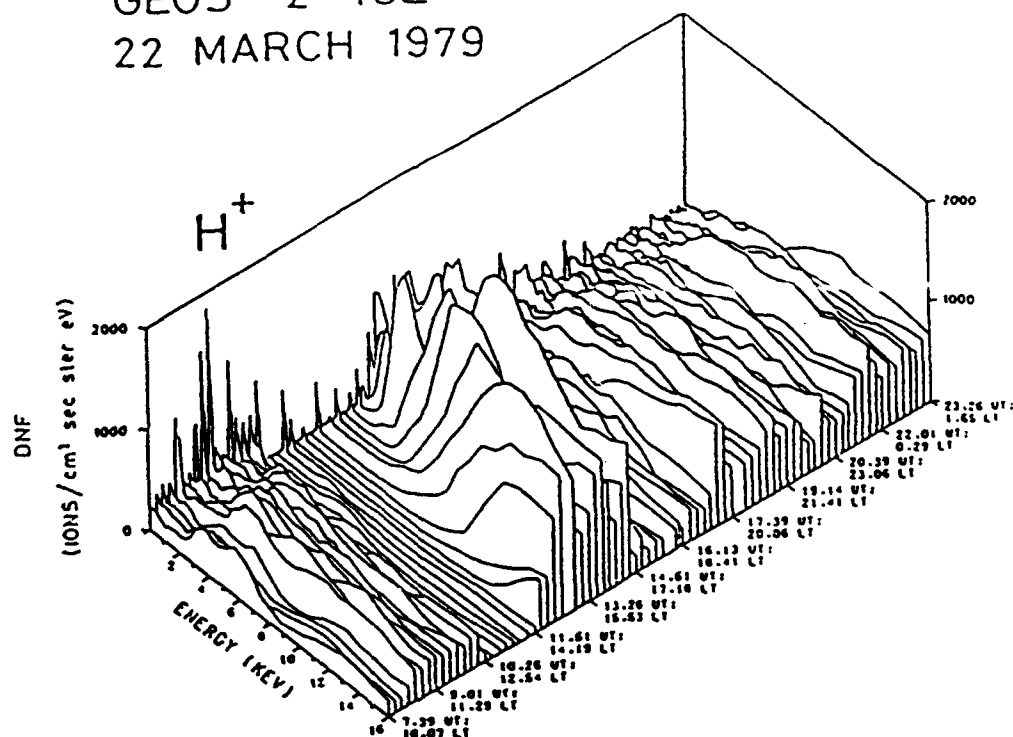
The graphs of the DMSP precipitating electron energy flux are given as Figures 4.8 and 4.9. The model values normalized to the data are represented by overlays. The model does not calculate precipitation in the region poleward of our main modeling region; that excluded region includes the polar cap and the higher-latitude part of the auroral zone so this is not included. The data shown in Figure 4.8 are for the pre-substorm period. In all three examples both the shape and the magnitude of the fluxes agree well with the satellite data. Figure 4.9 presents the results after the substorm onset and Figure 4.10 is the substorm recovery period. As with the geosynchronous fluxes, for both cases the magnitude is again too high by a factor of 2.

#### D. Interpretation and Implication

This model represents an attempted simulation of the inner-magnetosphere processes associated with magnetospheric substorms, including the magnetic field collapse at the onset of the substorm expansion phase and the subsequent injection of particles into



GEOS 2 ICE  
22 MARCH 1979



After Stokholm, Amata, Balsiger, Candidi, Orsini, and Anderson, J.  
Geophys. Res., 90, pp 1253-1261, 1985

Figure 4.7 Calculated ion flux values and GOES 2 observed ion flux values.

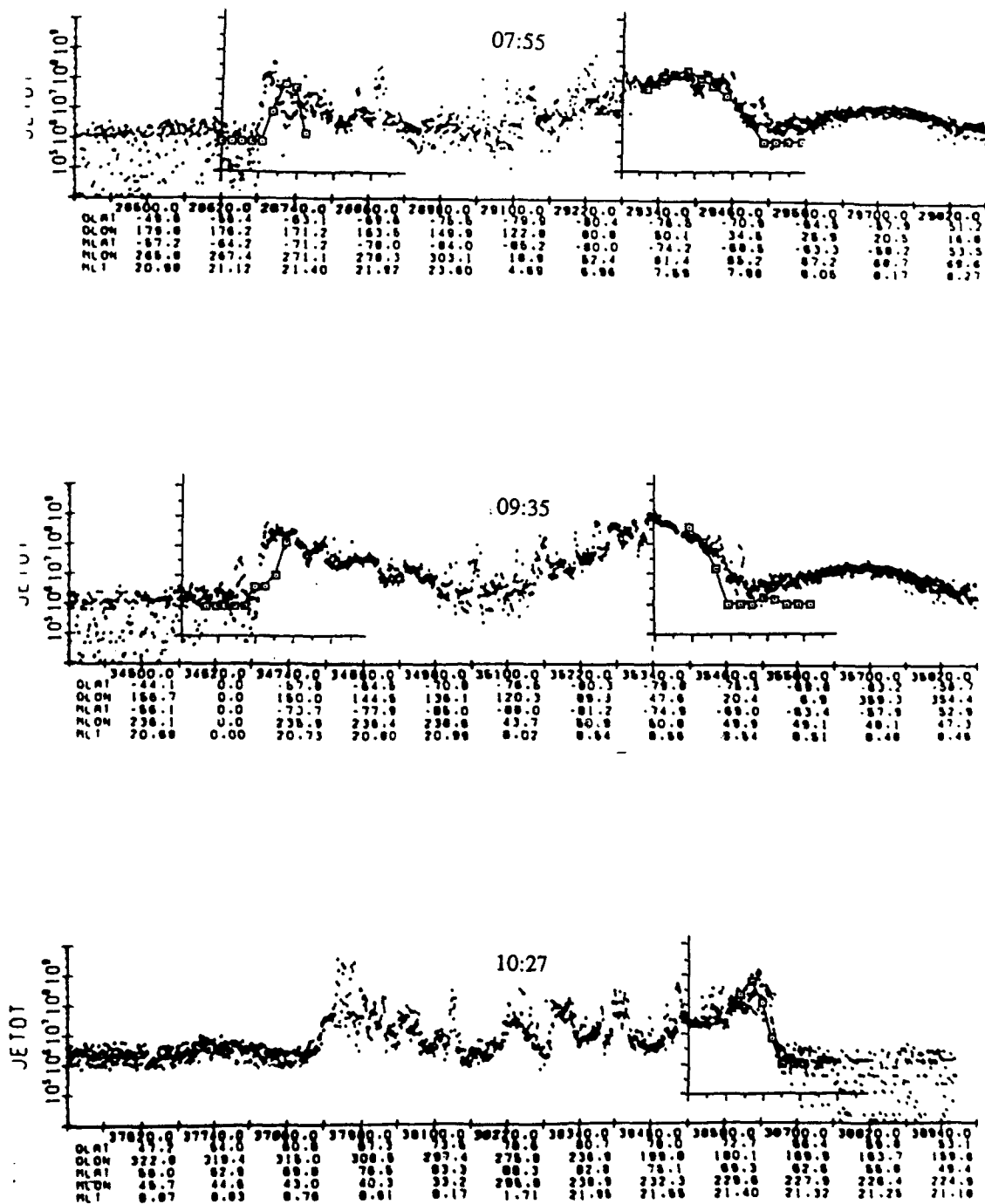


Figure 4.8 DMSP precipitating electron energy flux before substorm onset.

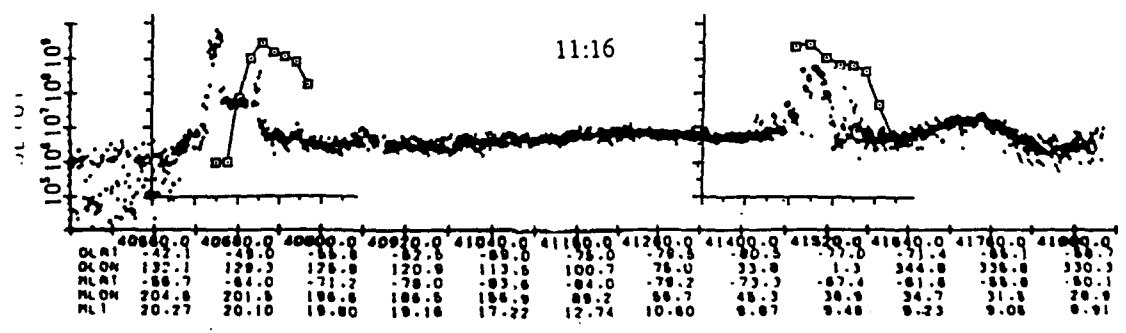


Figure 4.9 DMSP precipitating electron energy flux after substorm onset.



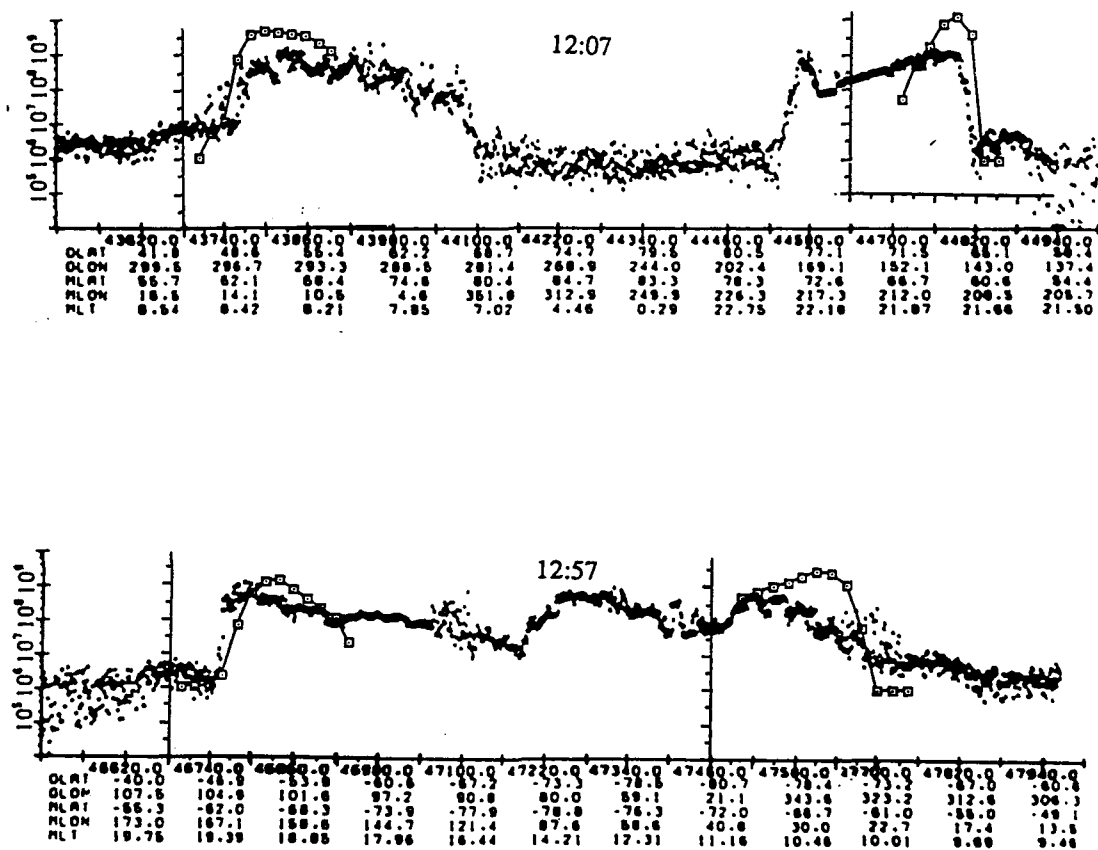


Figure 4.10 DMSP precipitating electron energy flux during substorm recovery period.

geosynchronous orbit. The arrival times of the electrons near dawn and the ions which have drifted to noon local time agree with the satellite data. However, assuming that middle plasma sheet flux tubes are convected adiabatically through the inner plasma sheet to synchronous orbit in a substorm with allowances for precipitation loss, the model results imply unrealistically high synchronous fluxes and unrealistically high precipitation rates. In addition, the modeled, geosynchronous 40 keV electron flux does not decrease during the recovery phase late in the event as the data shows. It may be that we are underestimating the pitch-angle scattering rate for these particles. The Hones (1979) substorm theory implies that a portion of the plasma on tail-plasma-sheet flux tubes escapes down the tail as a plasmoid. Therefore, for the initial model runs, we decreased the plasma sheet density by a factor of 2 at substorm onset. This still produced fluxes and precipitation too high by a factor of 5. The results presented here, from a later model run, assume a factor- of- 5 depletion after substorm onset. The model predictions and observations agree to within a factor of 2 in flux levels and precipitation. The implication is that the substorm process must involve a powerful electron loss process in addition to precipitation, or the flux tubes which convect into geosynchronous orbit have previously been depleted.

## V. CONCLUSION

### A. Summary of Results

The project to develop and test a model of the inner magnetosphere for the Air Weather Service has presented several challenges. First, there were stringent Air Force requirements to limit both the size and the run-time required to obtain results from the program. To this end, the Magnetospheric Specification Model represents a different approach to the efforts to model the inner magnetosphere. It is neither purely theoretical nor strictly empirical, but instead emphasizes the use of real-time data to improve the model's accuracy.

The second challenge was to examine how well the program results compared with actual measurements. To test the model's capability to simulate magnetospheric disturbances, we chose the well-documented CDAW-6 substorm on March 22, 1979. The large amount of satellite data available enabled us to follow the model results over a period of time from the initial quiet conditions through the substorm recovery and over a wide spatial area.

The most interesting challenge, of course, is the physical interpretation of the results and the understanding of the physics involved. One of the livelier controversies in magnetospheric physics today is the debate on what mechanisms are involved in the substorm process. Although not without critics, the most widely accepted theory of substorms involves the formation of a near-earth neutral line and the subsequent ejection of a plasmoid down the magnetotail. This means that a fraction of the particles are lost after a substorm. The Magnetospheric Specification Model provided us with the ability to try to quantify the fraction of particles lost.

The first attempt to simulate the depletion effect was simply to halve the number of particles in each flux tube at substorm onset. This produced geosynchronous 40keV

electron and 1-16keV ion fluxes and precipitating electrons a factor of 5 higher than those observed. The arrival times of the electrons and ions at synchronous orbit showed good agreement with the satellite data, however, which suggests that the electric field and magnetic field and the drift velocities calculated from these values must be reasonable accurate.

The results presented in chapter 4 include a reduction in the number of particles contained in a flux tube by 80% at substorm onset. That is, the plasmoid carries 80% of the particles down the tail. Again the modelled fluxes are high, but we are now within a factor of 2.

#### B. Possibilities for Further Study

During the recovery phase, the modelled 40 keV geosynchronous electron fluxes to not decrease as rapidly as those observed. This may imply that we are underestimating the pitch-angle scattering rate of these particles. Additional runs with the Magnetospheric Specification Model might lead to a more precise way of determining the pitch-angle scattering efficiency rate during quiet, disturbed, and recovery periods.

### APPENDIX A: Derivation of Electron Flux in Terms of Model Parameters

The formula used to calculate the differential particle flux ( $\text{cm}^{-2}\text{s}^{-1}\text{eV}^{-1}\text{ster}^{-1}$ ) in terms of a maxwellian distribution function  $f$  is

$$j = \frac{\int v f v^2 dv d\Omega}{dE d\Omega} \quad (\text{A.1})$$

Using  $E = 1/2 mv^2$  and assuming no mass is lost, we obtain

$$j = \frac{\int v f v^2 dv d\Omega}{m v dv d\Omega} = \frac{v^2 f}{m} \quad (\text{A.2})$$

Within the model  $\eta$  = number of particles/unit magnetic flux =  $n \times (\int ds/B)$ . In terms of a maxwellian distribution for species with energy  $k$ ,  $\eta$  for a given species  $k$  can be written

$$\eta_k = \int_{\frac{E_k + E_{k-1}}{2} < E < \frac{E_k + E_{k+1}}{2}} f v^2 dv d\Omega \cdot \int \frac{ds}{B} \quad (\text{A.3})$$

Integrating over the solid angle assuming an isotropic distribution function, and converting to energy, gives

$$\eta_k = f \times 4\pi v \left[ \frac{v_{k+1/2}^2}{2} - \frac{v_{k-1/2}^2}{2} \right] \int \frac{ds}{B} \quad (\text{A.4})$$

$$\eta_k = \frac{4\pi v}{m} \left[ \frac{E_{k+1} + E_k}{2} - \frac{E_{k-1} + E_k}{2} \right] f \int \frac{ds}{B} \quad (\text{A.5})$$

$$\eta_k = \frac{2\pi v}{m} (E_{k+1} - E_{k-1}) f \int \frac{ds}{B} \quad (\text{A.6})$$

Using the relationship  $E_k = \lambda (\int ds/B)^{-2/3}$  yields

$$\eta_k = \frac{2\pi f v}{m} (\lambda_{k+1} - \lambda_{k-1}) \left[ \int \frac{ds}{B} \right]^{1/3} \quad (\text{A.7})$$

$$\frac{f v_k}{m} = \frac{\eta_k}{2\pi} \times \left[ \int \frac{ds}{B} \right]^{-1/3} \left[ \frac{1}{\lambda_{k+1} - \lambda_{k-1}} \right] \quad (\text{A.8})$$

Multiplying both sides of equation (A.8) by  $v_k$  will give a relationship for  $j$  in terms of  $f$

in the same form as equation A.2.

$$j(E_k) = \frac{f v_k^2}{m} = v_k \frac{\eta_k}{2\pi} \times \left[ \int \frac{ds}{B} \right]^{-1/3} \left[ \frac{1}{\lambda_{k+1} - \lambda_{k-1}} \right] \quad (\text{A.9})$$

Solving for  $v_k$  in terms of model parameters

$$E_k = \frac{1}{2} m v_k^2 = |\lambda_k| \left[ \int \frac{ds}{B} \right]^{-2/3} \quad (\text{A.10})$$

$$v_k = \sqrt{\frac{2|\lambda_k|}{m}} \left[ \int \frac{ds}{B} \right]^{-1/3} \quad (\text{A.11})$$

Substituting (A.11) into (A.9)

$$j(E_k) = \sqrt{\frac{|\lambda_k|}{2m}} \frac{\eta_k}{\pi} \left[ \int \frac{ds}{B} \right]^{-2/3} \frac{1}{|\lambda_{k+1} - \lambda_{k-1}|} \quad (\text{A.12})$$

Within the program

$$\lambda_k = \text{ALAM}(K)$$

$$(\int ds/B)^{-2/3} = \text{VM}$$

$$|\lambda_{k+1}| = |\lambda_{k\text{max}}|$$

$$|\lambda_{k-1}| = |\lambda_{k\text{min}}|$$

$$\eta_k = \text{EETA}(K)$$

With the conversion from program units to ( $\text{cm}^{-2} \text{s}^{-1} \text{eV}^{-1} \text{ster}^{-1}$ ) and including the mass of the electron and the  $1/2\pi$  factor, the constant becomes  $7.392 \times 10^{-16}$ . The expression for the differential flux is then

$$\left[ \frac{d^2J}{dE d\Omega} \right]_{\text{cm}^{-2} \text{s}^{-1} \text{eV}^{-1} \text{ster}^{-1}} = 7.392 \times 10^{-16} \frac{|\text{ALAM}(K)|^{1/2} \times \text{VM} \times \text{EETA}(K)}{|\lambda_{k\text{max}}| - |\lambda_{k\text{min}}|} \quad (\text{A.13})$$

## REFERENCES

- Akasofu, S.-I., Polar and Magnetospheric Substorms, D. Reidel, Hingham, Massachusetts, 1968.
- Chiu, Y.T., R. Anderson, J. Fennell, L. Frank, R. Hoffman, M. Hudson, L. Lyons, P. Palmadesso, E. Ungstrup, R. Vondrak, D. Williams and R.A. Wolf, Connection between the Magnetosphere and Ionosphere, in Solar Terrestrial Physics: Present and Future, NASA Reference Publication 1120, D. M. Butler and K. Papadopoulos, eds., NASA, Washington, DC, 1984.
- Crooker, N. U., G. L. Siscoe, D. P. Mullen, C. T. Russell, and E. J. Smith, Magnetic Field Compression at the Dayside Magnetosphere, J. Geophys. Res., **87**, 10407, 1982.
- DeForest, S. E. and C. E. McIlwain, Plasma Clouds in the Magnetosphere, J. Geophys. Res., **76**, 3587, 1971.
- Dungey, J. W., Interplanetary Magnetic Field and the Auroral Zones, Phys. Rev. Letters, **6**, 47, 1961.
- Eastman, T. E., L. A. Frank, W. K. Peterson, and W. Lennartsson, The Plasma Sheet Boundary Layer, J. Geophys. Res., **89**, 1553, 1984.
- Gussenhoven, M. S., D. A. Hardy, and W. J. Burke, DMSP/F2 Electron Observations of Equatorward Auroral Boundaries and their Relationship to Magnetospheric Electric Fields, J. Geophys. Res., **86**, 768, 1981.
- Gussenhoven, M. S., D. A. Hardy, and N. Heinemann, Systematics of the Equatorward Diffuse Auroral Boundary, J. Geophys. Res., **88**, 5692, 1983.
- Goertz, C.K., and R.A. Smith, The Thermal Catastrophe Model of Substorms, J. Geophys. Res., **94**, 6581, 1989.
- Gonzales, C. A., M. C. Kelley, B. G. Fejer, J. F. Vickrey, R. F. Woodman, Equatorial Electric Fields during Magnetically Disturbed Conditions 2. Implications of Simultaneous Auroral and Equatorial Measurements, J. Geophys. Res., **84**, 5803, 1979.
- Harel, M., R. A. Wolf, P. H. Reiff, R. W. Spiro, W. J. Burke, F. J. Rich, and M. Smiddy, Quantitative Simulation of a Magnetospheric Substorm 1, Model Logic and Overview, J. Geophys. Res., **86**, 2217, 1981a.
- Harel, M., R. A. Wolf, R. W. Spiro, P. H. Reiff, C.-K. Chen, W. J. Burke, F. J. Rich, and M. Smiddy, Quantitative Simulation of a Magnetospheric Substorm 2, Comparison with Observations, J. Geophys. Res., **86**, 2242, 1981b.
- Heppner, J. P., and N. C. Maynard, Empirical High-Latitude Electric Field Models, J. Geophys. Res., **92**, 4467, 1987.

- Hilmer, R. V., A Magnetospheric Magnetic Field Model with Flexible Internal Current Systems, Rice University PhD. Thesis, Houston, Texas, 1989.
- Hones, E. W., Jr., Plasma Flows in the Magnetotail and its Implications for Substorm Theories, in Dynamics of the Magnetosphere, S.I.- Akasofu, ed., D. Reidel Publ. Co., Dordrecht, Holland, 545, 1979.
- Iijima, T., and T. A. Potemra, Field-Aligned Currents in the Dayside Cusp Observed by TRIAD, J. Geophys. Res., **81**, 5971, 1976.
- Kan, J.R., L. Zhu, and S.-I. Akasofu, A Theory of Substorms: Onset and Subsidence, J. Geophys. Res., **93**, 5624, 1988.
- Kaye, S. M. and M. G. Kivelson, Time-Dependent Convection Electric Fields and Plasma Injections, J. Geophys. Res., **84**, 4183, 1979.
- Kelley, M. C., B. G. Fejer, and C. A. Gonzales, An Explanation for Anomalous Equatorial Ionospheric Electric Fields Associated with a Northward Turning of the Interplanetary Magnetic Field, Geophys. Res. Lett., **6**, 301, 1979.
- Kivelson, M.G. and H. E. Spence, On the Possibility of Quasi-Static Convection in the Quiet Magnetotail, Geophys. Res. Lett., **15**, 1541, 1988.
- Lu, G., P. H. Reiff, M. R. Hairston, R. A. Heelis, and J. L. Karty, Distribution of Convection Potential Around the Polar Cap Boundary as a Function of the Interplanetary Magnetic Field, J. Geophys. Res., **94**, 13,447, 1989.
- McIlwain, C. E., Substorm Injection Boundaries, in Magnetospheric Physics, B. M. McCormac, ed., D. Reidel, Hingham, Mass., p. 143, 1974.
- McPherron, R. L., and R. H. Manka, Dynamics of the 1054 UT March 22, 1979, Substorm Event: CDAW 6, J. Geophys. Res., **90**, 1175, 1985.
- Moore T. E., R. L. Arnoldy, J. Feynman, and D. A. Hardy, Propagating Substorm Injection Fronts, J. Geophys. Res., **86**, 6713, 1981.
- Nishida, A., Geomagnetic DP-2 Fluctuations and Associated Magnetic Phenomena, J. Geophys. Res., **73**, 1795, 1968a.
- Nishida A., Coherence of Geomagnetic DP-2 Fluctuations with Interplanetary Magnetic Variations, J. Geophys. Res., **73**, 5549, 1968b.
- Northrup, T. G., The Adiabatic Motion of Charged Particles, Interscience Publishers, New York, 1963.
- Paschmann, G., N. Sckopke, and E. W. Hones, Jr., Magnetotail Plasma Observations During the 1054 UT Substorm on March 22, 1979 (CDAW 6), J. Geophys. Res., **90**, 1985.
- Reiff, P. H., and J. G. Luhmann, Solar Wind Control of the Polar Cap Voltage, Solar Wind-Magnetosphere Coupling, edited by Y. Kamide and J. Slavin, pp 453-476, Terra Sci. Publ. Co., Tokyo, 1986.